Title	Improving mechanical properties and reliability of eutectic Sn58Bi alloy and its joints by modified composition
Author(s)	Zhou, Shiqi
Citation	大阪大学, 2019, 博士論文
Version Type	VoR
URL	https://doi.org/10.18910/73571
rights	
Note	

Doctoral Dissertation

Improving mechanical properties and reliability of eutectic Sn58Bi alloy and its joints by modified composition

Shiqi Zhou

July 2019

Graduate School of Engineering
Osaka University

Supervisor

Professor Hiroshi Nishikawa, Ph. D.
Joining and Welding Research Institute
Osaka University

Doctoral Committee

Professor Hiroshi Nishikawa, Ph. D.
Joining and Welding Research Institute
Osaka University

Professor Michihiko Ike, Ph. D.
Division of Sustainable Energy and Environmental Engineering, Graduate School of Engineering
Osaka University

Professor Soshu Kirihara, Ph. D.
Joining and Welding Research Institute
Osaka University

Associate Professor Shinji Fukumoto, Ph. D.
Division of Materials and Manufacturing Science, Graduate School of Engineering
Osaka University

Contents

Chapter 1

Chapter 2

Chapter 3

Chapter 4

Chapter 5

Chapter 6

List of figures

List of tables

Chapter 1

Research Background

1.1 Electronic Packaging

1.1.1 By now

The semiconductor integrated circuits (ICs) are fundamental to electronic industries. IC design, electronic packaging, and fabrication are three key components for realization of the function required in electronic devices. In detail, the “package” describes the “bridge” that interconnects ICs, components, substrates, and boards to form an electronic product.

An electronic packaging is defined as an electronic encapsulation which can protect interiors, such as chips and circuits from exterior environment. Moreover, electrical, thermal and functions were provided by electronic packaging [1].

In the late 1940s, transistor was discovered leading to the beginning of microelectronic packaging technology. To date, it has been continued to evolve and to serve the increasing complexity and performance of ICs. In the early days, microelectronic packaging was relatively easy to realize, for example, connecting diodes and housing transistors in plastic packages. With the development of microelectronics, packaging technology evolved greatly. During the 1960s and 1970s, dual-in-line (DIP) was invented. DIP is the packaging type where pins are perpendicular to the body. Automatic insertion machinery was need to place package. In the 1980s, DIP was replaced by surface-mount technology (SMT) in order to perusing a higher packaging density. Quad flatpacks (QFPs) and thin, small outline packaging (TSOP) are two typical SMT types. To achieving the fine packaging space and miniaturized circuit path length, in 1990s, ball-grid-array (BGA) packaging emerged, owing to its high I/O density and shorter electrical path. The electronic industry experienced an explosion of BGA designs, the latest examples, such as System-in-Package (SIP) and three-dimensional (BGA) package, can be beneficial to the latest electronic devices. Since then, the BGA packaging has been considered as a standard for high-density and high I/O ICs.

1.1.2 Future

The next generation of integrated micro-system technologies can only keep up with the functionality and performance demands by using third dimension. 3D integration technology can be grouped into three categories, namely 3D on-chip integration, 3D IC-stacking, and 3D packaging [2].

Figure 1-1 shows a schematic example of five individual functional blocks integrated into two types of micro-systems. Traditionally, these functional blocks are integrated at 2-Dimension (2D) on a Print Wiring Board (PWB). In 3D structure, each functional blocks are stacked on top of each other. Each block is connected with each other via vertical interlayer interconnects. This innovation enables form-factor shrinkage of micro-system. In other words, X and Y dimensions reduced significantly with very small increase in Zn dimension. System performance was therefore improved owing to the reduction of interconnect length.

By now, some technologies related to the 3D packaging has been currently developed. Three categories can be divided for a detailed explanation.

First, 3D on-chip integration. As a vertical extension of IC technology, semiconductor device layers are subsequently built on top of the previous IC layer. Most of these technology is still under investigation and design [3].

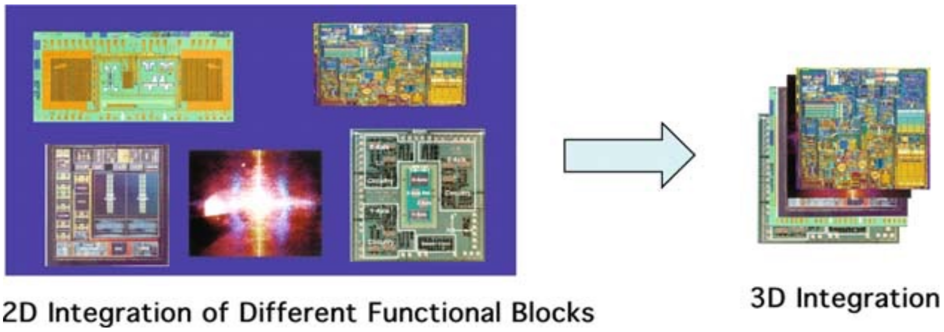

Figure 1-1 Integrated microsystem in 2D and in 3D [2].

Secondly, 3D IC-stacking with Thru-Silicon Vias (TSVs). Individual wafers or ICs are fabricated first and then they are stacked in 3D form factor with TSVs which providing interconnection capability. Recently, this technology has been mostly investigated. Figure 1-2 shows a wafer level version of this technology.

Last but not least, 3D packaging. This is the least disruptive way of integrate ICs in 3D dimension. Two categories can be divided, wire-bonded die-stack and BGA-stack, as shown in Figure 1-3. These two types of 3D packaging technology have been widely used in consumer products currently.

However, there are still many issues need to be addressed before 3D IC-stacking technology can be fully commercialized. The author here lists two main issues, namely thermal management and cost.

Thermal management: the extend of the thermal problem for application using 3D IC technology is currently not well understood and still under evaluation. The solutions are several. Using more efficient and advanced cooling concept, such as micro-gap cooling; Architecture design of the functional blocks, such as avoiding having two heat-generating functional blocks in close proximity to each other.

Cost: Thru-Si via technology used in 3D IC-stacking is expensive because of high capital investment as well as high direct production cost. However, with the technology maturation and higher production volume, like many technologies involved in the past, the cost will come down.

In recent years, wearable electronics have been the trend in electronic industries, due to the integration of mobile technology and portable electronic technologies. Traditional electronics are based on the integrated circuits which are mostly manufactured in rigid and

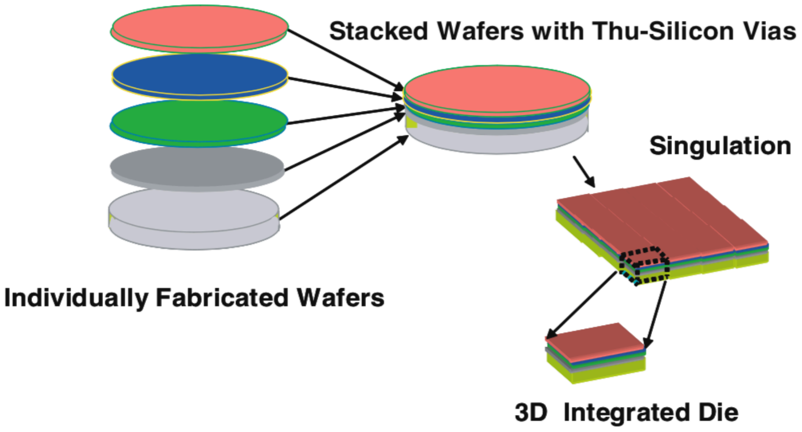

Figure 1-2 Wafer level version of 3D packaging [2].

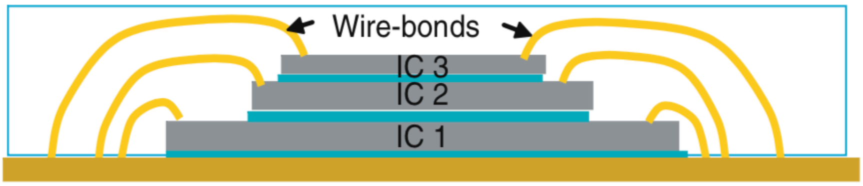

(a) Wire-bonded Die-Stack

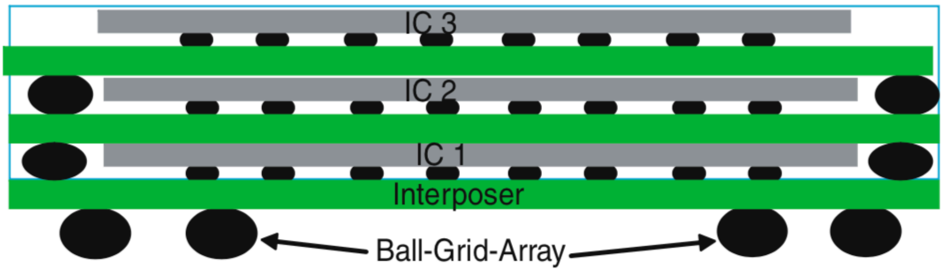

(b) BGA-Stack

Figure 1-3 Two samples of 3D packaging [2].

planar semiconductor wafers. Wearable devices, however, are integrated on soft or moving objects such as wrinkled clothes and human skin. These devices including, flexible battery, flexible display, comfortable RFID tags, biomedical instruments, etc. In contrast with the traditional electronics, wearable devices tend to undergo large mechanical deformation and still require high performance. Therefore, new materials, such as graphene, carbon nanotubes and conductive polymer, etc. have been constantly developing to meet the demand of the flexible technology [4].

1.2 Solder interconnection in electronic packaging

Solder has been used to join copper wire for circuity connection in nearly every electronic product these days. The essential process in solder joining is the chemical reaction between copper and tin to form intermetallic compounds, resulting in a strong metallic bonding.

1.2.1 Lead-free soldering

Traditionally, a solder alloy consisted of lead and tin were used to join copper parts. In the early 1990s, a series of legislations were proposed for banning the use of lead for many applications in electronic industries. This argument raised word attention on developing lead-free solders. After several years of researching and development, a number of institutes, including the National Center of Manufacturing Science (NCMS) in the U.S. and the Japan Institute of Electronics Packaging (JIEP), and the Japan Electronics Industry Development Association (JEIDA) in Japan, etc. collected their efforts in producing a ‘road map’ for lead-free solders in small-scale mass production and collecting reliable information. In 1998, the environmental committee of European Union (EU) issued proposal for the directives on Waste Electrical and Electronic Equipment (WEEE) and the Restriction of the Use of Hazardous Substances (RoHS), which were finalized by early 2002. This proposal called ban on using heavy metals such as Pb, Hg, Cd, etc. with the exception of some applications that cannot be replaced by another current technology. Owing to the driving force of this proposal, activity on developing lead-free solders has increased since then.

In these developing progress, the new lead-free solder alloys have been always compared with the traditional near eutectic Sn-Pb alloys. The general performance of these lead-free solders therefore, will be expected equally will or surpass their counterparts in most aspects. Some basic requirements should newly develop lead-free solder follow are listed below [5][6][7][8].

- Reduce surface tension of pure Sn to improve wettability.
- Enable quick IMC formation between solder and substrate by diffusion.
- Keep the melting point around 183 ℃ with eutectic or near-eutectic composition.
- Prevent the occurrence of Tin whisker growth.

Table 1-1 summarizes some of the lead-free solder candidates. Solders for soldering processes, i.e., wave and reflow soldering are listed. Among them, Sn-3Ag-0.5Cu alloy is one of the best alloys for all types of soldering processes, owing to its excellent reliability and good

Table 1-1 Some Lead free solders in Japanese Market [5], [8].

Lead-free solder candidates		
Soldering process	Category	Alloy
Wave soldering	Sn-Ag	Sn-3.5Ag, Sn-3Ag-0.5Cu
	Sn-Cu	Sn-0.7Cu with additions: Au, Ag, Ni, Ge, In, etc.
Reflow soldering	Sn-Ag	Sn-3.5Ag, Sn-3Ag-0.5Cu, Sn-(2-4)Ag-(1-6)Bi-(1-3)In
	Sn-Zn	Sn-9Zn, Sn-8Zn-3Bi
	Sn-Bi	Sn-47Bi-(0.5-1)Ag

reliability. However, it is not suitable for Sn-Pb surface-finished component for through-hole circuits.

In April 2000, the new roadmap for lead-free soldering was released by JEITA (former JEIDA). Due to the lift-off problem for wave soldering is difficult to overcome until all components are all plated with lead-free solders, reflow soldering with lead-free solders has been introduced ahead of wave soldering. In recent years, various roadmaps, such as ITRI [9] and IPC [10] roadmaps of lead free solder were introduced, Another key point of lead-free solder promotion is the head-resistance of components and PWBs,

1.2.2 Surface finishes

Traditionally, Cu is used for package-side pads and board-side PCB pads. Cu can react with Sn forming strong Cu-Sn intermetallic compound layer (IMC). However, exposure of Cu can be easily oxidized in air, causing dewetting and other solderability problems. In order to prevent oxidation, a coating layer is applied on top of the Cu pads. This coating layer is also known as surface finish. Surface finish not only prevent Cu from oxidation, but also act as a diffusion barrier layer between Cu and solder, slowing down the reaction. Moreover, surface finish can accelerate wetting. Some surface finishes are widely used in the industry. Such as, organic solderability preservatives (OSP) [11], [12], solder on pad (SOP) [13]–[15], Immersion Sn (ImSn) [16]–[19], Electrolytic Ni gold (NiAu) [20], [21], electroless nickel immersion gold (ENIG) [22], [23], and electroless nickel/electroless palladium/immersion gold (ENEPIG) [22], [24]. In this thesis, ENIG is the surface finish the author selects to produce solder joint [25].

ENIG is formed by the deposition of electroless nickel-phosphorus (Ni-P) layer on a Cu surface, all below a thin layer of immersion gold. ENIG has been widely used in industry due to its low-cost, diffusion barrier ability against reaction with solder, as well as good wettability and solderability. The role of immersion gold is protecting nickel layer from oxidation. The drawback of ENIG surface finish is that electroless nickel layer is brittle and prone to break during mechanical stress. Also, a galvanic hypercorrosion occurs on Ni-P layer due to Au layer solution, which as known as “black pad” [25].

The reaction evolution on a SAC/ENIG interface is illustrated in Figure 1-4. In the step one, immersion gold layer dissolves into solder very quickly during the bonding process. Then, Ni dissolves into solder and reacts with Sn, forming Ni_3Sn_4 and Ni_3Sn_2 IMCs on top of the Ni-P layer. Due to the consumption of Ni, a P-rich zone may form in between the Ni-Sn IMC and Ni-P layer. Continuing reaction, Ni_3Sn_4 reacts with Cu, forming $(Cu, Ni)_6Sn_5$ with the increase

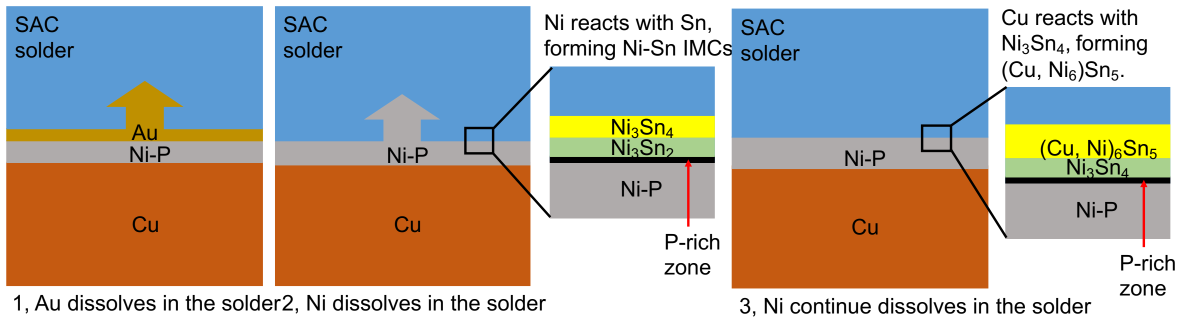

Figure 1-4 Schematic illustration of the reaction evolution on SAC/ENIG interface.

of IMC layer thickness. The reason of IMC composition change is that, Cu_6Sn_5-based IMC containing with Ni is the main phase SAC/Ni interface, providing the SAC solder containing Cu higher than 5 wt.% [26]. Additionally, Ni has a high solubility in Cu_6Sn_5, by replacing Cu atom sublattice and forming $(Cu, Ni)_6Sn_5$, which reported has 9 kJ/mol less Gibbs free energy and much stable than Cu_6Sn_5 [27].

1.2.3 Reflow soldering process

Reflow soldering process is designed to assemble electronic components on boards, such as PCBs. The electronic components firstly temporary attached to their contact pads by using solder paste (a mixture of powdered solder and flux). Then, the entire reflow process is subjected to controlled heat. The solder paste being reflowed in a molten state, after solidification, permanent solder joints were made. Traditionally, reflow soldering with a long industrial convection oven is a preferred method for soldering surface mount components to PCBs. Each segment of the oven has a regulated temperature, according to the specific thermal requirement of each assembly. The temperature profile allows solder reflowed on a substrate without damaging electronic components by exceeding their temperature tolerance. Basic reflow soldering profile usually involves three stages, i.e., preheat, reflow and cooling [25].

i. Preheat: this is the first stage of the reflow process. During this phase, the entire assembled board reaches a dwell temperature. The goal of preheat is to get the entire assembly safe and constantly to a preheat temperature in order to eliminate thermal shock during the temperature increasing afterwards. Another benefit of preheat is to volatile and to activate fluxes in solder pastes. The activation temperature really determines the preheat temperature. Too high a temperature can lead to solder spattering as well as oxidation of the pastes, the components and the pads. Fluxes may not be activated if the temperature is too low.

ii. Reflow: as known as ‘time above liquidus (TAL)’. this is the stage where maximum reflow temperature is reached. The peak temperature is limited by the component in assembly with the lowest tolerance for high temperature. It is important to monitor the reflow process temperature to keep it from exceeding its limit. A common peak temperature is set 20-40 ℃ above liquidus.

iii. Cooling: this last step of reflow process is a cooling zone to gradually cool the processed board and solder joints. A proper cooling can eliminate thermal shock to the components.

Two standard board assembly reflow profiles are shown in Figure 1-5. These two thermal profiles have same time at peak temperature (TAP). However, due to different peak temperature and heating speed, time above liquidus temperatures (TAL) are different.

All in all, each reflow profile should be designed based not only on solder materials, but also on the specific practical use.

1.2.4 Solder interconnects

After previous discussion of solder materials, surface finishes and reflow soldering process. Solder joint interconnection can be realized by applying these processes. To these days, the most advanced electronic packaging techniques is 3D packaging, which is the solution of high level integration and miniaturization.

Figure 1-6 shows a simple structure of 3D packaging; some packaging technologies are shown as well. For example, 3D IC, 3D wafer-level packaging (WLP), flip-chip packaging

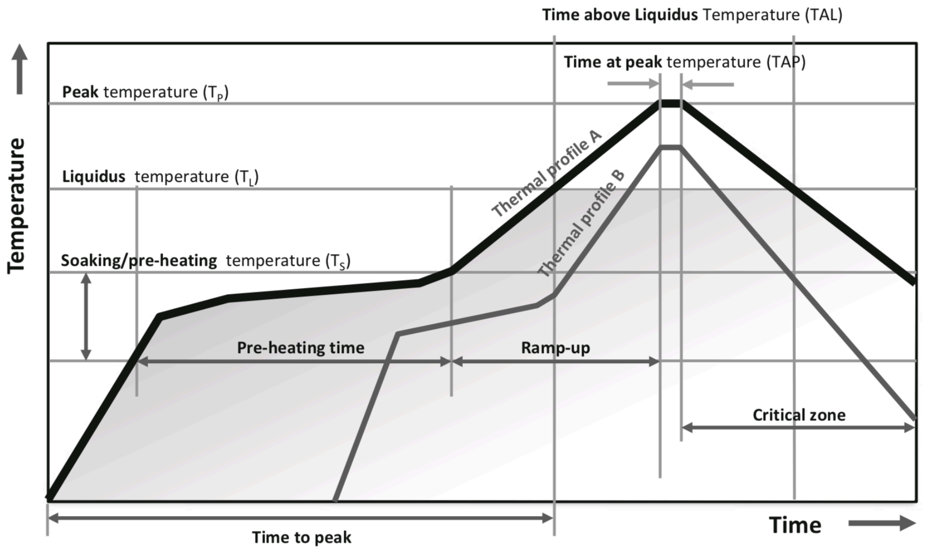

Figure 1-5 Reflow profiles [9].

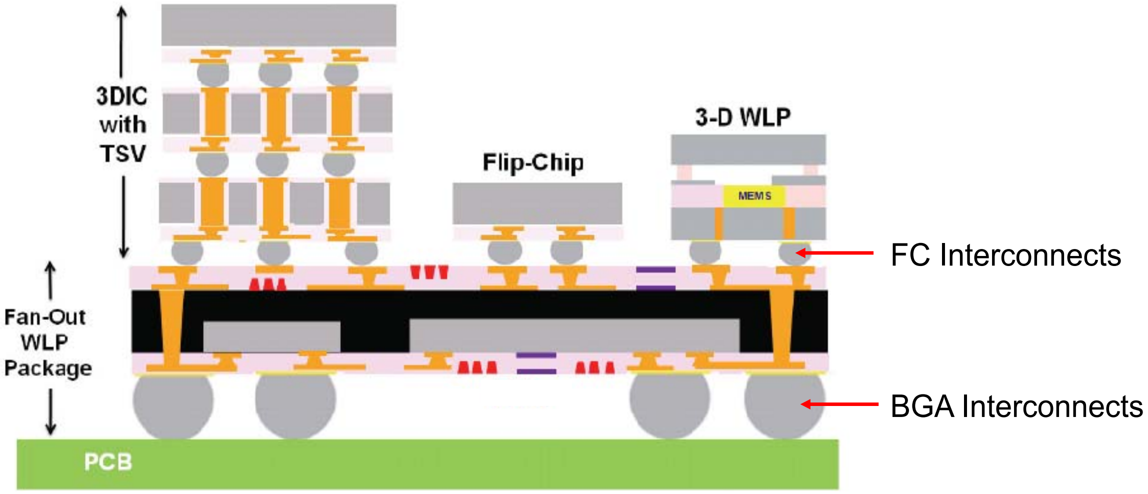

Figure 1-6 Illustration of 3D packaging [12].

(FC). All in all, solders are important interconnection materials for packaging technology, two types of solder interconnect are listed below.

i. FC interconnection

   FC is the interconnection technology between silicon dies and substrates. Silicon dies in this case are flipped upside down, facing substrates. In general, the solder bump with the diameter around of 100 μm are used.

ii. BGA interconnection

   The size of BGA bumps are relatively large, with around several hundred micrometer. They are applied to assemble packaged ICs with PCBs.

1.2.5 Effects of additives in solder

Adding minor additives into solder materials has been approved as an efficient method of refining microstructure and improve mechanical properties both solder alloy bulk and solder joint. Various kinds of additives have been added into solder materials, such as SAC, eutectic Sn58Bi etc. as well as for solder joints for improving mechanical properties and reliability. The followings are some examples for eutectic Sn58Bi alloy bulk and joint.

For alloy bulk, Yang et al. [28] have reported the improvement in the UTS and YS of Sn58Bi alloy by 1 wt % Ni addition and Ni restrains the structure coarsening. Li et al. reported that a 0.05 wt.% nanoscale Cu_6Sn_5 particle addition can refine the eutectic Sn58Bi alloy microstructure and increase the elongation, but decrease the ultimate tensile strength (UTS) [29]. Yang et al. showed that the introduction of a 0.07 wt.% nanosized graphite significantly increased the eutectic Sn58Bi elongation [30], but simutaniusly decreased the UTS.

McCormack et al. found that the addition of a small amount of Ag improved the Sn55Bi alloy elongation three times [31]. Mokhtari and Nishikawa [32], reported that the elongation increment of indium-added Sn58Bi alloys was obtained, but the UTS showed a decrease in their results. Recently, the addition of copper (Cu) [33], carbon nanotube [34] and zinc (Zn) [33], [35], [36] also have been investigated for improving the mechanical properties. The detailed discussion of effects of additives in eutectic Sn58Bi will be held in section 1.4.1.

For solder joint, Li and Chan [37] have reported that the addition of 76-nm-sized silver nanoparticles effectively refines the microstructure of the Sn58Bi alloy, suppresses the IMC layer growth and improves the as a result improves shear strength. Nowottnick et al. [38] proposed the barrier Al-Cu layer at solder/Cu interface by minor Al addition to eutectic Sn58Bi alloy. However, the oxidation of Al is severe. Addition of minor amount of Co into eutectic Sn58Bi suppresses the Cu_3Sn IMC layer growth, since Co has a low solubility in Cu_6Sn_5 IMC layer [39]. Ga addition was also found to be effective in suppressing the IMC layer between Sn58Bi solder and Cu substrate [40]. An incomplete summery of the effects of additives on Sn-Bi based alloys was listed in Table 1-2. The effects concluded in the table were the results of each individual study, therefore, it was not appropriate to compare them across studies, since different testing conditions were provided. However, we can get the idea of what impacts these additives can give on Sn-Bi based alloys.

1.3 Low-temperature solder materials

1.3.1 Low-temperature lead-free soldering

Because the melting temperatures of newly developed lea-free solders differ from traditional Sn-Pb solder, the reflow process must be modified accordingly. Table 1-3 lists a number of lead-free solders with their melting temperatures [5]. It is noted that most of the Pb-free solders have a melting temperatures higher than that of eutectic Sn37Pb alloy (183 ℃). A higher melting temperature requires a reflow profile with a higher peak temperature. The increase of the peak temperature always results in reliability issues. It is noted that several materials are usually composed of a packaged chip, such as, polymeric PCBs, polymeric molding components, silicon dies and metallic conductive layers. These materials have different coefficient of thermal expansion (CTE). During the reflow soldering process, materials with different CTE extent differently, resulting in different level of thermal mismatch

Table 1-2 Effects of additives on eutectic Sn-Bi based alloy and its solder joints.

Additives (composition, wt.%)	Microstructure	Elongation	UTS	Solder/substrate IMC layer
Ni (1)	Refine	-	Increase	-
Cu6Sn5 nanoparticle (0.05)	Refine	Increase	Decrease	-
Graphite (0.07)	Refine	Increase	Decrease	-
Ag (1)	Refine	Increase	Decrease	-
In (0.5)	-	Increase	Decrease	Suppress (on ENIG)
Zn (1)	Refine	Increase	Increase	Suppress (on Cu and ENIG)
Ti (0.5)	Refine	Decrease	Increase	Suppress (on ENIG)
Cu (0.1)	Refine	Increase	Increase	-
Ag nanoparticle (1)	Refine	-	-	Suppress (on Cu)
Al (N/A)	-	-	-	Suppress (on Cu)
Co (1)	-	-	-	Suppress (on Cu)
Ga (0.25-0.3)	-	-	-	Suppress (on Cu)

and thermal stress inside the chip. Moreover, high reflow peak temperature can lead to thermal shock to the temperature sensitive components.

On the other hand, in recent year, an increasing number of companies are focusing 2.5D and 3D packaging using silicon interposer. Benefits of 2.5D and 3D packaging on high-end server and CMOS image sensor were widely reported, since improved electronic performance and miniaturization can be achieved [41]–[43]. It is worth mentioning that 2.5D and 3D packaging require high bonding accuracy to achieve high reliability. Therefore, a low-stress and low-temperature bonding process is the key to achieve these higher dimensional packaging.

The general knowledge is that a solder alloy with melting temperature between 183 ℃ to 50 ℃ can be called low-temperature solders [44]. In fact, low-temperature soldering has been a subject of research in HP's Electronic Assembly Development Center (EADC). Some

Table 1-3 Example of lead-free solders with different melting ranges.

Alloy system	Composition	Melting range (℃)	Remarks
Bi-In	Bi-33In (eutectic)	109	Brittle Bi, high-cost, melting point too low for some applications
Sn-In	Sn-52In	118	High-cost
	Sn-50In	118-125	
Sn-Bi	Sn-58Bi (eutectic)	138	Low-melting point, brittle
Sn-Bi-In	Sn-20Bi-10In	143-193	Cracking problem with increase Bi content
Sn-Zn	Sn-9Zn (eutectic)	198.5	Poor corrosion resistance, low wettability
Sn-Ag	Sn-3.5Ag (eutectic)	221	Primary replacement candidates of Sn-Pb alloy, high melting temperature
	Sn-1Ag-0.5Cu	Around 227	
	Sn-3Ag-0.5Cu		
	Sn-3.8Ag-0.7Cu		
	Sn-4Ag-0.5Cu		
Sn-Cu	Sn-0.7Cu (eutectic)	227	Poor mechanical properties, for wave soldering

benefits are associating with low-temperature soldering technology, including thermal shock reduction, step soldering capability, thermal warpage etc. These three issues are discussed below.

Thermal shock reduction: The risk of thermally induced damages will be reduced once peak assembly temperature is reduced. Therefore, by reducing the peak temperature of reflow soldering process, components will suffer reduced thermal damage. As shown in Table 1-3, currently, the most popular peak reflow temperature is around 220 ℃ by using Sn-Ag based solders. These temperatures are sufficient to cause warping of PCBs and damage to ICs.

Step soldering: Multiple reflow processed on a single board is only possible by using a series of solders with different melting temperature. For example, the components that can tolerate higher reflow temperature should be soldered to a board using a reflow profile with higher peak temperature. Then, components with lower temperature tolerance could be soldered using solder alloys with lower melting temperature in the following reflow processes [45], [46].

Thermal warpage: This is another issue associated with reflow process. Too much warpage can cause stress on solder interconnects, resulting in reliability failure of the packages. Or severe consequences, such as undue shorts or opens may happen as well. Equation (1) is the thermal expansion equation used in general engineering solids. This equation represents how a material change in dimension in response to temperature change.

$$\frac{\Delta L}{L} = \alpha_L \Delta T \qquad (1)$$

Where, ΔL is the change in length of a material; ΔL is the original length; α_L is the liner coefficient of thermal expansion. Because of the CTE difference between each part of the packaging materials, the higher the change of temperature ΔT, the higher the fractional change in length of a solid material ΔL/L, as shown in Equation (1).

Figure 1-7 illustrates two types of SMT defects. They are Head on Pillow (HoP) and Non Wet Open (NWO). Both of these defects are developed on FCBGA package when gaps are developed due to dynamic warpage induced by reflow process [47]. In HoP the gap exist between paste and solder ball, while in NOW the gap located between paste and PCB land. Therefore, to eliminate the occurrence of these defects, lowering the temperature change during reflow is certainly one of the effective methods.

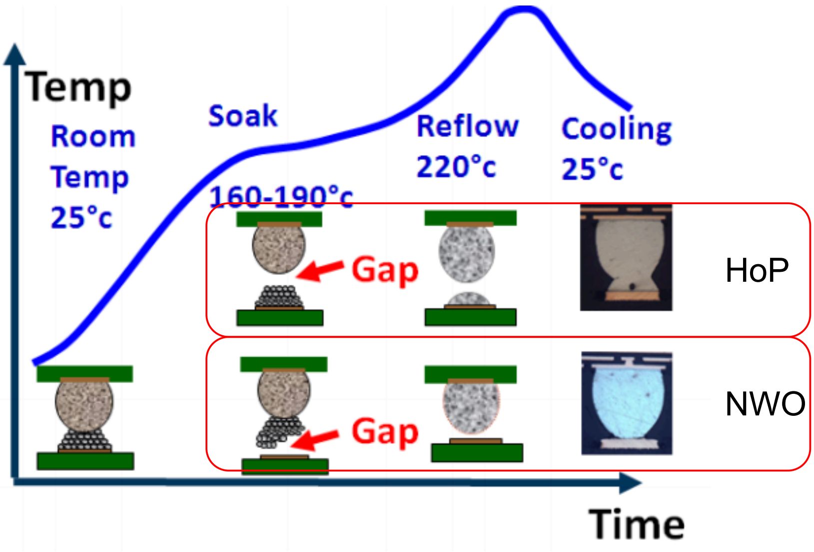

Figure 1-7 Formation of two types of SMT defects, i.e., HoP and NWO [18].

1.3.2 Eutectic Sn-58Bi alloy

Sn-Bi is a simple eutectic system with a eutectic composition of 42 wt. % Sn and 58 wt. % Bi, which has a single melting point of 139 ℃. Figure 1-8a shows a Sn-Bi phase diagram [48]. The microstructure of as-solidified eutectic Sn-58Bi alloy consists a primary Sn phase and a eutectic Sn-Bi mixture, as shown in Figure 1-8b.

Table 1-4 from reference [49] shows some of thermal, electrical, and mechanical properties of eutectic Sn-58Bi alloy, in comparison with Sn-37Pb solder alloy. For CTE, the measurement made by Indium Corp. shows eutectic Sn-58Bi has lower CTE compared with that of Sn-37Pb. The low CTE of eutectic Sn-58Bi reduces thermal mismatch during soldering, thereby extending thermal fatigue life of solder joints. Furthermore, eutectic Sn-58Bi expands 0.77 % during melting, which is less compared to ordinary Sn-37Pb. Thermal conductivity and electrical resistivity are related, the higher the thermal conductivity, the higher the electrical resistivity. Pure Bi has much higher electrical resistivity and lower thermal conductivity than Sn and Pb, so eutectic Sn-58Bi has higher electrical resistivity than Sn-37Pb. For surface tension, eutectic Sn-58Bi also has a lower value.

Besides the low melting temperature feature and these advantages eutectic Sn-58Bi has compared to Sn-37Pb mentioned in Table 1-4, simplicity is another advantage of eutectic Sn-58Bi. It has been well understood and it is commercially provided in paste form [50].

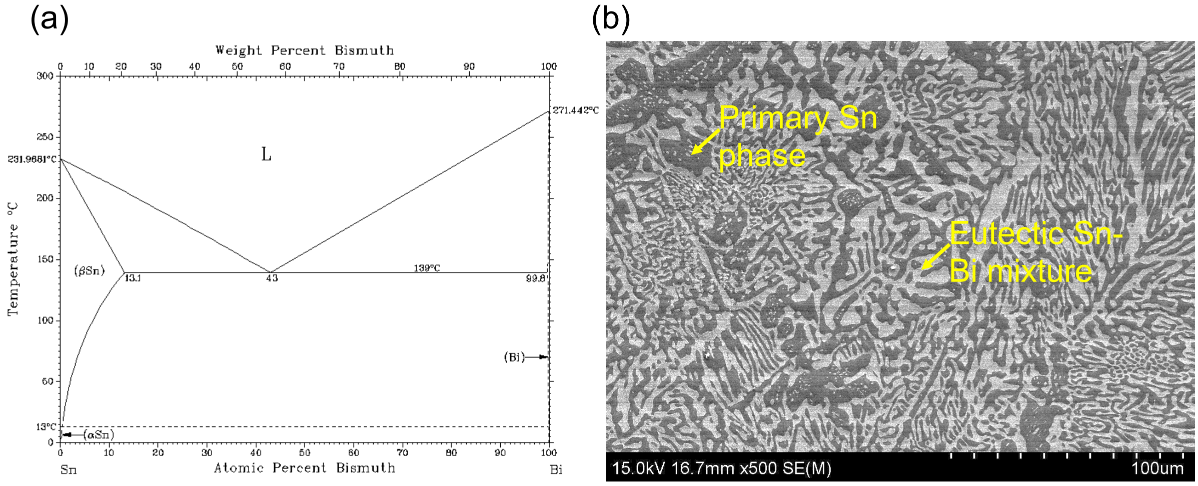

Figure 1-8 (a) Sn-Bi phase diagram and (b) a typical cross-sectional eutectic Sn-58Bi lamellar structure.

Table 1-4 Physical properties comparison between eutectic Sn-58Bi and Sn-37Pb.

Properties	Eutectic Sn-58Bi	Sn-37Pb
Coefficient of thermal expansion (10^{-6}/℃)	15	25
Volume change during melting (%)	0.77	4
Thermal conductivity ($Wm^{-1}K^{-1}$)	-	50
Electrical resistivity (Ω · m)	30-35	14.5
Surface tension at peak reflow temperature	349	464
Young modulus (GPa)	-	14.51

1.4 Reliability concern of eutectic Sn-58Bi alloy

1.4.1 Phase coarsening

It has been widely reported that the coarsening of eutectic Sn-58Bi is difficult to avoid, because of its low melting point and phase equilibria point of view. The mechanism of phase coarsening is illustrated in Figure 1-9. When a eutectic Sn-58Bi alloy solidified from molten state to room temperature quickly, a relatively fine, Sn-Bi interlocked lamellar structure is formed, as shown in Figure 1-9b. The Sn-rich side of Sn-Bi phase diagram shows that when temperature increases, solubility of Bi in Sn phase increases simultaneously. Around 10 wt.% Bi that was present as separate phase at room temperature dissolved into Sn phase at around 80 ℃. This phenomenon results in an increasing volume fraction of Sn phase at evaluated temperature, as shown in Figure 1-9c. Then, during cooling, Bi grain will precipitate out from coarsened Sn grain in order to accommodate the change of solubility. Moreover, increased temperature can cause Bi coarsening as well. Bi grows its size by the attachment of previously formed and precipitated Bi grain via thermally activated diffusion which leads to Ostwald ripening as the large Bi grains grow at the expense of the small ones [32], [35], [51]. The coarsening, the non-uniform microstructure, all contributes to the degradation of mechanical properties of eutectic Sn-58Bi alloy.

1.4.2 Brittleness

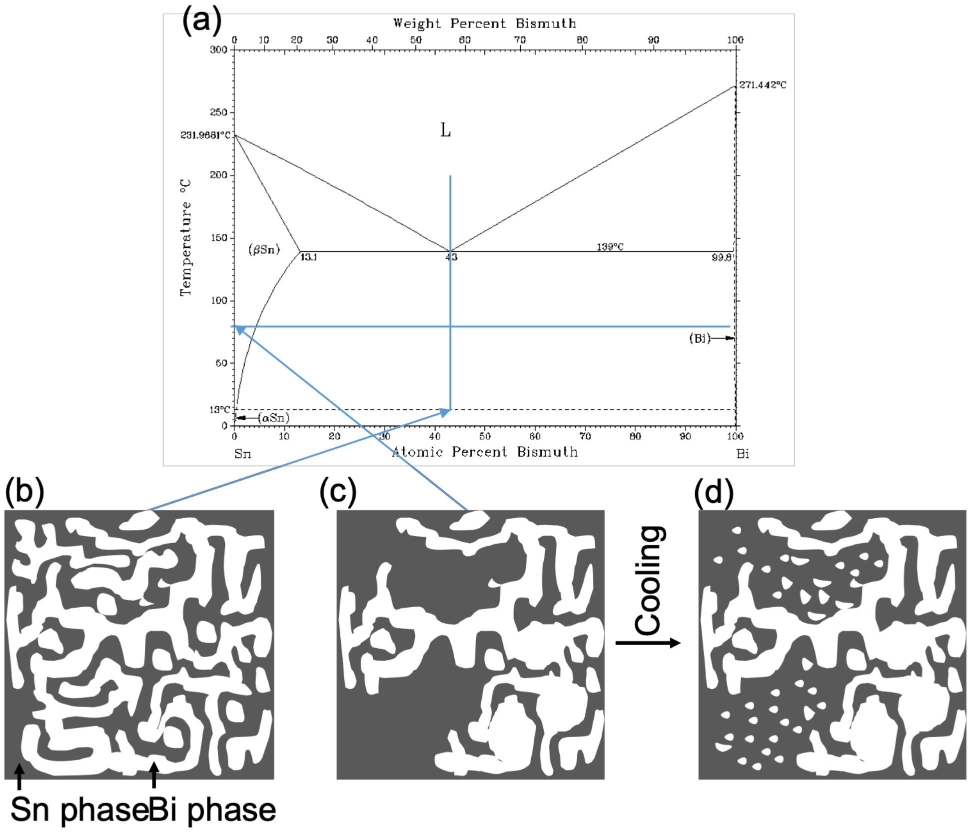

Figure 1-9 (a) Sn-Bi binary phase diagram and schematic illustrations of phase coarsening in eutectic Sn-58Bi alloy. (b) As-solidified state. (c) phase equilibria at 80 . (d) Cooled to RM from (c).

At room temperature, Bi solid solubility in Sn phase is approximately 3 wt. %. Bi solutes solid solute strengthens Sn phase [52], [53]. Plus, the brittle characteristic of Bi phase, eutectic Sn-58Bi alloy is considered lack of ductility in many publications [28], [32], [35], [51], [52].

Table 1-5 summarizes some advantages and disadvantages of the usage of eutectic Sn58Bi alloy. The motivations of this study was therefore focused on the disadvantages of eutectic Sn58Bi alloy.

1.5 Research motivations

1.5.1 Current state of eutectic Sn58Bi study

Most of the current studies of eutectic Sn58Bi alloy study can be divided into two categories, i.e., the study of solder bulks and the study of solder joints.

Table 1-5 Advantages and disadvantages of eutectic Sn58Bi alloy.

Advantages	Disadvantages
Low melting temperature (139 ℃)	Coarsening of microstructure after thermal aging
Good wettability and tensile strength	Brittleness of Bi and Sn phase with Bi solid solution

i. Solder Bulk

For solder bulk, improvement in mechanical properties is the main target. Mainly, to increase the elongation and ultimate tensile strength (UTS) of the bulk. To achieve these targets, brittleness of the alloy and phase coarsening are the two problems which require solutions. Figure 1-10 shows the correlation between grain size of an alloy and its mechanical properties. Actually, it is quite obvious that for almost all materials, this relation applies. To explain in detail, refined gains contain smaller flaws, which requires greater strength to achieve failure [54]. Additionally, mechanical reliability is of great importance as well. Especially phase coarsening becomes extremely severe after long time thermal aging for eutectic Sn58Bi alloy [32]. Experimental methods for mechanical property test generally involves tensile testing.

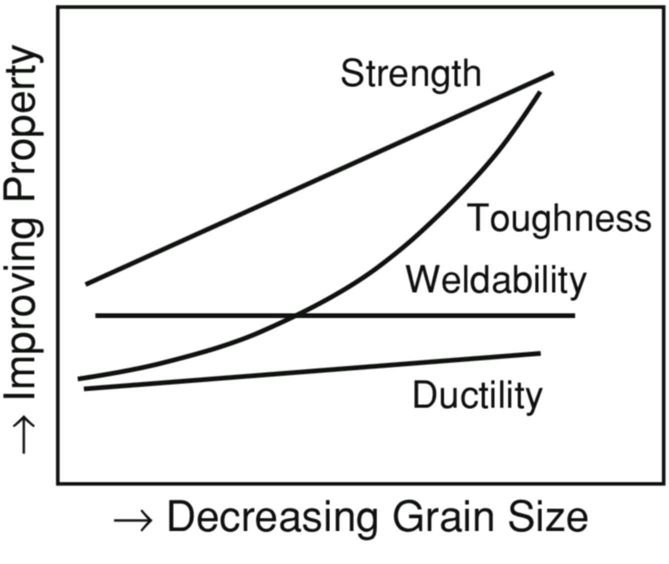

Figure 1-10 Grain refinement results in simultaneous improvement of mechanical properties of an alloy [29].

However, it is fairly difficult to compare mechanical property results from study to study, especially from different research groups, due to different geometry of tensile sample and different strain rates applied in tensile tests.

As discussed previously, refining microstructure and preventing it from coarsening during thermal aging is imperative in terms of mechanical properties improvement. To achieve microstructure refinement, minor element addition to a solder alloy is a common method. In detail, these additives can be further divided into two categories.

First, the additives with higher liquidus temperature, such as Ag_3Sn, Cu_6Sn_5, Ni_3Sn_4, SnSb, Ti_6Sn_5, Ti_2Sn_3 and Carbon nanotube (CNT) etc [28], [29], [31], [33], [34], [51], [55]. These additives generally stay as solid phase during reflow process due to their high melting temperature. Therefore, the solder paste fabrication usually involves mechanical blending between commercially available eutectic Sn58Bi solder paste and added particles. Thus, these particles act as extra heterogeneous nucleation sites, refining microstructure and prohibiting the grain growth of Sn and Bi phases during reflow and thermal aging. The refined microstructure can compensate the intrinsic brittleness of Bi phase, resulting in better mechanical properties. For example, Figure 1-11 shows a microstructure refined by minor nanoscale Cu_6Sn_5 IMC addition into eutectic Sn58Bi alloy. Nanoscale Cu_6Sn_5 IMCs remain solid state during reflow due to its very high melting point. Owning to these extra introduced nucleation sites, microstructure was refined. Consequently, elongation and elastic module were increased. Specifically, 0.05 wt.% Cu_6Sn_5 added Sn58Bi shows the best result.

The another type of additives is with relatively lower liquidus temperature, such as In and Zn etc. [32], [56], [57]. Therefore, there is normally no size requirement for these added element since they have to be fully melted in an alloying process (usually 700 ℃ for eutectic Sn58Bi alloy) to ensure homogenization of the alloy. These elements exist as possibly third phase in solder alloy after alloying process, namely, elementary substances, solid solutes and intermetallic compounds. For example, Zn flakes are found homogenously dispersed in Zn added Sn58Bi alloy matrix after allying at 700 ℃ for 5 h [57]. These elementary substances have limited interaction with base eutectic Sn58Bi alloy, thus the mechanical alteration mainly comes from microstructure change since they can act as nucleation sites during solidification, thereby refining microstructure. On the other hand, In was discovered to be either as solid solutes in Sn phase, or Bi-In IMCs dispersed in matrix [32], [52]. It is reported In alters the mechanical properties of Sn phase in eutectic Sn58Bi, since In interacts with Bi solid solutes and softens the Sn phase, as a result, elongation increases. However, the amount of In addition

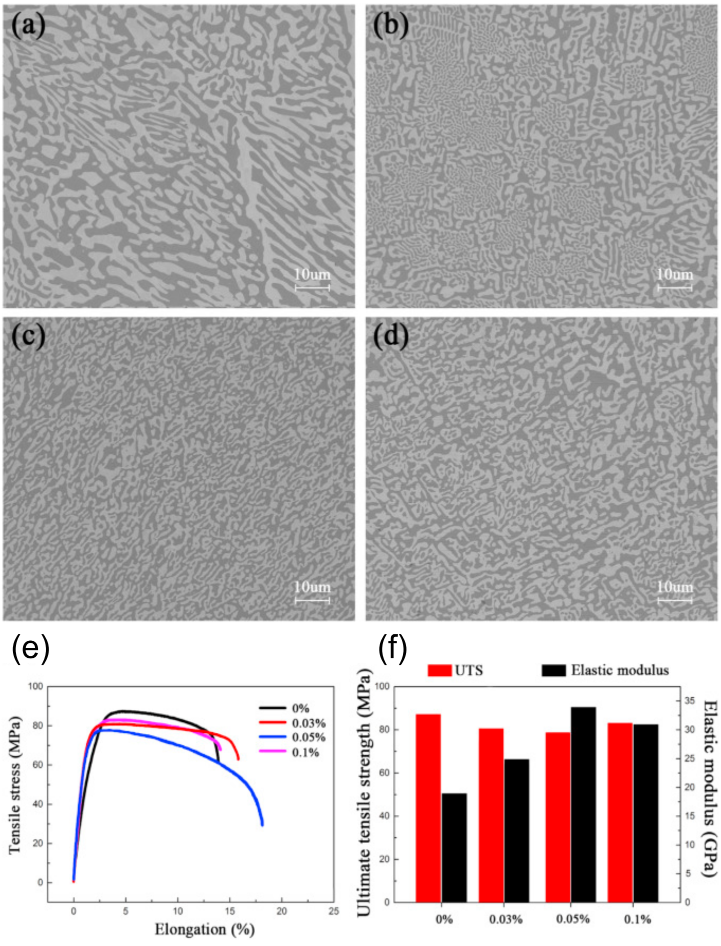

Figure 1-11 Microstructure in (a) eutectic Sn-58Bi, (b) Sn-58BiBi-0.03 wt.%Cu6Sn5, (c) Sn-58Bi-0.05 wt.%Cu6Sn5 and (d) Sn-58Bi-0.1 wt.%Cu6Sn5 solders. (e) and (f) Mechanical performance [34].

need to be carefully designed, since Bi-In IMC may form and deteriorate the mechanical properties of alloy [52].

ii. Solder joint

For solder joint, improving mechanical properties is the target as well. In this case, the joint strength can be investigated by a number of experimental methods, such as shear test [56], [57], drop test [24], tensile test [35], [51] etc. Reliability test for solder joint involves thermal cycling test [58], thermal aging test [35], and corrosion test [59] etc. There are two important factor affects shear strength of a solder joint. They are microstructure of solder bulk and solder/substrate IMC layer. The growth of a IMC layer can affect shear strength of a solder joint dramatically. The growth of an IMC layer can alter the fracture path in a solder joint from within solder bulk to within a IMC layer, due to its brittleness [60]–[63].

Moreover, the substrate is of paramount importance for solder technology. The reaction between solder and substrates give rises to IMC layers, which determine the overall reliability of a solder joint. Cu as a most common metal conductor in electronic industry, forming reliable solder joint with Cu is important. Most recently, ENIG substrates are of most interest in research field for better oxidation prevention, better wettability and better mechanical reliability of solder/substrate IMC layer [22]–[24], [64]–[68]. In ENIG substrate, the top Au thin film provides protection against oxidation and acts as a wetting layer for the melted solder. The Ni film acts as a barrier layer to prevent diffusion between Cu and the solder [64]. Many studies have analyzed the joint reliability and interfacial reliability between the ENIG substrate and various solders, including eutectic Sn58Bi alloy [24], [64], [66], [67]. As discussed previously, minor element addition plays an important role in modifying not only solder bulk microstructure but also solder/substrate IMC layer formation. As a result, change the mechanical and electrical property and reliability of a solder joint. Based on the different mechanism of generally improve the solder joint performance, added elements can be divided into two types.

First, the element reacts with substrate, forming new IMC layers, instead of the products of Sn-Cu reaction if using a Cu substrate. One example is that, it is reported that 42Sn-Bi-5In/Cu IMC layer is Cu-Sn-In IMC, resulting in a better wettability compared to eutectic Sn58Bi/Cu joint [56]. Another is that, by alloying 1 wt.% Zn into eutectic Sn58Bi alloy, Cu5(Sn, Zn)$_8$ IMC layer forms on solder/Cu interface instead of Cu-Sn IMCs. The Cu_5(Sn, Zn)$_8$ layer is much thinner and providing a better mechanical reliability to the solder joint than Cu-Sn IMC layers [57]. Figure 1-12 shows the illustration of these two types and the type one is shown in Figure 1-12b.

Second, the element does not involve in the solder/substrate reaction. In this type. Researchers often doping nanoscale particles into solder matrix to ensure their ability of refining the microstructure of solder bulk. In addition, these small-sized particles tend to be adsorbed on top of the solder/substrate IMC layer. Because small particles are more surface active, they are more likely to be adsorbed on the IMC layers. Therefore, IMC layer grain surface energy will reduce, decreasing the growth velocity of IMC grains [37], as shown in Figure 1-12c. As a result, enhancing the shear strength and reliability of a solder joint.

1.5.2 The strategy of my study

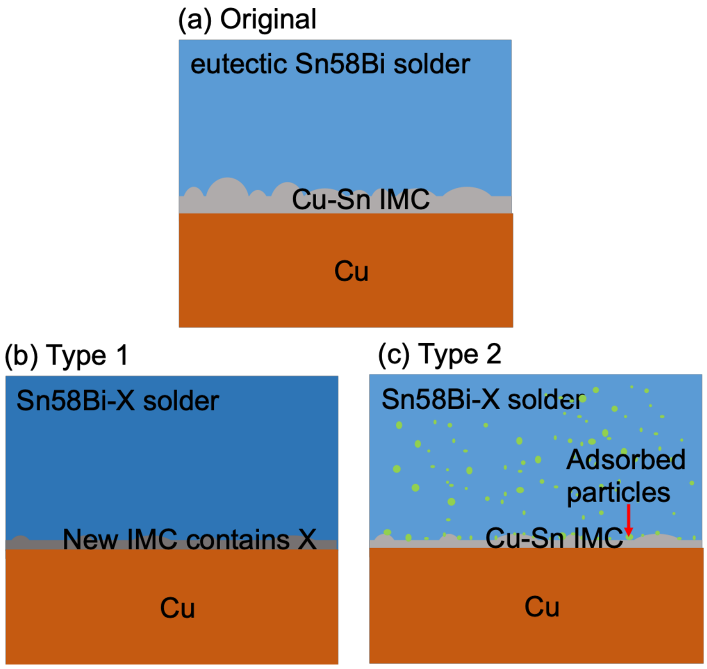

Figure 1-12 Illustration of two types of IMC modification mechanisms by element addition.

In response to the aforementioned two issues, i.e., microstructure coarsening and brittleness of eutectic Sn58Bi alloy during practical use. The design of this study was focusing on these two parts. Several ideas were proposed and corresponding experiments were conducted in order to address these issues.

i. Microstructural refinement mechanisms

As discussed in previous sections, by doping some elements into a solder alloy. Microstructure can be effectively refined since extra nucleation sites are introduced to the matrix, resulting in smaller grain size. This method has been studied thoroughly in Sn-Ag-Cu solder alloys and some of these composite alloys are already commercially available [69]–[73]. In order to overcome the brittleness and phase coarsening issue of eutectic Sn58Bi alloy, a number of composite solder alloys were designed [30], [74]–[77]. The benefits are obvious. For example, refined microstructure; improved elongation and UTS; improved hardness etc. However, drawbacks should not be ignored. For instance, first, the cost of these doped particles could be high due to their microscale or even nanoscale size. Second, the amount of added element sometime could be difficult to control since agglomeration is an unavoidable issue due to the high surface energy of a small-sized particle. Third, adhesively is unpredictable between added particles and solder alloy, which can result in segregation of additives and wetting problem [34]. Forth, additives may react with solder alloy, forming IMCs, which make the solder alloy even more brittle.

It is noted that, for eutectic Sn58Bi, the microstructure is recognizably different from most of other common Sn-rich lead-free solder alloys such as, Sn-1Ag-0.5Cu, Sn-3Ag-0.5Cu, Sn-3.8Ag-0.7Cu, Sn-0.7Cu, Sn-9Zn etc. Owing to the near equal volume fractions of Sn and Bi (42 vs. 58 wt.%), eutectic Sn58Bi is composed of entirely interlocked lamellar structure, while other mentioned solders are composed of mostly Sn-rich phase. Figure 1-13 illustrates the microstructure difference between Sn-3.5Ag-0.5Cu [69] and eutectic Sn58Bi solder. It is clear that Sn-Bi phase boundary distributed throughout the entire matrix. It is reported that Sn-Bi phase boundary is very alike a non-coherent grain boundary, which provides extra surface energy for the diffusion of Sn and Bi atoms [1], [78]. It is a common knowledge that diffusion velocity is the fastest on the free surface, that is

$$V_{fs} > V_{gb} > V_v \tag{2}$$

Where V_{fs} stands for free surface diffusion, V_{gb} is grain boundary diffusion and V_v is volume fraction [79]. It is noted that free surface diffusion is more frequently happen in eutectic Sn58Bi alloy than in a Sn-rich alloy, as shown in Figure 1-13. Therefore, it is much reasonable to have a diffusion barrier existed on the Sn-Bi phase boundary, slowing down the diffusion activity and suppressing the phase coarsening, especially during thermal aging. However, how to realize this implementation is the real task. From previous studies, additives rather dispersed randomly in solder matrix than segregated on Sn-Bi phase boundary natively. Thus, a new approach is required to realizing this idea. We gained the idea from a reality that solutes precipitate during ambient temperature decreasing due to solubility change during temperature

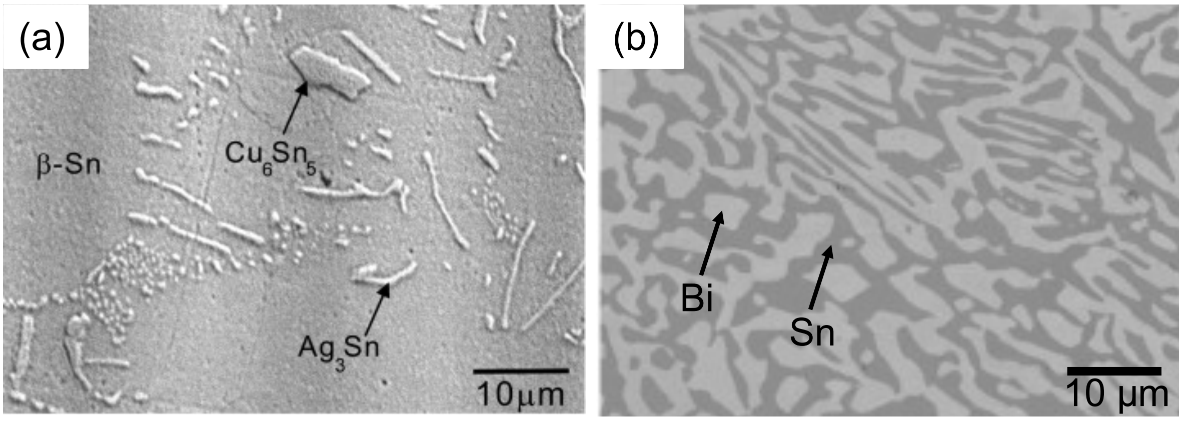

Figure 1-13 Microstructure difference between (a) Sn-3.5Ag-0.5Cu and (b) eutectic Sn58Bi alloy, respectively.

change. For example, Bi precipitates out and dispersed in Sn-rich phase even when temperature dropping from 80 to 25 ℃ [80]. Many other element has this characteristic as well and what if they precipitate out and diffuse towards Sn-Bi boundary and this could be a perfect solution. Unfortunately, this implementation has never been realized before.

ii. Solving the brittleness issue by reducing Bi content

As discussed in the previous sections, brittleness is another fundamental issue associate with eutectic Sn58Bi alloy. The source of this issue has few. First is the intrinsic brittleness of Bi phase and the high volume fraction of Bi phase (58 wt.%) at eutectic point. Second, due to solid solution hardening of approximately 3 wt.% Bi solid solutes in Sn phase, the hardness of Sn phase in eutectic Sn58Bi increased as well. In the research [53], Sn phase with different amounts of Bi addition was tested to reveal their hardness property. The hardness nearly doubled in Sn phase with 3 wt.% Bi solid solution compared with the pure Sn phase (hardness increased from approximately 0.14 to 0.25 GPa). Therefore, reducing Bi volume fraction is considered an effective method of reducing brittleness and improving elongation. However, according to phase diagram, for example, with the decrease of Bi content by 10 wt.%, liquidus temperature will increases around 20 ℃, resulting in wide mushy zone and deteriorated solderability. Therefore, the challenge is to narrow the widened mushy zone. In the chapter, the melting behavior was controlled by alloying another element. The new solder alloy can form sound joint with substrates by using the same reflow profile applying to eutectic Sn58Bi.

iii. Thermal dynamic calculation implementation

Developing new materials to tailor existing material to meet the requirement from new applications are important to the industry. Traditionally, empirical approach is the most common method. Researchers was trying to build the relation between structure and properties and to establish data bases. Nowadays, the approach is transforming from experimental based knowledge creation to integrated computational-prediction [81]. The reliable thermodynamic and kinetic data is required for implementing computational prediction. In the recent three decades, the calculation of phase diagram (CALPHAD) has always been a viable method in building thermodynamic data base and calculation phase equilibria in multicomponent materials [82], [83]. The CALPHAD method implements the fundamental concept of lattice stability. They are, first, the Gibbs energy difference between the stable structure and other structures of pure element. Second, the methodology of evaluation in multidimensional space, pressure and components. In addition, CALPHAD method is based on mathematically formulated models which describes the thermodynamic of individual phases. The model parameters are evaluated from thermochemical data of individual phases and phase equilibrium between each phases [81]. Although a large number of studies related to the thermodynamic calculation of solder materials have been studies previously [84]–[90], the studies on Sn-Bi system, such as eutectic Sn58Bi are limited [40], [86], [91]–[93].

As a tool to get the deep understanding of this study, thermodynamic calculation based on CALPHAD method was conducted on some of our studied alloys. Phase equilibria of these alloys, including liquidus projections, isothermal sections and solidification paths etc. were calculated for explaining the phase transformation and microstructures.

1.6 Purpose and scope of this study

The purpose of this study was to address the two main issues of eutectic Sn58Bi solder alloy, i.e., microstructure coarsening and brittleness. These two main issues were the focusing points of this study and they were addressed by using different methods presented in the following chapters. These attempts were made to deal with the ductility shortage of eutectic Sn58Bi. Solder joints by using each newly developed solder alloy were evaluated as well. The contents of study include: process, mechanism, and mechanical reliability of Ti-added Sn58Bi, Zn-added Sn58Bi, Sn58Bi with Zn and In double addition and Sn45Bi2.6Zn alloy. Solder bulk as well as solder joints by using these solder alloys were investigated respectively.

In Chapter 1, the brief introduction of electronic packaging, solder interconnection, eutectic Sn58Bi solder alloy were given. Reliability concerns of eutectic Sn58Bi alloy were listed and designed solutions to address these concerns were proposed.

In Chapter 2, the effects of minor Ti addition to eutectic Sn58Bi solder alloy was studied in the form of solder bulk and solder joint. The formation of Ti-Sn IMCs was studied using CALPHAD method. Microstructure refinement mechanism, mechanical properties and thermal reliability were investigated.

In Chapter 3, the effects of minor Zn addition to eutectic Sn58Bi solder alloy was investigated. Zn segregation on the Sn-Bi phase boundary was proposed as a new microstructural refinement method. Reliability of solder joints were studied before and after thermal aging.

In Chapter 4, the effects of In and Zn double addition on eutectic Sn58Bi alloy was studied as a extend study of chapter 3. In was found softened the Sn phase significantly. Zn was found segregated to Sn-Bi phase boundary during thermal aging. These two effects were combined and resulted in a further improved elongation.

In Chapter 5, In order to reduce Bi volume fraction in eutectic Sn58Bi maintain the same melting behavior as eutectic Sn58Bi, Sn45Bi2.6Zn was designed based on the thermodynamic calculation. Elongation was increased dramatically owing to the reduced Bi volume fraction. Sound solder joints were reflowed using the same reflow profile of eutectic Sn58Bi alloy.

In Conclusion, brief achievements and results of each chapter in this thesis were summarized. Future plan was listed as well.

Reference

[1] D. P. Seraphim, R. C. Lasky, and C.-Y. Li, *Principles of electronic packaging*. McGraw-Hill College, 1989.

[2] D. Lu and C. P. Wong, *Materials for advanced packaging*, vol. 181. Springer, 2009.

[3] K. Banerjee, S. J. Souri, P. Kapur, and K. C. Saraswat, “3-D ICs: A novel chip design for improving deep-submicrometer interconnect performance and systems-on-chip integration,” *Proc. IEEE*, vol. 89, no. 5, pp. 602–633, 2001.

[4] M. Zou, Y. Ma, X. Yuan, Y. Hu, J. Liu, and Z. Jin, “Flexible devices: from materials, architectures to applications,” *J. Semicond.*, vol. 39, no. 1, p. 011010, Jan. 2018.

[5] H. R. Kotadia, P. D. Howes, and S. H. Mannan, “A review: On the development of low melting temperature Pb-free solders,” *Microelectron. Reliab.*, vol. 54, no. 6–7, pp. 1253–1273, 2014.

[6] M. Abtew and G. Selvaduray, “Lead-free Solders in Microelectronics,” *Mater. Sci. Eng. R Rep.*, vol. 27, no. 5, pp. 95–141, 2000.

[7] T. Laurila, V. Vuorinen, and M. Paulasto-Kröckel, “Impurity and alloying effects on interfacial reaction layers in Pb-free soldering,” *Mater. Sci. Eng. R Rep.*, vol. 68, no. 1, pp. 1–38, 2010.

[8] T. Laurila, V. Vuorinen, and J. K. Kivilahti, “Interfacial reactions between lead-free solders and common base materials,” *Mater. Sci. Eng. R Rep.*, vol. 49, no. 1, pp. 1–60, 2005.

[9] “Solders-Technology-Roadmap-2015.pdf.” .

[10] “solder - Not Found.” [Online]. Available: http://www.solder.net/BEST_LFRoadmap.pdf. [Accessed: 25-May-2019].

[11] D. Chang, F. Bai, Y. P. Wang, and C. S. Hsiao, “The study of OSP as reliable surface finish of BGA substrate,” in *Proceedings of 6th Electronics Packaging Technology Conference (EPTC 2004)(IEEE Cat. No. 04EX971)*, 2004, pp. 149–153.

[12] K. T. Eng, W. J. HETZEL, W. J. REISS, F. Ammer, Y. C. KOH, and S. Jimmy, “Copper on organic solderability preservative (osp) interconnect,” Jan-2009.

[13] H.-C. Bae, H. Lee, K.-S. Choi, and Y.-S. Eom, “Fine-Pitch Solder on Pad Process for Microbump Interconnection,” *ETRI J.*, vol. 35, no. 6, pp. 1152–1155, 2013.

[14] K.-S. Choi *et al.*, “Novel Bumping Material for Solder-on-Pad Technology,” *ETRI J.*, vol. 33, no. 4, pp. 637–640, 2011.

[15] K.-S. Choi, H.-E. Bae, H.-C. Bae, and Y.-S. Eom, “Novel bumping process for solder on pad technology,” *ETRI J.*, vol. 35, no. 2, pp. 340–343, 2013.

[16] A. M. Holtzman and J. Relis, “Use of immersion tin and tin alloys as a bonding medium for multilayer circuits,” Nov-1989.

[17] A. M. Holtzman and J. Relis, “Use of immersion tin coating as etch resist,” Apr-1987.

[18] E. Huttunen-Saarivirta, “Observations on the uniformity of immersion tin coatings on copper,” *Surf. Coat. Technol.*, vol. 160, no. 2–3, pp. 288–294, 2002.

[19] Y.-H. Chen, Y.-Y. Wang, and C.-C. Wan, “Microstructural characteristics of immersion tin coatings on copper circuitries in circuit boards,” *Surf. Coat. Technol.*, vol. 202, no. 3, pp. 417–424, 2007.

[20] J.-M. Koo, J.-W. Yoon, and S.-B. Jung, “Interfacial reactions between In–48Sn solder and electroless nickel/immersion gold substrate during reflow process,” *Surf. Interface Anal. Int. J. Devoted Dev. Appl. Tech. Anal. Surf. Interfaces Thin Films*, vol. 38, no. 4, pp. 426–428, 2006.

[21] K. Zeng, R. Stierman, D. Abbott, and M. Murtuza, “Root cause of black pad failure of solder joints with electroless nickel/immersion gold plating,” in *Thermal and Thermomechanical Proceedings 10th Intersociety Conference on Phenomena in Electronics Systems, 2006. ITHERM 2006.*, 2006, pp. 1111–1119.

[22] J.-W. Yoon, B.-I. Noh, and S.-B. Jung, “Comparative study of ENIG and ENEPIG as surface finishes for a Sn-Ag-Cu solder joint,” *J. Electron. Mater.*, vol. 40, no. 9, pp. 1950–1955, 2011.

[23] D.-J. Lee and H. S. Lee, “Major factors to the solder joint strength of ENIG layer in FC BGA package,” *Microelectron. Reliab.*, vol. 46, no. 7, pp. 1119–1127, 2006.

[24] W.-R. Myung, Y. Kim, K.-Y. Kim, and S.-B. Jung, “Drop Reliability of Epoxy-contained Sn-58 wt.% Bi Solder Joint with ENIG and ENEPIG Surface Finish Under Temperature and Humidity Test,” *J. Electron. Mater.*, vol. 45, no. 7, pp. 3651–3658, 2016.

[25] T.-K. Lee, T. R. Bieler, C.-U. Kim, and H. Ma, *Fundamentals of lead-free solder interconnect technology*. Springer, 2015.

[26] K. Zeng and K. N. Tu, “Six cases of reliability study of Pb-free solder joints in electronic packaging technology 2002.pdf,” vol. 38, pp. 55–105, 2002.

[27] P. Yao, P. Liu, and J. Liu, “Interfacial reaction and shear strength of SnAgCu–xNi/Ni solder joints during aging at 150 C,” *Microelectron. Eng.*, vol. 86, no. 10, pp. 1969–1974, 2009.

[28] L. Yang *et al.*, “Effects of Ni addition on mechanical properties of Sn58Bi solder alloy during solid-state aging,” *Mater. Sci. Eng. A*, vol. 667, pp. 368–375, 2016.

[29] X. Li, Y. Ma, W. Zhou, and P. Wu, “Effects of nanoscale Cu6Sn5 particles addition on microstructure and properties of SnBi solder alloys,” *Mater. Sci. Eng. A*, vol. 684, pp. 328–334, 2017.

[30] L. Yang, C. Du, J. Dai, N. Zhang, and Y. Jing, “Effect of nanosized graphite on properties of Sn–Bi solder,” *J. Mater. Sci. Mater. Electron.*, vol. 24, no. 11, pp. 4180–4185, Nov. 2013.

[31] M. Mccormack, H. S. Chen, G. W. Kammlott, and S. Jin, “Significantly improved mechanical properties of Bi-Sn solder alloys by Ag-doping,” *J. Electron. Mater.*, vol. 26, no. 8, pp. 954–958, 1997.

[32] O. Mokhtari and H. Nishikawa, “Correlation between microstructure and mechanical properties of Sn-Bi-X solders,” *Mater. Sci. Eng. A*, vol. 651, pp. 831–839, 2016.

[33] J. Shen, Y. Pu, H. Yin, D. Luo, and J. Chen, “Effects of minor Cu and Zn additions on the thermal, microstructure and tensile properties of Sn-Bi-based solder alloys,” *J. Alloys Compd.*, vol. 614, pp. 63–70, 2014.

[34] L. Yang *et al.*, “Effect of Ni and Ni-coated Carbon Nanotubes on the interfacial reaction and growth behavior of Sn58Bi/Cu intermetallic compound layers,” *J. Mater. Sci. Mater. Electron.*, vol. 27, no. 11, pp. 12264–12270, 2016.

[35] S. Zhou, O. Mokhtari, M. G. Rafique, V. C. Shunmugasamy, B. Mansoor, and H. Nishikawa, “Improvement in the mechanical properties of eutectic Sn58Bi alloy by 0.5 and 1 wt.% Zn addition before and after thermal aging,” *J. Alloys Compd.*, 2018.

[36] M. G. Cho, S. K. Kang, D. Y. Shih, and H. M. Lee, “Effects of minor additions of Zn on interfacial reactions of Sn-Ag-Cu and Sn-Cu solders with various Cu substrates during thermal aging,” *J. Electron. Mater.*, vol. 36, no. 11, pp. 1501–1509, 2007.

[37] Y. Li and Y. C. Chan, “Effect of silver (Ag) nanoparticle size on the microstructure and mechanical properties of Sn58Bi-Ag composite solders,” *J. Alloys Compd.*, vol. 645, pp. 566–576, 2015.

[38] M. Nowottnick, U. Pape, K. Wittke, and W. Scheel, “Solder joints for high temperature electronics,” in *2003 SMTA International Conference Proceedings*, 2003, pp. 21–25.

[39] Y. Huang and S. Chen, “Effects of Co alloying and size on solidification and interfacial reactions in Sn-57 wt.% Bi-(Co)/Cu couples,” *J. Electron. Mater.*, vol. 40, no. 1, pp. 62–70, 2011.

[40] S. Lin, T. L. Nguyen, S. Wu, and Y. Wang, “Effective suppression of interfacial intermetallic compound growth between Sn–58 wt.% Bi solders and Cu substrates by minor Ga addition,” *J. Alloys Compd.*, vol. 586, pp. 319–327, 2014.

[41] J. U. Knickerbocker *et al.*, “2.5 D and 3D technology challenges and test vehicle demonstrations,” in *Electronic Components and Technology Conference (ECTC), 2012 IEEE 62nd*, 2012, pp. 1068–1076.

[42] B. Banijamali, R. Chaware, S. Ramalingam, and M. Kim, “Quality and reliability of 3d tsv interposer and fine pitch solder micro-bumps for 28nm technology,” in *International Symposium on Microelectronics*, 2011, vol. 2011, pp. 000189–000192.

[43] R. Chaware, K. Nagarajan, and S. Ramalingam, “Assembly and reliability challenges in 3D integration of 28nm FPGA die on a large high density 65nm passive interposer,” in *Electronic Components and Technology Conference (ECTC), 2012 IEEE 62nd*, 2012, pp. 279–283.

[44] Z. Mei, “Low-Temperature Solders,” *Ldots Symp. Test. Ldots*, no. August, pp. 1–10, 1994.

[45] W. K. Choi *et al.*, “Development of novel intermetallic joints using thin film indium based solder by low temperature bonding technology for 3D IC stacking,” *Proc. - Electron. Compon. Technol. Conf.*, pp. 333–338, 2009.

[46] C. T. Ko and K. N. Chen, “Wafer-level bonding/stacking technology for 3D integration,” *Microelectron. Reliab.*, vol. 50, no. 4, pp. 481–488, 2010.

[47] D. Amir, S. Walwadkar, S. Aravamudhan, and L. May, “THE CHALLENGES OF NON WET OPEN BGA SOLDER DEFECT,” p. 11.

[48] A. S. M. Handbook, “Alloy phase diagrams,” *ASM Int.*, vol. 3, pp. 2–319, 1992.

[49] F. Hua, Z. Mei, and J. Glazer, “Eutectic Sn-Bi as an alternative to Pb-free solders,” in *Electronic Components & Technology Conference, 1998. 48th IEEE*, 1998, pp. 277–283.

[50] J. F. Li, S. H. Mannan, M. P. Clode, D. C. Whalley, and D. A. Hutt, “Interfacial reactions between molten Sn-Bi-X solders and Cu substrates for liquid solder interconnects,” *Acta Mater.*, vol. 54, no. 11, pp. 2907–2922, 2006.

[51] S. Zhou *et al.*, “Effects of Ti addition on the microstructure, mechanical properties and electrical resistivity of eutectic Sn58Bi alloy,” *Mater. Sci. Eng. A*, vol. 744, pp. 560–569, 2019.

[52] X. Chen, F. Xue, J. Zhou, and Y. Yao, “Effect of in on microstructure, thermodynamic characteristic and mechanical properties of Sn-Bi based lead-free solder,” *J. Alloys Compd.*, vol. 633, pp. 377–383, 2015.

[53] L. Shen, P. Septiwerdani, and Z. Chen, “Elastic modulus, hardness and creep performance of SnBi alloys using nanoindentation,” *Mater. Sci. Eng. A*, vol. 558, pp. 253–258, 2012.

[54] G. Grossmann and C. Zardini, *The ELFNET book on failure mechanisms, testing methods, and quality issues of lead-free solder interconnects*. Springer Science & Business Media, 2011.

[55] S. Sakuyama, T. Akamatsu, K. Uenishi, and T. Sato, “Effects of a Third Element on Microstructure and Mechanical Properties of Eutectic Sn – Bi Solder,” vol. 2, no. 1, pp. 98–103, 2009.

[56] O. Mokhtari and H. Nishikawa, “Effects of in and Ni addition on microstructure of Sn-58Bi solder joint,” *J. Electron. Mater.*, vol. 43, no. 11, pp. 4158–4170, 2014.

[57] O. Mokhtari, S. Zhou, and H. Nishikawa, “Effect of Zn addition on interfacial reactions between Sn-Bi solder and Cu substrate,” *Mater. Trans.*, vol. 57, no. 8, pp. 1272–1276, 2016.

[58] Y. Zuo, L. Ma, S. Liu, Y. Shu, and F. Guo, “Evolution of Microstructure Across Eutectic Sn-Bi Solder Joints Under Simultaneous Thermal Cycling and Current Stressing,” *J. Electron. Mater.*, vol. 44, no. 1, pp. 597–603, 2015.

[59] A. Torres, L. Hernández, and O. Domínguez, “Effect of Antimony Additions on Corrosion and Mechanical Properties of Sn-Bi Eutectic Lead-Free Solder Alloy,” *Mater. Sci. Appl.*, vol. 03, no. 06, pp. 355–362, 2012.

[60] Y. Liu, F. Sun, H. Zhang, and P. Zou, “Solderability, IMC evolution, and shear behavior of low-Ag Sn0.7Ag0.5Cu-BiNi/Cu solder joint,” *J. Mater. Sci. Mater. Electron.*, vol. 23, no. 9, pp. 1705–1710, 2012.

[61] F. Sun, P. Hochstenbach, W. D. Van Driel, and G. Q. Zhang, “Fracture morphology and mechanism of IMC in Low-Ag SAC Solder/UBM (Ni (P)-Au) for WLCSP,” *Microelectron. Reliab.*, vol. 48, no. 8–9, pp. 1167–1170, 2008.

[62] K. E. Yazzie, H. X. Xie, J. J. Williams, and N. Chawla, “On the relationship between solder-controlled and intermetallic compound (IMC)-controlled fracture in Sn-based solder joints,” *Scr. Mater.*, vol. 66, no. 8, pp. 586–589, 2012.

[63] W. J. Zhu, H. S. Liu, J. Wang, and Z. P. Jin, “Formation of intermetallic compound (IMC) between Sn and Co substrate,” *J. Alloys Compd.*, vol. 456, no. 1–2, pp. 113–117, 2008.

[64] T. H. Chuang, C. C. Jain, and S. S. Wang, “Intermetallic Compounds Formed in In-3Ag Solder BGA Packages with ENIG and ImAg Surface Finishes,” *J. Mater. Eng. Perform.*, vol. 18, no. 8, p. 1133, 2009.

[65] J.-W. Yoon and S.-B. Jung, “Interfacial reactions between Sn–0.4 Cu solder and Cu substrate with or without ENIG plating layer during reflow reaction,” *J. Alloys Compd.*, vol. 396, no. 1–2, pp. 122–127, 2005.

[66] J.-W. Yoon, H.-S. Chun, and S.-B. Jung, “Interfacial Reaction and Mechanical Characterization of Eutectic Sn–Zn/ENIG Solder Joints during Reflow and Aging,” *Mater. Trans.*, vol. 46, no. 11, pp. 2386–2393, 2005.

[67] J.-W. Yoon, B.-I. Noh, and S.-B. Jung, “Effects of third element and surface finish on interfacial reactions of Sn–Ag–xCu (or Ni)/(Cu or ENIG) solder joints,” *J. Alloys Compd.*, vol. 506, no. 1, pp. 331–337, 2010.

[68] J.-W. Yoon, W.-C. Moon, and S.-B. Jung, “Interfacial reaction of ENIG/Sn-Ag-Cu/ENIG sandwich solder joint during isothermal aging,” *Microelectron. Eng.*, vol. 83, no. 11–12, pp. 2329–2334, 2006.

[69] L. C. Tsao, S. Y. Chang, C. I. Lee, W. H. Sun, and C. H. Huang, “Effects of nano-Al2O3 additions on microstructure development and hardness of Sn3.5Ag0.5Cu solder,” *Mater. Des.*, vol. 31, no. 10, pp. 4831–4835, Dec. 2010.

[70] M. I. I. Ramli, N. Saud, M. A. A. M. Salleh, M. N. Derman, and R. M. Said, “Effect of TiO2 additions on Sn-0.7Cu-0.05Ni lead-free composite solder,” *Microelectron. Reliab.*, vol. 65, pp. 255–264, Oct. 2016.

[71] E. Efzan Mhd Noor and A. Singh, “Review on the effect of alloying element and nanoparticle additions on the properties of Sn-Ag-Cu solder alloys,” *Solder. Surf. Mt. Technol.*, vol. 26, no. 3, pp. 147–161, May 2014.

[72] L. Aryasomayajula and K.-J. Wolter, “Carbon Nanotube Composites for Electronic Packaging Applications: A Review,” *Journal of Nanotechnology*, 2013. [Online]. Available: https://www.hindawi.com/journals/jnt/2013/296517/abs/. [Accessed: 22-Feb-2019].

[73] E. Efzan Mhd Noor, A. Singh, and Y. Tze Chuan, “A review: influence of nano particles reinforced on solder alloy,” *Solder. Surf. Mt. Technol.*, vol. 25, no. 4, pp. 229–241, Sep. 2013.

[74] S. Sakuyama, T. Akamatsu, K. Uenishi, and T. Sato, “Effects of a Third Element on Microstructure and Mechanical Properties of Eutectic Sn-Bi Solder,” *Trans. Jpn. Inst. Electron. Packag.*, vol. 2, no. 1, pp. 98–103, 2009.

[75] Y. Ma, X. Li, W. Zhou, L. Yang, and P. Wu, “Reinforcement of graphene nanosheets on the microstructure and properties of Sn58Bi lead-free solder,” *Mater. Des.*, vol. 113, pp. 264–272, Jan. 2017.

[76] Y. Liu, H. Fu, F. Sun, H. Zhang, X. Kong, and T. Xin, “Microstructure and mechanical properties of as-reflowed Sn58Bi composite solder pastes,” *J. Mater. Process. Technol.*, vol. 238, pp. 290–296, Dec. 2016.

[77] J. Shen, Y. Pu, H. Yin, D. Luo, and J. Chen, “Effects of minor Cu and Zn additions on the thermal, microstructure and tensile properties of Sn–Bi-based solder alloys,” *J. Alloys Compd.*, vol. 614, pp. 63–70, Nov. 2014.

[78] S. Zhou, O. Mokhtari, M. G. Rafique, V. C. Shunmugasamy, B. Mansoor, and H. Nishikawa, “Improvement in the mechanical properties of eutectic Sn58Bi alloy by 0.5 and 1 wt.% Zn addition before and after thermal aging,” *J. Alloys Compd.*, 2018.

[79] D. R. Askeland and P. P. Phule, *The science and engineering of materials*. Springer, 2003.

[80] Y.-A. Shen, S. Zhou, J. Li, K. N. Tu, and H. Nishikawa, “Thermomigration induced microstructure and property changes in Sn-58Bi solders,” *Mater. Des.*, p. 107619, 2019.

[81] Z.-K. Liu, “First-Principles Calculations and CALPHAD Modeling of Thermodynamics,” *J. Phase Equilibria Diffus.*, vol. 30, no. 5, pp. 517–534, Oct. 2009.

[82] L. Kaufman, “Computational thermodynamics and materials design,” *Calphad*, vol. 25, no. 2, pp. 141–161, 2001.

[83] P. J. Spencer, “A brief history of CALPHAD,” *Calphad*, vol. 32, no. 1, pp. 1–8, 2008.

[84] S. Lin, C. Yeh, W. Xie, Y. Liu, and M. Yoshimura, “Ab initio-aided CALPHAD thermodynamic modeling of the Sn-Pb binary system under current stressing,” *Sci. Rep.*, vol. 3, p. 2731, 2013.

[85] Y. Xie, Z. Y. Qiao, and A. Mikula, “The Sn-In-Zn system-application of Calphad technique to phase diagram measurement,” *Calphad*, vol. 25, no. 1, pp. 3–10, 2001.

[86] S. W. Yoon and H. M. Lee, “A thermodynamic study of phase equilibria in the Sn-Bi-Pb solder system,” *Calphad*, vol. 22, no. 2, pp. 167–178, 1998.

[87] J. H. Kim, S. W. Jeong, and H. M. Lee, “A thermodynamic study of phase equilibria in the Au-Sb-Sn solder system,” *J. Electron. Mater.*, vol. 31, no. 6, pp. 557–563, 2002.

[88] H. M. Lee, S. W. Yoon, and B.-J. Lee, “Thermodynamic prediction of interface phases at Cu/solder joints,” *J. Electron. Mater.*, vol. 27, no. 11, pp. 1161–1166, 1998.

[89] K.-W. Moon, W. J. Boettinger, U. R. Kattner, F. S. Biancaniello, and C. A. Handwerker, “Experimental and thermodynamic assessment of Sn-Ag-Cu solder alloys,” *J. Electron. Mater.*, vol. 29, no. 10, pp. 1122–1136, 2000.

[90] I. Ohnuma, X. J. Liu, H. Ohtani, and K. Ishida, “Thermodynamic database for phase diagrams in micro-soldering alloys,” *J. Electron. Mater.*, vol. 28, no. 11, pp. 1164–1171, 1999.

[91] U. r Kattner and W. J. Boettinger, “On the Sn-Bi-Ag ternary phase diagram,” *J. Electron. Mater.*, vol. 23, no. 7, pp. 603–610, 1994.

[92] Z. Li, Z. Cao, S. Knott, A. Mikula, Y. Du, and Z. Qiao, “Thermodynamic investigation of the Ag–Bi–Sn ternary system,” *Calphad*, vol. 32, no. 1, pp. 152–163, 2008.

[93] J. Vizdal *et al.*, “Thermodynamic assessment of the Bi–Sn–Zn system,” *Calphad*, vol. 31, no. 4, pp. 438–448, 2007.

Chapter 2

Refining microstructure of eutectic Sn58Bi alloy by a minor amount of Ti addition

2.1 Introduction

As discussed in previous Chapter, microstructure coarsening of eutectic Sn58Bi alloy is the issue need to be addressed in order to achieve improved mechanical properties. Adding another additive into the solder alloy has been proved is an effective method to address this issue [1]–[4].

Titanium (Ti) is a chemically active transition metal, which has been widely used in the aluminum industry to not only refine the structure but also increase the strength and ductility of aluminum alloys [5]. Some studies have reported that the minor Ti addition to Sn–Ag, Sn–Cu [6], Sn–1.0Ag–0.5Cu [7], and Sn–3.5Ag–0.5Cu [8] solders lead to a refined microstructure and improved mechanical properties, namely, yield strength (YS), ultimate tensile strength (UTS), and microhardness. However, the effects of Ti addition on Sn58Bi alloy have not yet been reported.

In addition to the mechanical property, the electrical property of the solder materials is equally important. The electrical properties, such as the electrical resistivity is responsible for the heat generation because the portable electronic products are in the trend towards smaller, lighter, and more functional complex [24, 25]. By now, the electrical resistivities of Sn-Ag-Cu solders, such as Sn–1Ag–0.5Cu, Sn–2.6Ag–0.1Cu, Sn–3.5Ag–0.7Cu, and Sn–3.7Ag–0.9Cu and the effects of some minor element additions on them have been studied by other researchers [26-29]. However, the available electrical resistivity data for the eutectic Sn58Bi and the Ti added Sn58Bi alloys are limited.

In this chapter, for solder bulk, the effects of Ti addition on the microstructure and mechanical properties of the eutectic Sn58Bi alloy were investigated both before and after thermal aging. The resultant microstructures are elaborated with calculated liquidus projection [30]. In addition, the electrical resistivity of the eutectic Sn58Bi alloy was tested at room temperature. The electrical resistivity of the eutectic Sn58Bi alloy decreased by Ti addition and the possible explanation was discussed. For solder joint, Ti-added Sn58Bi alloys with electroless Nickle/immersion gold (ENIG) substrate solder joints were prepared. Solid-state thermal aging was applied as well.

2.2 Experimental

2.2.1 Materials

A commercial eutectic Sn58Bi rod (NIHON GENMA MFG. Co. Ltd) was used as a master alloy. Alloys with the addition of 0.5 and 1 wt. % of Ti (99.98%) (The Nilaco Co. Ltd) were subsequently prepared using a vacuum arc melting furnace, hereafter called Sn58Bi0.5Ti and Sn58Bi1Ti, respectively. The compositions were analyzed using an inductively coupled plasma optical emission spectroscopy (ICP-OES), as shown in Table 2-1.

Next, the specimens were separately remelted at 250 °C for 2 h in a crucible, and the molten solders were manually stirred every 30 min to ensure the formation of a homogeneous alloy. Then, the alloys were cast into a bar-shaped steel mold. Some of these solder bulks were directly mounted in epoxy, and cross-sectional microstructures were observed and analyzed. Other alloys were machined into a dumbbell shape for tensile testing. Figure 2-1 shows the dimensions of specimens for tensile testing. In addition to the as-cast samples, thermally aged samples were also prepared. A number of bar-shaped rods for each of the three compositions were immersed in an oil bath at a constant temperature of 80 °C at two aging periods of 504 and 1008 h. Then, to prepare the specimens for microstructure observation and tensile testing, the same processes as those applied for the as-cast samples were followed.

The schematic illustration of a solder joint was displayed in Figure 2-2(a). The disk-shaped alloy used in this chapter was cut by slicing machine and scissors. Thickness and diameter of a solder disk were controlled to be approximately 0.1 and 5 mm, respectively. ENIG top and

Table 2-1 Chemical composition of the solder alloys.

Solder alloy (wt. %)	Sn58Bi0.5Ti	Sn58Bi1Ti
Sn	42.08	42.43
Bi	57.55	57.56
Ti	0.36	0.72
Pb	0.00	0.00
Ag	0.00	0.00
Sb	0.00	0.00
Cu	0.00	0.00
Zn	0.00	0.00
Fe	0.00	0.00
Al	0.00	0.00
As	0.00	0.00
Cd	0.00	0.00
In	0.00	0.00
Ni	0.00	0.00
Au	0.00	0.00

bottom substrates used in this study were on each side of the solder disk, making it a ENIG/Solder/ENIG sandwich structure. The main purpose of using this structure is to perform shear tests, which will be explained in detail in the following section. Figure 2-2(b) shows the reflow profile measured using a thermal couple. This profile consisted two phases, i.e., preheat and peaking. Preheat temperature was 100 °C for around 150 seconds, while peak was 182 °C for around 60 seconds. The structure of ENIG substrates used in this study was detailed

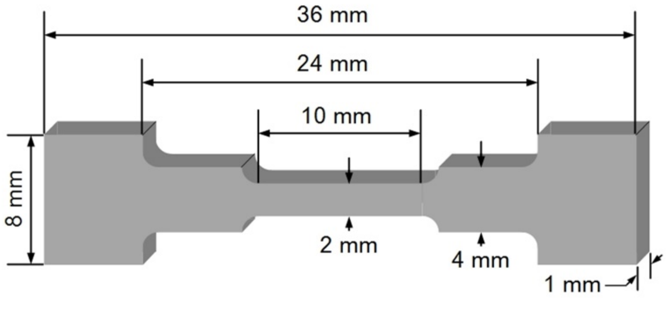

Figure 2-1 The schematic illustration of tensile test samples.

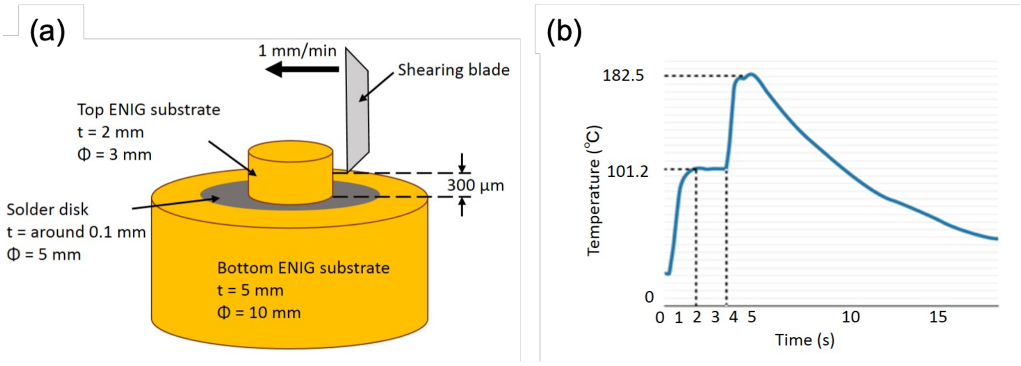

Figure 2-2 Solder joint samples and reflow profile. (a) Schematic illustration of solder joint. (b) Measured reflow profile.

investigated in the previous [9], in which Au and Ni (P) layers were measured to be 60 nm and 2 µm, respectively.

2.2.2 Characterization methods

The tensile test was performed on a Shimadzu Autograph AG-X machine equipped with a Shimadzu DVE-201 Video Extensometer at room temperature (25 °C). Strain rate was 0.01/s. the strain-stress curve (SS curve) was obtained after each test. Based on each SS curve, mechanical properties, i.e., elongation and UTS were calculated. For each alloy composition, three samples were tested and the data were collected for calculating the average value of each mechanical property. Shear tests were conducted using a Rhesca STR-1000 testing machine at room temperature of 25 ℃. The shearing speed was 1 mm/min and the fly height was 300 µm from the top surface of the bottom substrate, as shown in Figure 2-2(a).

The cross-sectional microstructures and fracture surface of the tensile tested samples were studied by a field-emission scanning electron microscope (FESEM, Hitachi SU-70) equipped with an energy dispersive X-ray spectroscopy (EDS). Differential scanning calorimetry (DSC) was used to determine the thermal behavior of the alloys in a experimental perspective. For this experiment, samples of approximately 10 mg with each composition were prepared, sealed in a hermetic aluminum pan, and examined under nitrogen. These samples were heated to 170 °C at a heating rate of 10 °C/min and before cooling to room temperature at a cooling rate of 10 °C/min, the temperature was maintained at 170 °C for 5 min to ensure the thermal stability of molten alloys. Electrical resistivity measurements were standard four-probe technique using SCIENTIFIC EQUIPMENT RROORKEF with constant current source and the temperature was controlled at ± 50 mK using a Pil controlled oven. All the resistivity measurements were carried out in the warm-up cycle. Low current (10 – 100 ml) was applied to the sample and a digital microvoltmeter (DMV - 001) was used to measure the voltages and therefore to calculate the electrical resistivity. The dimension of the tested bulk cubic alloy was around 15 mm length, 5 mm width, and 1 mm thick. Thermodynamic calculations based on the CALPHAD (calculation of phase diagram) method were performed using the PANDAT software with the PanNoble database [10]. In this database, thermodynamic descriptions of the Sn-Bi-Ti ternary system was interpreted based on the models of constituent binary systems without incorporating ternary interacting parameters in the Gibbs free energy functions. Phase equilibria of the Sn-Bi-Ti ternary system, including isothermal sections, liquidus projections, and solidification paths were calculated for elucidating the resultant phase transformation and microstructures.

2.3 Characteristic of bulk alloy

2.3.1 Microstructure of as-cast alloy

Figure 2-3 shows the FE-SEM microstructure of the eutectic Sn58Bi alloy. In which the Bi and Sn regions, denoted by bright and dark areas in the solder matrix, respectively. In Figure 2-3(a), Sn dendrites, large size Bi phase, and eutectic lamellar structures, i.e., regular and irregular eutectic regions, coexisted in the solder matrix. It is noted that a number of large size Bi phases (observed as squares) were clearly observed in the as-cast solder bulk. In addition, eutectic structure was observed. Their corresponding eutectic spacing values were estimated to be around 1.4 μm and 4.5 μm. Figure 2-3(b) and (c) show the SEM images of the finer and coarser eutectics, respectively. The microstructure characteristic of eutectic Sn58Bi before aging was identical compared to those described in the following chapters, thus this description will be simplified after here.

Figure 2-4 shows the cross-sectional microstructure images of Sn58Bi0.5Ti and Sn58Bi1Ti, respectively. Figure 2-4(a), (c) and (e) show the microstructure and Ti-Sn IMCs in a Sn58Bi0.5Ti, while Figure 2-4(b), (d) and (f) show those images in a Sn58Bi1Ti. The eutectic structure and the Sn phase were easily observed within the matrix. However, a large size Bi phase was not found. In addition, some rod-shaped phases with two different contrasts, i.e., dark gray and gray, were observed, as shown in Figure 2-4(c) and (d). EDS was carried out to identify these phases (Table 2-2). The result indicated the phases with dark gray contrast were Ti_6Sn_5 IMCs, while the gray phases were Ti_2Sn_3 IMCs. Figure 2-3(e) and (f) show much

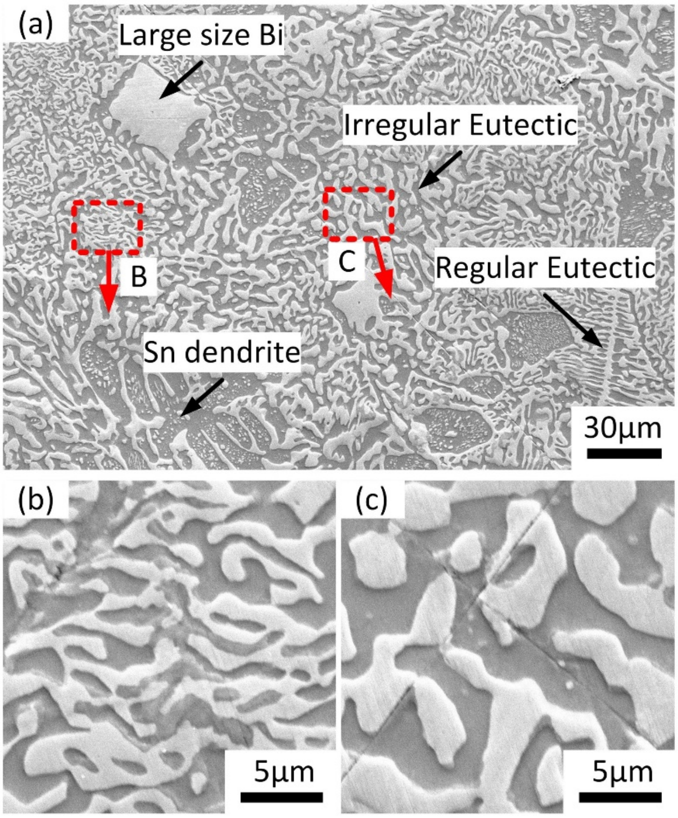

Figure 2-3 FE-SEM images of microstructure of eutectic Sn58Bi alloy. (a) low magnification image; (b) high magnification image of region B. (c) high magnification image of region C.

smaller gray Ti_2Sn_3 IMCs, corresponding to the E and F areas in Figure 2-3(a) and (b). The sizes of these smaller IMCs were measured and calculated on the basis of 20 randomly chosen IMCs (Table 2-3). The width and length of these smaller IMCs in the as-cast Sn58Bi0.5Ti samples were 0.35 and 6.39 µm, while their corresponding values in the Sn58Bi1Ti were 0.42 and 4.99 µm.

2.3.2 Thermodynamic calculation on as-cast alloy

Thermal dynamic calculated Sn-Bi-Ti liquidus projection and isothermal section at 250 °C was displayed in figure 2-5. Figure 2-5(a) shows the partial liquidus projection of the Ti-lean Sn-Bi-Ti ternary system, where the isotherms of liquidus surface (thin green lines) are expressed with an interval of 30 °C and the two alloys of interests, namely the 0.5 and 1 wt % Ti added Sn-Bi alloys, are labeled, respectively. The calculated solidification paths based on either the lever rule or the Scheil model of each alloy were superimposed on the liquidus projection as shown in Figure 2-5(a). Given there were finite rates of diffusion during

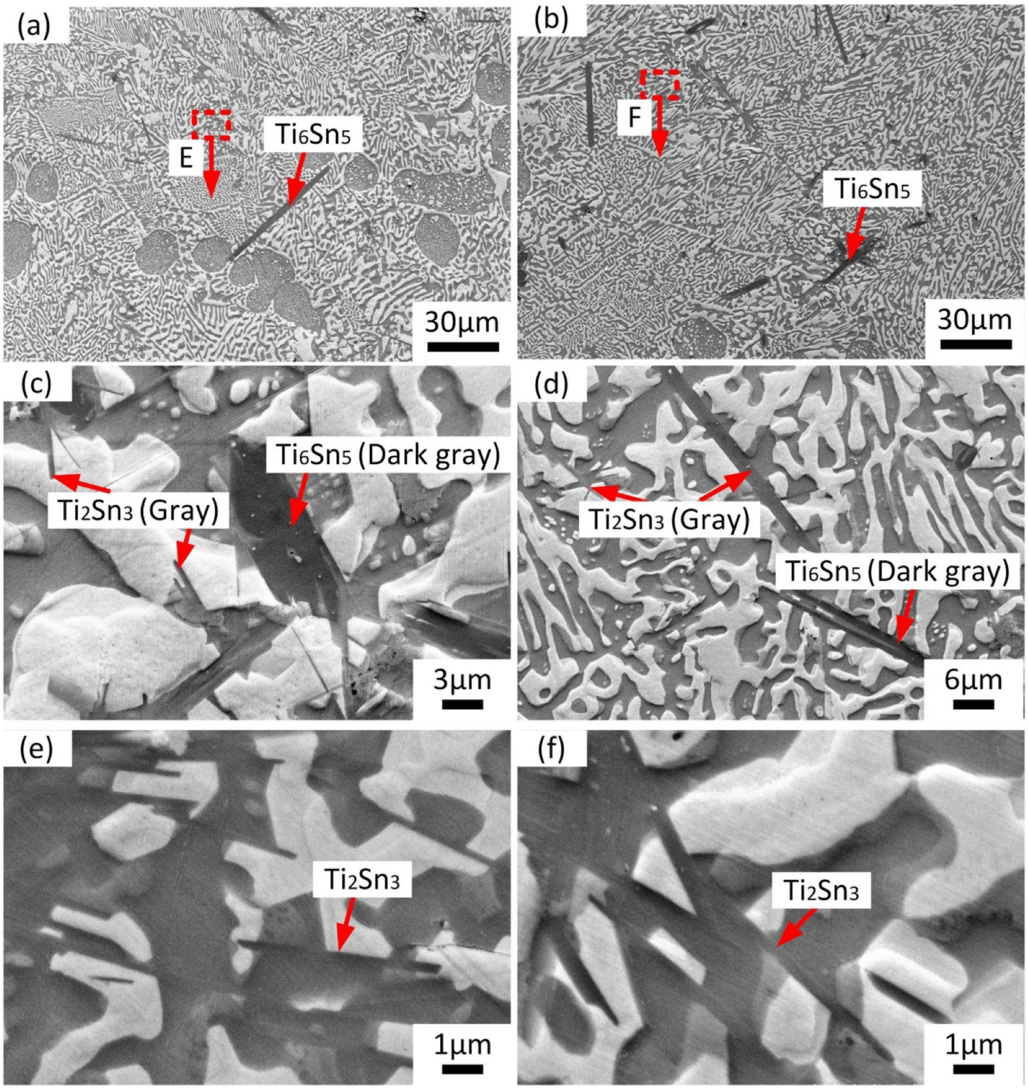

Figure 2-4 FE-SEM images. (a) low magnification image of Sn58Bi0.5Ti alloy; (b) low magnification image of Sn58Bi1Ti alloy; (c, d) the comparison of the gray and dark gray IMCs in Sn58Bi0.5Ti and Sn58Bi1Ti, respectively; (e, f) high magnification images of spot E and F.

solidification, the realistic solidification paths should lie between those derived based on the Scheil model and Lever rule; nevertheless, the two models outline the extreme cases as the boundary conditions. As shown in Figure 2-5(a), since the liquidus temperatures for the 0.5 and 1.0 wt % Ti added alloys are calculated to be as high as 753.98 and 651.29 °C, respectively, the initial solidification occurred during alloy preparation with an arc melting furnace, while the following re-melting process at 250 °C involved molten alloy with solid inclusions. As shown in Figure 2-5(a), the Ti_6Sn_5 was the primary solidification phase, i.e., $L \rightarrow Ti_6Sn_5$ reaction, for both alloys which was observed as a dark gray IMC shown in Figure 2-4. As

Table 2-2 EDX spectra data of three test points within dark gray and gray phases.

Phase contrast	Sn (at %)	Ti (at %)	Estimated phases
Dark gray	47.51	52.49	Ti_6Sn_5
Dark gray	46.05	53.95	Ti_6Sn_5
Dark gray	45.23	54.77	Ti_6Sn_5
Gray	60.04	39.95	Ti_2Sn_3
Gray	60.25	39.75	Ti_2Sn_3
Gray	61.23	38.77	Ti_2Sn_3

shown in Figure 2-5(b), a close-up at the Sn-Bi-rich region of the Sn-Bi-Ti ternary liquidus projection, followed by the precipitation of the Ti_6Sn_5 phase, the Ti_2Sn_3 phase subsequently solidified via the L → Ti_6Sn_5 + Ti_2Sn_3 co-precipitation reaction which was recognized as a gray contrast IMC shown in Figure 2-3. For the Scheil model (broken line), the following solidification path penetrates the L → Ti_6Sn_5 + Ti_2Sn_3 univariant line, proceeds with precipitating the Ti_2Sn_3 phase, reaches the L → (Bi) + (Ti_2Sn_3) univariant line with the (Bi) and Ti_2Sn_3 phases co-precipitation, and finally completes the solidification at the Class I reaction: L → (Bi) + (Sn) + (Ti_2Sn_3). For the lever rule (solid line), on the other hand, the solidification phase goes along the L → (Ti_6Sn_5) + (Ti_2Sn_3) univariant line for some extents, and then follows a similar path as the Schiel model, jumping into Ti_2Sn_3 primary phase region, then co-precipitating (Bi) and (Ti_2Sn_3) phases, and also ending at the Class I reaction: L → (Bi) + (Sn) + (Ti_2Sn_3).

As previously discussed, two methods of achieving microstructure refinement in a solder alloy was presented in introduction section of this chapter. They are introducing extra nucleation sites and blocking the diffusion in Sn-Bi phase boundary. In the Ti added Sn58Bi

Table 2-3 Average size of smaller Ti2Sn3 IMCs within Ti added Sn58Bi solder alloys before and after thermal aging at 504 and 1008 h.

Alloys (wt %)	Average size of small scale Ti_2Sn_3 IMCs (μm)					
	As-cast		504h		1008h	
	Width	Length	Width	Length	Width	Length
Sn58Bi0.5Ti	0.35	6.39	0.55	7.10	0.32	5.01
Sn58Bi1Ti	0.42	4.99	0.30	4.35	0.46	5.54

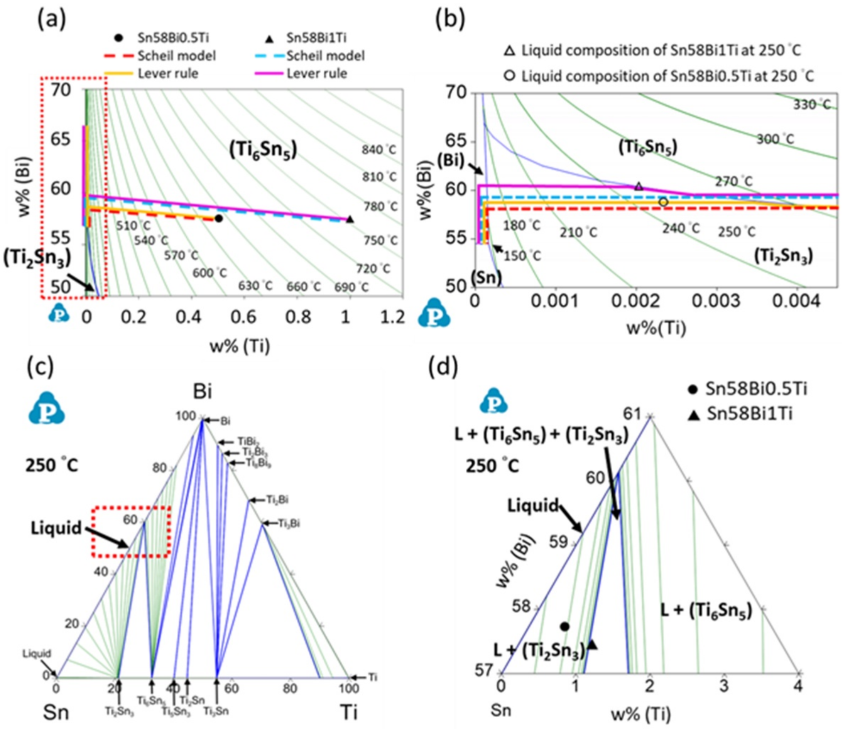

Figure 2-5 Thermal dynamic calculation result. (a) The calculated solidification paths of Sn58Bi0.5Ti and Sn58Bi1Ti after arc-melting by Lever rule and Scheil model on liquidus projection; (b) a close-up at the Sn-Bi boundary of Sn-Bi-Ti ternary liquidus projection; (c) The isothermal section of Sn-Bi-Ti ternary liquidus projection; (c) The isothermal section of Sn-Bi-Ti ternary system at 250 ℃; (d) a close-up at the compositional range of interest in (c).

alloys, the first method was realized in achieving refined microstructure. Prior to the microstructural analyses and characterizations, the alloys were re-melt at 250 °C for 2 h. Figures 2-5(c) and (d) show the 250 °C isothermal section of the Sn-Bi-Ti ternary system and its close-up at the compositional range of interest, respectively. As shown in Figure 2-5(d), the Sn58Bi0.5Ti, and Sn58Bi1Ti alloys are in the Ti_2Sn_3 + liquid two-phase region and the Ti_2Sn_3 + Ti_6Sn_5 + liquid three-phase region, respectively, meaning the previously formed Ti_6Sn_5 and/or Ti_2Sn_3 phases are pre-existing inclusions in the melts of the Sn58Bi0.5Ti and Sn58Bi1Ti alloys.

2.3.3 Microstructure refinement mechanism of as-cast alloy

The solid inclusions, i.e., Ti_6Sn_5 and/or Ti_2Sn_3 IMCs could then serve as the heterogeneous nucleation sites for solidification for the following soldering processes. Presumably, the liquid phases in both alloys were equilibrated after the re-melting process at 250 °C for 2 h. The composition of liquid phase in Sn58Bi0.5Ti and Sn58Bi1Ti at 250 °C are calculated to be Sn-58.6064 wt % Bi-0.0025 wt % Ti and Sn-59.2349 wt % Bi-0.0024 wt % Ti, respectively, as marked in Figure 2-5(b). Only *ca.* 25 ppm Ti in both alloys actually involved in the solidification of the re-melting process. The fine microstructure of (Bi) precipitation in both alloys is likely owing to the pre-existing Ti_6Sn_5 and Ti_2Sn_3 inclusions. While the presence of inclusion inhibited the phase coarsening, particularly for the (Bi) phase, an excess amount of inclusions may also lead to brittle properties. The calculated fraction of the Ti_2Sn_3 and Ti_6Sn_5 phases after solidification are 0.0318 and 2.9770 %, respectively, for the Sn58Bi0.5Ti alloy, while those are 0.0240 and 5.9154 %, respectively, for the Sn58Bi1Ti alloy.

It is noted that, a number of large size Bi grains were observed in eutectic Sn58Bi, but not in Ti added Sn58Bi. We believe kinetic of atom attachment was the theory to explain this finding. For the growth of a atomically-flat crystal, such as Bi, a large force difference between atom/crystal and atom/liquid must exist [11]–[13]. Owing to the undercooling in eutectic Sn58Bi alloy, the activation energy was provided for Bi atom to bond with each other and to grow its size, producing large size Bi grain. On the other hand, undercooling in Ti added Sn58Bi were much smaller and activation energy provided on bonding Bi atom was insufficient, resulting in refined Bi grain.

2.3.4 Thermal behaviors

DSC curves of eutectic Sn58Bi and Ti added Sn58Bi were obtained for the thermal behavior study, as shown in Figure 2-6. Endothermic and exothermic peaks were detected, as shown in Table 2-4. It is noted that undercooling is represented by the difference between onset of endothermic peak and onset of exothermic peak [14]. As shown as the equation:

$\varDelta T_u = T_{onset\text{-}endo} - T_{onset\text{-}exo}$

The undercooling for eutectic Sn58Bi is 7.31 °C, while those for 0.5 and 1 wt% Ti added Sn58Bi were 4.94 and 4.79 °C, respectively. It can be concluded that the pre-exiting solid-state Ti_6Sn_5 and Ti_2Sn_3 IMCs promoted the nucleation. As a result, decreasing the level of undercooling for Ti added Sn58Bi alloys.

2.3.5 Microstructure after thermal aging

Microstructure of eutectic Sn58Bi and Ti added Sn58Bi before and after thermal aging were shown in Figure 2-7. Finer microstructure was observed in Ti added Sn58Bi. The result of eutectic spacing was shown in Table 2-5. Eutectic spacing and the number of coarsened Sn and Bi phases for eutectic Sn58Bi increased during aging.

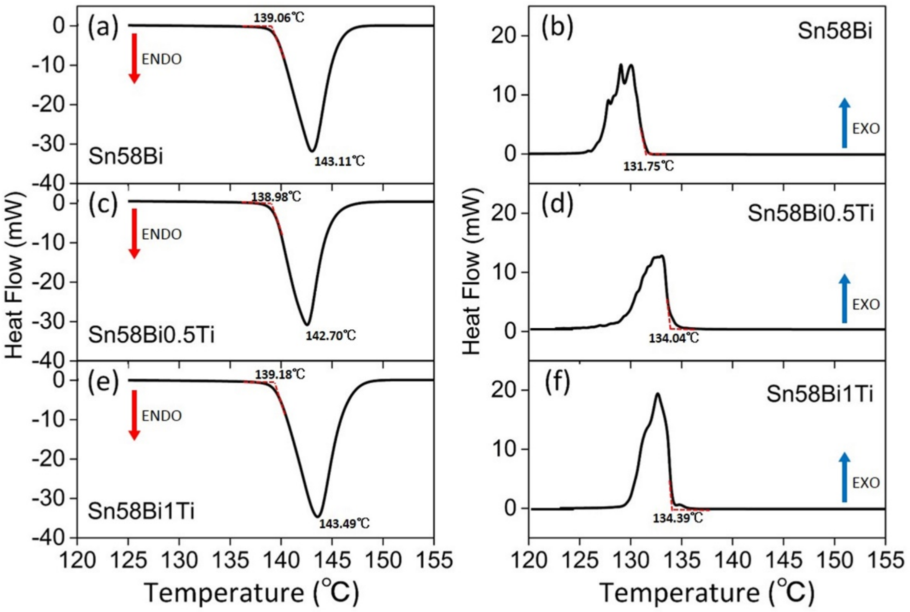

Figure 2-6 Differential scanning calorimetry (DSC) results of eutectic Sn58Bi and Ti-added alloys. (a, c, e) Heating processes of Sn58Bi, Sn58Bi0.5Ti, and Sn58Bi1Ti, respectively. (b. d, f) cooling processes of Sn58Bi, Sn58Bi0.5Ti, and Sn58Bi1Ti, respectively.

The small-size Ti_2Sn_3 IMCs were shown in Figure 2-8. The morphology of this IMCs in Ti added Sn58Bi did not change after either 504 h and 1008 h aging. Two information can be concluded. Firstly, the size of Ti_2Sn_3 IMCs was not related to the added Ti content. Secondly, these IMCs were very stable during solid-state thermal aging, probably due to the slow diffusion rate of Ti atom in Sn58Bi matrix under 80 °C aging condition. A previous study [6] reported this stable Ti_2Sn_3 IMC as well. Moreover, the reason of refined microstructure of Ti added Sn58Bi after aging was still unknown and we may attribute it to the existence of Ti-Sn IMCs.

Table 2-4 Specific temperature (°C) of DSC results. Solidus temperature ($T_{onset\text{-}endo}$) upon heating and liquidus temperature ($To_{nset\text{-}exo}$) upon cooling for Sn58BiXTi (X=0, 0.5, 1) alloys. And the undercooling comparisons of these alloys.

Alloys (wt %)	Heating	Cooling	Undercooling
	$T_{onset\text{-}endo}$	$T_{onset\text{-}exo}$	(ΔT_u)
Sn58Bi	139.06	131.75	7.31
Sn58Bi0.5Ti	138.98	134.04	4.94
Sn58Bi1Ti	139.18	134.39	4.79

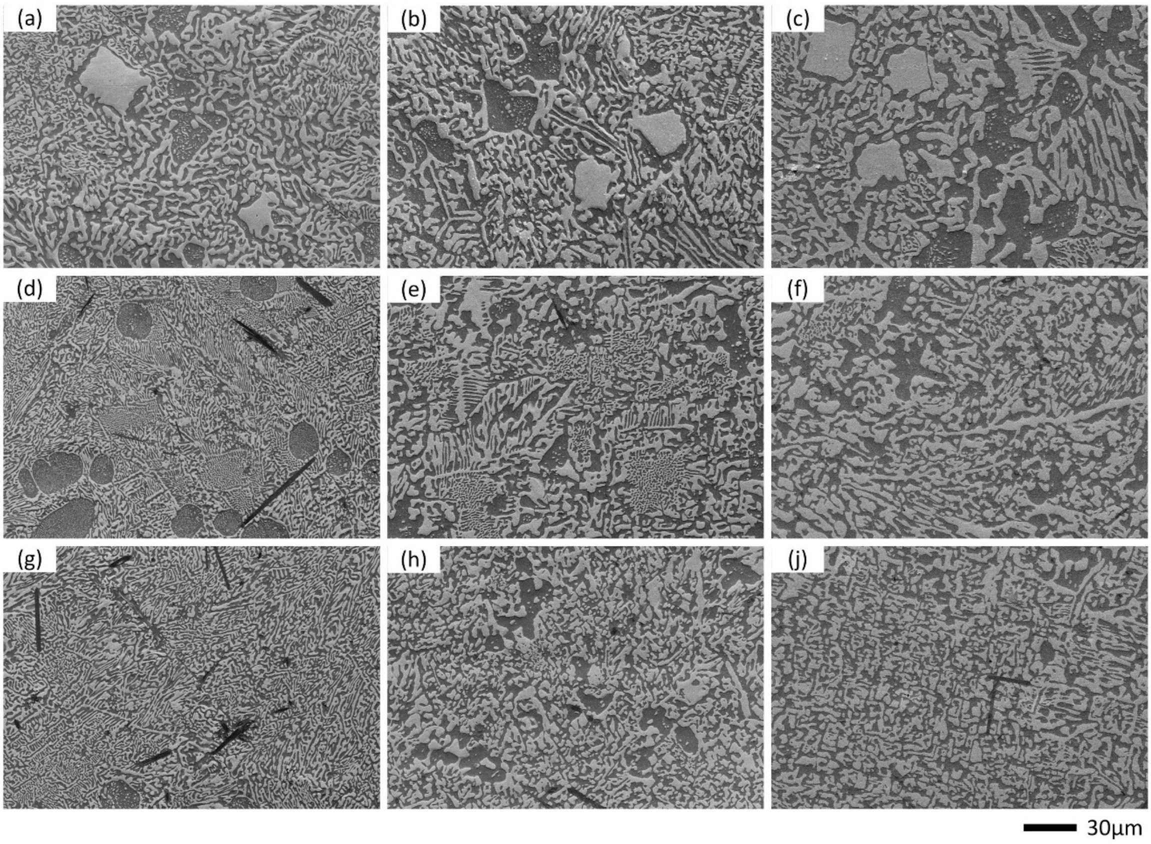

Figure 2-7 FE-SEM images of the cross-sectional microstructure of solder bulks. (a, b, c) Sn58Bi alloy aged for 0, 504, 1008 h. (d, e, f) Sn58Bi0.5Ti alloy aged for 0, 504, 1008 h. (g, h, j) Sn58Bi1Ti alloy aged for 0, 504, 1008 h.

2.3.6 Tensile test result

The mechanical properties of alloys were studied by tensile tests. Figure 2-9(a)-(c) shows the typical engineering stress-strain curves of samples before thermal aging. Figure 2-9(d) and (e) show the comparison of UTS and elongation at the three aging times. Before aging, the addition of Ti increased the YS and UTS of Ti added samples, while decreased elongation, as shown in Figure 2-8. The highest YS (51.81 MPa) and UTS (65.19 MPa) were observed for

Table 2-5 Average eutectic spacing within eutectic and Ti added Sn58Bi solder alloys before and after thermal aging at 504 and 1008 h.

Alloys (wt %)	Average eutectic spacing (μm)		
	As-cast	504h	1008h
Sn58Bi	4.52	4.97	7.22
Sn58Bi0.5Ti	1.79	3.57	4.78
Sn58Bi1Ti	2.01	3.35	4.04

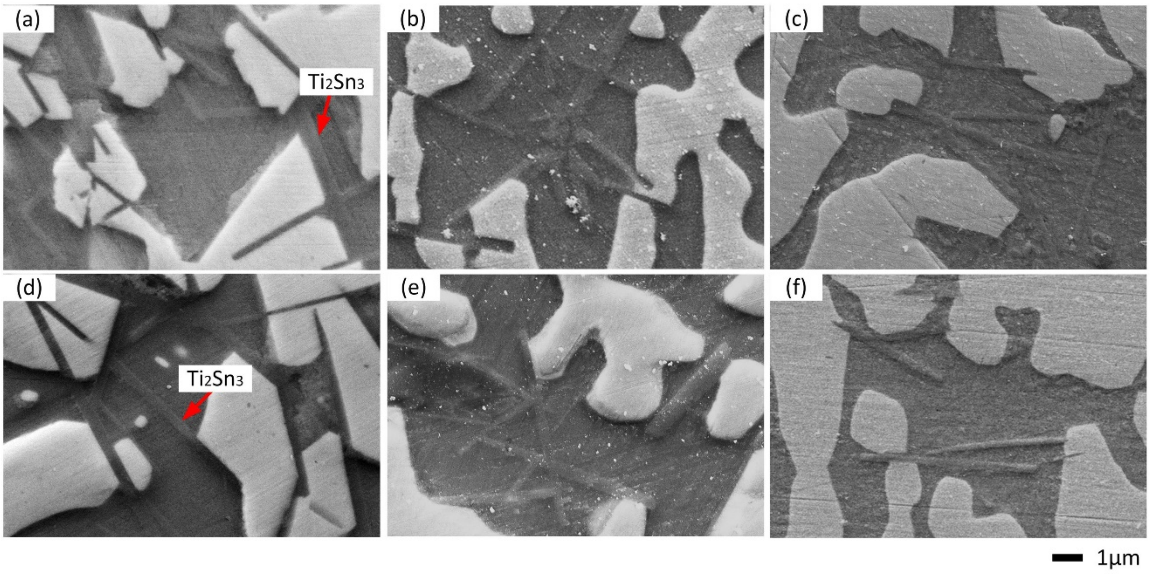

Figure 2-8 FE-SEM images of smaller Ti6Sn5 IMCs dispersed in solder matrix. (a, b, c) The Ti6Sn5 IMCs in Sn58Bi0.5Ti alloy aged for 0, 504, 1008 h. (d, e, f) The Ti6Sn5 IMCs in Sn58Bi1Ti alloy aged for 0, 504, 1008 h.

the 1Ti added Sn58Bi alloy. After thermal aging at 1008 h, the YS and UTS showed a decrease trend for eutectic Sn58Bi, while these values were maintained almost constant for Ti added samples. In addition, the elongation of the Sn58Bi0.5Ti almost unchanged during thermal aging, whereas the eutectic Sn58Bi and Sn58Bi1Ti both showed an obvious decrease in elongation. Especially after 1008 h aging, the elongation of the Sn58Bi0.5Ti was noticeably higher than that of the eutectic Sn58Bi.

Two classical theories can be applied to explain the improvement in YS and UTS. Because YS and UTS were improved by the addition of Ti, the refinement strength can be explained using the Hall-Petch relationship [15]:

$$\sigma_y = \sigma_0 + k_y d^{-1/2} \qquad (1)$$

Here, σ_y is the yield stress, d is the average grain diameter, σ_0 and k_y are the material constants. Based on Eq.(1), YS increased for Ti added Sn58Bi alloys, because of the refined microstructure in these alloy matrices.

In addition, Ti–Sn IMCs were served as obstacles to the dislocation movement and impede the grain-boundary sliding [2], [16], dispersion strengthening can be explained by the Orowan mechanism [17].

$$\sigma_{Org} = \frac{2Gb}{\lambda} \qquad (2)$$

Here, σ_{Org} is the yield stress, G is the shear modulus of the material, b is the Burger's vector of the dislocation, and λ is the distance between the dispersed second-phase particles.

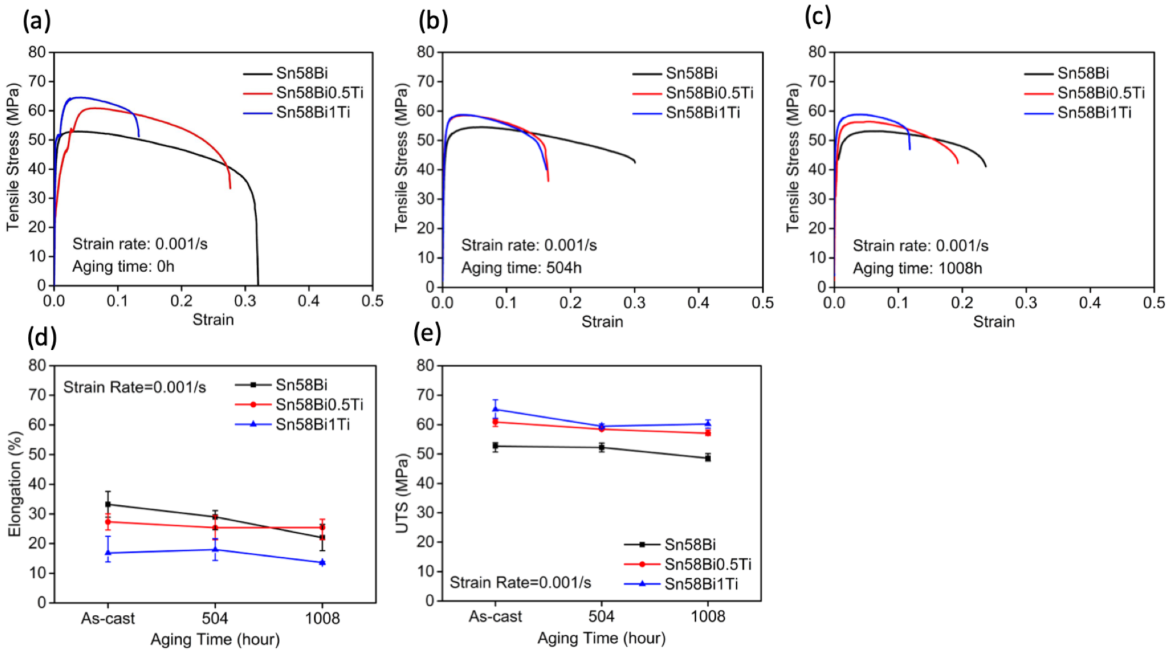

Figure 2-9 Tensile tests result of Ti-added Sn58Bi bulk alloy. (a, b, c) Tensile stain-stress curves of Sn58BiXTi (X=0, 0.5, 1) solder slabs after aging at 0, 504, 1008 h, respectively. The comparison of (d) ultimate tensile strength and (e) elongation on different aging times for Sn58BiXTi (X=0, 0.5, 1) solder slabs.

With an increase in the content of the added Ti, the number of Ti–Sn IMCs increased, and λ decreased. Hence, higher YS and UTS values of Sn58Bi1Ti alloy were obtained compared with those observed in the Sn58Bi0.5Ti alloy.

In addition, it has been reported that for the Sn based solder alloy, the finer the microstructure, the higher the elongation and the UTS a sample can perform [18]. Thus, the superior elongation property obtained in the Sn58Bi0.5Ti after 1008 h aging can be attributed to its fine microstructure. On the other hand, the Ti–Sn IMCs can act as the crack and microvoid nucleation sites due to the local stress concentration provided by these IMCs. This may be the reason why the elongations for Ti-added samples were lower than that of the eutectic Sn58Bi before aging, despite the refined microstructure. However, the microstructure coarsened in the eutectic Sn58Bi after 1008 h aging. The effect of a fine microstructure may trump the effect of Ti–Sn IMCs on elongation, resulting in a higher elongation for the Sn58Bi0.5Ti. For Sn58Bi1Ti, the lowest elongation before and after aging among the tested samples was largely attributed to the crack and microvoid nucleation sites introduced by the Ti–Sn IMCs, even though its microstructure was finer than that of the eutectic Sn58Bi.

2.3.7 Deformation behavior

Figure 2-10 shows the side view of fractured tensile samples before and after aging. It is clear that the morphology of each fractured samples are similar. They all fractured with a minimum amount of plastic deformation. Figure 2-11 shows the FE-SEM images of the fracture surfaces of each fracture sample. The fracture morphologies of the eutectic Sn58Bi and Ti added Sn58Bi alloys were similar before aging, while with increasing aging time, the noticeably different fracture morphology was observed in each sample. In addition, the cleavage fracture morphology of the Bi phase [19], [20] was clearly observed for all fracture surfaces. Also, because of the relatively narrow eutectic spacing of the Sn58Bi matrix, it was difficult to observe dimples within the Sn phase. Instead, the Sn phase always showed bulge fracture.

It is worth noting that the fracture mechanism for eutectic Sn58Bi is the combination of the two fracture modes of the Sn and Bi phases. Gain has reported this fracture mode is the "semi-ductile failure" [21]. During thermal aging, the size of the Bi phase in the eutectic Sn58Bi alloy increased. Also, because the deformation by twinning is easier for Bi compared to other metals [22], the crack path is more likely to follow the coarsened Bi phase rather than the fine eutectic and the Sn dendrite cells in an aged sample. The same fracture mechanism has been previously reported [2], [20]. Thus, visually, the area fraction of Bi phase within the fracture surface possibly increased with increasing aging time (Figure 2-11(a), (d), and (g), particularly in Figure 2-10(g), where the fractured Bi phase was dominant on the entire fracture surface.

On the other hand, in the Ti added Sn58Bi alloys. The Bi and Sn phases were clearly observed in the fracture surfaces, both before and after aging. This indicates that the fracture of Ti added samples mainly passed through the Sn-Bi eutectic structure. It is because Ti added

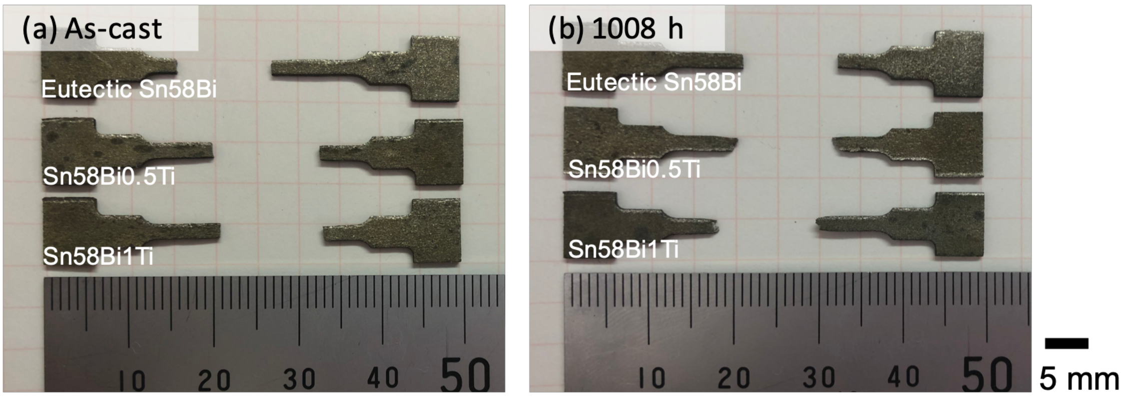

Figure 2-10 FE-SEM images of side views of tensile fractured samples.

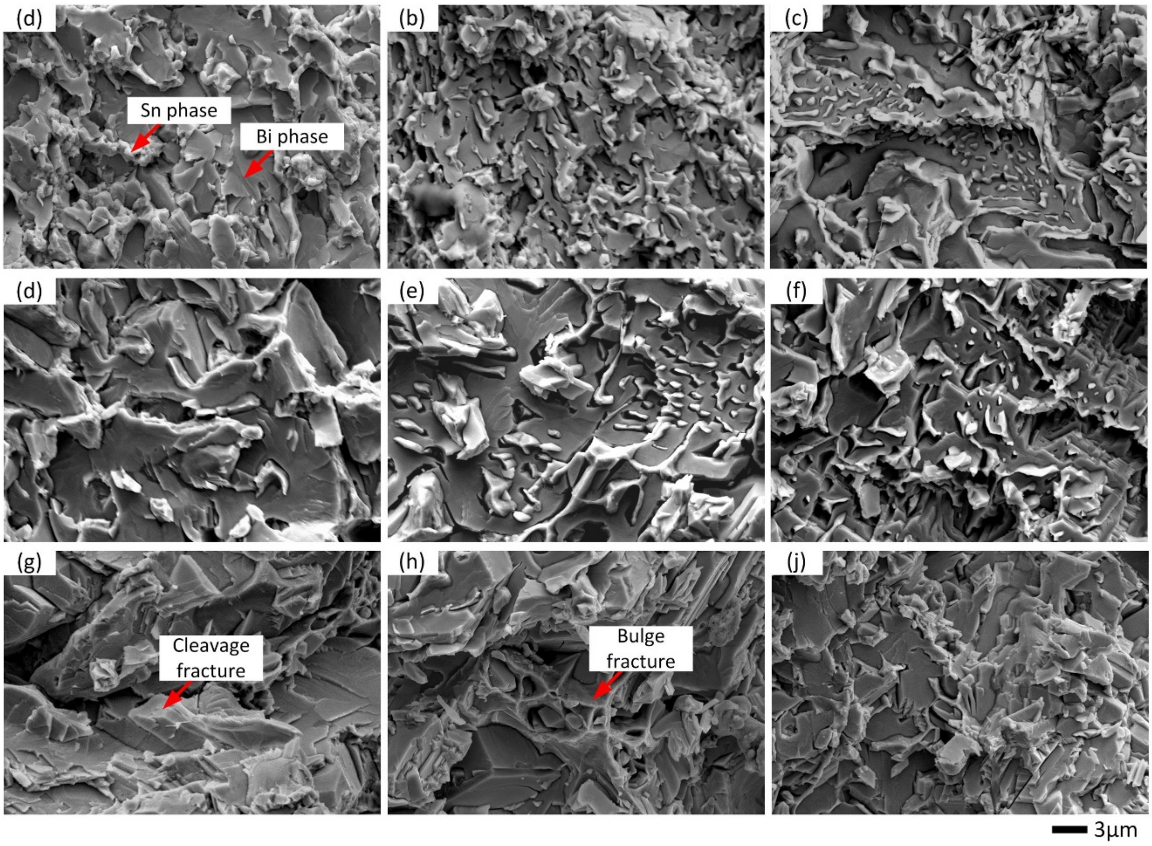

Figure 2-11 FE-SEM images of tensile fracture surfaces. (a, d, g) eutectic Sn58Bi aged for 0, 504 and 1008 h. (b, e, h) Sn58Bi0.5Ti aged for 0, 504 and 1008 h. (c, f, i) Sn58Bi1Ti aged for 0, 504 and 1008 h.

samples exhibited a considerably finer and more stable microstructure compared with the eutectic Sn58Bi alloy, and the coarsened Bi was completely avoided during aging.

2.3.8 Electrical resistivity

The tested electrical resistivity of eutectic Sn58Bi, Sn58Bi0.5Ti, and Sn58Bi1TI alloys, as well as those of the Sn, Bi, and Ti_2Sn_3 IMC phases found in the literature, are shown in Table 2-6. The Ti-added Sn58Bi alloys showed lower electrical resistivity compared with that of the eutectic Sn58Bi alloy. Since the eutectic Sn58Bi alloy has two distinct phases, *i.e.*, Bi and Sn phases, the resistivity mixture rule [23] (Eq. 3) was applied to verify the tested result.

$$\rho_{\mathrm{Sn58Bi}} = \chi_{Sn}\rho_{Bi} + \chi_{Sn}\rho_{Bi} \qquad (3)$$

Where ρ_{Sn58Bi} is the effective resistivity of the eutectic Sn58Bi alloy, χ_{Sn} and χ_{Bi} are the volume fraction of the Sn and Bi phases, while ρ_{Sn} and ρ_{Bi} are the electrical resistivities of these two phases. The χ_{Sn} and χ_{Bi} was 42 % and 58 %, respectively. Based on the data from the literature, ρ_{Sn} = 12 μΩ cm and ρ_{Bi} = 129 μΩ cm, therefore the calculated result of ρ_{Sn58Bi}

Table 2-6 Electrical resistivity of different materials at room temperature.

Materials	Electrical resistivity, ρ (μΩ cm)	Refs.
Sn58Bi	72.3	This study
Sn58Bi0.5Ti	69.9	This study
Sn58Bi1Ti	65	This study
Sn	12	[23]
Bi	129	[24]
Ti_2Sn_3	22	[25]
Ti_6Sn_5	N/A	N/A

is 79.89 μΩ cm, which is similar compared with the tested result (72.3 μΩ cm). We consider it is acceptable to apply the resistivity mixture rule on the eutectic Sn58Bi alloy.

On the other hand, since the Ti added Sn58Bi alloys consisted of Bi, Sn, and Ti–Sn IMC distinct phases, the corresponding resistivity mixture rule (Eq. 4) was again applied. The eutectic Sn58Bi was considered as one phase, Ti_2Sn_3, and Ti_6Sn_5 IMCs are the other two phases for a clear explanation.

$$\rho_{\mathrm{Sn58BiXTi}} = \chi_{Sn58Bi}\rho_{Sn58Bi} + \chi_{Ti2Sn3}\rho_{Ti2Sn3} + \chi_{Ti6Sn5}\rho_{Ti6Sn5} \qquad (4)$$

Where $\rho_{\mathrm{Sn58BiXTi}}$ (x = 0.5, 1) is the effective resistivity of the Ti added Sn58Bi alloys. χ_{Sn58Bi}, χ_{Ti2Sn3}, and χ_{Ti6Sn5} are the volume fractions of the eutectic Sn58Bi, Ti_2Sn_3, and Ti_6Sn_5 IMCs. ρ_{Sn58Bi}, ρ_{Ti2Sn3}, and ρ_{Ti6Sn5} are the electrical resistivities of the eutectic Sn58Bi alloy, Ti_2Sn_3, and Ti_6Sn_5 IMCs, as shown in Table 2-6. Since the volume fraction of the Ti_6Sn_5 IMC was significantly higher than that of the Ti_2Sn_3 IMC in the Ti added Sn58Bi alloys (χ_{Ti6Sn5} = 2.977 % and χ_{Ti2Sn3} = 0.0318 % in the Sn58Bi0.5Ti; χ_{Ti6Sn5} = 5.915 % and χ_{Ti2Sn3} = 0.024 % in the Sn58Bi1Ti), the Ti_6Sn_5 IMC had more impact on the electrical resistivity than the Ti_2Sn_3 IMC. However, to our best knowledge, the electrical resistivity of Ti_6Sn_5 IMC is still remained unknown. In conclusion, by introducing the Ti-Sn IMCs into the alloy, the lower electrical resistivity of Ti added Sn58Bi than that of the eutectic Sn58Bi alloy was successfully obtained.

2.4 ENIG/alloy/ENIG joint

2.4.1 Cross-sectional microstructure

Figure 2-12 shows the side views of solder joints using eutectic Sn58Bi and Sn58Bi0.5Ti. It is noted that sound and dense joints were produced using these two alloys. Figure 2-13 shows the EPMA mapping result of the bottom interfacial layer of eutectic Sn58Bi/ENIG joint before aging. In the black-scattered electrons (BSE) image, the bright and dark regions in the solder bulk represent Bi and Sn, respectively [24], [25]. A scallop-like IMC layer was observed on top of the substrate. Sn, Au, and Ni were detected in this IMC layer region. It is reported that the entire layer of Au diffuses into the molten solder in the SAC305/ENIG interface [26]. However, in this study, Au seemed to not diffuse entirely into EPMA mapping result of the bottom interfacial layer of eutectic Sn58Bi/ENIG joint before aging the solder bulk but gathered near the eutectic Sn58Bi/ENIG interface. Additionally, Sn and Ni were clearly observed in the interface layer region. EPMA point analysis indicated that the composition of this IMC layer was (Au, Ni)(Sn, Bi)$_4$, as shown in Table 2-7. The same IMC layer was also reported in another study [27] where Sn57.6Bi0.4Ag solder was reflowed on an Au/Ni/Cu pad.

The EPMA mapping result of Sn58Bi0.5Ti/ENIG interface before aging was displayed in Figure 2-14. The IMC layer showed similar morphology compared with that of eutectic Sn58Bi/ENIG interface. EPMA point result showed that the IMC layer was (Au, Ni)(Sn, Bi)$_4$ as well (point2 in Table 2-7), indicating Ti was not involved in the interfacial reaction between solder and substrate.

Figure 2-15 shows the comparison of the growth behaviors of the interfacial IMC layers of eutectic Sn58Bi and Sn58Bi0.5Ti solder joints during thermal aging. As shown in Figures 2-15(a)-(c), the thicknesses of the IMC layers on eutectic Sn58Bi/ENIG interfaces increased during thermal aging. The morphology of this layer transformed from a scallop-like to a

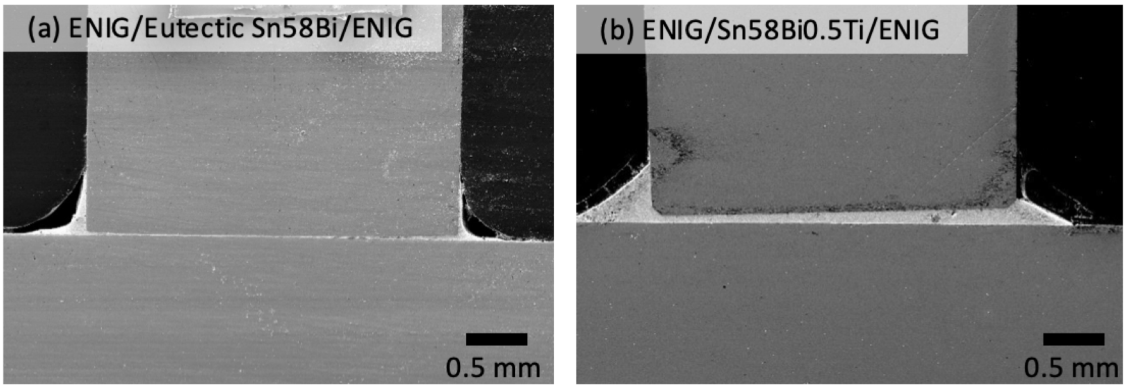

Figure 2-12 FE-SEM images of side views of solder joints.

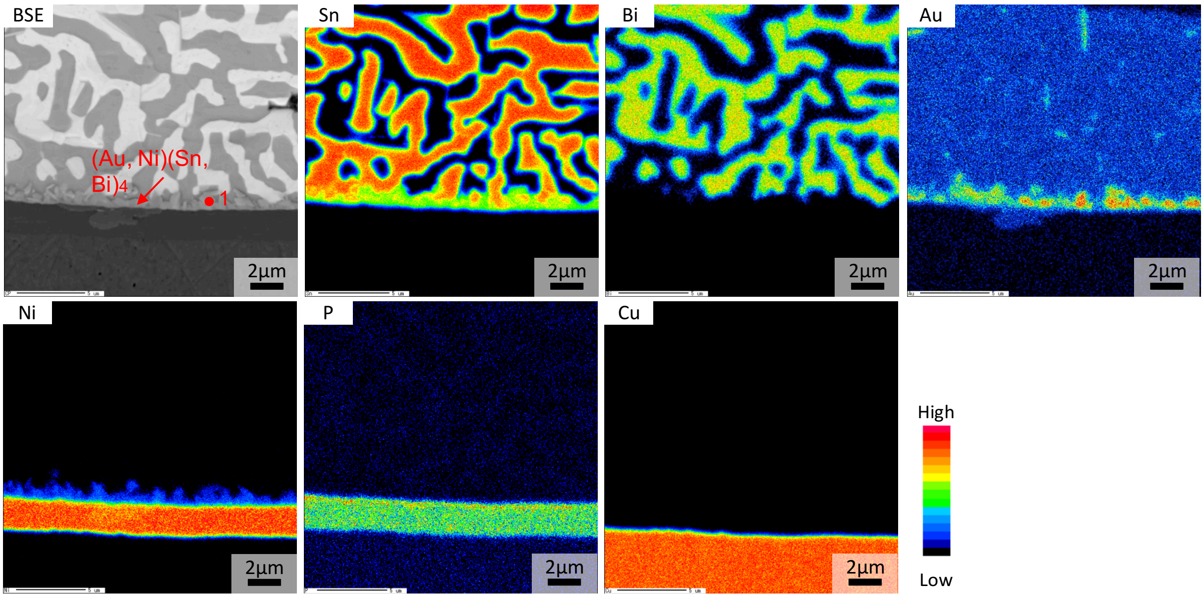

Figure 2-13 EPMA mapping of the bottom interfacial layer of eutectic Sn58Bi/ENIG joint before aging.

faceted-like morphology. The compositions of IMC layers at different aging stages were tested by EPMA point analysis. As mentioned in the previous section, the IMC layer in an as-reflowed eutectic Sn58Bi joint was the (Au, Ni)(Sn, Bi)$_4$ IMC layer. During thermal aging, previously dissolved Au diffused back towards the Ni-rich interface and thickened the (Au, Ni)(Sn, Bi)$_4$ IMC layer. After 1008 h aging, another interfacial IMC layer was observed underneath the (Au, Ni)(Sn, Bi)$_4$ layer, as shown in Figure 2-15(c). The EPMA point analysis results indicated this was the Ni$_3$Sn$_4$ IMC layer, as shown in Table 2-7. Interestingly, Woo-Ram et al. [28] found

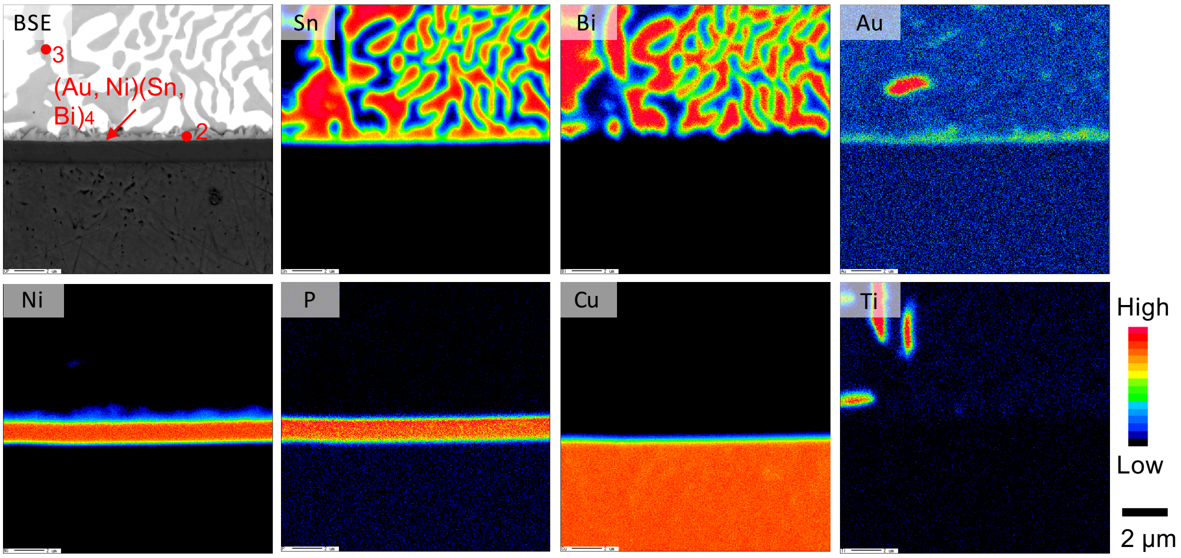

Figure 2-14 EPMA mapping of the bottom interfacial layer of eutectic Sn58Bi0.5Ti/ENIG joint before aging.

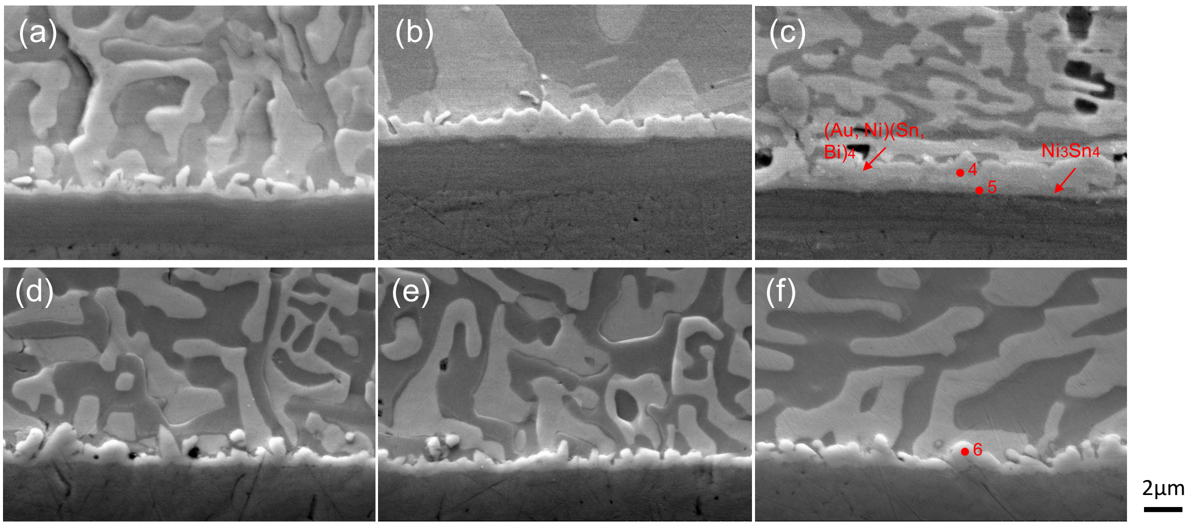

Figure 2-15 Interfacial IMC layers of eutectic Sn58Bi and Sn58Bi0.5Ti solder joints during thermal aging. (a)-(c) Eutectic Sn58Bi/ENIG interfacial IMC layer during aging; (d)-(f) Eutectic Sn58Bi0.5Ti/ENIG interfacial IMC layer during aging.

that Ni_3Sn_4 IMC layer was first formed on the as-reflowed eutectic Sn58Bi/ENIG instead of the (Au, Ni)$(Sn, Bi)_4$ IMC layer, as in our study.

On the other hand, the microstructure evolution of Sn58Bi0.5Ti/ENIG interface was displayed in Figures 15(d)-(f). The morphology remained almost unchanged between after aged samples and as-cast one. The composition of IMC layer after 1008 h aging was obtained as (Au, Ni)$(Sn, Bi)_4$, as shown in point 6 in Table 2-7. It is interesting that the IMC layer on Sn58Bi0.5Ti/ENIG interface could maintained its morphology during thermal aging. This is because two IMC layer growth suppression mechanisms we discussed in the introduction section were not observed. They are, first, Ti was not involved in the reaction of IMC layer formation during reflow process. Second, Ti was not adsorbed on top of the IMC layers and suppressing the IMC layer growth. It is noted that, in Figure 2-5(b), the amount of Ti involved in the solidification of remelting process was around 25 ppm. Therefore, these Ti solid solutes may responsible in suppressing the IMC layer growth. However, the detailed mechanism was unclear.

The IMC layer thickness change during aging was displayed in Figure 2-16. Even though (Au, Ni)$(Sn, Bi)_4$ was obtained in both eutectic Sn58Bi and Sn58Bi0.5Ti joints, it grow slower on Sn58Bi0.5Ti/ENIG interface than that on eutectic Sn58Bi/ENIG interface.

2.4.2 Shear test and fracture surface

Table 2-7 EPMA elemental-point analyses at various locations shown in the SEM images (locations are indicated by red dots and numbers).

Location	IMC type	Composition (at.%)					
		Sn	Bi	Ni	Zn	Au	Ti
Figure 2-13, point 1	(Au, Ni)(Sn, Bi)$_4$	60.2	13.2	14.1	-	4.5	-
Figure 2-14, point 2	(Au, Ni)(Sn, Bi)$_4$	62.1	13.9	16.1	-	7.9	-
Figure 2-14, point 3	Ti_6Sn_5	44.7	-	-	-	-	55.3
Figure 2-15, point 4	(Au, Ni)(Sn, Bi)$_4$	63.5	8.9	14.5	-	3.8	-
Figure 2-15, point 5	Ni_3Sn_4	45.5	-	39.5	-	-	-
Figure 2-15, point 6	(Au, Ni)(Sn, Bi)$_4$	60.8	12.7	15.8	-	10.7	-

EPMA mappings of fractured joint surfaces are displayed in Figure 2-17 and 2-18. Top and bottom substrates were both analyzed for a better understanding of fracture paths. In as-reflowed eutectic Sn58Bi joints, Ni and P were hardly observed and the fracture surfaces were completely covered by both Sn and Bi. This indicated that the fracture paths were entirely in

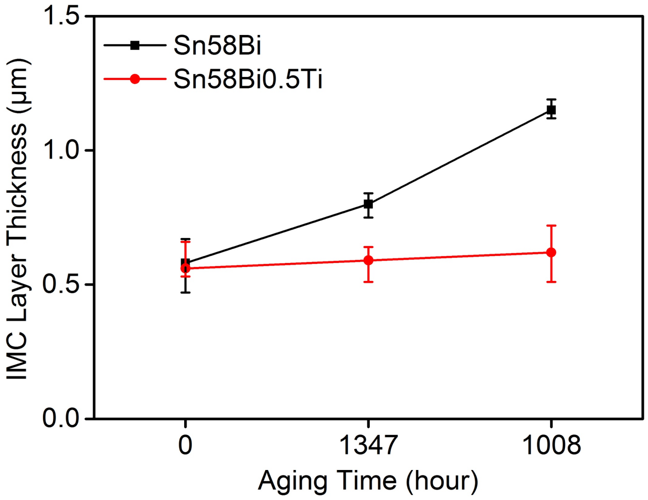

Figure 2-16 The IMC layer thickness change of eutectic Sn58Bi and Sn58Bi0.5Ti joints during aging.

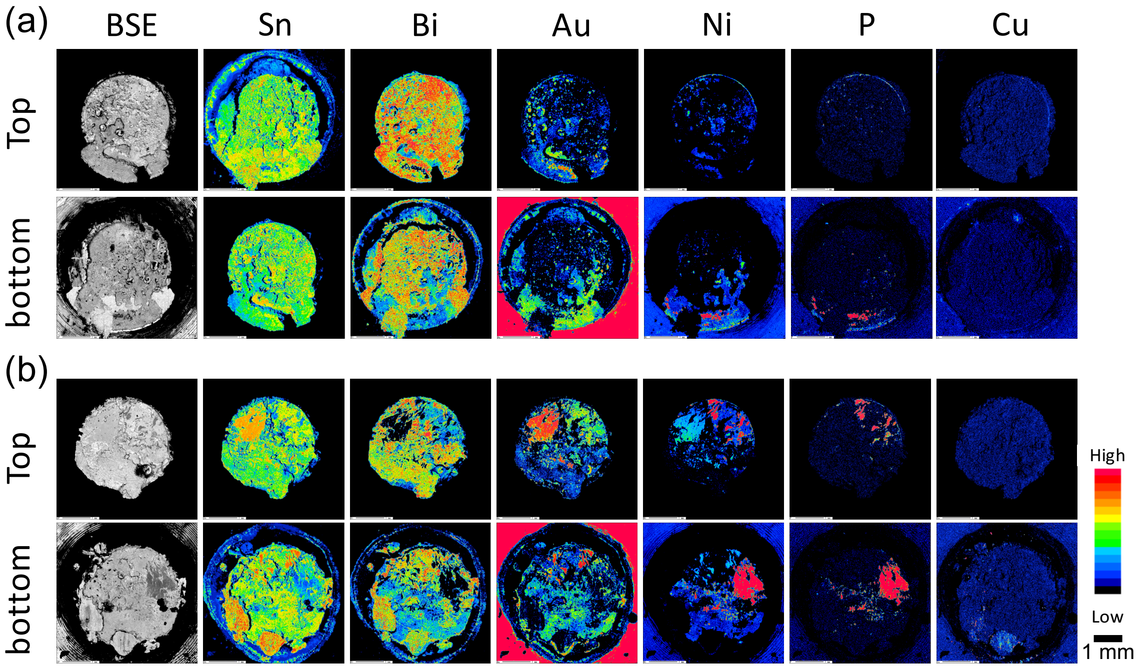

Figure 2-17 EPMA mappings of fractured eutectic Sn58Bi joint surfaces. (a) Before aging and (b) after 1008 h aging.

the solder bulk, as shown in Figure 2-17(a). After 1008 h aging, a large area of Ni and P was seen on fracture surfaces of both the bottom and top substrates, while the corresponding area shows no signal of Bi, as shown in Figure 2-17(b). This means that the fracture path was partially through the interfacial IMC layer, specifically the Ni_3Sn_4 and Ni(P) layers, where no Bi was present. This change in the fracture mode was caused by the brittleness of the Ni_3Sn_4 IMC layer, which has been reported elsewhere [29].

In contrast, neither Ni nor P were observed in fracture surfaces of Sn58Bi0.5Ti joints before and after 1008 h aging, as shown in Figure 2-18. This indicated that the fracture path in Sn58Bi0.5Ti joint did not pass through the interfacial IMC layer, which contained Ni element. The absence of Ni and P in fracture surface was attributed to the thin $(Au, Ni)(Sn, Bi)_4$ IMC layer in Sn58Bi0.5Ti/ENIG interface after 1008 h aging.

Comparing the top view of the fracture surface of two kinds joints, Sn58Bi0.5Ti joints contained more voids than eutectic Sn58Bi joints (BSE images in Figures 2-18 had more voids in Figure 2-17). A close look of a void was shown in Figure 2-19. A number of bar-shaped IMCs were observed inside a void, and the EDS result indicated it was Ti_6Sn_5 IMC. It is assumed that Ti_6Sn_5 IMC triggered formation of voids. On the other hand, owing to the stable $(Au, Ni)(Sn, Bi)_4$ IMC layer, the shear strength was superior than that of eutectic Sn58Bi joint. Figure 2-20 shows the shear strength comparison of the eutectic Sn58Bi and Sn58Bi0.5Ti joints. It is clear that Sn58Bi0.5Ti joints had a better shear strength stability than eutectic Sn58Bi

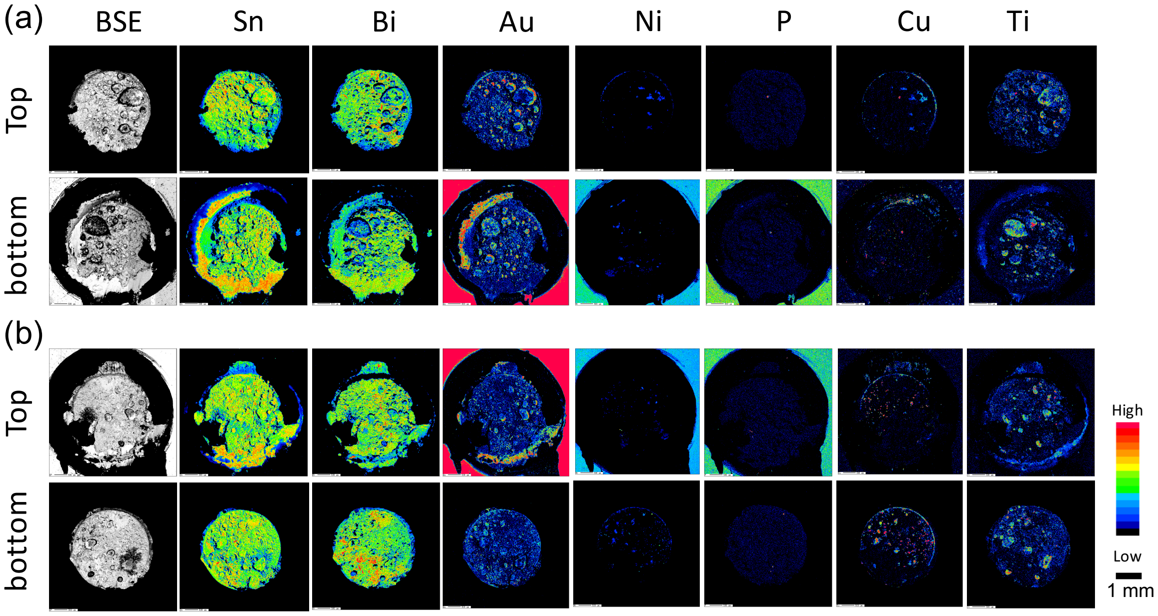

Figure 2-18 EPMA mappings of fractured eutectic Sn58Bi0.5Ti joint surfaces. (a) Before aging and (b) after 1008 h aging.

joints. The shear strength of the eutectic Sn58Bi joints decreased by 25 % after 1008 h of aging, while only a slight strength decrease was observed in Sn58Bi0.5Ti joints (around 10 %). It is noted that either before or after aging, Sn58Bi0.5Ti joint had a higher shear strength than eutectic Sn58Bi joint. This was attributed to the Ti-Sn IMCs dispersed in the matrix, resulting in a strengthened solder joint. Moreover, the decrease of the shear strength of Sn58Bi0.5Ti joints was not related to change of the fracture mode, since fracture pathed through solder bulk for Sn58Bi0.5Ti joints either before or after thermal aging.

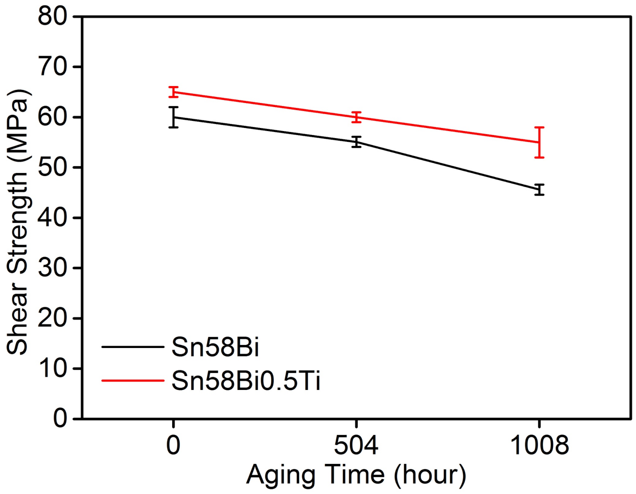

Figure 2-19 The shear strength change of eutectic Sn58Bi and Sn58Bi0.5Ti joints during aging.

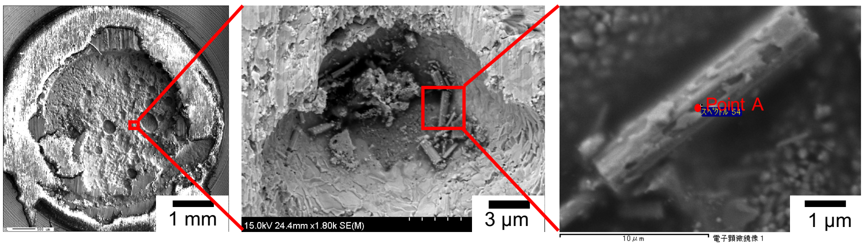

Point A:

Element	Concentration (wt%)
Ti	53.43
Sn	46.57

Figure 2-20 A close look of a void in the fracture surface of Sn58Bi0.5Ti joint before aging.

Conclusion

The effects of the Ti addition on the microstructures and tensile properties of eutectic Sn58Bi alloys were investigated before and after thermal aging. In addition, the electrical resistivities of these Ti-added Sn58Bi alloys were studied at room temperature.

For solder bulk:

Compositional characterizations and thermodynamic analyses show that in addition to the large Ti_6Sn_5 IMCs, a large amount of Ti_2Sn_3 IMCs of two particle sizes are uniformly dispersed in the Ti added Sn58Bi alloy matrices. During thermal aging, these IMCs remained in their original morphologies and stabilized the grain structure of the solder matrix.

The pre-existing Ti_6Sn_5 inclusions suppressed the undercooling of the Ti added Sn58Bi alloys during re-melting process.

The UTS and YS of Ti added Sn58Bi solders increased with increasing Ti content and remained constant during thermal aging. The elongation of Sn58Bi0.5Ti remained almost unchanged during thermal aging and surpassed the eutectic Sn58Bi after 1008 h aging.

The tested electrical resistivity of the eutectic Sn58Bi alloy was verified by the resistivity mixture rule. On the other hand, the lower electrical resistivity of Ti added Sn58Bi alloy was obtained.

For solder joints:

(Au, Ni)(Sn, Bi)4 was observed on both the eutectic Sn58Bi/ENIG and Sn58Bi0.5Ti/ENIG interfaces before aging. After 1008 h thermal aging, another Ni3Sn4 IMC layer formed underneath the (Au, Ni)(Sn, Bi)4 layer on eutectic Sn58Bi/ENIG interface, while no change for Sn58Bi0.5Ti/ENIG interface. The IMC layer thickness for Sn58Bi0.5ti joint was much lower than that of eutectic Sn58Bi joint after 1008 h thermal aging.

Owing to the suppressed IMC layer on the Sn58Bi0.5Ti/ENIG interface during thermal aging, fracture occurred inside the Sn58Bi0.5Ti solder bulk but not IMC layer.

Shear strength of Sn58Bi0.5Ti joints was higher than that of eutectic Sn58Bi joints, although both of them experienced strength decrease during aging. Ti-Sn IMCs distributed inside the Sn58Bi0.5Ti solder acted as a strengthening phase and increased the shear strength.

Reference

[1] Y. Li and Y. C. Chan, “Effect of silver (Ag) nanoparticle size on the microstructure and mechanical properties of Sn58Bi-Ag composite solders,” *J. Alloys Compd.*, vol. 645, pp. 566–576, 2015.

[2] L. Yang *et al.*, “Effects of Ni addition on mechanical properties of Sn58Bi solder alloy during solid-state aging,” *Mater. Sci. Eng. A*, vol. 667, pp. 368–375, 2016.

[3] L. Yang *et al.*, “Effect of Ni and Ni-coated Carbon Nanotubes on the interfacial reaction and growth behavior of Sn58Bi/Cu intermetallic compound layers,” *J. Mater. Sci. Mater. Electron.*, vol. 27, no. 11, pp. 12264–12270, 2016.

[4] Y. Ma, X. Li, W. Zhou, L. Yang, and P. Wu, “Reinforcement of graphene nanosheets on the microstructure and properties of Sn58Bi lead-free solder,” *Mater. Des.*, vol. 113, pp. 264–272, Jan. 2017.

[5] K. R. Cardoso, D. N. Travessa, A. G. Escorial, and M. Lieblich, “Effect of mechanical alloying and Ti addition on solution and ageing treatment of an AA7050 aluminium alloy,” *Mater. Res.*, vol. 10, no. 2, pp. 199–203, 2007.

[6] W. M. Chen, S. K. Kang, and C. R. Kao, “Effects of Ti addition to Sn-Ag and Sn-Cu solders,” *J. Alloys Compd.*, vol. 520, pp. 244–249, 2012.

[7] L. W. Lin, J. M. Song, Y. S. Lai, Y. T. Chiu, N. C. Lee, and J. Y. Uan, “Alloying modification of Sn-Ag-Cu solders by manganese and titanium,” *Microelectron. Reliab.*, vol. 49, no. 3, pp. 235–241, 2009.

[8] C. L. Chuang, L. C. Tsao, H. K. Lin, and L. P. Feng, “Effects of small amount of active Ti element additions on microstructure and property of Sn3.5Ag0.5Cu solder,” *Mater. Sci. Eng. A*, vol. 558, pp. 478–484, 2012.

[9] M.-S. Kim and H. Nishikawa, “Transmission electron microscopy investigation on the Oxidation behavior of Electroless Ni/Immersion Au surface finish at 250 C,” *J. Nanosci. Nanotechnol.*, vol. 17, no. 11, pp. 8522–8527, 2017.

[10] W. Cao *et al.*, “PANDAT software with PanEngine, PanOptimizer and PanPrecipitation for multi-component phase diagram calculation and materials property simulation,” *Calphad*, vol. 33, no. 2, pp. 328–342, 2009.

[11] O. Mokhtari and H. Nishikawa, “Correlation between microstructure and mechanical properties of Sn-Bi-X solders,” *Mater. Sci. Eng. A*, vol. 651, pp. 831–839, 2016.

[12] W. Kurz and D. J. Fisher, *Fundamentals of solidification*, vol. 1. trans tech publications Aedermannsdorf, Switzerland, 1986.

[13] M. F. X. Gigliotti, G. A. Colligan, and G. L. F. Powell, “Halo formation in eutectic alloy systems,” *Metall. Trans.*, vol. 1, no. 4, pp. 891–897, 1970.

[14] G. Zeng *et al.*, “The influence of Ni and Zn additions on microstructure and phase transformations in Sn–0.7 Cu/Cu solder joints,” *Acta Mater.*, vol. 83, pp. 357–371, 2015.

[15] W. D. Callister Jr and D. G. Rethwisch, *Fundamentals of materials science and engineering: an integrated approach*. John Wiley & Sons, 2012.

[16] L. C. Tsao and S. Y. Chang, “Effects of Nano-TiO2 additions on thermal analysis, microstructure and tensile properties of Sn3.5Ag0.25Cu solder,” *Mater. Des.*, vol. 31, no. 2, pp. 990–993, 2010.

[17] F. Hou, W. Wang, and H. Guo, “Effect of the dispersibility of ZrO2 nanoparticles in Ni–ZrO2 electroplated nanocomposite coatings on the mechanical properties of nanocomposite coatings,” *Appl. Surf. Sci.*, vol. 252, no. 10, pp. 3812–3817, 2006.

[18] G. Grossmann and C. Zardini, *The ELFNET book on failure mechanisms, testing methods, and quality issues of lead-free solder interconnects*. Springer Science & Business Media, 2011.

[19] J. Shen, Y. Pu, H. Yin, D. Luo, and J. Chen, “Effects of minor Cu and Zn additions on the thermal, microstructure and tensile properties of Sn-Bi-based solder alloys,” *J. Alloys Compd.*, vol. 614, pp. 63–70, 2014.

[20] Q. Li, N. Ma, Y. P. Lei, J. Lin, H. G. Fu, and J. Gu, “Characterization of Low-Melting-Point Sn-Bi-In Lead-Free Solders,” *J. Electron. Mater.*, vol. 45, no. 11, pp. 5800–5810, 2016.

[21] A. K. Gain and L. Zhang, “Growth mechanism of intermetallic compound and mechanical properties of nickel (Ni) nanoparticle doped low melting temperature tin–

bismuth (Sn–Bi) solder," *J. Mater. Sci. Mater. Electron.*, vol. 27, no. 1, pp. 781–794, 2016.

[22] J.-M. Song, H.-Y. Chuang, and T.-X. Wen, "Thermal and tensile properties of Bi-Ag alloys," *Metall. Mater. Trans. A*, vol. 38, no. 6, pp. 1371–1375, 2007.

[23] S. O. Kasap, *Principles of electronic materials and devices*, vol. 2. McGraw-Hill New York, 2006.

[24] O. Mokhtari, S. Zhou, and H. Nishikawa, "Effect of Zn addition on interfacial reactions between Sn-Bi solder and Cu substrate," *Mater. Trans.*, vol. 57, no. 8, pp. 1272–1276, 2016.

[25] S. Zhou, O. Mokhtari, M. G. Rafique, V. C. Shunmugasamy, B. Mansoor, and H. Nishikawa, "Improvement in the mechanical properties of eutectic Sn58Bi alloy by 0.5 and 1 wt.% Zn addition before and after thermal aging," *J. Alloys Compd.*, 2018.

[26] J.-W. Yoon, B.-I. Noh, and S.-B. Jung, "Effects of third element and surface finish on interfacial reactions of Sn–Ag–xCu (or Ni)/(Cu or ENIG) solder joints," *J. Alloys Compd.*, vol. 506, no. 1, pp. 331–337, 2010.

[27] Y. Li, K. Luo, A. B. Y. Lim, Z. Chen, F. Wu, and Y. C. Chan, "Improving the mechanical performance of Sn57.6Bi0.4Ag solder joints on Au/Ni/Cu pads during aging and electromigration through the addition of tungsten (W) nanoparticle reinforcement," *Mater. Sci. Eng. A*, vol. 669, pp. 291–303, 2016.

[28] W.-R. Myung, Y. Kim, K.-Y. Kim, and S.-B. Jung, "Drop Reliability of Epoxy-contained Sn-58 wt.% Bi Solder Joint with ENIG and ENEPIG Surface Finish Under Temperature and Humidity Test," *J. Electron. Mater.*, vol. 45, no. 7, pp. 3651–3658, 2016.

[29] J.-M. Koo and S.-B. Jung, "Effect of surface finish of substrate on mechanical reliability of In-48Sn solder joints in MOEMS package," *Microsyst. Technol.*, vol. 13, no. 11–12, pp. 1567–1573, 2007.

Chapter 3

Phase stabilized by Zn segregation on Sn and Bi phase boundary in Zn added Sn58Bi alloy

3.1 Introduction

In this chapter, the second method of refining microstructure in section 1.4.2 was introduced. The fastest diffusion path in eutectic Sn58Bi alloy, i.e., Sn-Bi boundary was blocked by another added element, thereby refining microstructure after aging. To realize the block of the diffusion path, the effects of Zn addition into eutectic Sn58Bi alloy on microstructure were investigated.

The precent study investigats the microstructure and the mechanical properties of 0.5 and 1 wt.% Zn-added Sn58Bi alloys both before and after solid-state thermal aging. Additionally, nanoindentation tests were conducted on individual Sn and Bi phases in 1 wt.% Zn added Sn58Bi alloys. Nanoindentation can help in obtaining properties in different phases of an alloy. Existing literature on nanoindentation shows that Sn-based solders have been tested using loads in the range of mN and mechanical properties have been reported for the bulk solder [1]–[5]. The authors, however, believe that nanoindentation on individual phases will give insight on the correlation between the mechanical properties and microstructure of the solder and is attempted for the first time in the current study.

In the study of ENIG/solder/ENIG joint, we selected Sn58Bi1Zn as our candidate solder alloy since Sn58Bi1Zn showed the best tensile mechanical properties as a solder bulk.

Previously, the study about interfacial reaction between Sn58Bi1Zn and Cu substrate can be found. It is reported that 1 wt.% Zn addition to eutectic Sn58Bi alloy effectively suppressed the interfacial IMC layer growth on the Cu substrate during thermal aging. The composition of the IMC layer was $Cu_5(Zn, Sn)_8$ before aging. After aging, two IMC layers were observed: $Cu_5(Zn, Sn)_8$ and $Cu_6(Sn, Zn)_8$. The addition of Zn into different solder alloys can effectively suppress IMC layer growth [6], [7]. However, it has been reported that solder alloys with Zn always show reduced wettability on a Cu substrate, so void formation inside solder joints and decrease shear strength [8]–[10].

In this work, we investigated, for the first time, the effects of the addition of 1 wt.% Zn on the interfacial reaction and mechanical properties of ENIG/eutectic Sn58Bi/ENIG sandwich solder joints in the section 3.4. In addition, ENIG/eutectic Sn58Bi/ENIG joints were prepared for comparison. A very thin (approximately 0.25 μm) Au-Zn-Ni-Sn IMC layer was observed on the Sn58Bi1Zn/ENIG interface after detachment of the $AuZn_3$ IMC. This IMC layer was extremely thermally stable. The correlation between the excellent mechanical reliability and the newly observed Au-Zn-Ni-Sn IMC layer was discussed in detail.

3.2 Experimental

3.2.1 Materials

The eutectic Sn–58 wt.% Bi solder (Sn58Bi) (NIHON GENMA MFG. Co. Ltd) used in this study was a commercially available solder rod. Accordingly, 0.5 and 1 wt.% Zn (99.99%) wires (The Nilaco Co. Ltd) were alloyed with the eutectic Sn58Bi to produce Zn-added Sn58Bi alloys, hereafter called Sn58Bi0.5Zn and Sn58Bi1Zn, respectively. Corresponding metallic Sn58Bi solder rods and Zn wires were melted in-house at 700°C for 5 h after being weighted using a balance with a 0.0001-g precision. During the alloying process, manual stirring was performed to the molten solders every 30 min to ensure a homogenous alloy. The compositions of the alloys were tested using inductively coupled plasma optical emission spectroscopy (ICP-OES) after the alloying procedure. The precise Zn composition was found to be 0.35 wt.% Zn for Sn58Bi0.5Zn alloy and 0.67 wt.% for Sn58Bi1Zn alloy, as shown in Table 3-1. It is believed that a fraction of the added Zn was oxidized during the alloying. After the alloying, alloys were subsequently remelted at 250°C for 1 h before the casting. A bar-shaped steel mold was then used for casting. After which, some of the alloy bulks were prepared for a cross-sectional microstructure observation. For the tensile testing experiment, a number of these bulks were machined into a dumbbell shape, as shown in Figure 3-1.

The schematic illustration of a solder joint and reflow profile were displayed in Figure 3-2(a) and (b). The disk-shaped alloy used in this chapter was cut by slicing machine and scissors. Thickness and diameter of a solder disk were controlled to be approximately 0.1 and 5 mm, respectively. ENIG top and bottom substrates used in this study were on each side of the solder disk, making it a ENIG/Solder/ENIG sandwich structure. The main purpose of using this structure is to perform shear tests, which will be explained in detail in the following section. Figure 3-2b shows the reflow profile measured using a thermal couple. This profile consisted two phases, i.e., preheat and peaking. Preheat temperature was 100 °C for around 150 seconds, while peak was 182 °C for around 60 seconds. The structure of ENIG substrates used in this study was detailed investigated in the previous [11], in which Au and Ni (P) layers were measured to be 60 nm and 2 μm, respectively.

Table 3-1 The chemical composition of the solder alloys.

Solder alloy (wt %)	Sn58Bi0.5Zn	Sn58Bi1Zn
Sn	41.08	42.33
Bi	58.54	57.06
Ti	0.38	0.61
Pb	0.00	0.00
Ag	0.00	0.00
Sb	0.00	0.00
Cu	0.00	0.00
Zn	0.00	0.00
Fe	0.00	0.00
Al	0.00	0.00
As	0.00	0.00
Cd	0.00	0.00
In	0.00	0.00
Ni	0.00	0.00
Au	0.00	0.00

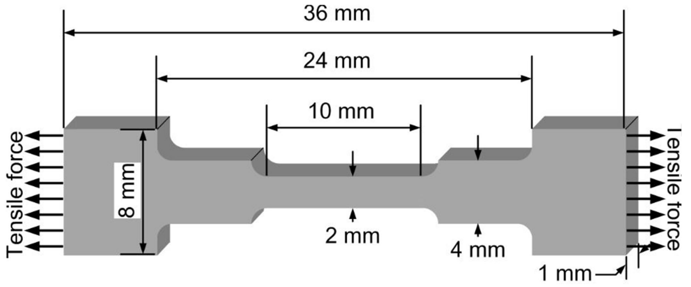

Figure 3-1 The schematic illustration of tensile test samples.

In thermal aging studies, some of these solder bulks were subsequently immersed in an oil bath at 80°C temperature for 504 and 1008 h. The specimens for the microstructure observations and the tensile tests were prepared following the processes applied to the as-cast samples.

3.2.2 Characterization methods

The morphological study of the microstructure and the fracture surface, following the tensile tests, was performed using a field-emission scanning electron microscope (FESEM, Hitachi SU-70) equipped with an energy dispersive X-ray spectroscopy (EDS). The phase identification was analyzed using elemental-mapping, elemental-line, elemental-point, and line analysis on a JEOL JXA-8530F field-emission electron probe microanalyzer (EPMA).

A Shimadzu Autograph AG-X machine was used to conduct the tensile tests at room temperature under a strain rate of 0.0005/s. The strain-stress curves of each alloy were generated and the mechanical properties (e.g., UTS and elongation) were then calculated.

A nanoindentation test was conducted at room temperature using a HYSITRON TI Premier TriboIndenter to evaluate the mechanical properties of individual Sn and Bi phases within an

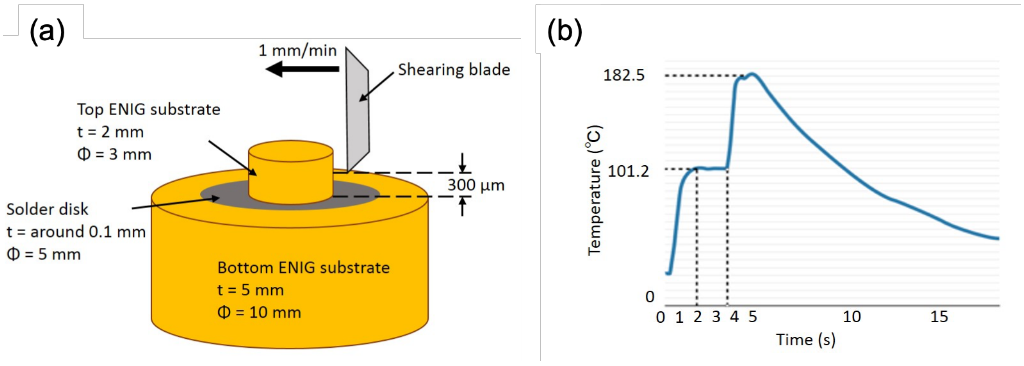

Figure 3-2 Solder joint samples and reflow profile. (a) Schematic illustration of solder joint. (b) Measured reflow profile.

as-cast alloy. Berkovich indenter with 100 nm tip radius and 142.3° total included angle was used to perform the indents. A load function with a peak load of 300 µN and a loading time of 15 s was employed for the tests. The indenter was then held at the peak load for 20 s before it was completely withdrawn from the specimen with a 5 s unloading time. The peak load applied to the specimen was kept small to ensure that each indent was within a single phase. The data was used to generate force–displacement curves and calculate the mechanical properties, such as reduced modulus (E_r), and hardness (H) corresponding to each indent. The nanoindentation results presented are average values obtained over at least 15 indents on each phase.

3.3 Characteristic of bulk alloy

3.3.1 Microstructure before thermal aging

Figure 3-3 presents the FE-SEM cross-sectional microstructure of the as-cast alloys. Figure 3a shows the microstructure of the as-cast eutectic Sn58Bi. The Sn and Bi phases were represented by the dark and light regions in this image, respectively [12]. The eutectic structure indicated in Figure 3-3(a) depicts an interlocked lamellar structure [12]. In addition, the Sn dendrite phases with Bi precipitation within it and a large-size Bi phase were also identified in Figure 3-3(a).

The microstructure of the newly synthesized Sn58Bi0.5Zn and Sn58Bi1Zn alloys was observed in detail, as shown in Figure 3-3(b) and (c). The lamellar eutectic structure and the *β*–Sn dendrite phase were observed within both 0.5 and 1 wt.% Zn added samples. The black color platelet-shaped phase indicated in the matrix was recognized as a Zn-rich (Zn flake) phase, which has been mostly reported in Sn–Zn solders by other researchers [10], [13].

The precise composition and distribution of each element were analyzed using elemental-mapping and point analysis using an EPMA, as shown in Figure 3-4. Figures 3-4(a) to (c) show

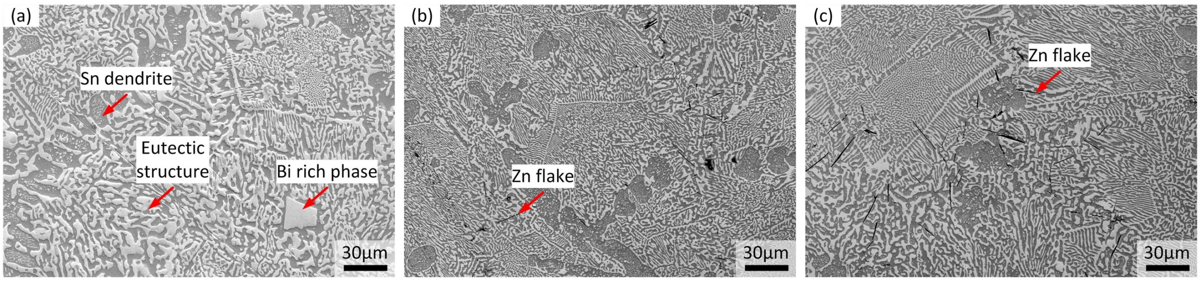

Figure 3-3 FE-SEM images of the cross-sectional microstructure of as-cast solder bulks. (a) eutectic Sn58Bi. (b) Sn58Bi0.5Zn. (c) Sn58Bi1Zn.

the mapping image of the distribution of element Sn, Bi in eutectic Sn58Bi, and Sn, Bi, and Zn in the Sn58Bi0.5Zn and Sn58Bi1Zn alloys, respectively. The dark area in the eutectic structure was the Sn phase. The Sn distribution was dominantly detected within the dark area, while Bi distributed not only in the light area but also in the dark area. This result indicated that Sn almost had no solid solution in the Bi phase, while Bi can dissolve in the Sn phase as a solid solution [14]. In contrast, Zn was detected in both the Sn and Bi phases based on the mapping and electrical-point result in Table 3-2.

Notably, Figures 3-4b and c show that a large amount of Zn segregated in the Sn–Bi phase boundaries. The crystal structure difference between the body-centered tetragonal Sn and the rhombohedral Bi was the reason why the phase boundaries between them were very likely to be non-coherent phase boundaries with high surface energy and a large amount of defects [15]. Because of the limited solubility of Zn in both the Sn and Bi phases. In this study, 0.51 and 0.46 wt.% Zn were detected in the Sn phase within 0.5 and 1 wt.% Zn added samples,

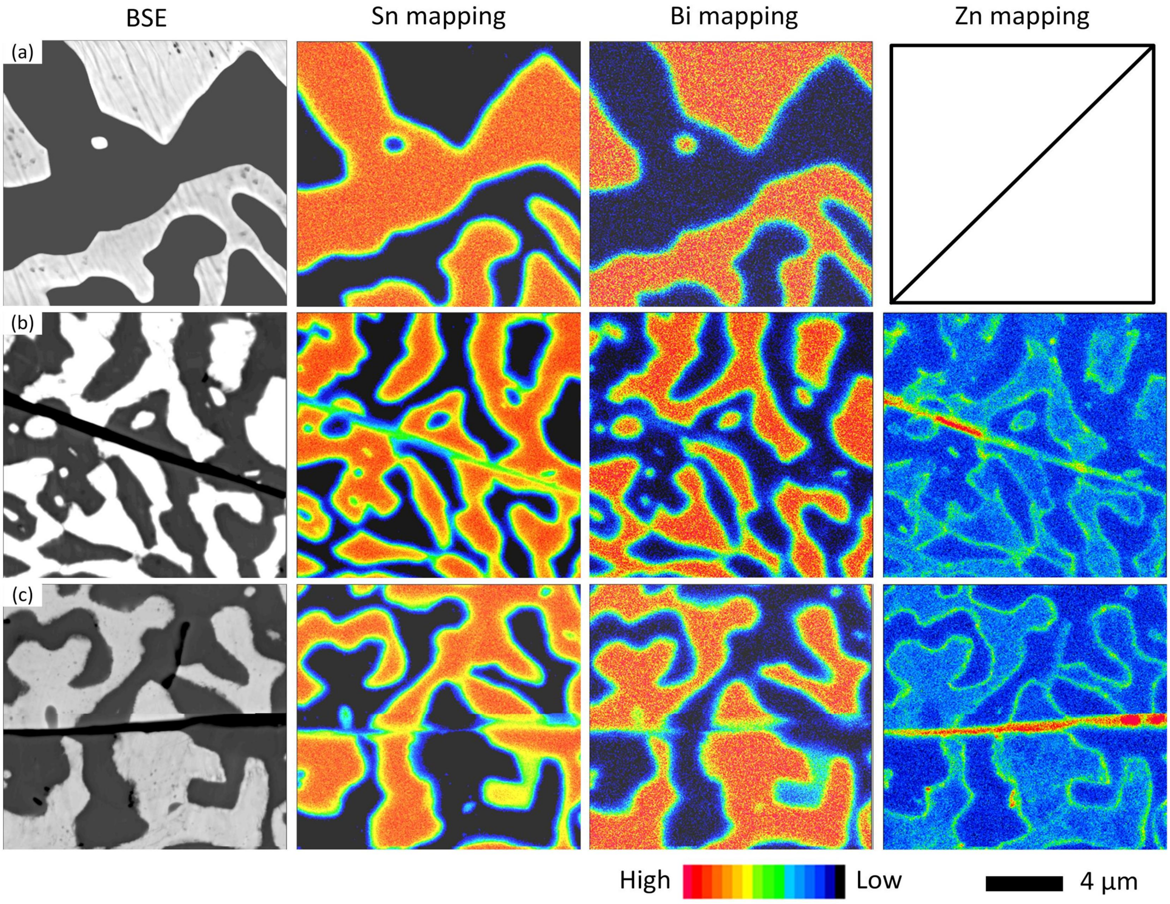

Figure 3-4 EPMA mapping images of the microstructure of solder bulks before aging. (a) eutectic Sn58Bi. (b) Sn58Bi0.5Zn. (c) Sn58Bi1Zn.

Table 3-2 The change of the element composition in Sn and Bi phases within Sn58Bi0.5Zn alloy during aging.

Phase	**Element**	**Composition of each phase in Sn58Bi0.5Zn (Norm%)**		
		As-cast	504h	1008h
Sn	Sn	95.10	95.18	94.48
	Bi	4.39	4.56	5.29
	Zn	0.51	0.26	0.23
Bi	Sn	0.67	0.27	0.31
	Bi	98.94	99.69	99.65
	Zn	0.39	0.04	0.04

respectively. According to the literature [16], the maximum solubility of Zn in Sn was 0.34 wt.%. Thus, we can assume that Zn can be considered a supersaturated solution in the Sn phase because the alloys we used herein were air-cooled within a steel mold to room temperature after alloying. The actual cooling rate may be faster than the Zn precipitation rate. Lastly, the Zn solubility in Bi was detected as 0.39 and 0.65 wt.% for 0.5 and 1 wt.% Zn added samples, respectively. Comparing the actual Zn solubility in the Sn and Bi phases with the amount of Zn added into the Sn58Bi alloy, the extra Zn was assumed to exist in the form of segregated Zn on the Sn–Bi phase boundary and the Zn flakes. Therefore, the Zn elements may tend to segregate within these boundaries to reduce the Gibbs free energy in the whole system [15]. Thermodynamic calculation was conducted to reveal the Zn solubility change during solidification process. Figure 3-5 shows the thermodynamic calculated result of Sn rich region. It is clear that with decreasing temperature, the solubility of Zn in Sn phase decreased rapidly. Because the tested alloy was cooled from remelting temperature of 250 °C. The solubility of Zn simultaneously decreased and Zn was predicted diffused towards the place in eutectic Sn58Bi matrix where contains high Gibbs free energy, which was Sn-Bi phase boundary.

The microstructures of the Zn-added Sn58Bi alloys were much finer than those of the eutectic Sn58Bi. As previously reported [17], during solidification, the impurities are believed to act as extra heterogeneous nucleation sites within the eutectic Sn58Bi system, which can significantly refine the system microstructure. As shown in Figures 3-3 and 3-4, the pre-existing solid state Zn flakes can act as extra heterogeneous nucleation sites during the

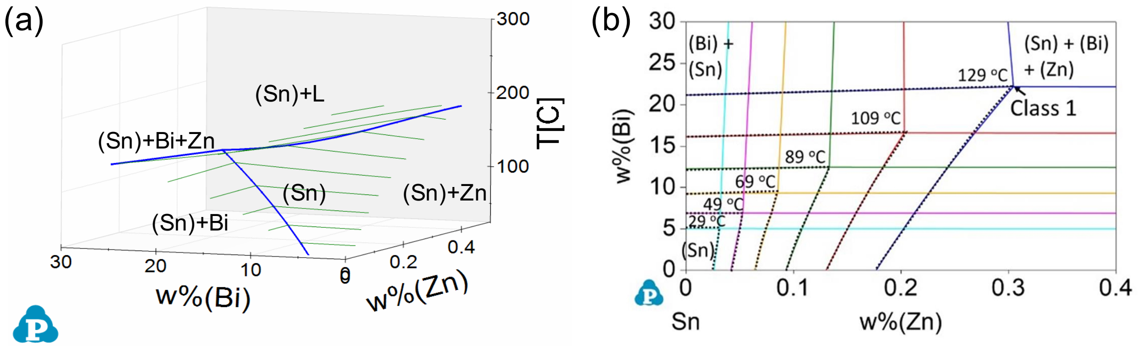

Figure 3-5 Thermodynamic calculated result in Sn-rich region in Sn-Bi-Zn system. (a) the 3D section of the single Sn rich region in the Sn-Bi-Zn system. (b) The calculated isothermal a with different temperature in the Sn rich region.

solidification process after remelting, which results in the refined microstructure in the as-cast Zn-added Sn58Bi alloys.

3.3.2 Microstructure after thermal aging

Figure 3-6 shows the cross-sectional microstructure change of the three alloys after being thermally aged for 504 and 1008 h, respectively. The eutectic structure in the eutectic Sn58Bi alloy coarsened as the thermal aging time increased. Several coarsened Bi phases were also observed in Figures 3-6(a) and (d). This coarsened microstructure had a negative effect on the alloy's mechanical properties [1]. In contrast, the eutectic structure in the Zn-added samples

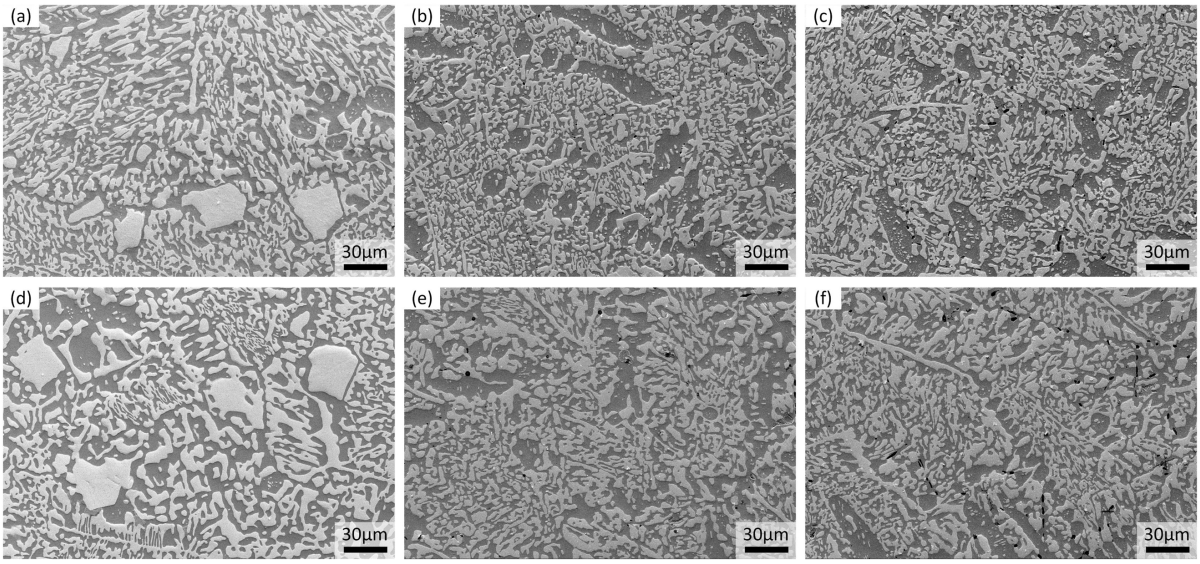

Figure 3-6 FE-SEM images of the cross-sectional microstructure of solder bulks after thermal aging. (a) and (d) eutectic Sn58Bi aged for 504 and 1008 h. (b) and (e) Sn58Bi0.5Zn aged for 504 and 1008 h. (c) and (f) Sn58Bi1Zn aged for 504 and 1008 h.

was much finer and more homogeneous than the eutectic Sn58Bi. Moreover, no sign of a coarsened Bi phase was observed in these matrices both before and after aging. The eutectic spacing of these alloys was measured using Image-pro Plus software to quantify the magnitude of this microstructural change during thermal aging. Figure 3-7 presents the results. The eutectic spacings of 0.5 and 1 wt.% Zn-added samples were much smaller than that of the eutectic Sn58Bi (2.06 and 2.34 μm versus 4.39 μm) before thermal aging. After 504 h thermal aging, almost similar eutectic spacings were observed in these three alloys. However, by the time of 1008 h thermal aging, the eutectic spacing for the eutectic Sn58Bi increased to 7.12 μm, while the data for the Zn-added samples remained unchanged (approximately 4.6 μm).

During thermal aging, the eutectic spacing for the eutectic Sn58Bi increased because of the accelerated diffusion rate between the Sn and Bi phases and the tendency to achieve chemical equilibrium under a high temperature [18]. Especially after 1008 h aging, the eutectic spacing reached its highest value, 7.12 μm, which was approximately one-third higher than that of the as-cast one. In contrast, Zn-added samples also experienced a eutectic spacing increase between 0 and 504 h aging. However, the value remained almost unchanged after 1008 h aging, which was significantly lower than that of the 1008 h aged eutectic Sn58Bi, as shown in Figure 3-7.

Figure 3-8 illustrates the EPMA mappings of how the Zn distribution changed during thermal aging. The concentration of the Zn segregation on the Sn–Bi phase boundaries was

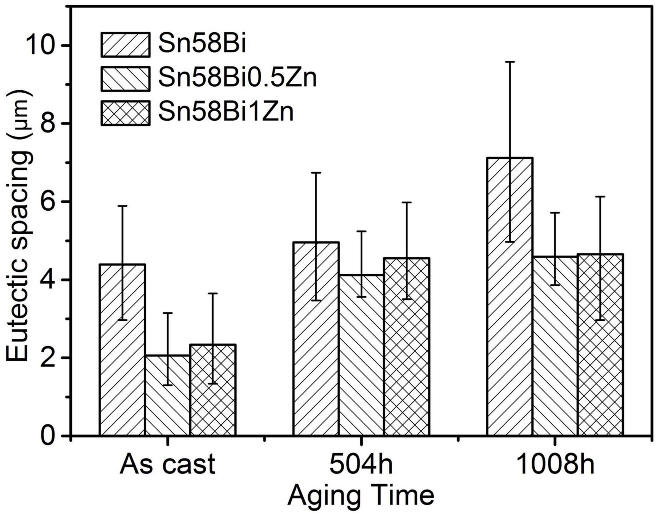

Figure 3-7 Average eutectic spacing within eutectic Sn58Bi, Sn58Bi0.5Zn and Sn58Bi1Zn solder bulks, before and after 504 and 1008 h thermal aging.

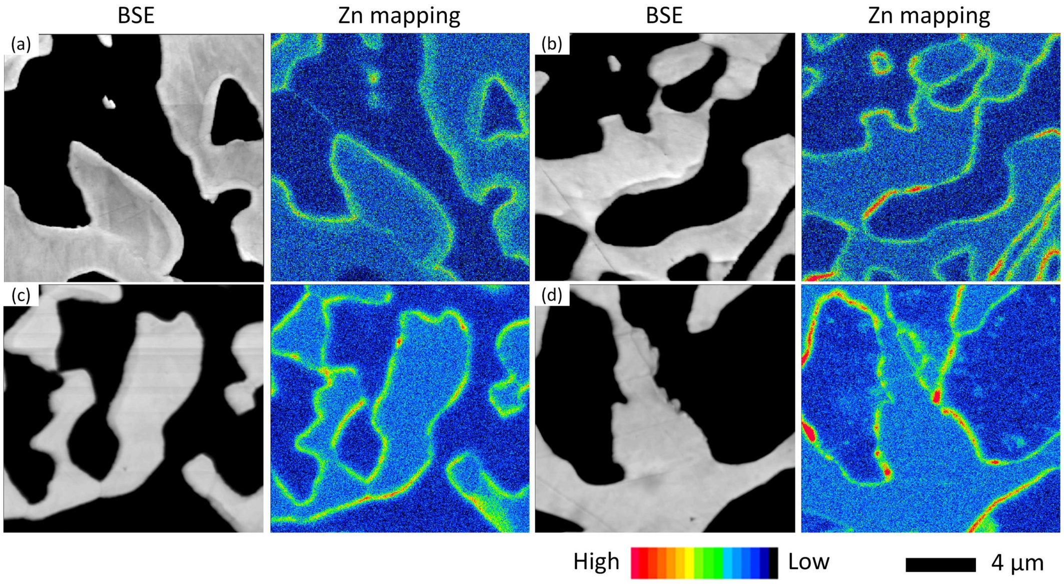

Figure 3-8 EPMA mapping images of the microstructure of solder bulks after aging. (a) and (b) Sn58Bi0.5Zn after 504 and 1008 h aging, respectively. (c) and (d) Sn58Bi1Zn after 504 and 1008 h aging, respectively.

observed to increase during thermal aging. This phenomenon was also demonstrated though the EPMA elemental-point result in Table 3-2 for Sn58Bi0.5Zn and Table 3-3 for Sn58Bi1Zn and the elemental-line results in Figure 3-9. Table 3-2 and Table 3-3 present the three points within each individual Sn and Bi phases tested for both as-cast and thermal aged 0.5 and 1 wt.% Zn added samples. The result showed that the amount of the Zn solid solution within both Sn and Bi phases decreased during thermal aging. Especially in the Bi phase, the atomic percentage of Zn dropped to a very low level (below 0.05 wt.%) compared to the as-cast 0.389 and 0.648 wt.% in 0.5 and 1 wt.% Zn-added samples. Figure 3-7c also shows that in the as-

Table 3-3 The change of the element composition in Sn and Bi phases within Sn58Bi1Zn alloy during aging.

Phase	**Element**	**Composition of each phase in Sn58Bi1Zn (Norm%)**		
		As-cast	504h	1008h
Sn	Sn	94.97	95.15	94.01
	Bi	4.57	4.51	5.67
	Zn	0.46	0.34	0.32
Bi	Sn	0.32	0.34	0.23
	Bi	99.03	99.64	99.77
	Zn	0.65	0.02	0.00

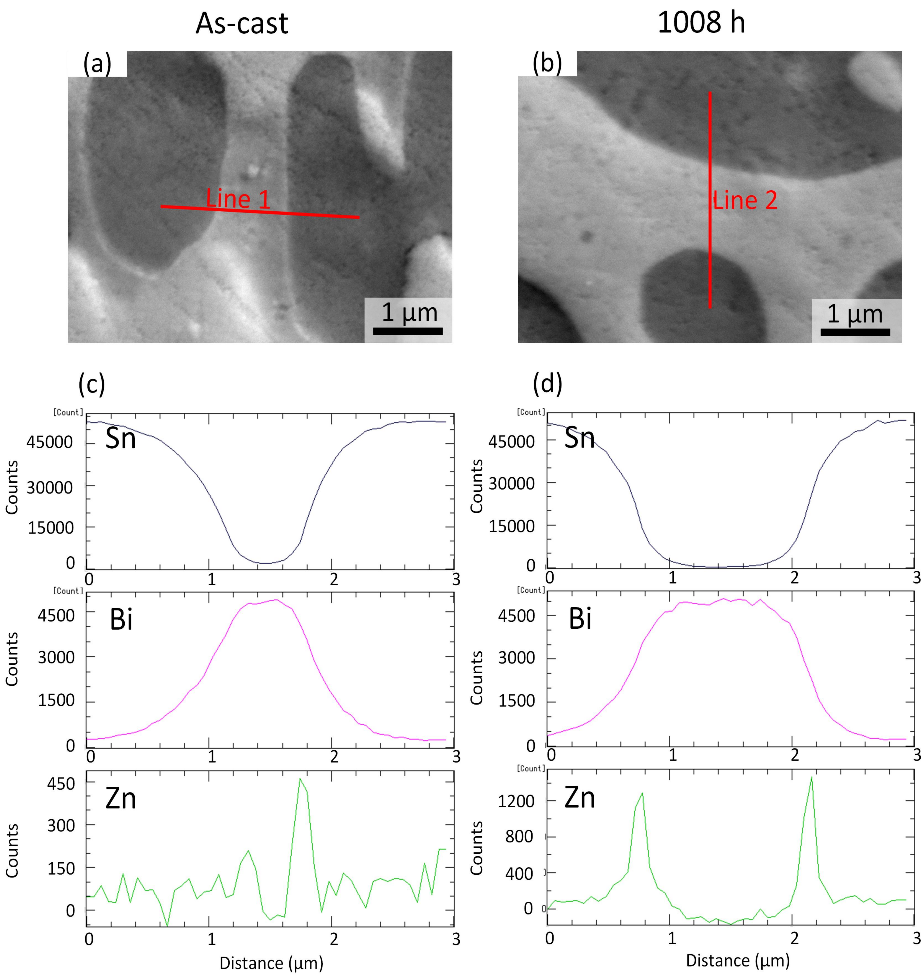

Figure 3-9 EPMA elemental-line results obtained with a testing distance of 3 μm crossing two Sn–Bi phase boundaries in each Sn58Bi1Zn solder. bulk and the corresponding SEM images. (a) and (c) In an as-cast sample. (b) and (d) In a 1008 h aged sample.

cast Sn58Bi1Zn alloy, the phase boundary segregation of Zn was not obvious. The elemental count level was low, and distinguishing the Zn segregation on Sn-Bi boundaries was difficult. In contrast, as shown in Figure 3-9(d), the Zn count level on the phase boundaries in a 1008 h aged Sn58Bi1Zn alloy was much higher than that in the as-cast one, indicating an obvious Zn segregation (Figure 3-9(a) and (b) are the corresponding SEM images to the Figure 3-9(c) and (d)). As previously mentioned, the Sn–Bi phase boundaries were very alike non-coherent grain boundaries, which provides an energy difference between the lattice inside the phase and the phase boundaries. Moreover, the Zn atoms may tend to diffuse out of the individual supersaturated phase and predictably toward the phase boundaries to minimize the overall free energy in the matrix because Zn was considered a supersaturated solid solution in Sn and Bi phases. In addition, the Zn segregation on the Sn–Bi phase boundaries can be considered homogeneous throughout the entire matrix because the eutectic Sn58Bi alloy was mainly composed of a homogeneous Sn–Bi eutectic structure.

Based on the earlier discussion, the segregation of a large proportion of Zn atoms on the Sn–Bi phase boundaries is believed to act as an obstacle on the Sn–Bi phase boundary diffusion paths and, therefore, slowed down the diffusion rate of the Sn and Bi atoms crossing the phase boundaries. Consequently, the eutectic spacing was nearly unchanged for both the 0.5 and 1 wt.% Zn-added samples after aging for 504 h.

3.3.3 Mechanical property and deformation behavior

Figure 3-10 displayed the side views of fractured tensile tested samples. It is clear that eutectic Sn58Bi alloy bulk fractured in a brittle manner regardless of aging time, while Zn-added Sn58Bi showed fracture with plastic deformation, indicating ductile fracture. Figure 3-11 illustrates the tensile test result of the eutectic Sn58Bi and Zn-added samples, with the strain–stress curves in Figure 3-11a and the mechanical properties, i.e., UTS and elongation under the same strain rate of 0.0005/s. Before aging, the elongations of the 0.5 and 1 wt.% Zn added samples and that of the eutectic Sn58Bi were 41.3%, 45.0%, and 37.5%, respectively, as shown in Figure 3-11b. The elongations of all the alloys decreased as the thermal aging time increased. The elongation of the Sn58Bi1Zn alloy remained the highest throughout the aging period, whereas that of the eutectic Sn58Bi was the lowest. Figure 3-11(c) depicts the UTS. Both 0.5 and 1 wt.% Zn-added samples showed a higher UTS compared to that of the eutectic Sn58Bi both before and after aging. Moreover, the UTS for the eutectic Sn58Bi remained almost unchanged after thermal aging, whereas that for both 0.5 and 1 wt.% Zn-samples noticeably increased.

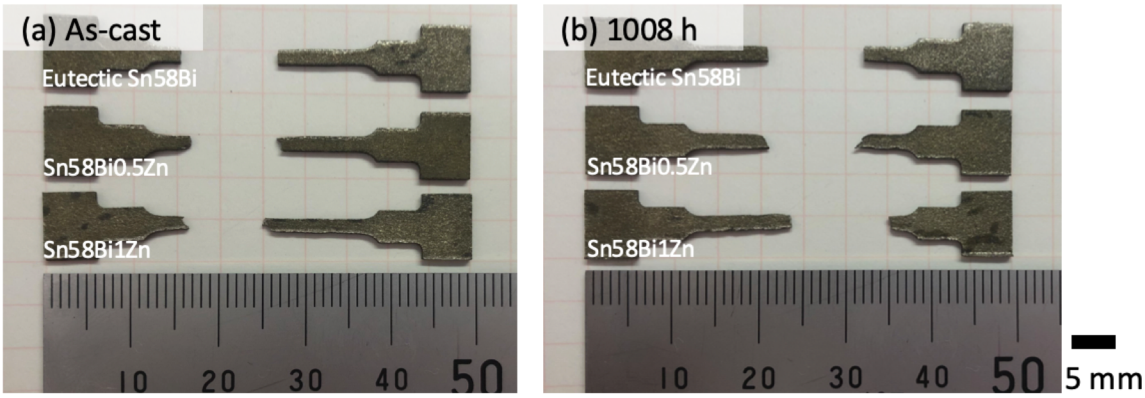

Figure 3-10 FE-SEM images of side views of tensile fracture surfaces.

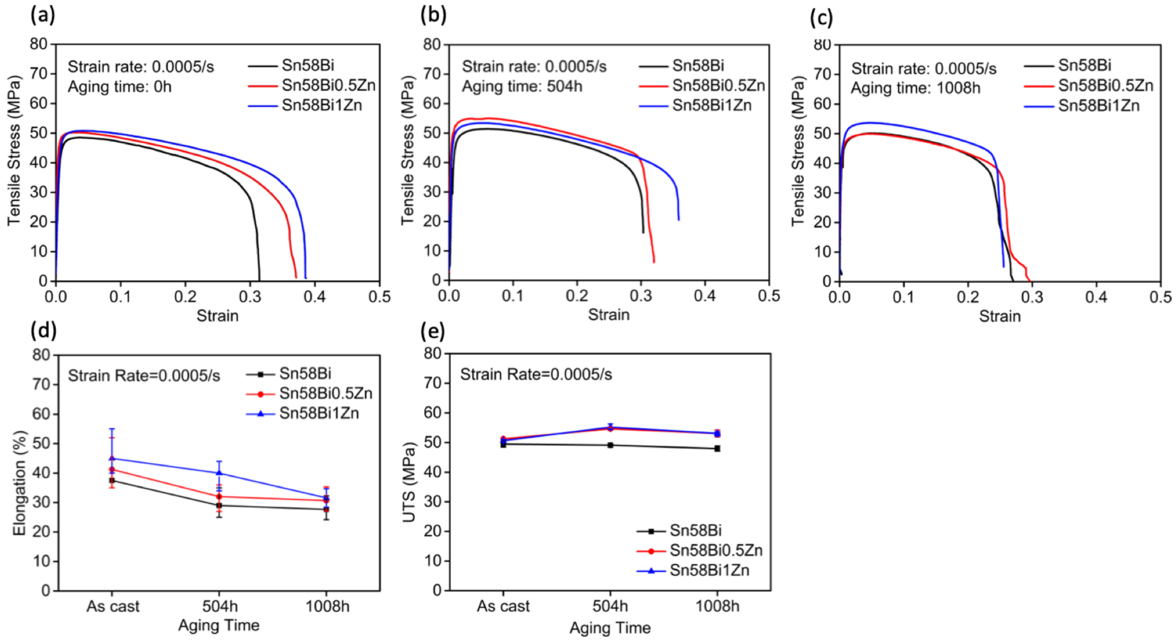

Figure 3-11 Tensile tests result. (a) and (b) Tensile stain-stress curves of eutectic Sn58Bi and Zn-added Sn58Bi solder slabs before and after aging. (c) Elongations of eutectic Sn58Bi and Zn-added Sn58Bi before and after aging. (d) UTSs of eutectic Sn58Bi and Zn-added Sn58Bi before and after aging.

Figure 3-12 shows that the fracture surfaces of all the samples were tested before and after thermal aging. It is obvious that the fracture morphologies for the samples tested after different thermal aging times were different. Before aging, all the three fracture surfaces were dominated with a bulge structure, indicating the ductile fracture mode [19] and the relatively small eutectic spacing. After 504 h thermal aging, a number of cleavage fractured phases and a bulge structure were observed in the eutectic Sn58Bi, as shown in Figure 3-12(d). According to the previous studies, the cleavage phases were fractured brittle Bi phases [20], and the bulge structure indicated the ductile Sn phase. The fracture for the Zn-added samples were finer than that of the eutectic Sn58Bi in Figures 3-12(e) and (f). After 1008 h thermal aging, as shown in Figure 3-12(g), the cleavage and the bulge structure in the eutectic Sn58Bi became much easier to distinguish, indicating that the eutectic structure became significantly coarsened at this aging stage.

As previously reported by others, the finer the microstructure, the higher the UTS and the elongation a tensile sample can produce [21]. Compared with the eutectic Sn58Bi before and after aging, the superior elongation properties were obtained in the Zn-added samples because the Zn-added samples contained a fine microstructure with a small eutectic spacing before and after aging, whereas the eutectic spacing of Sn58Bi noticeably increased after 504 h thermal aging. On the other hand, the increase of the UTS of the Zn-added Sn58Bi during thermal aging

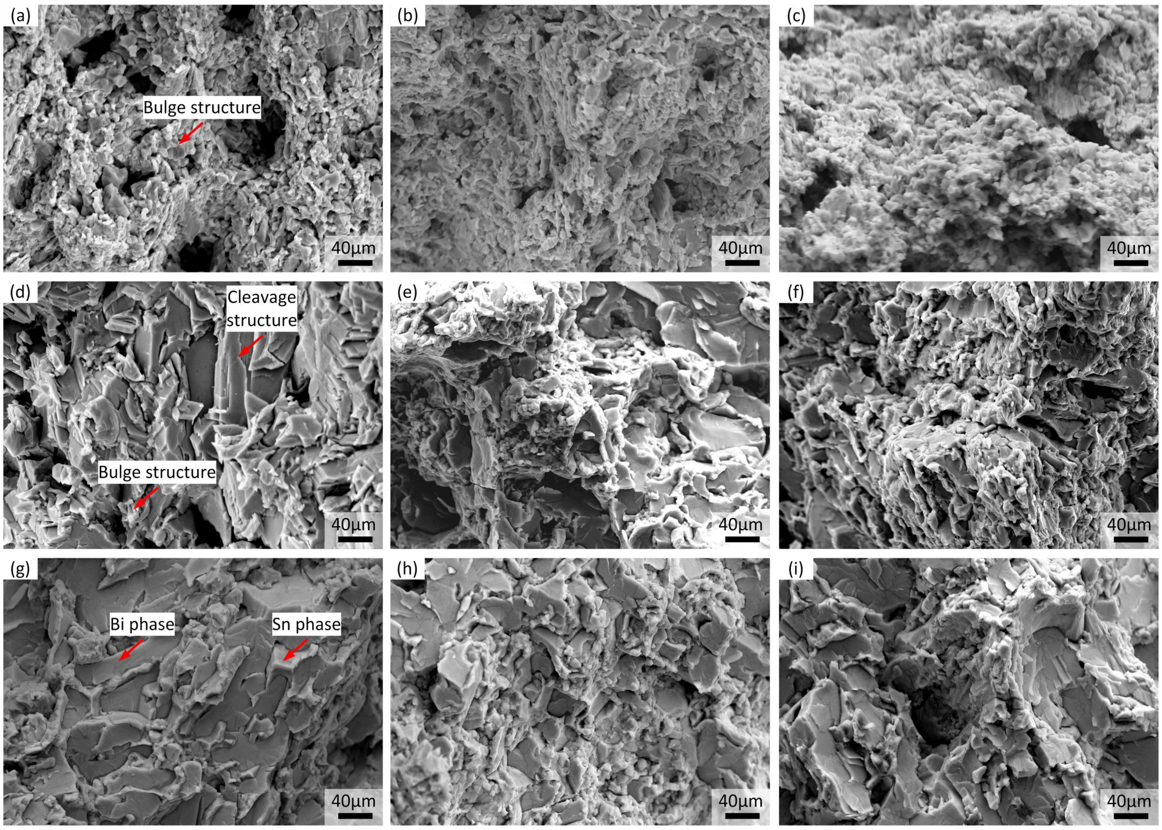

Figure 3-12 FE-SEM images of tensile fracture surfaces. (a), (d) and (g) eutectic Sn58Bi aged for 0, 504 and 1008 h. (b), (e) and (h) Sn58Bi0.5Zn aged for 0, 504 and 1008 h. (c), (f) and (i) Sn58Bi1Zn aged for 0, 504 and 1008 h.

can be potentially attributed to the pinning effect of the Zn segregation on the phase boundaries, thereby impeding the phase boundaries from sliding during the tensile tests [22].

Attributing the promising increase of mechanical properties, i.e., elongation and UTS to the microstructure refinement of the Zn-added Sn58Bi alloys induced by the phase boundary segregation of Zn was reasonable. However, the effects of the Zn solid solution on the mechanical properties of the individual Sn and Bi phases must also be taken into account. Thus, nanoindentation testing was conducted to investigate how the mechanical properties of each single phase (i.e., Sn and Bi phases) in Zn-added Sn58Bi change. In addition, a possible explanation of how the two influencing factors (i.e., microstructure and single phases' mechanical properties) co-affect the tensile test results is discussed in the next section.

3.3.4 Mechanical property of individual Sn and Bi phase in Sn58Bi1Zn.

Figure 3-13 presents a comparison of the load–displacement curves (P–h curves) of the individual phases tested under the same conditions, which were explained in the experimental

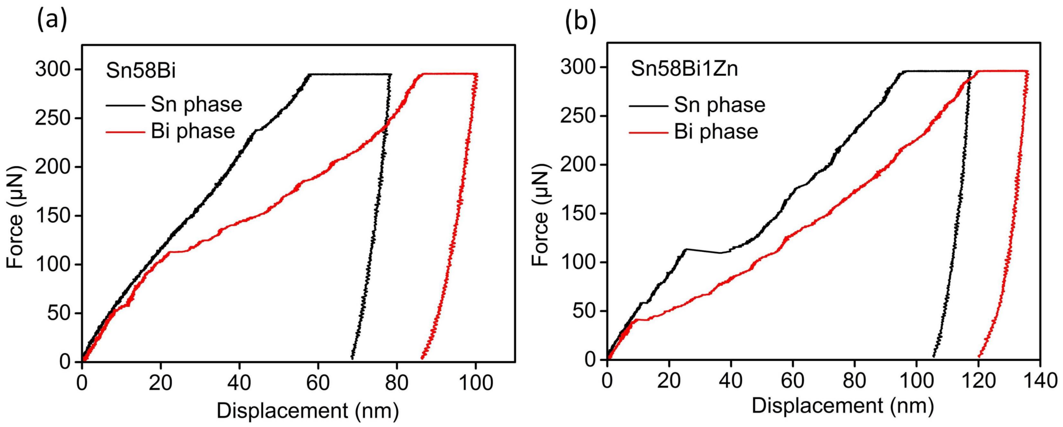

Figure 3-13 Representative load-displacement curves of individual Sn and Bi phases within (a) eutectic Sn58Bi and (b) Sn58Bi1Zn before aging.

section. Figure 3-13(a) shows the P–h curves of the Sn and Bi phases from the as-cast Sn58Bi alloy. For comparison, Figure 3-13(b) displays the P–h curves of the Sn and Bi phases from the as-cast Sn58Bi1Zn alloy. The P–h curves in Figure 3-13 were representatives of the entire data set for each sample. The displacement of the Sn and Bi phases in Sn58Bi1Zn were noticeably higher than those of the eutectic Sn58Bi.

Figures 3-14(a) and (b) show the two scanning probe images of the post-indent areas in our tested samples. The white arrows in the figure indicate the indent positions in each sample, where points 1–4 and points 5–8 represent the indent positions within the Sn and Bi phases, respectively.

The initial unloading part of P-h curve represents elastic recovery and slope of this part is used to calculate reduced modulus. The elastic modulus is calculated based on reduced modulus as [40]:

$$\frac{1}{E_r} = \frac{1-v_i^2}{E_i} + \frac{1-v^2}{E} \qquad (1)$$

Where, the elastic modulus (E) of the tested specimen is related to the indenter modulus (E_i), reduced modulus (E_r), Poisson’s ratio of tested materials (v), and the diamond indenter (v_i). For each parameter in this case, v_i = 0.07; E_i = 1140 for the diamond indenter; and v = 0.35 for the Sn-based alloys [14]. Accordingly, E_r for each indent was automatically generated from the TriboIndenter.

Figures 3-14(c) and (d) show the elastic modulus (E) and the hardness (H) between the Sn and Bi phases within the eutectic Sn58Bi and Sn58Bi1Zn alloys, respectively. Notably, the elastic modulus and the hardness of both the Sn and Bi phases in Sn58Bi1Zn, were lower than those in the eutectic Sn58Bi, especially the significant hardness decrease for the Sn phase.

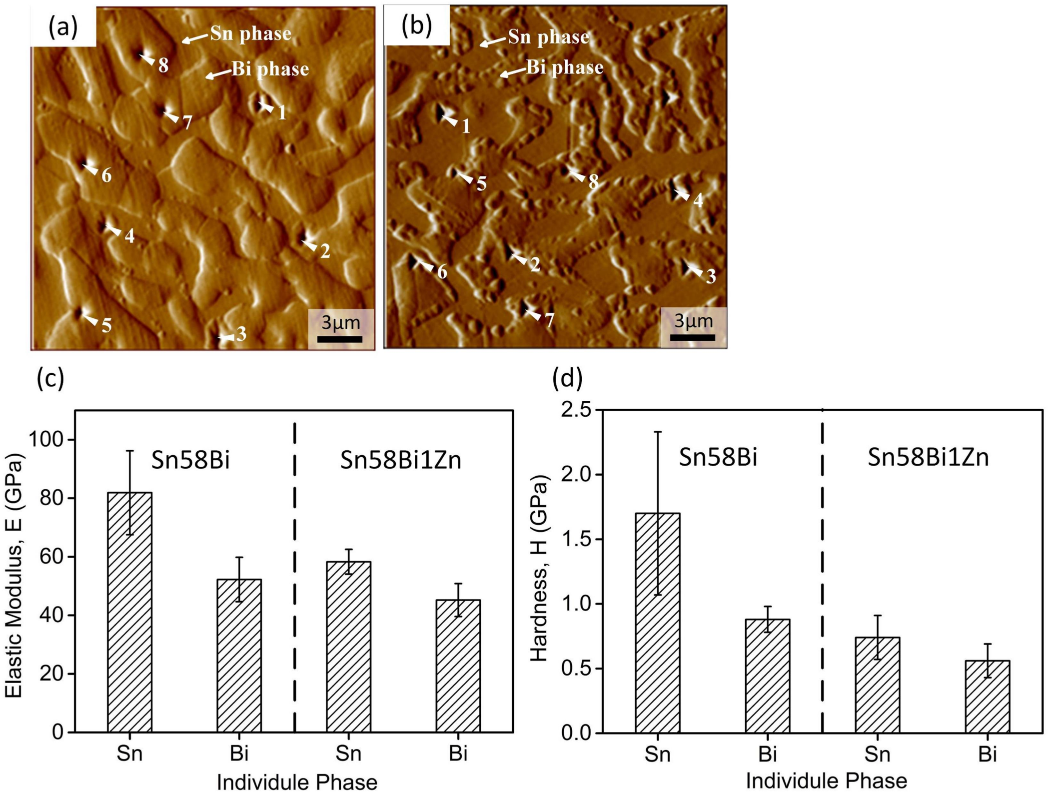

Figure 3-14 Post-indent surfaces as well as elastic modulus and hardness result. (a) and (b) Post-indent surfaces of eutectic Sn58Bi and Sn58Bi1Zn, respectively. (c) and (d) Elastic modulus and hardness comparison of Sn and Bi phases within eutectic Sn58Bi and Sn58Bi1Zn alloys, respectively.

Based on the elemental-point results in Table 3-2, in the Sn phase composition within the eutectic Sn58Bi system, Sn phase was the solvent with approximately 4.5 at. % Bi solid solution. A little amount of the Bi solid solution in the phase slightly increases the elastic modulus and dramatically increases the hardness because Bi can effectively hinder the dislocation movement within the Sn bulk lattice [14]. Moreover, the Bi solid solution in Sn phase can reduce the Sn phase ductility because of the intrinsic brittleness of the Bi, thereby increasing the brittleness of the eutectic Sn58Bi solder alloy [23]. Thus, for the case of the reduced hardness and the slightly reduced elastic modulus observed in Sn58Bi1Zn alloy and combining the fact that the Zn was also a solid solution in both the Sn and Bi phases, the Zn solid solution was very likely responsible for this phenomenon.

Many studies reported that the solid solution not only can harden a material but also soften one [24]–[28]. In other words, the solid solute softening (SSS) can reduce the material's ability to resist indentation (hardness) [25]. The SSS in metals with a body-centered cubic (BCC) crystal structure with various solid solutes was mostly studied in these reports. For the SSS specifically attributed to the Zn solid solution, Soldatov at el. [24] found that a small amount of Zn can decrease the yield stress of pure β–Sn at low temperatures (1.6–150 K) because impurity atoms can act as the centers of nucleation of paired kinks and lead to a potential relief of a Peierls crystal. Wu and Lee [27] found that 15 at.% Zn-added Ag significantly increases the UTS and elongation probably because of the ease of destroying the short-range order for the leading dislocation. In this study, we can conclude that aside from the refined microstructure, the SSS of the Zn solid solution was also responsible for the elongation improvement of the Zn-added Sn58Bi alloys.

The hardness, which is directly related to the ability of a material to resist plastic deformation showed a decrease in our nanoindentation test results because the irreversible plastic deformation easily happened in the Sn phase in the Sn58Bi1Zn alloy. Because the indents of the nanoindentation tests were within the individual phases, i.e., the Sn and Bi phases, the mechanical properties of the Sn and Bi phases can be considered independently, regardless of the other influence factors, such as eutectic structure and the phase boundary. Moreover, based on the linear positive correlation in the equation (2) [1], [29], [30], theoretically, the hardness reduction can lead to the UTS decrease of the Sn phase in the Sn58Bi1Zn alloy.

$$\mathrm{H}_v \approx 3\sigma_{UTS} \qquad (2)$$

However, the UTS result from the tensile test in this study was slightly higher in both the Sn58Bi0.5Zn and Sn58Bi1Zn compared to the eutectic Sn58Bi in Figure 3-11(c). The microstructure refinement can result in a simultaneous effective improvement in the alloy strength but only slightly in the ductility because a finer structure may contain smaller flaws, which need great stress to achieve failure [21]. Hence, the effect of both the microstructure refinement and the Zn segregation pinning was believed to overlap and trump the effect of the hardness reduction, and was more dominant in terms of the UTS increase. On the other hand, the increase of the elongation observed in the 0.5 and 1 wt.% Zn-added Sn58Bi alloys can be attributed to the possible solid solution softening effect of the Zn solid solution mainly in the Sn phase. In addition to the SSS discussion, Chen at el. [23] reported an impressive elongation improvement of 2.5 wt.% In-added Sn58Bi alloy. They explained that the In solid solution in the Sn phase interacted with the strengthening effect of the Bi solution, thereby softening the Sn phase. In this study, considering the 0.51 and 0.46 wt.% Zn solid solution in Sn phase (Table 3-2 and 3-3), this Zn solid solution may also has the similar effect as the In solid solution counteract with the Bi solution, therefore softening the Sn phase.

The eutectic spacings of both 0.5 and 1 wt.% Zn-added samples remained almost unchanged when compared to that of the eutectic Sn58Bi after 504 h thermal aging. This might be the reason why the superior UTS of these Zn-added samples after aging were obtained, as shown in Figure 3-11. On the other hand, the effect of solid solution softening may decrease during the aging process because the Zn solid solution content in both Sn and Bi phases reduced. As a result, the elongation for both 0.5 and 1 wt.% Zn-added samples decreased probably because the solid solution softening was very sensitive to the solute concentration [25].

3.4 Solder joints

3.4.1 Interfacial reaction

Figure 3-15 shows the side views of ENIG/alloy/ENIG joint appearance of tested alloys. Both eutectic Sn58Bi and Sn58Bi1Zn alloy produced sound joint with no voids. Figure 3-16 shows the EPMA mapping results of the bottom interfacial IMC layer of as-reflowed solder/ENIG joints. Figure 3-16(a) shows the eutectic Sn58Bi/ENIG interface. The detailed discussion was provided in section 2.4.1 in Chapter 2.

EPMA mapping of the bottom IMC layer of the as-reflowed ENIG/Sn58Bi1Zn/ENIG joint is displayed in Figure 3-16(b). Interestingly, the distribution of Au differed from that in the eutectic Sn58Bi/ENIG interface. Au and Zn appeared to react with each other, and the Au-Zn IMC detached from the solder/ENIG interface and move into the solder bulk. The EPMA point study results indicate that this detached Au-Zn IMC was a $AuZn_3$ IMC. The detachment of the $AuZn_3$ IMC layer has also been reported in a previous study [31], which investigated the Sn9Zn/Au/Ni/Cu interfacial reaction. However, in that study, the detached $AuZn_3$ IMC was a continuous layer, which resulted in low mechanical reliability. In the current study, the $AuZn_3$ IMCs were entirely separated. This difference was probably because of the difference in adhesion strength between the $AuZn_3$/Ni and $AuZn_3$/Ni (P) interfaces [31]. It is worth noting

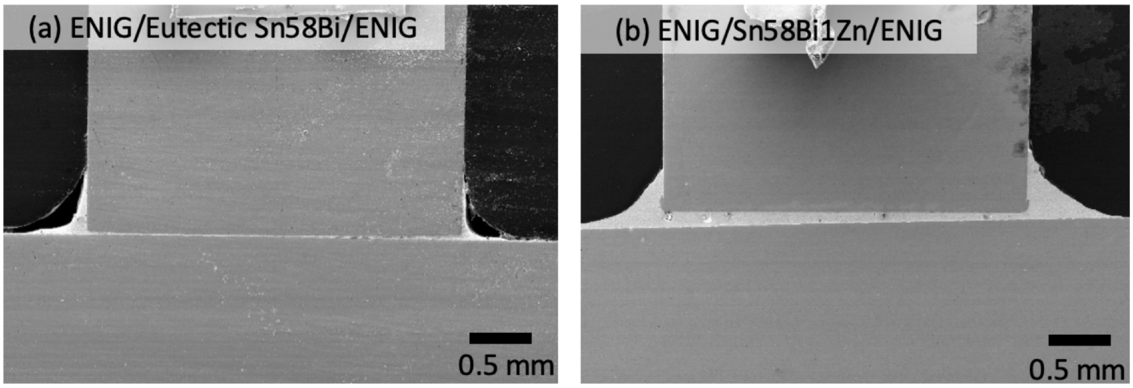

Figure 3-15 FE-SEM images of side views of solder joints.

(a) Eutectic Sn58Bi/ENIG

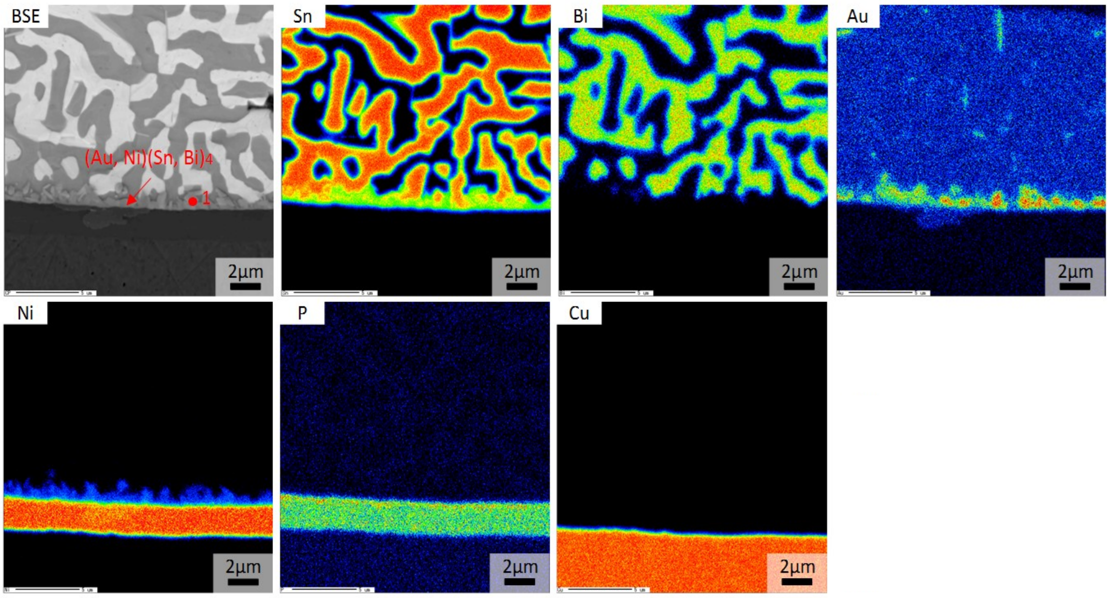

(b) Sn58Bi1Zn/ENIG

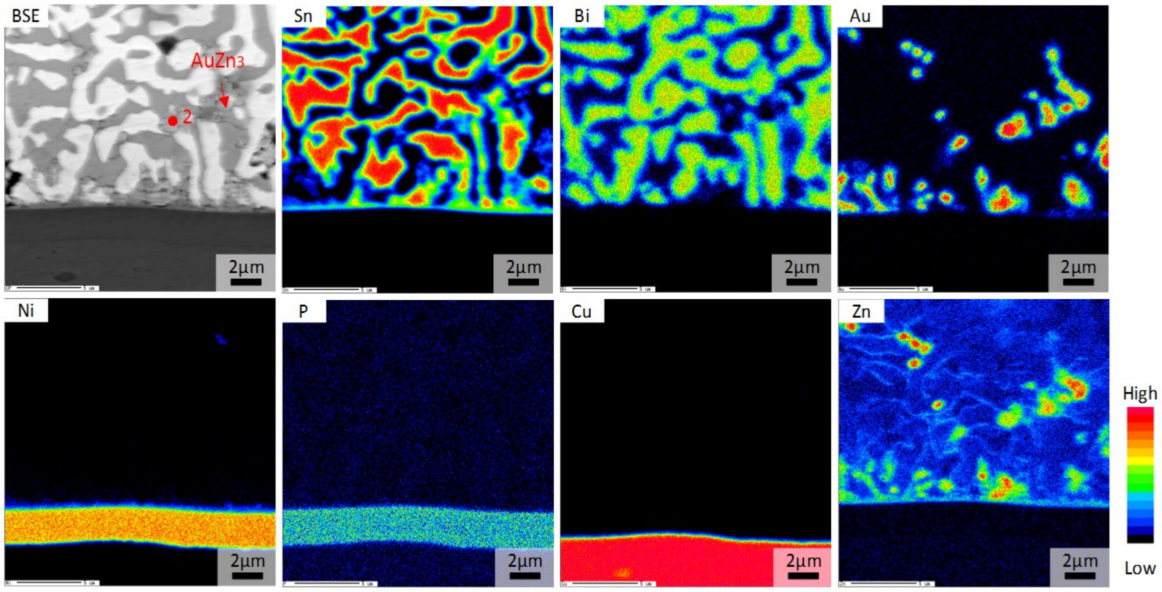

Figure 3-16 EPMA mappings of (a) eutectic Sn58Bi/ENIG interface and (b) Sn58Bi1Zn/ENIG interface.

that a very thin IMC layer remained on the Sn58Bi1Zn/ENIG interface after the detachment of the $AuZn_3$ IMC, as shown in Figure 3-16(b). Figure 3-17(a) shows a high-magnification image of this thin IMC layer. The EPMA line analysis was conducted to determine the composition of this IMC, as shown in Figure 3-17(b). However, due to its extremely small thickness (less than 500 nm), the composition of this phase could not be accurately determined. The peaks in the line analysis results indicate that this IMC was composed of Au, Zn, Ni, and Sn (Au-Zn-Ni-Sn IMC). In the study [32], the Au-Zn-Ni-Sn IMC whose composition also could not be defined was obtained on the Sn9Zn/ENIG interface.

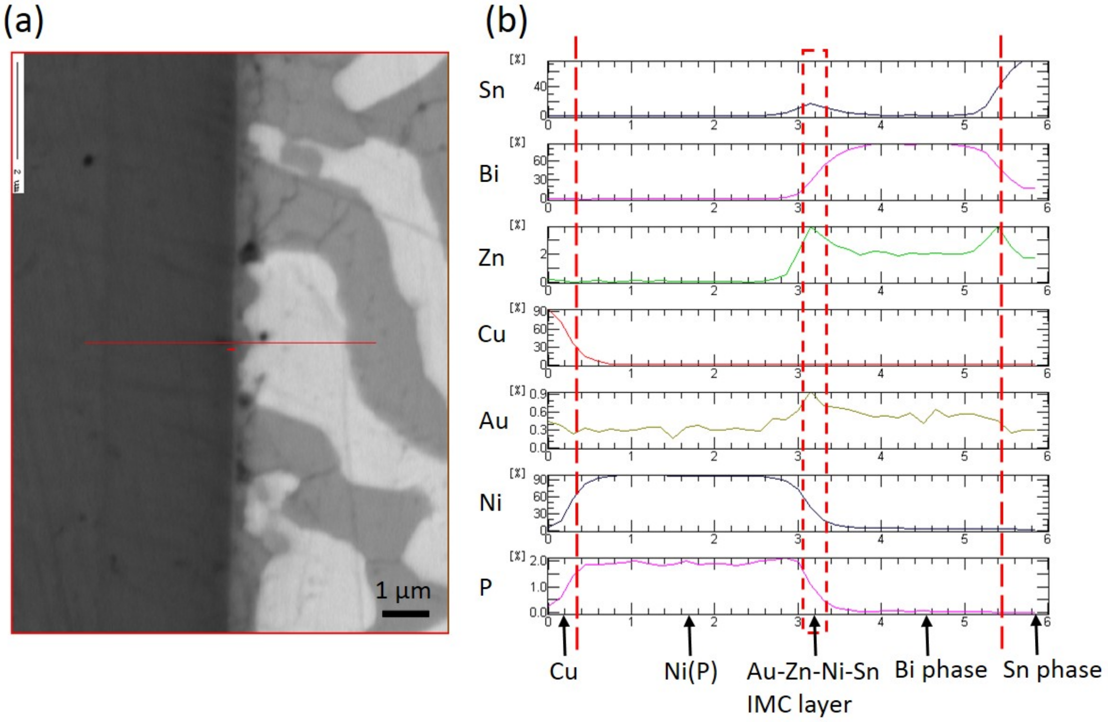

Figure 3-17 EPMA elemental-line result of the very thin IMC layer on Sn58Bi1Zn/ENIG interface. Au-Zn-Ni-Sn IMC was assumed.

3.4.2 Effects of the thermal aging on IMC growth

Figure 3-18(a) shows the growth behaviors of the interfacial IMC layers of eutectic Sn58Bi solder joints during thermal aging. The thicknesses of the IMC layers on eutectic Sn58Bi/ENIG interfaces increased during thermal aging. The morphology of this layer transformed from scallop-like to faceted-like morphology. The IMC layer in the as-reflowed eutectic Sn58Bi joint was the (Au, Ni)(Sn, Bi)$_4$ IMC layer, and during thermal aging, previously dissolved Au diffused back to the Ni-rich interface and thickened the (Au, Ni)(Sn, Bi)$_4$ IMC layer. After 1008 h, another interfacial IMC layer was observed underneath the (Au, Ni)(Sn, Bi)$_4$ layer. The EPMA point analysis results indicate that this layer was the Ni_3Sn_4 IMC layer. Woo-Ram et al. [33] also found that a Ni_3Sn_4 IMC layer first formed on the as-reflowed eutectic Sn58Bi/ENIG instead of the (Au, Ni)(Sn, Bi)$_4$ IMC layer. By contrast, the morphology and thickness of the Au-Zn-Ni-Sn IMC layers in the Sn58Bi1Zn/ENIG interface remained nearly unchanged during thermal aging, as shown in Figure 3-18b. The introduction of Zn in the Au-Zn-Ni-Sn IMC layer effectively blocked the element diffusion across the IMC layer during aging, thereby resulting in a stable IMC layer. The suppressing effect of Zn in the IMC layers have been previously reported by many studies. Mokhtari et al. reported that the thicknesses of $Cu_5(Zn, Sn)_8$ and

(a) Eutectic Sn58Bi/ENIG

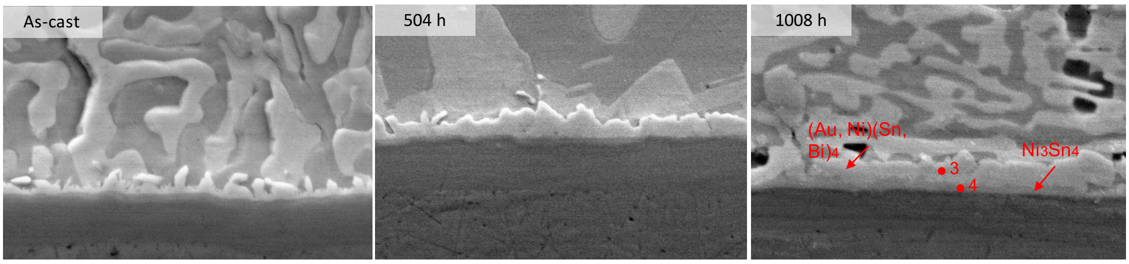

(b) Sn58Bi1Zn/ENIG

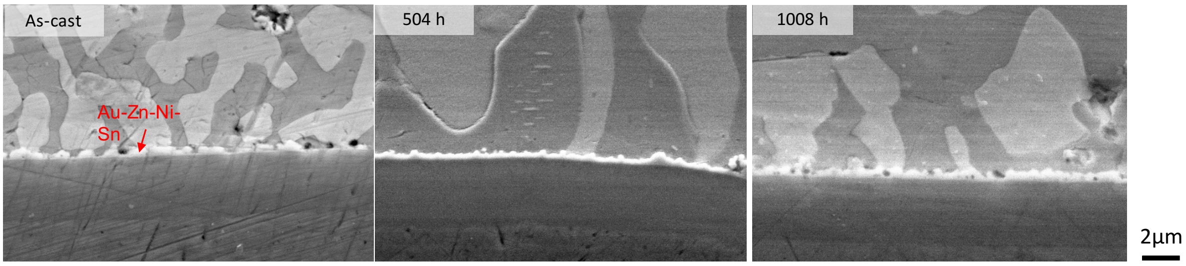

Figure 3-18 FE-SEM images of IMC layer growth on (a) eutectic Sn58Bi/ENIG interface and (b) Sn58Bi1Zn/ENIG interface during thermal aging.

$Cu_6(Sn, Zn)_5$ layers remained unchanged during aging on a Sn-Bi/Cu interface [8]. Yoon et al. studied the reaction between Sn-9Zn and an ENIG substrate and reported that the Au-Zn IMC layer thickness stays the same after increasing reflow time [32].

Figure 3-19 shows IMC layer thicknesses during aging. The thickness of the eutectic Sn58Bi/ENIG interfacial IMC layer increased from approximately 0.6 μm to thicker than 1 μm. By contrast, the Au-Zn-Ni-Sn IMC layer in the Sn58Bi1Zn/ENIG interface remained between 250 and 300 nm during aging, likely due to the suppressing effects of Zn. The eutectic Sn58Bi/Cu interfacial reaction was studied in our previous research [8], in which the Cu_6Sn_5 IMC layer thickness increased from 0.75 to 2 μm after 1008 h of aging. However, (Au, Ni)(Sn,

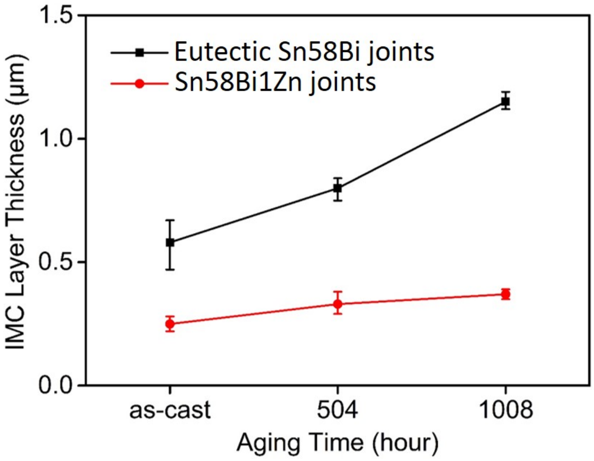

Figure 3-19 IMC layer thickness comparison between eutectic Sn58Bi joints and Sn58Bi1Zn joints during thermal aging.

Bi)$_4$ and Ni_3Sn_4 double IMC layer structure on eutectic Sn58Bi/ENIG after 1008 h aging was much thinner (approximately 1.2 μm) than the IMC layer observed in this study. The addition of Zn further suppressed IMC layer growth. Therefore, we expected more reliable mechanical property of the joint.

3.4.3 Shear strength and fracture surfaces

EPMA mapping of fractured joint surfaces are displayed in Figures 3-20 and 3-21. Top and bottom substrates were analyzed to clarify fracture paths. The result of as-reflowed eutectic Sn58Bi joints were discussed in detail in section 2.4.2 in Chapter 2.

In contrast to the eutectic Sn58Bi joint, Ni and P were rarely observed in the fracture surfaces of the Sn58Bi1Zn joints, even after 1008 h aging, as shown in Figure 3-21(b). This indicates that the fracture paths were inside the solder bulks. Since the very thin Au-Zn-Ni-Sn IMC layer maintained its thickness during aging, therefore mechanical reliability was achieved. Figure 3-22 shows the schematic illustration of the fracture path in eutectic Sn58Bi joints and Sn58Bi1Zn joints before and after aging. For eutectic Sn58Bi joints, fracture path moved from entirely inside solder bulk to partially through solder/substrate IMC layer. On the other hand, Sn58Bi1Zn joints fractured inside solder bulk for both before and after aged samples owing to the stable and thin Au-Zn-Ni-Sn IMC layer.

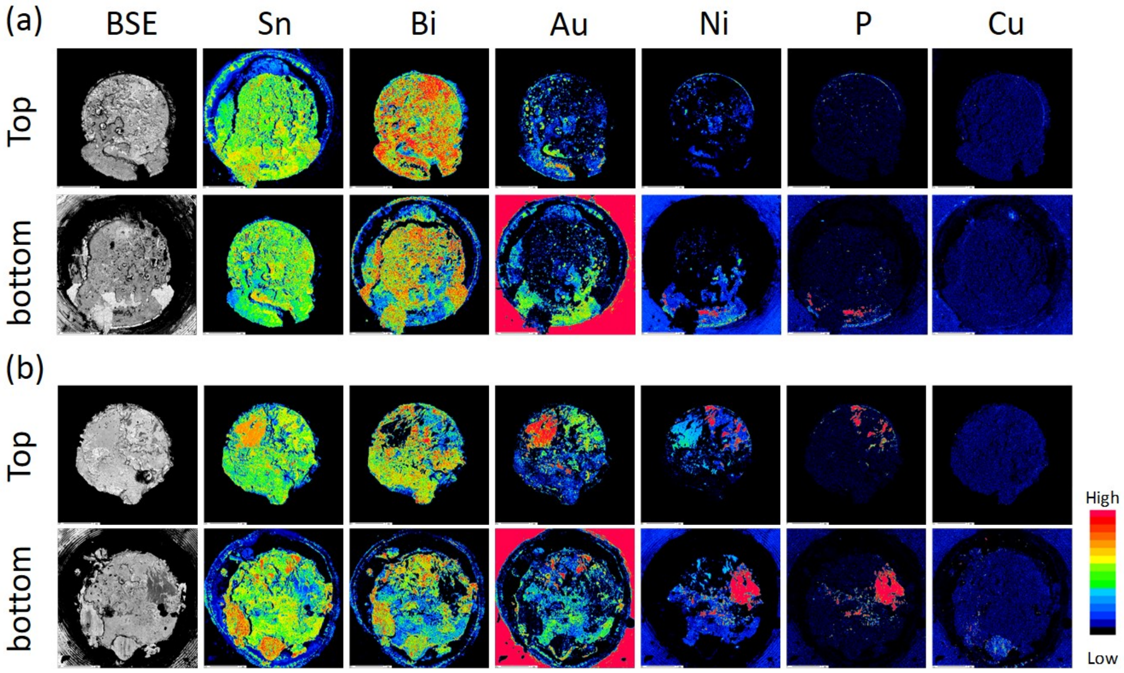

Figure 3-20 EPMA mappings of the fracture surfaces of eutectic Sn58Bi joints. (a) as-reflowed. (b) after 1008 h thermal aging.

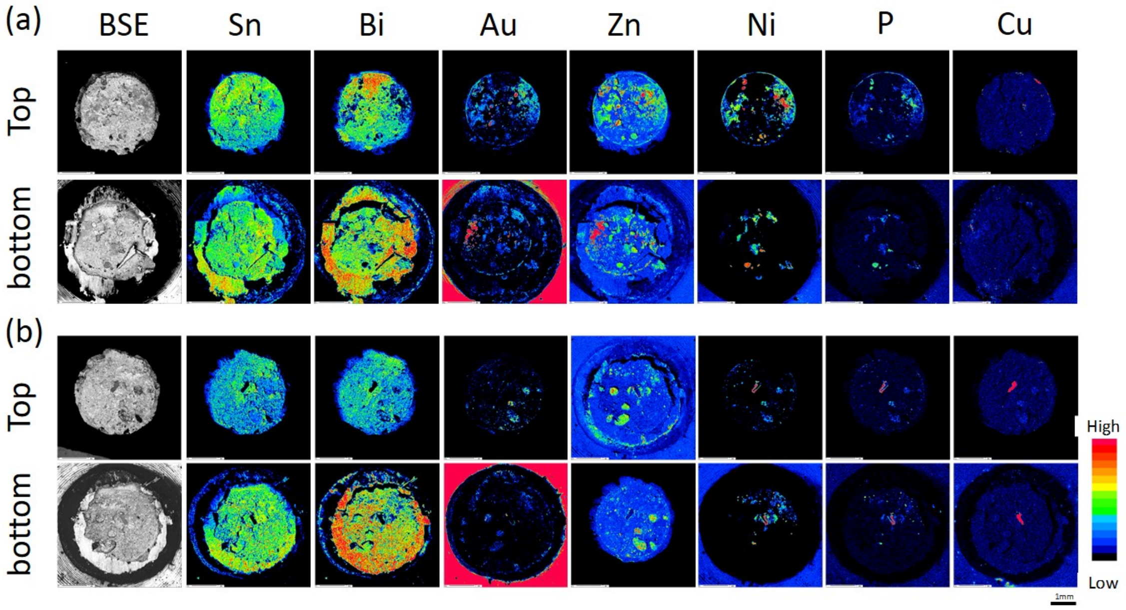

Figure 3-21 EPMA mappings of the fracture surfaces of Sn58Bi1Zn joints. (a) as-reflowed. (b) after 1008 h thermal aging.

Figure 3-23 shows the shear strength for the eutectic Sn58Bi and Sn58Bi1Zn joints. It is clear that Sn58Bi1Zn joints had a better shear strength stability than eutectic Sn58Bi joints. The shear strength of the eutectic Sn58Bi joints decreased by 25 % after 1008 h of aging, while we found no obvious change in shear strength in Sn58Bi1Zn joints. Two kinds of joints showed similar shear strength before aging (approximately 59 MPa); after 1008 h of aging, Sn58Bi1Zn

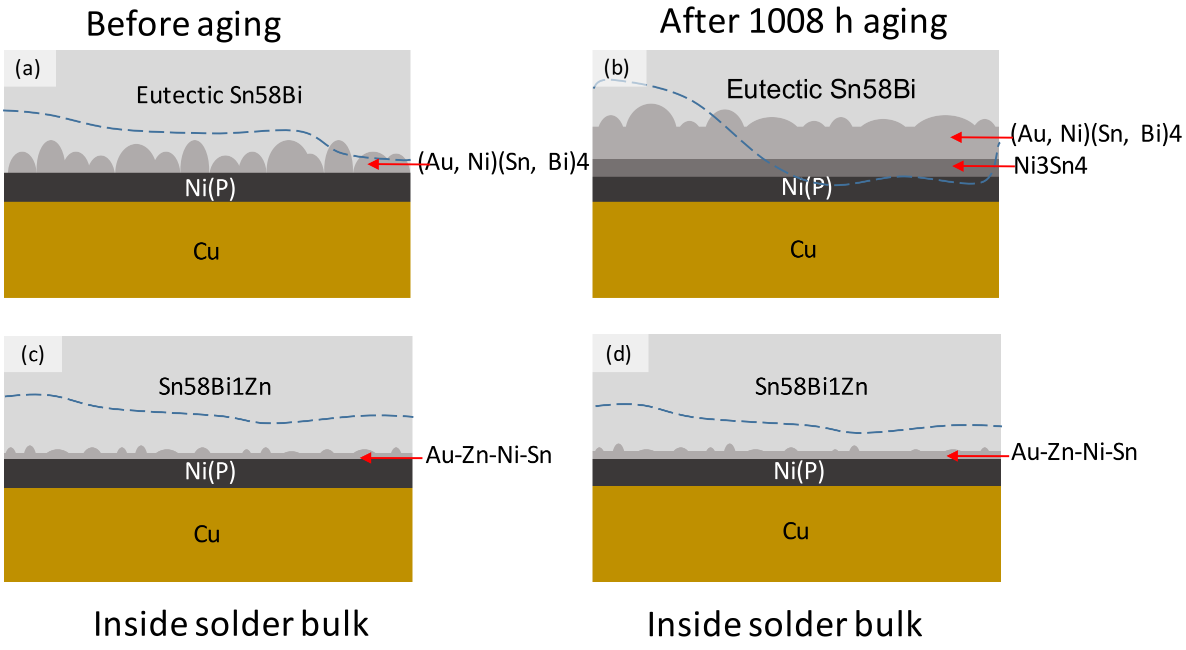

Figure 3-22 Schematic illustration of the fracture paths in (a) and (b) eutectic Sn58Bi joints, as well as (c) and (d) Sn58Bi1Zn joints before and after aging.

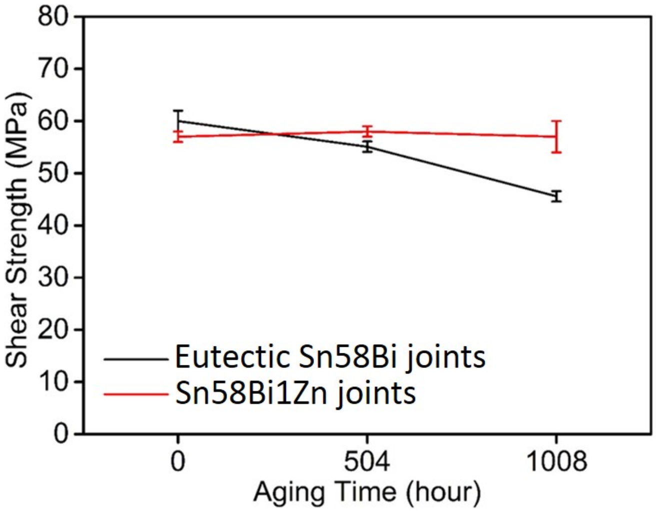

Figure 3-23 Shear strength comparison between eutectic Sn58Bi joints and Sn58Bi1Zn joints during thermal aging.

maintained its strength and had higher shear strength than that of eutectic Sn58Bi joints (59 MPa vs. 45 MPa). As previously mentioned in another study [31], because the detached $AuZn_3$ IMC exists as a continuous layer, decreased shear strength was obtained since the fracture occurred in the $AuZn_3$ IMC layer. In contrast, in the present study the $AuZn_3$ detached in separate pieces. Therefore, the fracture path and shear strength were not closely related to the detached $AuZn_3$ IMCs.

Conclusion

The effects of the microstructure and the mechanical properties induced by 0.5 and 1 wt.% Zn addition in the eutectic Sn58Bi alloy were studied in section 3.3. This work also provided a new potential method and understanding of how to refine the eutectic Sn58Bi alloy microstructure.

Both 0.5 and 1 wt.% Zn effectively refined the eutectic Sn58Bi alloy microstructure. During aging, Zn atoms were found to move from the solid solution within both the Sn and Bi phases to the Sn–Bi phase boundaries as a Zn segregation, which was believed to suppress the microstructure from coarsening.

A significant hardness decrease of the Sn phase was observed in the Sn58Bi1Zn sample. And a potential SSS phenomenon of 1 wt.% Zn solid solution in the Sn phase was proposed.

The improved mechanical properties, i.e., elongation and UTS were obtained both before and after thermal aging by conducting the tensile test.

The interfacial reaction and shear strength of eutectic Sn58Bi and 1 wt.% Zn-added Sn58Bi solder on ENIG substrates during solid-state thermal aging were investigated in section 3.4.

The (Au, Ni)(Sn, Bi)$_4$ IMC layer formed on the eutectic Sn58Bi/ENIG interface after reflow. Then, a Ni_3Sn_4 IMC layer was observed underneath the (Au, Ni)(Sn, Bi)$_4$ IMC layer after 504 h of aging.

For Sn58Bi1Zn solder joints, the $AuZn_3$ IMC formed and then detached from the Sn58Bi1Zn/ENIG interface after reflow. After detachment, a very thin Au-Zn-Ni-Sn IMC layer was observed on the Sn58Bi1Zn/ENIG interface. The thickness of this IMC layer stayed constant during aging.

The shear strength of eutectic Sn58Bi joints decreased after aging. By contrast, Sn58Bi1Zn joints had a stable shear strength during thermal aging due to the stable IMC layer structure.

Fracture paths were revealed by EPMA mapping. Fracture path in eutectic Sn58Bi joints changed from within the solder bulk to partially within the IMC and Ni(P) layers.

We hypothesize that the very thin Au-Zn-Ni-Sn IMC layer on the Sn58Bi1Zn/ENIG interface was crucial for suppressing IMC layer growth and stabilizing the shear strength during aging.

Reference

[1] L. Yang *et al.*, “Effects of Ni addition on mechanical properties of Sn58Bi solder alloy during solid-state aging,” *Mater. Sci. Eng. A*, vol. 667, pp. 368–375, 2016.

[2] X. Li, Y. Ma, W. Zhou, and P. Wu, “Effects of nanoscale Cu6Sn5 particles addition on microstructure and properties of SnBi solder alloys,” *Mater. Sci. Eng. A*, vol. 684, pp. 328–334, 2017.

[3] Y. C. Liu, J. W. R. Teo, S. K. Tung, and K. H. Lam, “High-temperature creep and hardness of eutectic 80Au/20Sn solder,” *J. Alloys Compd.*, vol. 448, no. 1–2, pp. 340–343, 2008.

[4] Y. Ma, X. Li, W. Zhou, L. Yang, and P. Wu, “Reinforcement of graphene nanosheets on the microstructure and properties of Sn58Bi lead-free solder,” *Mater. Des.*, vol. 113, pp. 264–272, Jan. 2017.

[5] L. Yang, W. Zhou, Y. Liang, W. Cui, and P. Wu, “Improved microstructure and mechanical properties for Sn58Bi solder alloy by addition of Ni-coated carbon nanotubes,” *Mater. Sci. Eng. A*, vol. 642, pp. 7–15, 2015.

[6] J. F. Li, S. H. Mannan, M. P. Clode, D. C. Whalley, and D. A. Hutt, “Interfacial reactions between molten Sn-Bi-X solders and Cu substrates for liquid solder interconnects,” *Acta Mater.*, vol. 54, no. 11, pp. 2907–2922, 2006.

[7] H. R. Kotadia, O. Mokhtari, M. P. Clode, M. A. Green, and S. H. Mannan, “Intermetallic compound growth suppression at high temperature in SAC solders with Zn addition on Cu and Ni-P substrates,” *J. Alloys Compd.*, vol. 511, no. 1, pp. 176–188, 2012.

[8] O. Mokhtari, S. Zhou, and H. Nishikawa, “Effect of Zn addition on interfacial reactions between Sn-Bi solder and Cu substrate,” *Mater. Trans.*, vol. 57, no. 8, pp. 1272–1276, 2016.

[9] J. Zhou, Y. Sun, and F. Xue, “Properties of low melting point Sn – Zn – Bi solders,” *Stress Int. J. Biol. Stress*, vol. 397, no. December 2004, pp. 260–264, 2005.

[10] R. A. Islam, B. Y. Wu, M. O. Alam, Y. C. Chan, and W. Jillek, “Investigations on microhardness of Sn–Zn based lead-free solder alloys as replacement of Sn–Pb solder,” *J. Alloys Compd.*, vol. 392, no. 1–2, pp. 149–158, 2005.

[11] M.-S. Kim and H. Nishikawa, “Transmission electron microscopy investigation on the Oxidation behavior of Electroless Ni/Immersion Au surface finish at 250 C,” *J. Nanosci. Nanotechnol.*, vol. 17, no. 11, pp. 8522–8527, 2017.

[12] O. Mokhtari and H. Nishikawa, “Correlation between microstructure and mechanical properties of Sn-Bi-X solders,” *Mater. Sci. Eng. A*, vol. 651, pp. 831–839, 2016.

[13] L. R. Garcia, L. C. Peixoto, W. R. Osório, and A. Garcia, “Globular-to-needle Zn-rich phase transition during transient solidification of a eutectic Sn–9% Zn solder alloy,” *Mater. Lett.*, vol. 63, no. 15, pp. 1314–1316, 2009.

[14] L. Shen, P. Septiwerdani, and Z. Chen, “Elastic modulus, hardness and creep performance of SnBi alloys using nanoindentation,” *Mater. Sci. Eng. A*, vol. 558, pp. 253–258, 2012.

[15] W. D. Callister Jr and D. G. Rethwisch, *Fundamentals of materials science and engineering: an integrated approach*. John Wiley & Sons, 2012.

[16] N. Hamada, M. Hamada, T. Uesugi, Y. Takigawa, and K. Higashi, “Effect of small addition of zinc on creep behavior of tin,” *Mater. Trans.*, pp. 1009131184–1009131184, 2010.

[17] D. R. Askeland and P. P. Phule, *The science and engineering of materials*. Springer, 2003.

[18] D. A. Porter, K. E. Easterling, and M. Sherif, *Phase Transformations in Metals and Alloys, (Revised Reprint)*. CRC press, 2009.

[19] Z. Lai and D. Ye, “Microstructure and fracture behavior of non eutectic Sn–Bi solder alloys,” *J. Mater. Sci. Mater. Electron.*, vol. 27, no. 4, pp. 3182–3192, 2016.

[20] J. Shen, Y. Pu, H. Yin, D. Luo, and J. Chen, “Effects of minor Cu and Zn additions on the thermal, microstructure and tensile properties of Sn-Bi-based solder alloys,” *J. Alloys Compd.*, vol. 614, pp. 63–70, 2014.

[21] G. Grossmann and C. Zardini, *The ELFNET book on failure mechanisms, testing methods, and quality issues of lead-free solder interconnects*. Springer Science & Business Media, 2011.

[22] Y. Li and Y. C. Chan, “Effect of silver (Ag) nanoparticle size on the microstructure and mechanical properties of Sn58Bi-Ag composite solders,” *J. Alloys Compd.*, vol. 645, pp. 566–576, 2015.

[23] X. Chen, F. Xue, J. Zhou, and Y. Yao, “Effect of in on microstructure, thermodynamic characteristic and mechanical properties of Sn-Bi based lead-free solder,” *J. Alloys Compd.*, vol. 633, pp. 377–383, 2015.

[24] V. P. Soldatov, V. D. Natsik, A. N. Diulin, and G. I. Kirichenko, “Low-temperature softening of β-tin single crystals on doping with substitutional impurities,” *Low Temp. Phys.*, vol. 26, no. 2, pp. 160–168, 2000.

[25] D. R. Trinkle and C. Woodward, “The chemistry of deformation: How solutes soften pure metals,” *Science*, vol. 310, no. 5754, pp. 1665–1667, 2005.

[26] B. V. Petukhov, “Effect of solid-solution softening of crystalline materials,” *Crystallogr. Rep.*, vol. 52, no. 1, pp. 112–122, 2007.

[27] J. Wu and C. C. Lee, “The growth and tensile deformation behavior of the silver solid solution phase with zinc,” *Mater. Sci. Eng. A*, vol. 668, pp. 160–165, 2016.

[28] N. I. Medvedeva, Y. N. Gornostyrev, and A. J. Freeman, “Solid solution softening in bcc Mo alloys: Effect of transition-metal additions on dislocation structure and mobility,” *Phys. Rev. B*, vol. 72, no. 13, p. 134107, 2005.

[29] M. F. Ashby, H. Shercliff, and D. Cebon, *Materials: engineering, science, processing and design*. Butterworth-Heinemann, 2018.

[30] P. Zhang, S. X. Li, and Z. F. Zhang, “General relationship between strength and hardness,” *Mater. Sci. Eng. A*, vol. 529, pp. 62–73, 2011.

[31] P. Yao, P. Liu, and J. Liu, “Interfacial reaction and shear strength of SnAgCu–xNi/Ni solder joints during aging at 150 C,” *Microelectron. Eng.*, vol. 86, no. 10, pp. 1969–1974, 2009.

[32] J.-W. Yoon, H.-S. Chun, and S.-B. Jung, “Interfacial Reaction and Mechanical Characterization of Eutectic Sn–Zn/ENIG Solder Joints during Reflow and Aging,” *Mater. Trans.*, vol. 46, no. 11, pp. 2386–2393, 2005.

[33] W.-R. Myung, Y. Kim, K.-Y. Kim, and S.-B. Jung, “Drop Reliability of Epoxy-contained Sn-58 wt.% Bi Solder Joint with ENIG and ENEPIG Surface Finish Under Temperature and Humidity Test,” *J. Electron. Mater.*, vol. 45, no. 7, pp. 3651–3658, 2016.

Chapter 4

Further increased elongation by In and Zn double addition in eutectic Sn58Bi alloy

4.1 Introduction

Mechanical properties, i.e. elongation and ultimate tensile strength (UTS) of eutectic Sn58Bi alloy were increased by minor Ti addition in Chapter 2 and Zn addition in chapter 3. The main reason is that the microstructure was refined by these added elements. In order to further improve mechanical properties, especially the elongation, another method was required.

In this chapter, the authors were aiming to achieve further improved mechanical properties of eutectic Sn58Bi by In and Zn double addition (In & Zn added Sn58Bi). In this study, the Sn58Bi0.5In1Zn alloy was designed. Also, based on the nanoindentation (NI) test result, the SSS phenomenon of In as well as In & Zn additions are discussed in depth to supplement our previous study [1], which was discussed in Chapter 3. Additionally, the creep behaviors of the Sn and Bi phases in each alloy were discussed based on the load–displacement curves (p–h curves) of the NI test.

4.2 Experimental

4.2.1 Materials

1 wt. % Zn (99.99 %) and 0.5 wt. % In (99.99 %) (The Nilaco Co. Ltd) were alloyed with commercially available eutectic Sn58Bi alloy (NIHON GENMA MFG. Co. Ltd) to produce new alloys, i.e., Sn58Bi0.5In and Sn58Bi0.5In1Zn. The compositions of the alloys were tested using inductively coupled plasma optical emission spectroscopy (ICP-OES) after the alloying procedure, as shown in Table 4-1. The alloying process included two steps. First, precise amounts of starting materials were melted in-house at 700°C for 5 h. Next, the newly synthesized alloys were subsequently remelted at 250 °C for 1 h before casting. A bar-shaped mold was used for casting. Some of these bar-shaped alloys were then machined into tensile test specimens, as shown in Figure 4-1.

The schematic illustration of a solder joint was displayed in Figure 4-2(a). The disk-shaped alloy used in this chapter was cut by slicing machine and scissors. Thickness and diameter of a solder disk were controlled to be approximately 0.1 and 5 mm, respectively. ENIG top and bottom substrates used in this study were on each side of the solder disk, making it a ENIG/Solder/ENIG sandwich structure. The main purpose of using this structure is to perform

Table 4-1 The chemical composition of the solder alloys.

Solder alloy (wt %)	Sn58Bi0.5In	Sn58Bi0.5In1Zn
Sn	41.45	41.00
Bi	58.04	57.90
Ti	0.00	0.00
Pb	0.00	0.00
Ag	0.01	0.00
Sb	0.00	0.00
Cu	0.00	0.00
Zn	0.00	0.70
Fe	0.00	0.00
Al	0.00	0.06
As	0.00	0.00
Cd	0.00	0.00
In	0.50	0.51
Ni	0.00	0.00
Au	0.00	0.00

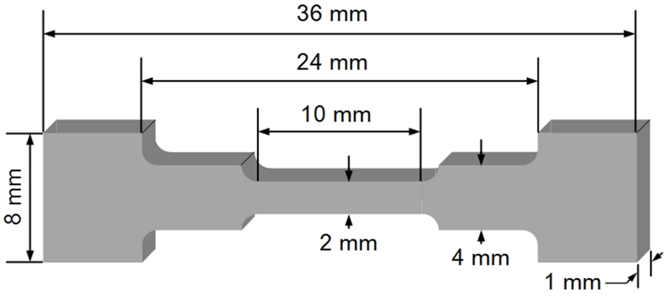

Figure 4-1 Tensile test sample.

shear tests, which will be explained in detail in the following section. Figure 4-2(b) shows the reflow profile measured using a thermal couple. This profile consisted two phases, i.e., preheat and peaking. Preheat temperature was 100 °C for around 150 seconds, while peak was 182 °C for around 60 seconds. The structure of ENIG substrates used in this study was detailed investigated in the previous [2], in which Au and Ni (P) layers were measured to be 60 nm and 2 μm, respectively.

4.2.2 Characterization methods

The thermal reliability of the alloys was examined using a solid-state aging test for 504 h and 1008 h in an oil bath at 80 °C. The oil bath was used to prevent potential oxidation of the alloys during the high-temperature storage.

To quantify the magnitude of this microstructural change during thermal aging, the eutectic spacing and number of coarsened Bi grains were measured and calculated using an Image-pro Plus software. Field-emission scanning electron microscope (FESEM, Hitachi SU-70) images (dimensions: 250 μm × 200 μm) with 50 randomly selected eutectic spacings in each image

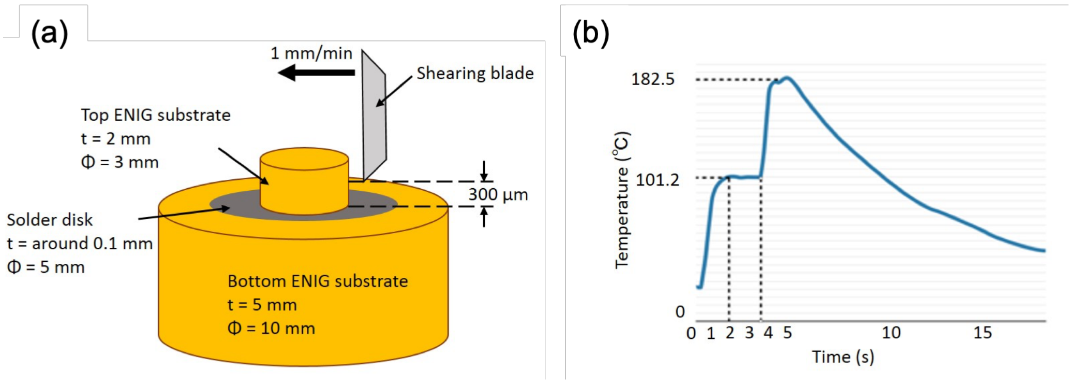

Figure 4-2 Solder joint samples and reflow profile. (a) Schematic illustration of solder joint. (b) Measured reflow profile.

were used to calculate the average eutectic spacing for each alloy. Ten SEM images (dimensions: 250 µm × 200 µm) were randomly chosen in each alloy for counting the coarsened Bi grains. A coarsened Bi grain normally has a rectangular shape [3]. In addition, we noticed that the size of a coarsened Bi grain in these 2D SEM images was usually larger than a 10 µm diameter circle. It was difficult to identify a coarsened Bi grain with a diameter smaller than 10 µm from a Bi phase in a eutectic structure; thus, we decided to base the counting on the two size categories: between 10 µm and 20 µm (small size) and larger than 20 µm (large size).

SEM was used to observe the microstructure of the alloys and fracture surfaces after tensile tests. In addition, elemental composition and distribution were obtained using elemental-mapping, elemental-line and elemental-point analyses on a JEOL JXA-8530F field-emission electron probe microanalyzer (EPMA).

Tensile tests was performed using a Shimadzu Autograph AG-X machine at room temperature of 25 °C and under a strain rate of 0.0005/s.

NI test results were used to study the mechanical properties of individual Sn and Bi phases in different alloys. NI tests were conducted on a Hysitron Nano-Indenter TI Premier at room temperature on the as-cast alloys. A Berkovich indenter with a tip radius of 100 nm and a total included angle of 142.3° was used to perform the indents. The well-known Oliver–Pharr method was employed in the tests by applying a load function with a peak load of 300 µN and a loading time of 15 s [4], which were the same as in the previous study [1]. The indenter was then held at a peak load for 20 s before it was completely withdrawn from the specimen with 5 s unloading time. The peak load applied to the specimen was kept small to ensure that each indent was within a single phase. Data from the NI tests were analyzed and exported through the analysis tab, where a summary of information was obtained (Reduced Modulus, Hardness, etc.) for each indentation made on the sample. The configurations of nanoinentation tests in this chapter is identical compared with that in chapter 3. The reason is for comparison purpose.

Shear tests were conducted using a Rhesca STR-1000 testing machine at room temperature of 25 ℃. The shearing speed was 1 mm/min and the fly height was 300 µm from the top surface of the bottom substrate, as shown in Figure 4-2. Cross-sectional and fracture surface were investigated using SEM and EPMA.

4.3 Characteristic of bulk alloy

4.3.1 Microstructure before aging

Figure 4-3 shows microstructure of eutectic Sn58Bi, Sn58Bi0.5In, and Sn58Bi0.5In1Zn alloys before thermal aging. All three alloys had typical lamellar eutectic structure, consisting of the Bi phase and Sn phase. In Figure 4-3c, the evenly distributed needle-shape Zn flakes were observed in Sn58Bi0.5In1Zn alloy.

The microstructure of Sn58Bi0.5In1Zn was obviously finer than those of other two alloys. The microstructure refinement degree was quantitated by the eutectic spacing, as shown in Figure 4-4. As reported in chapter 3, the fine microstructure of Sn58Bi1Zn can be attributed to the presence of Zn flakes, since they could act as the heterogeneous nucleation sites during the solidification after remelting. Zn flakes may have the same effect on refining microstructure of Sn58Bi0.5In1Zn alloy. By contrast, the eutectic spacing of eutectic Sn58Bi and Sn58Bi0.5In were identical and had a larger value than that of Sn58Bi0.5In1Zn.

Figure 4-5 shows the element distribution in In- and In & Zn-added Sn58Bi alloys before aging by EPMA elemental-mapping. The precise content is summarized in Table 4-1 and 4-2 (0 h column) by the EPMA elemental-point analysis. In Sn58Bi0.5In alloy, the In and Sn distribution were matched well, as shown in Figure 4-5. Table 4-2 shows that approximately 3.5 wt. % Bi and 1.6 wt. % In were dissolved into Sn phase as solid solutions, whereas around 0.3 wt. % Sn and no In were detected in the Bi phase. In a Sn58Bi0.5In1Zn alloy, the distributions of Sn, Bi, and In were almost identical, compared to those in Sn58Bi0.5In. On the other hand, Zn was detected in both the Sn phase and the Bi phase as solid solutions (approximately 0.7 wt. % and 0.5 wt. %, respectively), as shown in Table 4-3. The distribution of In in eutectic Sn58Bi alloy was consistent with the results demonstrated in the studies [3], [5], [6]. Even though Chen et al. reported that BiIn intermetallic compounds (IMCs) were found in Sn58Bi4In alloy [6], no BiIn IMC was observed in this study, probably due to the

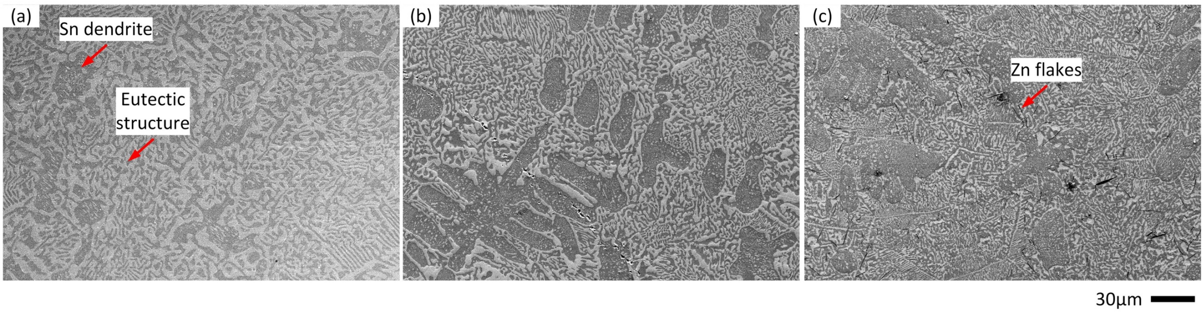

Figure 4-3 FE-SEM images of the cross-sectional microstructure of solder bulks before aging. (a) eutectic Sn58Bi (b) Sn58Bi0.5In (c) Sn58Bi0.5In1Zn.

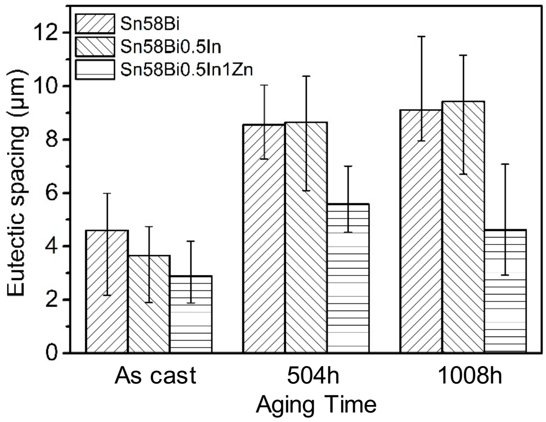

Figure 4-4 Average eutectic spacing of eutectic Sn58Bi, Sn58Bi0.5In, and Sn58Bi0.5In1Zn, before and after thermal aging.

limited amount of In addition in our work. Additionally, the distribution and the amount of Zn solid solution in the Sn and Bi phases in Sn58Bi0.5In1Zn are similar to those in chapter 3, in which Sn58Bi1Zn was analyzed. In summary, the addition of In does not affect the distribution of Zn in the Sn58Bi0.5In1Zn alloy in comparison to the Sn58Bi1Zn alloy.

4.3.2 Effects of thermal aging on microstructure

Figure 4-6 shows the microstructure of eutectic Sn58Bi, Sn58Bi0.5In, and Sn58Bi0.5In1Zn alloy after thermal aging. The finer microstructure in the Sn58Bi0.5In1Zn alloy was observed, as shown in Figures 4-6(c) and (f), compared to other two alloys. In detail, the lamellar structure in Sn58Bi0.5In1Zn was homogenously distributed, while a large number of coarsened

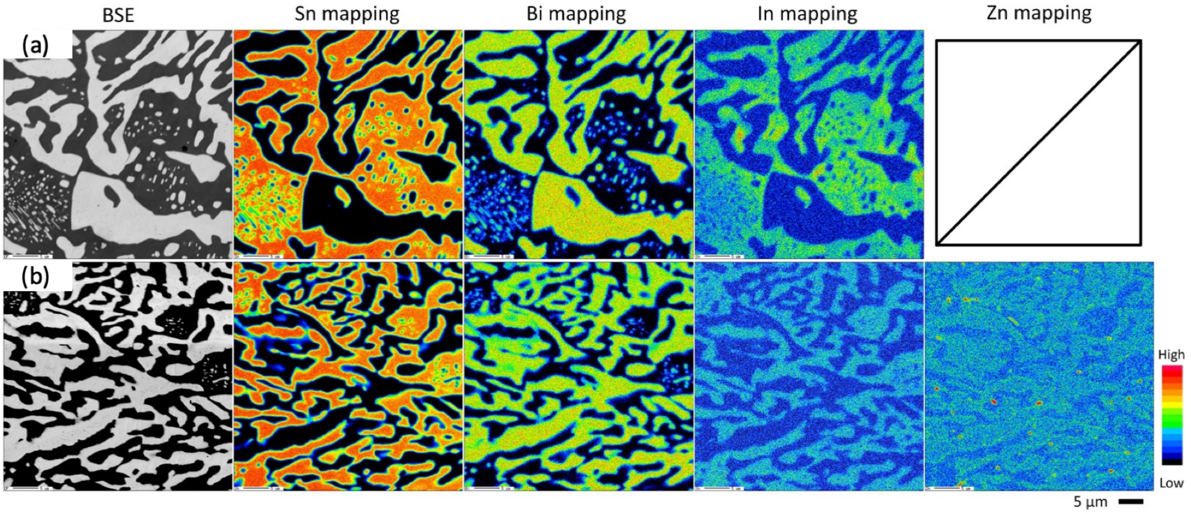

Figure 4-5 EPMA mapping images of the microstructure of solder bulks before aging. (a) Sn58Bi0.5In. (b) Sn58Bi0.5In1Zn.

Table 4-2 The element composition in Sn and Bi phases within Sn58Bi0.5In during aging.

Phase	Element	Composition of each phase in Sn58Bi0.5In (wt. %)		
		0 h	504 h	1008 h
Sn	Sn	94.96	93.75	94.77
	Bi	3.49	4.87	3.78
	In	1.55	1.38	1.45
Bi	Sn	0.29	0.3	0.33
	Bi	99.71	99.7	99.67
	In	0	0	0

lamellar structure was observed in eutectic Sn58Bi and Sn58Bi0.5In alloy. In addition, several coarsened Bi grains were found in eutectic Sn58Bi alloy after 504 h aging, while a very few in Sn58Bi0.5In and no sign in Sn58Bi0.5In1Zn alloy after aging. To quantify the change of microstructures during aging, the eutectic spacing was measured and the results are shown in Figure 4-4. During aging, the eutectic spacing grew continually for eutectic Sn58Bi and Sn58Bi0.5In alloy. In contrast, a slightly increased eutectic spacing was observed for Sn58Bi0.5In1Zn between 0 h to 504 h aging, but it remained nearly unchanged from 504 h to 1008 h. After 1008 h aging, the eutectic spacing of the Sn58Bi0.5In1Zn was approximately 4.5

Table 4-3 The element composition in Sn and Bi phases within Sn58Bi0.5In1Zn during aging.

Phase	Element	Composition of each phase in Sn58Bi0.5In1Zn (wt. %)		
		0 h	504 h	1008 h
Sn	Sn	93.15	92.13	93.51
	Bi	4.66	4.03	4.66
	In	1.5	1.35	1.39
	Zn	0.69	0.5	0.44
Bi	Sn	0.3	0.66	0.29
	Bi	99.22	99.2	99.69
	In	0	0	0
	Zn	0.48	0.14	0.02

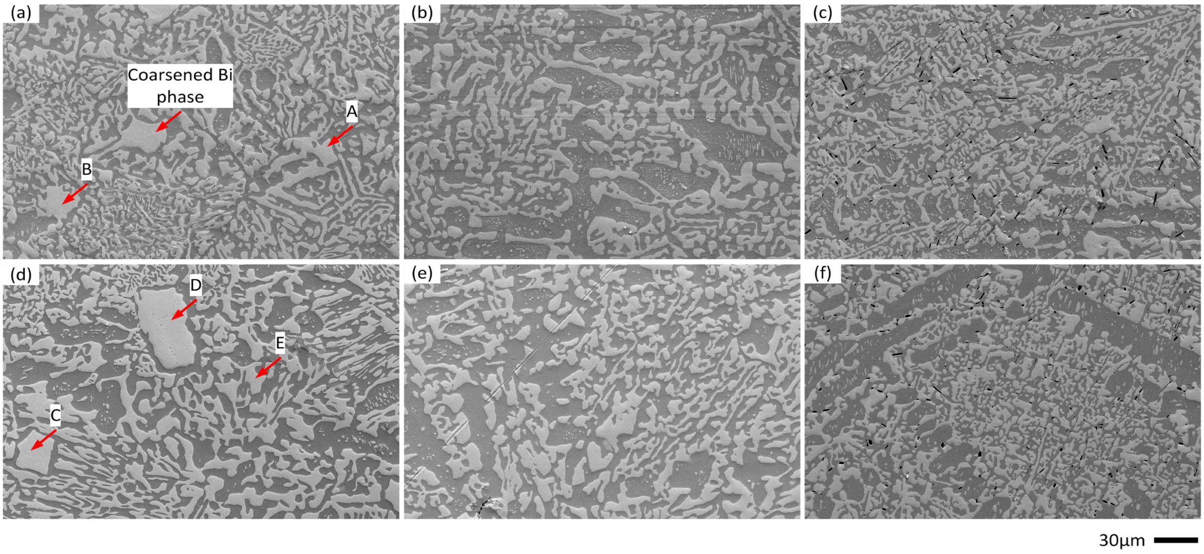

Figure 4-6 FE-SEM images of the cross-sectional microstructure of solder bulks after thermal aging. (a) and (d) eutectic Sn58Bi aged for 504 and 1008 h. (b) and (e) Sn58Bi0.5In aged for 504 and 1008 h. (c) and (f) Sn58Bi0.5In1Zn aged for 504 and 1008 h.

μm, half the value of eutectic Sn58Bi and Sn58Bi0.5In (approximately 8 μm and 9.5 μm, respectively).

Additionally, the number of coarsened Bi grains in each alloy after different aging times is summarized in Table 4-4. As an example, in Figure 4-6, grain A, B, and C were classified as small size coarsened Bi grains, while grain D had a large size. Grain E was hard to be distinguished from the eutectic structure by its size. For eutectic Sn58Bi and Sn58Bi0.5In alloy, the coarsened Bi grains increased their number during aging in both two size categories. For large-size coarsened Bi grains, in eutectic Sn58Bi alloy, the number increased drastically and reached 11 after 1008 h aging, while being 9 for Sn58Bi0.5In. In addition, both eutectic Sn58Bi and Sn58Bi0.5In contained 11 small-size coarsened Bi grains. Conversely, in Sn58Bi0.5In1Zn,

Table 4-4 Number of coarsened Bi grains in eutectic Sn58Bi, Sn58Bi0.5In, and Sn58Bi0.5In1Zn before and after aging.

Aging time (hours)	**The number of the coarsened Bi phase**					
	Eutectic Sn58Bi		Sn58Bi0.5In		Sn58Bi0.5In1Zn	
	10-20 μm	＞20 μm	10-20 μm	＞20 μm	10-20 μm	＞20 μm
0	6	3	2	4	0	0
504	6	5	6	5	3	0
1008	11	11	11	9	4	0

only 4 coarsened Bi grain with small sizes were found after 1008 h aging, while no large-size coarsened Bi grain was found. The effect of In addition on both the eutectic spacing and the growth of the coarsened Bi grains was negligible compared to the results for eutectic Sn58Bi. Moreover, in Sn58Bi0.5In1Zn, the growth of both the coarsened Bi grain and the eutectic spacing during aging were hindered significantly.

The EPMA mappings of the In- and In & Zn-added Sn58Bi alloys after 504 h aging, as shown in Figure 4-7. Combining with the embedded elemental-line, In remained as a solid solution in the Sn phase in both In- and In & Zn-added Sn58Bi alloy at this aging stage, as shown in Figures 4-7(b) and (d). In the meantime, the Zn solid solution existed in both Sn and Bi phases in Sn58Bi10.5In1Zn, as shown in Figure 4-7(e). Additionally, Figure 4-7(f) and (g) show the elemental-line of In and Zn. No obvious Zn segregation was observed in Figure 4-7(g).

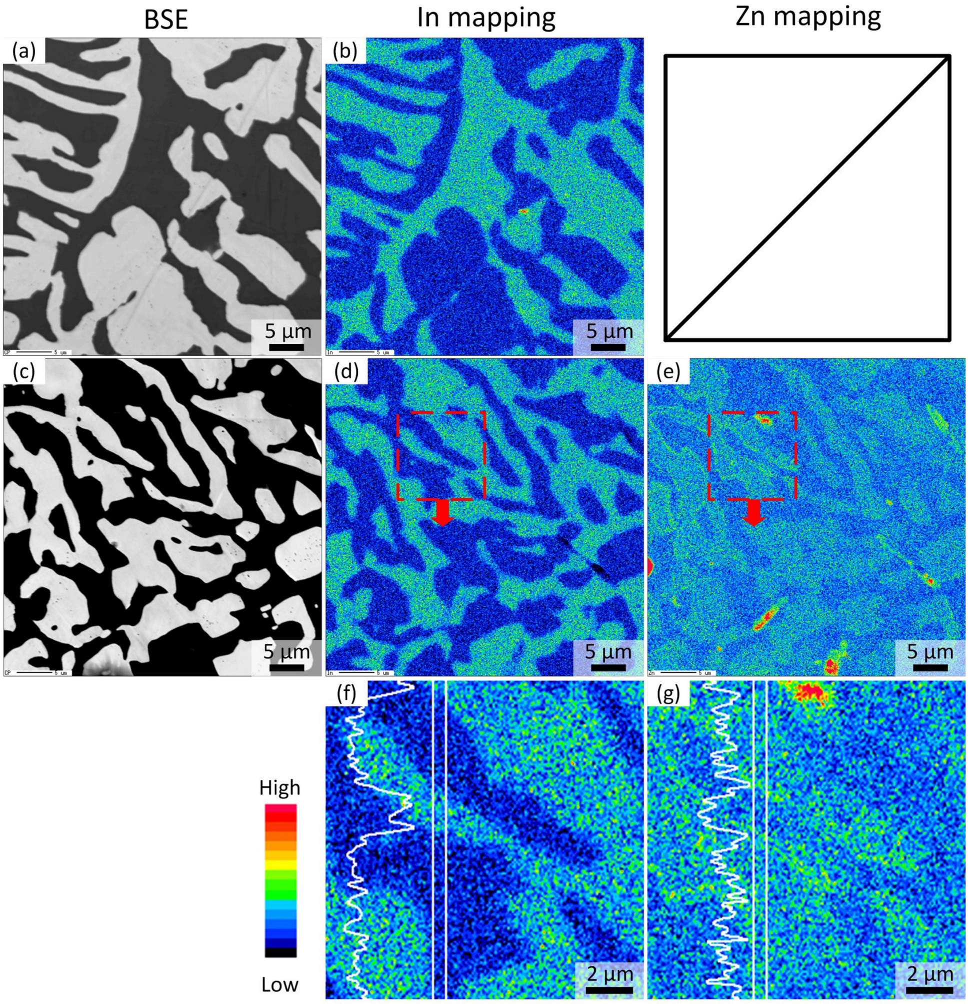

Figure 4-7 EPMA mapping images and elemental-line results of solder bulks after 504 h aging. (a) and (b) Sn58Bi0.5In. (c), (d), and (e) Sn58Bi0.5In1Zn. (f) and (g) the magnified images with the elemental-line embedded of the indicated areas inside (d) and (e).

Figure 4-8 shows the EPMA results of these two alloys after 1008 h aging. The form of In still remained as a solid solution in the Sn phase at this aging stage. In contrast, the Zn segregation on the Sn–Bi boundaries was detected in Sn58Bi0.5In1Zn, as shown in Figure 4-8(e). The magnified image of Figure 4-8(g) also shows clear Zn segregation, indicated by the Zn concentration peaks on the Sn-Bi boundary by elemental-line analysis.

Additionally, a demonstration of composition change in the individual Sn and Bi phases during aging was shown in Figure 4-9, including the EPMA elemental-point result from Table 4-2 and 4-3. In Sn58Bi0.5In, the Sn phase contained both Bi and In solid solutions, while the Bi phase had only a small amount of Sn solid solution. The compositions of these elements remained stable during thermal aging. In Sn58Bi0.5In1Zn alloy, the Sn phase had Bi, In, and Zn solid solutions, and the compositions also remained constant during thermal aging; however, the amount of Zn solid solution in the Bi phase dramatically dropped from 0.48 wt. % to 0.02

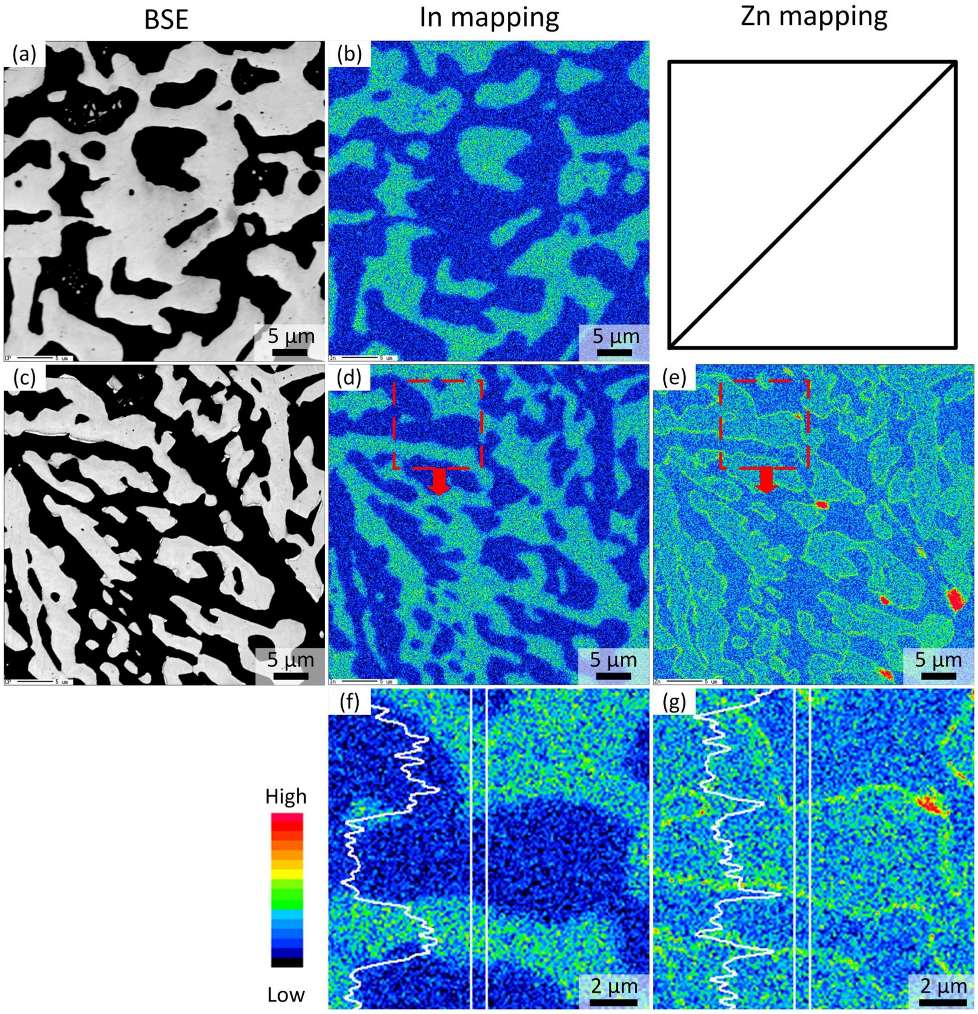

Figure 4-8 EPMA mapping images and elemental-line results of the solder bulks after 1008 h aging. (a) and (b) Sn58Bi0.5In. (c), (d), and (e) Sn58Bi0.5In1Zn. (f) and (g) the magnified images with the elemental-line embedded of the indicated areas inside (d) and (e)

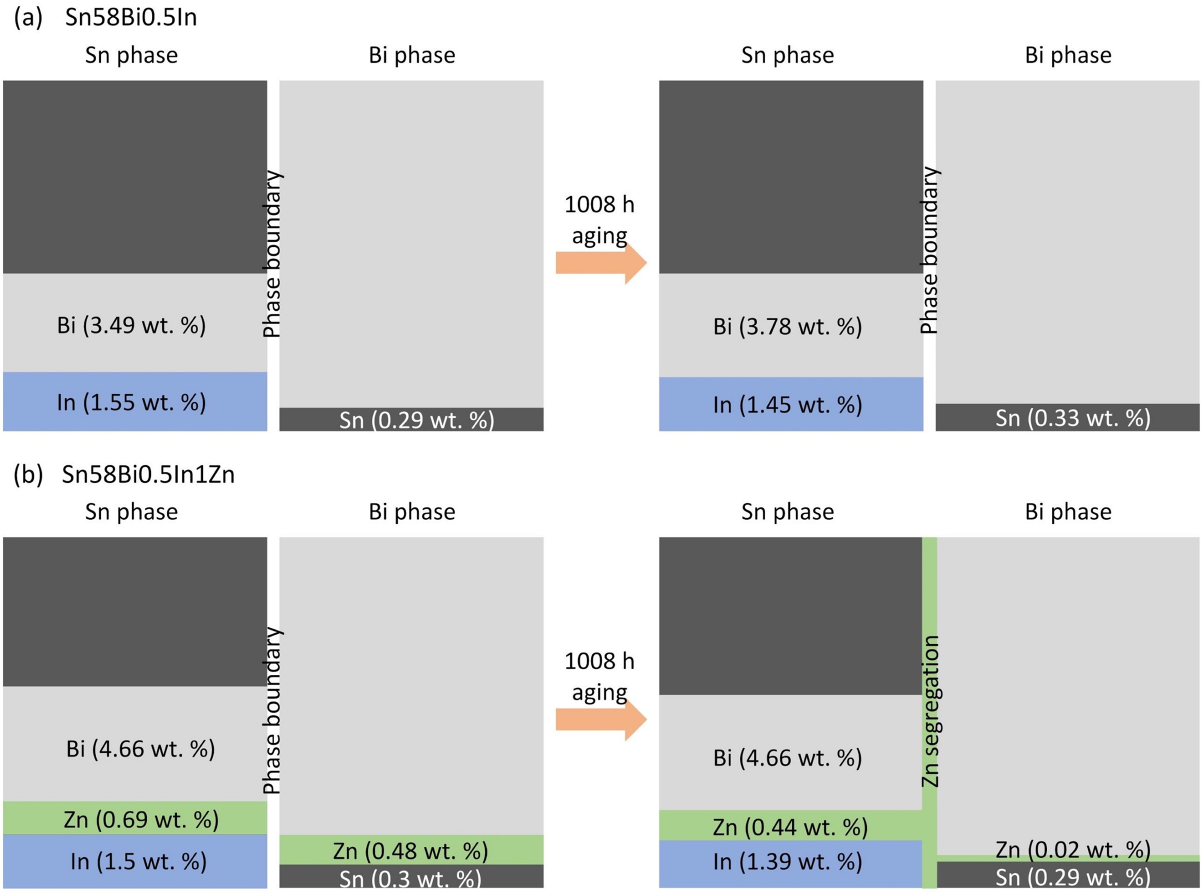

Figure 4-9 Schematic illustration of change in amount of the solid solutions in Sn and Bi phases in Sn58Bi0.5In and Sn58Bi0.5In1Zn alloy during aging (the weight percentages are not to scale).

wt. %. The Zn solution reduced in amount was predicted to move to Sn–Bi phase boundary as the Zn segregation. This result was consistent with the outcome of our previous study. That is caused by a supersaturated solid solution of Zn in Bi phase. During aging, Zn precipitated out and segregated on the Sn–Bi phase boundary. In the present study, the same reason for the Zn segregation was assumed. Therefore, the rarely appeared coarsened Bi phase and small eutectic spacing in Sn58Bi0.5In1Zn were well explained by the diffusion hindering effect of the Zn segregation on Sn–Bi phase boundary.

4.3.3 Mechanical properties before and after aging

Figure 4-10 displayed side views of tensile fractured samples before and after aging. It is clear that eutectic Sn58Bi had brittle fracture mode with almost no plastic deformation. On the other hand, Sn58Bi0.5In and Sn58Bi0.5n1Zn showed deformations with plastic deformation, indicating the ductile fracture mode. Figure 4-11 shows the tensile mechanical properties of

Figure 4-10 FE-SEM images of side views of tensile fracture surfaces.

the tested alloys. The strain-stress curves (SS curves) of the alloys before and after aging were shown in Figure 4-11(a) and (b), while the elongation and UTS were displayed in Figure 4-11(c) and (d). Sn58Bi0.5In1Zn showed the best elongation performance among all the tested alloys throughout the aging period. Compared to eutectic Sn58Bi, Sn58Bi0.5In1Zn exhibited an elongation improvement of approximately 36 % before aging and 41 % after 1008 h aging, while elongation of the Sn58Bi0.5In was between these two extreme cases. Figure 4-11d shows the UTS comparison. Sn58Bi0.5In and Sn58Bi0.5In1Zn had a similar UTS level at approximately 54 MPa. The UTS of eutectic Sn58Bi was the lowest compared in the alloys. The superior UTS property could be well explained by refined microstructures obtained in Zn-added alloys, i.e., Sn58Bi0.5In1Zn. On the other hand, in order to reveal the mechanism of the

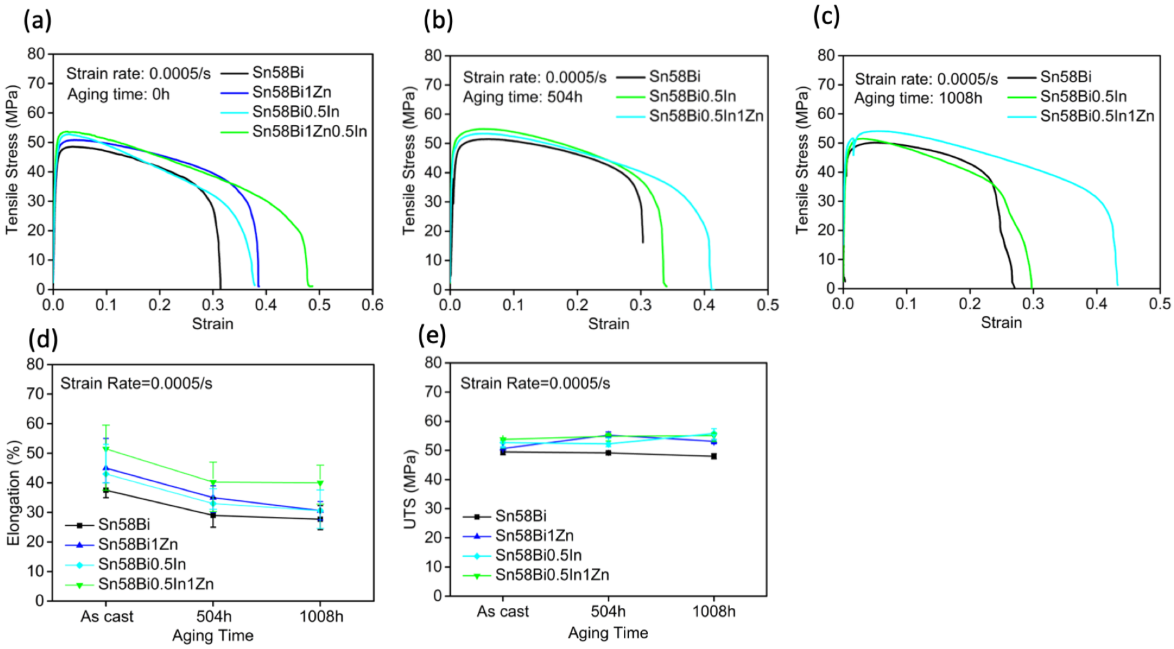

Figure 4-11 The tensile test results. (a) and (b) SS curves of as-casted and aged alloys. (c) The UTS result. (d) The elongation result. Improved elongation and UTS were obtained especially in Sn58Bi0.5In1Zn.

increased elongation, we believe the study via a microcosmic demonstration is necessary. For eutectic Sn58Bi based alloy system, its microstructure was mainly composed of a binary eutectic interlocked Sn-Bi structure. Thus, the mechanical properties of individual Sn and Bi phases have great impacts on the mechanical performance of a whole solder bulk. However, the study in this aspect is rarely seen, except for our previous study [1]. Therefore, in this study, nanoindentation tests was implemented to exam the individual Sn and Bi phases of Sn58Bi0.5In and Sn58Bi0.5In1Zn alloy. The newly obtained hardness, creep displacement data sets were discussed and the possible reason for elongation improvement was proposed in the following section.

Figure 4-12 shows the top view of the fracture surface of tested alloys before and after 1008 h aging. Before aging, in eutectic Sn58Bi, two phases with two different fracture modes, i.e., cleavage and bulge fractures, were observed, as shown in Figure 4-12(a). As reported by others [7], [8], the cleavage fractured phase was Bi phase, while Sn phase showed bulge fracture. By contrast, in In- and In & Zn-added Sn58Bi, no cleavage structure was observed and bulge fracture occupied almost entire fracture surfaces. After 1008 h aging, because the microstructure coarsened in both eutectic Sn58Bi and Sn58Bi0.5In, the Sn and Bi phases in the fracture surfaces became easier to distinguish. Conversely, the fractography of Sn58Bi0.5In1Zn remained unchanged after aging, since the microstructure was barely coarsened.

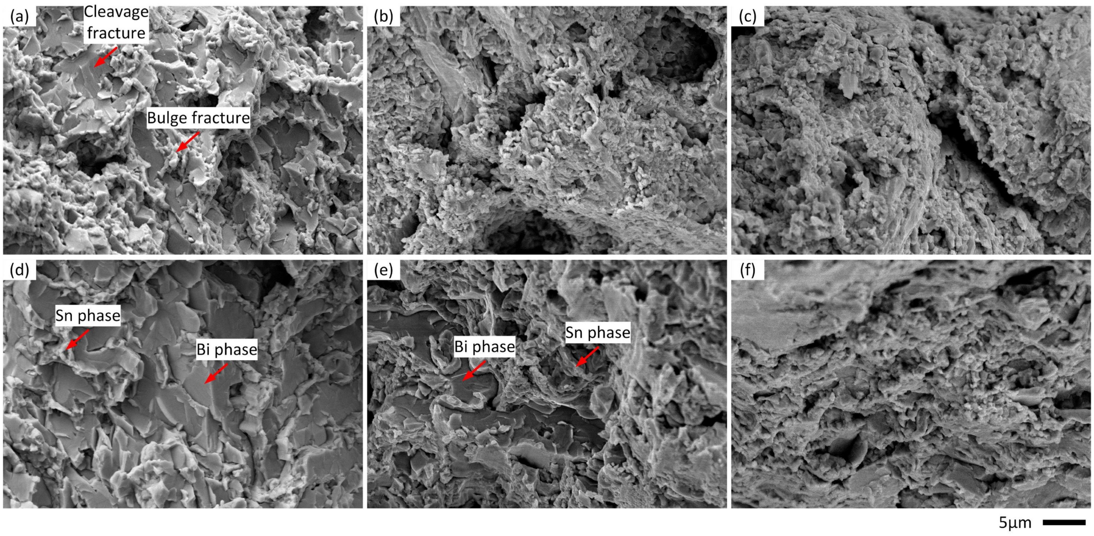

Figure 4-12 Top views of fracture surfaces of before aged (a) eutectic Sn58Bi, (b) Sn58Bi0.5In, and (c) Sn58Bi0.5In1Zn. After aged (d) eutectic Sn58Bi, (e) Sn58Bi0.5In, and (f) Sn58Bi0.5In1Zn.

4.3.4 Nanoindentation

Figure 4-13 shows the post-indent surfaces in In- and In & Zn-added Sn58Bi and compares the representative P–h curves of the individual Sn and Bi phases in the tested alloys. The indent displacement in the Sn phase in eutectic Sn58Bi was smaller than that in the Bi phase. This means that the hardness of Sn phase was higher than that of Bi phase in the eutectic Sn58Bi alloy. It is reported that pure Sn has a lower hardness than pure Bi, but the Bi solid solution hardens the Sn phase significantly in eutectic Sn58Bi alloy, owing to solid solution hardening [9]. For the In- and In & Zn-added Sn58Bi, the P–h curves of Sn and Bi phases are shown in Figures 4-13(d) and (e), respectively. Obviously, large displacements were observed in both Sn and Bi phases in the Sn58Bi0.5In. The Sn phase reached the maximum displacement (around 200 nm) during loading, nearly three times deeper than that in eutectic Sn58Bi. Interestingly, the displacement was larger in the Sn phase than in the Bi phase in Sn58Bi0.5In. This indicates that the Sn phase hardness was lower than that of Bi phase in Sn58Bi0.5In. Since In had a solubility of 1.55 wt. % in the Sn phase, but almost zero in the Bi phase in Sn58Bi0.5In, this effective softening of In on the Sn phase but not Bi phase seemed reasonable. The corresponding hardness result also shows that hardness of the Sn phase decreased dramatically from 1.7 GPa in eutectic Sn58Bi to just below 0.5 GPa in Sn58Bi0.5In, as shown in Figure 4-

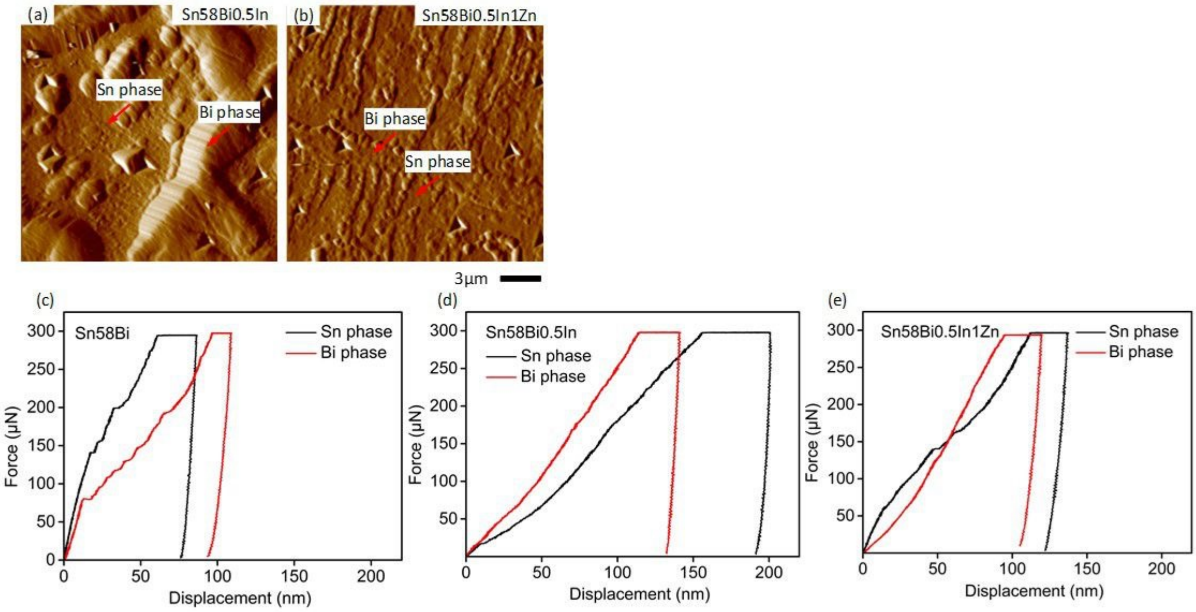

Figure 4-13 Post-indent surfaces as well as the P-h curves. (a) and (b) Post-indent surfaces of Sn58Bi0.5In and Sn58Bi0.5In1Zn, respectively. (c), (d), and (e) the P-h curves of Sn and Bi phases within Sn58Bi0.5In and Sn58Bi0.5In1Zn alloys, respectively.

14. This decreased Sn phase hardness was responsible for the elongation improvement of Sn58Bi0.5In bulk. The fundamental mechanism of this phenomenon still remains unknown, but the study [6] assumed that the In solid solution in Sn phase counteracts with the Bi phase and results in a reduced Sn phase hardness. Moreover, in Sn58Bi0.5In1Zn, the displacements for both Sn and Bi phases were smaller than those in the Sn58Bi0.5In, but larger than those for eutectic Sn58Bi.

The overall hardness result of the tested alloys shows a similar trend compared to the displacement change. Moreover, it has been reported that SSS can be manifested by yield strength decrease [10]–[12]. Tabor [13] suggested that for a work-hardening material, the relation between hardness and yield strength (known as the three-time relationship), and is represented as:

$$H_V \approx 3 * \delta_r \qquad (1)$$

Where H_V is the hardness and δ_r is the representative yield strength, which represents the uniaxial flow stress at some specific strain value; it has been reported that this strain is between 8 % and 10 %. Yang at el. studied that for Sn–Bi-based alloy, although the ratio of H_V and the yield strength δ_y is larger than three, it strongly follows a linear dependence [14], as shown in Equation (2).

$$H_V > 3 * \delta_y \qquad (2)$$

In Sn58Bi0.5In, because the hardness of the Sn phase decreased drastically, as shown in Figure 4-14, the yield strengths of these Sn phases were predicted to decrease as well, according to Equation (2). Since both Zn and In had solubility in Sn phase, the SSS induced by either of these two elements on the Sn phases was proved by the yield strength decrease. In addition, in Sn58Bi0.5In1Zn, the hardness of both Sn and Bi phase was slightly higher than that in

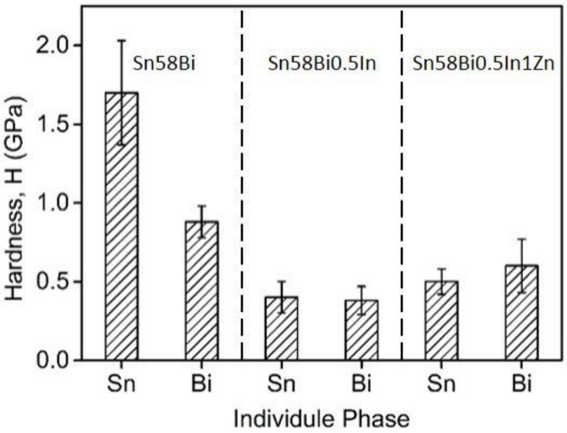

Figure 4-14 Hardness of the individual Sn and Bi phases in tested alloys. Significant hardness decrease was obtained in Sn58Bi0.5In and Sn58Bi0.5In1Zn.

Sn58Bi0.5In; nevertheless, they were still noticeably lower than those in eutectic Sn58Bi. This indicates that the SSS effect by the In and Zn double addition was still effective in Sn58Bi0.5In1Zn.

In addition to the hardness discussion, it has been reported that the intrinsic mechanism of SSS is the interactions between substitutional solute atoms and dislocations results in the increased dislocation mobility [10]. Dislocation can move through a crystal until it reaches a grain boundary or be impeded by defects or solid solutions. The latter always induces crystal hardening, the so-called dislocation hardening. Dislocation creep, involving dislocation gliding under a constant stress is a suitable mechanism to reveal the situation in a crystal [15], [16]. Figure 4-15 shows the creep behavior of the tested alloys at room temperature. These time-displacement curves were extracted from the NI test P–h curves at a peak load of 300 μN during a holding time from 15 s to 35 s. Table 4-5 shows the displacement change Δh during a holding time of 20 s. Since creep displacement is controlled by dislocation movement in a solder material [17], a larger creep displacement means that the dislocation glides easier in the crystal. After adding Zn or In into eutectic Sn58Bi, the Δh of both Sn and Bi phases was higher than those of the eutectic Sn58Bi. Especially for the Sn58Bi0.5In, the Δh of the Sn and Bi phases was the largest among the tested alloys, indicating that plastic deformation or dislocation movement became much easier after adding the In. Considering the yield strength change above discussed, which had a similar trend as the hardness result in Figure 4-14, the yield strengths of the Sn and Bi phases in Sn58Bi0.5In was the lowest among the four alloys as well. By comparing the hardness and the creep displacement of In- and In & Zn-added Sn58Bi, similar phenomena were obtained. Therefore, in this study, we believe that the creep displacement was directly related to the SSS and was the result of the interaction between the

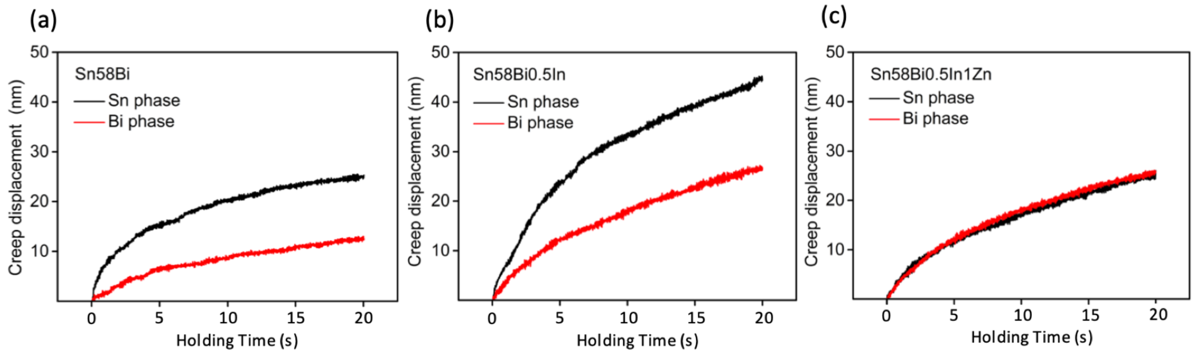

Figure 4-15 The time-displacement curves represent the creep behavior of the Sn and Bi phases in tested alloys at a constant holding load of 300 μN.

Table 4-5 Creep displacement in Sn and Bi phases in each alloy during 20 s holding period.

Phase	Creep displacement Δh (nm)		
	Eutectic Sn58Bi	Sn58Bi0.5In	Sn58Bi0.5In1Zn
Sn	19.6	43.8	24.3
Bi	12.5	26.8	25.1

solutes (In and Zn) and dislocations. Thus, the creep result served as another evidence of SSS in the studied alloy system.

It is considered that the superior ductility of the Sn58Bi0.5In and Sn58Bi0.5In1Zn was mainly attributed to the SSS. Interestingly, for Sn58Bi0.5In, the elongation decreased rapidly after 504 h aging. Because the microstructure coarsened in the Sn58Bi0.5In after 504 h aging (Figure 4-4), the elongation was deteriorated even though the In solute had the most promising SSS effect on the alloy. By contrast, although the hardness decrease in Sn58Bi0.5In1Zn was not as large as that in the Sn58Bi0.5In, owing to the fine microstructure controlled by Zn segregation on the Sn–Bi boundary, the SSS induced by In in the alloy can be therefore maintained during aging. Because of the two different diffusion behaviors of In and Zn solutes during aging, the elongation and UTS performance of Sn58Bi0.5In and Sn58Bi0.5In1Zn were different. This result suggests that the effects of In and Zn were well combined in the In & Zn-added Sn58Bi alloy.

4.4 ENIG/alloy/ENIG joint

4.4.1 Interfacial layer of solder/ENIG after reflow

The cross-sectional side views of various solder joints were shown in Figure 4-16. The results indicated that the sound joints were produced. Figure 4-17 shows the EPMA mapping results of eutectic Sn58Bi/ENIG interface before aging, which have been studied in chapter 2 and 3. In brief, the $(Au, Ni)_3(Sn, Bi)_4$ IMC layer formed on eutectic Sn58Bi/ENIG interface after reflow.

Figure 4-18 presents the EPMA mappings of newly synthesized Sn58Bi0.5In/ENIG and Sn58Bi0.5In1Zn/ENIG interfaces. In Figure 4-18a, a continues $(Au, Ni)(Sn, In)_4$ IMC layer

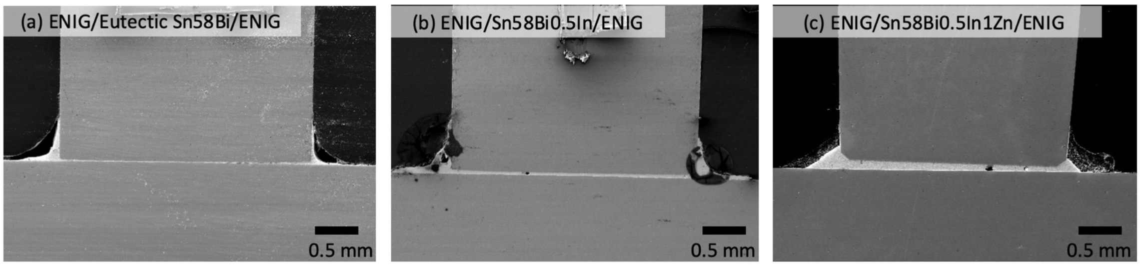

Figure 4-16 FE-SEM images of side views of solder joints.

indicated by EDS was observed on the solder/substrate interface, the EDS result is shown in point 3 in Table 4-5. In the interface of eutectic Sn58Bi/ENIG, (Au, Ni)(Sn, Bi)$_4$ IMC layer was detected after reflow. By alloying 0.5 wt% In in eutectic Sn58Bi alloy, the composition of IMC layer changed to (Au, Ni)(Sn, In)$_4$. This composition has never been published before on the solder/ENIG interface. However, the atom replacement between Sn and In in Ni3Sn4 has been reported in some studies [18], [19]. Figure 4-18b shows the interfacial layer of Sn58Bi0.5In1Zn/ENIG, several interesting points were observed. First, concentration of Sn on this IMC layer was low, indicating Sn did not or barely involved in the interfacial reaction. Second, Au did not diffuse into the solder matrix and gathered near the interface displayed as a form of a continues layer. Third, Zn gathered near the interface as well. Fourth, In gathered on top of the Zn layer. EPMA line analysis was conducted on the interface of Sn58Bi0.5In1Zn/ENIG interfacial layer, as shown in Figure 4-19. The result indicated two distinguishable layers were detected on Sn58Bi0.5In1Zn/ENIG interface. One layer was AuZn$_3$, which directly attached to the Ni(P) layer in ENIG substrate. The composition of AuZn$_3$

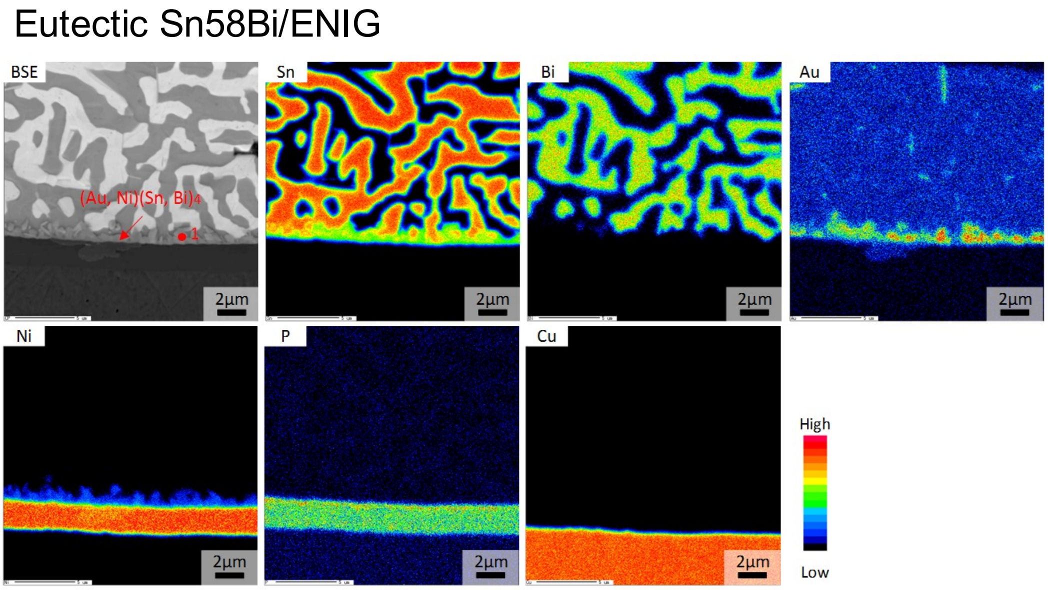

Figure 4-17 EPMA mappings at the interface of eutectic Sn58Bi/ENIG before aging.

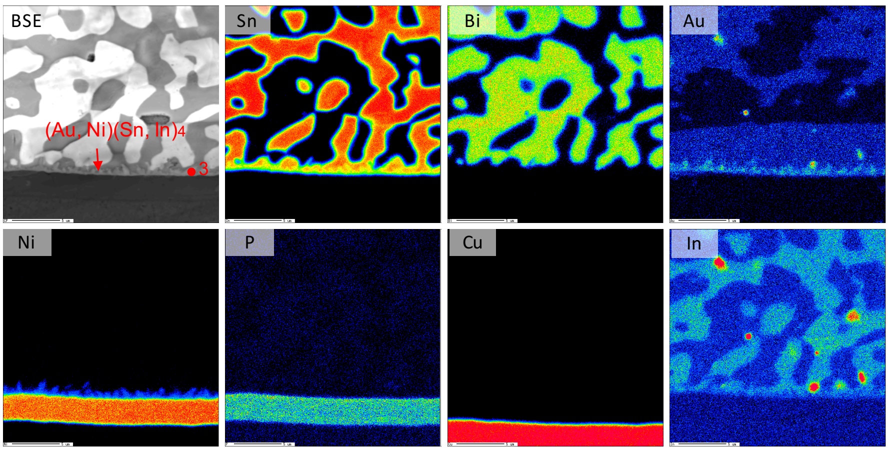
(a) Sn58Bi0.5In/ENIG

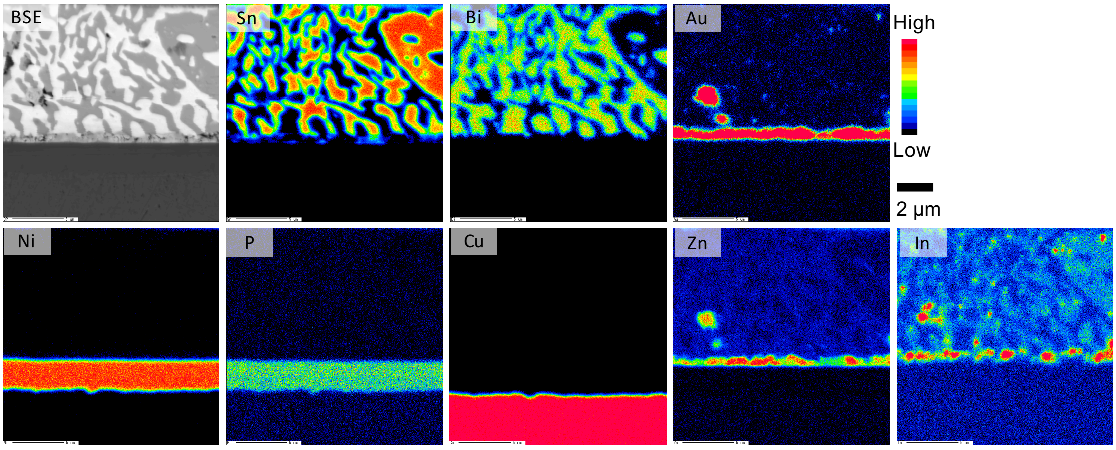
(b) Sn58Bi0.5In1Zn/ENIG

Figure 4-18 EPMA mappings of the interfaces before aging. (a) Sn58Bi0.5In/ENIG and (b) Sn58Bi0.5In1Zn/ENIG.

was obtained by EDS, as shown in point 4 in Table 4-6. Another layer was Au-In IMC layer, which had a thickness less than 0.5 micrometer and located on top of the $AuZn_3$ IMC layer. Due to the very thin Au-In layer, the composition was unclear.

In the Chapter 3, a detached $AuZn_3$ IMC layer was observed on Sn58Bi1Zn/ENIG interface after reflow. By contrast, a continues $AuZn_3$ IMC layer attached to the ENIG substrate was observed in Sn58Bi0.5In1Zn/ENIG interface. This is probably due to the Au-In layer formed on top of $AuZn_3$ layer and the Au-In layer prevented $AuZn_3$ layer from detaching.

4.4.2 IMC evolution at the interface after thermal aging

Figure 4-20 presents the IMC layer growth behaviors of tested solder joints during thermal aging. For Sn58Bi0.5In/ENIG interface, continues IMC layers was observed before and after aging, as shown in Figure 4-20(b). Before aging, the composition was (Au, Ni)(Sn, In)$_4$, as

Table 4-6 EPMA elemental-point analyses at various locations shown in the SEM images (locations are indicated by red dots and numbers).

Location	IMC type	Composition (at.%)					
		Sn	Bi	Ni	Zn	Au	In
Figure 4-17, point 1	$(Au, Ni)(Sn, Bi)_4$	60.2	13.2	14.1	-	4.5	-
Figure 4-18, point 3	$(Au, Ni)(Sn, In)_4$	62.0	-	16.2	-	7.8	14.0
Figure 4-19, point 4	$AuZn_3$	-	-	-	73.2	26.8	-
Figure 4-20, point 5	$(Au, Ni)(Sn, In)_4$	61.5	-	13.5	-	4.8	9.9

shown in Table 4-6. After 1008 h aging, the composition was $(Au, Ni)(Sn, In)_4$ as well, indicated by EPMA result as point 5 in Table 4-5. The IMC layer thickness was measured and displayed in Figure 4-19, the IMC layer thickness on Sn58Bi0.5In/ENIG interface was almost unchanged compared to that on eutectic Sn58Bi/ENIG. It was assumed that the involvement of In atom in IMC layer suppressed the growth rate of the IMC layer on Sn58Bi0.5In/ENIG interface. Moreover, Ni_3Sn_4 IMC layer was not observed on Sn58Bi0.5In/ENIG interface due to the slow growth of the $(Au, Ni)(Sn, In)_4$ IMC layer. For Sn58Bi0.5In1Zn/ENIG, an IMC layer with almost unchanged thickness was obtained as well, as shown in Figure 4-20 and 4-

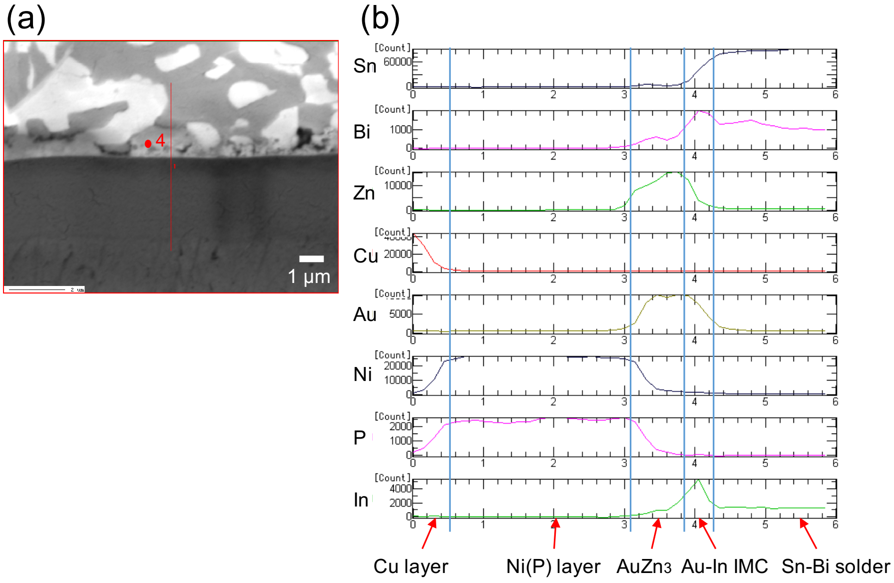

Figure 4-19 EMPA line analysis of the Sn58Bi0.5In1Zn/ENIG interface. (a) BSE image of tested location. (b) Elemental analysis results.

(a) Eutectic Sn58Bi/ENIG

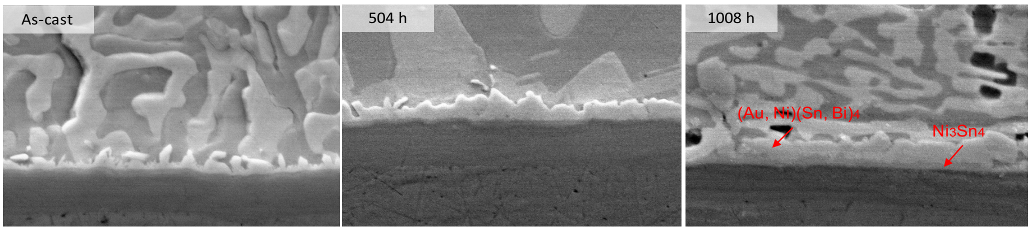

(b) Sn58Bi0.5In/ENIG

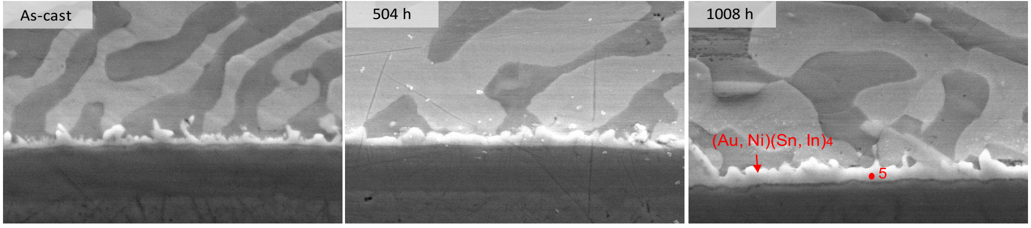

(c) Sn58Bi0.5In1Zn/ENIG

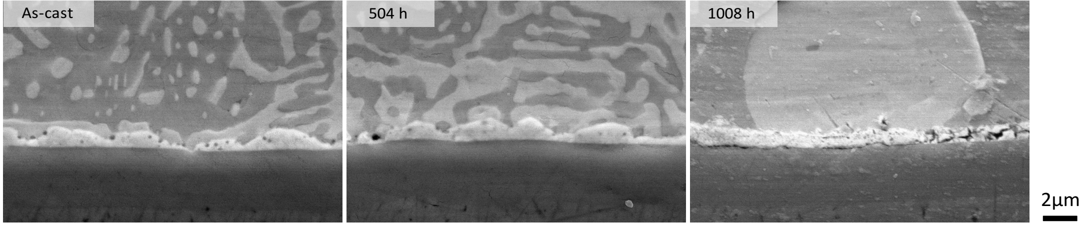

Figure 4-20 IMC layer growth comparison during thermal aging. (a) Eutectic Sn58Bi/ENIG. (b) Sn58Bi0.5In/ENIG. (c) Sn58Bi0.5In1Zn/ENIG.

21. The unchanged thickness of the $AuZn_3$ IMC layer seemed reasonable since Au was consumed completely during reflow. The same $AuZn_3$ IMC layer with a similar thickness result was obtained as well on Sn-Zn/Au/Ni interface in the study [20]. Additionally, the Au-In IMC layer could act as a diffusion barrier and prevent the growth of the $AuZn_3$ IMC layer. Figure 4-22 shows the EPMA mappings of the Sn58Bi0.5In1Zn/ENIG after 1008 h aging. The

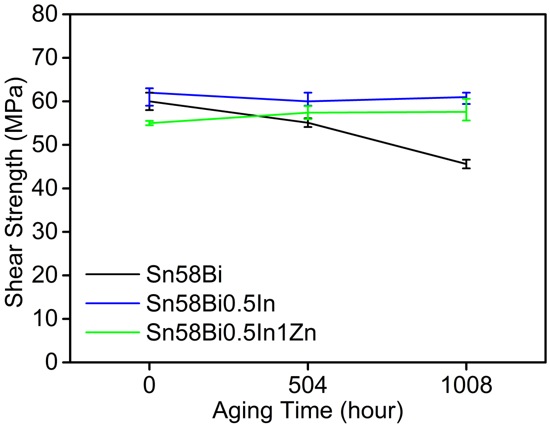

Figure 4-21 Shear strength comparison of eutectic Sn58Bi, Sn58Bi0.5In and Sn58Bi0.5In1Zn joints.

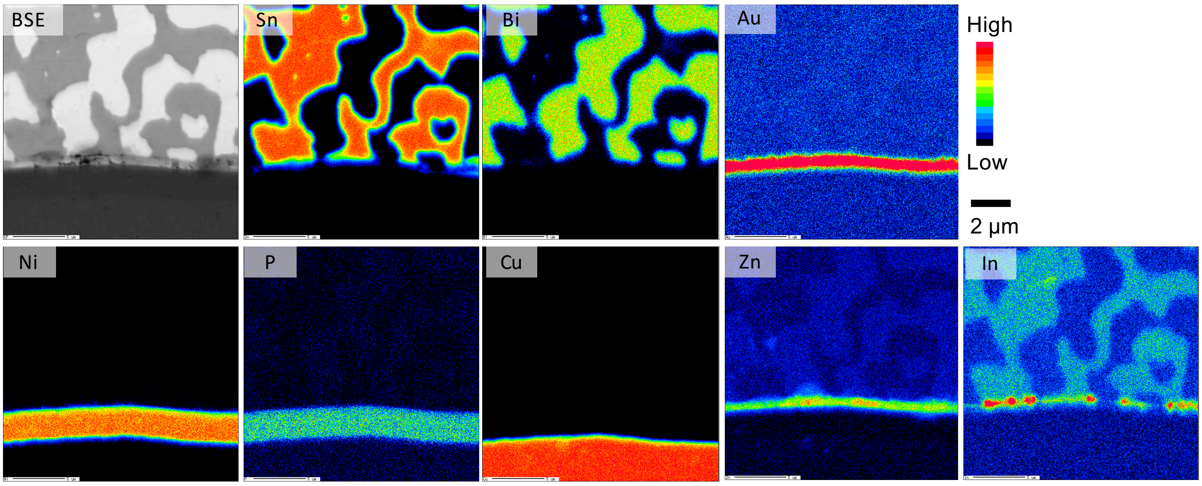

Figure 4-22 EPMA mappings of Sn58Bi0.5In1Zn/ENIG interfacial layer after 1008 h aging.

same Au-In/AuZn$_3$ two IMC layers structure remained unchanged, indicating the excellent thermal stability of Au-In and AuZn$_3$ IMC layers.

4.4.3 Fracture behaviors and shear strength

Figure 4-23 shows the EPMA mapping results of fractured surfaces of ENIG/Sn58Bi0.5In/ENIG solder joint both before and after aging. It is clear that no sign of Ni and P were detected on the both top and bottom fractured surface before and after thermal aging. This indicated that fracture path were entirely inside the solder bulk of Sn58Bi0.5In

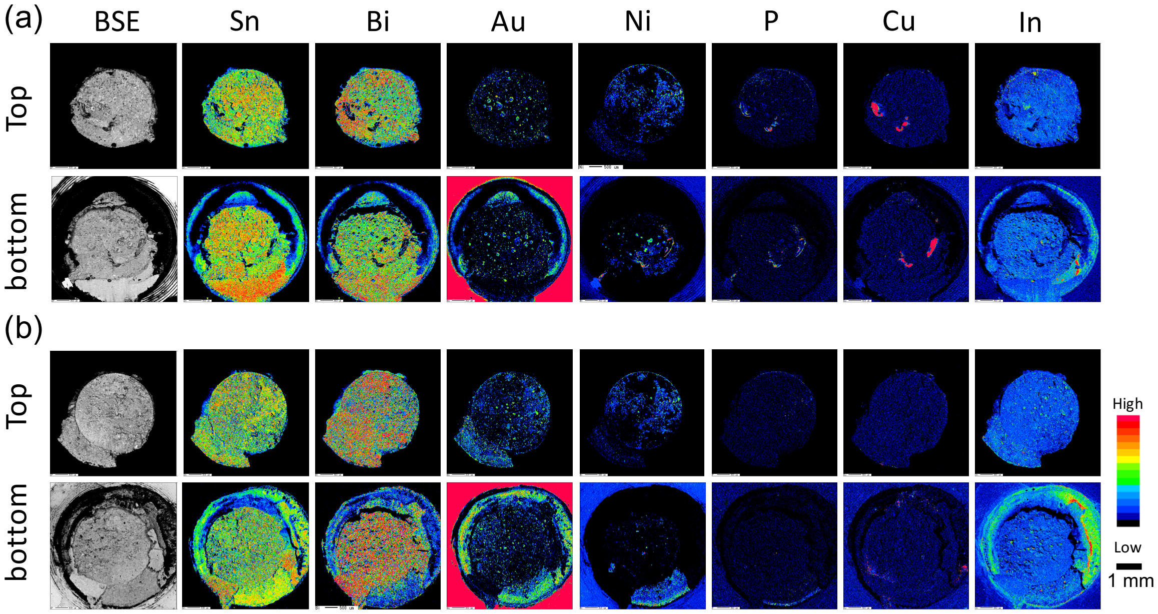

Figure 4-23 EPMA mappings of fracture surfaces of Sn58Bi0.5In joints. (a) Before aging. (b) After 1008 h aging.

joint. Due to the slow growth of the (Au, Ni)(Sn, In)$_4$ IMC on Sn58Bi0.5In/ENIG interface, the fracture remained in the solder bulk even after 1008 h aging. Figure 4-24 shows the EPMA results of fractured surfaces of Sn58Bi0.5In1Zn joint. A large area fraction of Ni and P were observed in both top and bottom fractured surfaces both before and after aging. In addition, some amount of Au, Zn and In were observed. This indicates that fracture occurred partially inside Ni(P) layer and Au-In/AuZn$_3$ IMC layers. The shear strength of tested solder joints were shown in Figure 4-25. It is clear that the shear strength change was closely related to the fracture path change inside solder joints. For eutectic Sn58Bi joint, shear strength decreased after aging since the rapid IMC layer thickness growth during aging. For Sn58Bi0.5In joints, the strength was stabled due to the stable (Au, Ni)(Sn, In)$_4$ IMC layer. On the other hand, the strength was almost unchanged for Sn58Bi0.5In1Zn joint owing to the unchanged Au-In/AuZn$_3$ double IMC layer structure, although this structure was found brittle. Study [21] reported that fracture could occur alongside AuZn$_3$ IMC layer due to its brittleness. In the present study, because AuZn$_3$ IMC layer was in a continues layer form, fracture pathed through brittle AuZn$_3$ IMC. Figure 4-26 shows the fracture mode comparison of tested solder alloys. Since the (Au, Ni)(Sn, In)$_4$ IMC layer on Sn58Bi0.5In/ENIG interface was thinner and more stable than the (Au, Ni)(Sn, Bi)$_4$ on eutectic Sn58Bi/ENIG interface, the fracture pathed through entirely in solder bulk in Sn58Bi0.5In both before and after aging. On the other hand, fracture path remained inside Au-In/AuZn$_3$ IMC layers and Ni(P) layers in Sn58Bi0.5In1Zn/ENIG, because of the brittleness of AuZn$_3$.

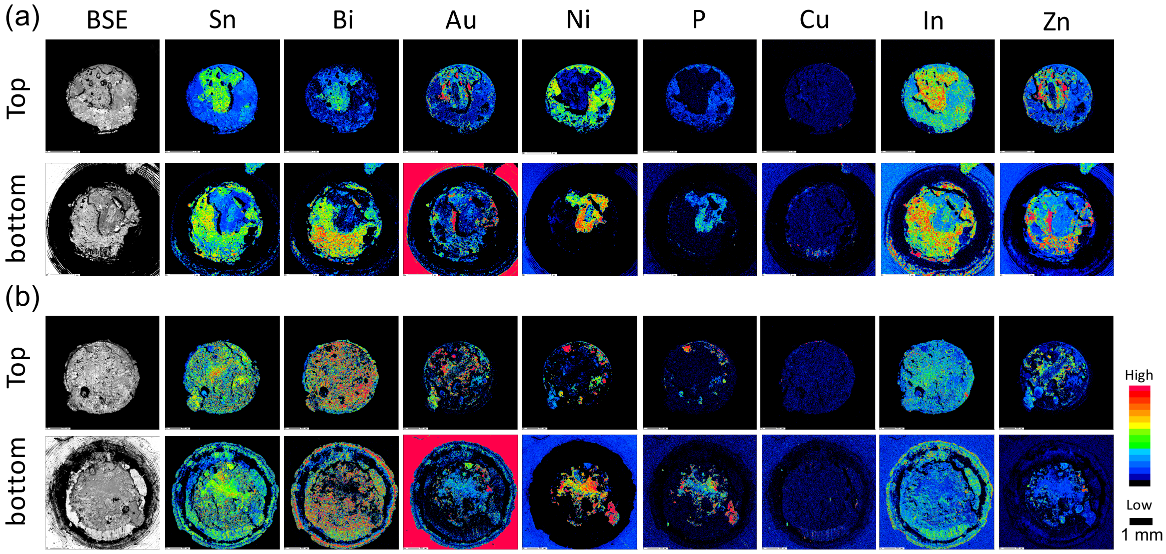

Figure 4-24 EPMA mappings of fracture surfaces of Sn58Bi0.5In1Zn joints. (a) Before aging. (b) After 1008 h aging.

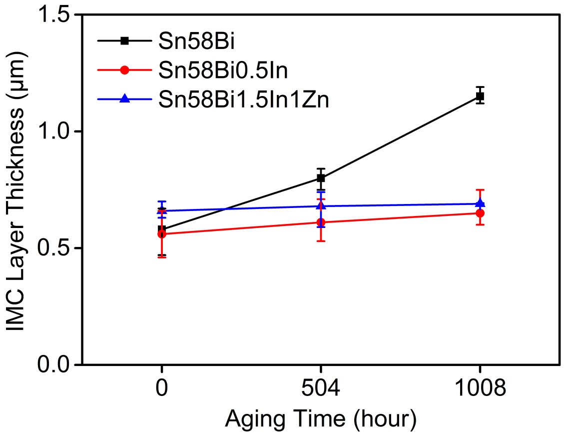

Figure 4-25 IMC thickness of tested solder joints.

Conclusion

In this chapter, for solder bulk. Sn58Bi0.5In and Sn58Bi0.5In1Zn alloys were synthesized. The microstructural and mechanical properties of these new alloys were investigated in depth. The results show that the minor In and Zn addition has potential in solving the brittle issue of eutectic Sn58Bi alloy.

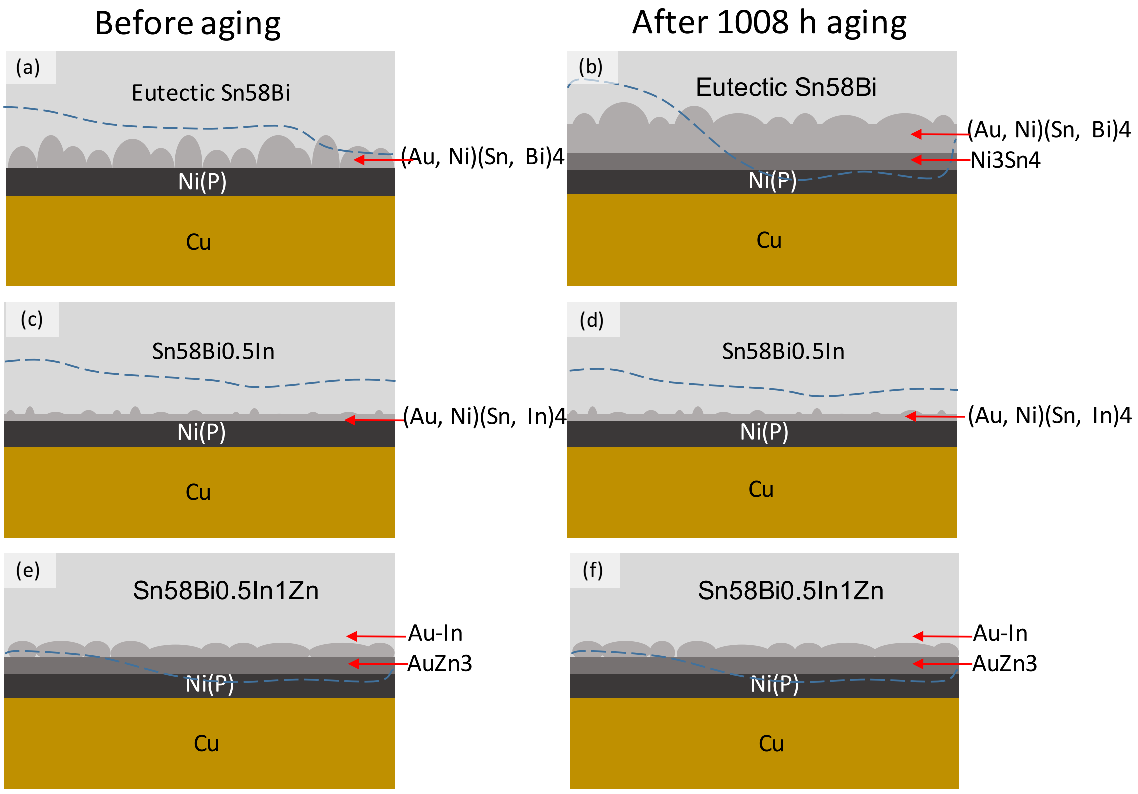

Figure 4-26 Schematic illustration of fracture paths of tested alloys.

Compared to eutectic Sn58Bi, the In & Zn-added Sn58Bi had finer microstructure, i.e., smaller eutectic spacing and fewer coarsened Bi grains, due to the Zn segregation phenomenon, while In had a negligible effect on the microstructure refinement.

Elongation improvements of 36 % and 41 % were obtained in the Sn58Bi0.5In1Zn before and after 1008 h aging by conducting tensile tests.

The softening of the Sn phase induced by the In solid solution was proposed in Sn58Bi0.5In and Sn58Bi0.5In1Zn. Quantitative hardness and creep data of individual Sn and Bi phases in each alloy were obtained.

The fine microstructure induced by the Zn addition as well as the In solid solution triggered SSS were combined responsible for the elongation improvement and mechanical thermal reliability in Sn58Bi0.5In1Zn.

For solder joint, on Sn58Bi0.5In/ENIG interface, we observed a continues (Au, Ni)(Sn, In)4 IMC layer, which maintained its thickness and morphology during thermal aging. The shear strength, as a result, remained almost unchanged during aging (approximately 62 MPa both before and after aging). On the other hand, Au-In/AuZn3 IMC layers were observed on Sn58Bi0.5In1Zn/ENIG interface. The thickness and morphology of these IMC layers did not change during thermal aging as well. However, due to the brittleness of AuZn3 IMC layer, the fracture pathed through Au-In/AuZn3 IMC layers and Ni(P) layer. The shear strength of Sn58Bi0.5In1Zn joint was lower than that of Sn58Bi0.5In joint, but they were remained almost unchanged despite the aging time.

Reference

[1] S. Zhou, O. Mokhtari, M. G. Rafique, V. C. Shunmugasamy, B. Mansoor, and H. Nishikawa, “Improvement in the mechanical properties of eutectic Sn58Bi alloy by 0.5 and 1 wt.% Zn addition before and after thermal aging,” *J. Alloys Compd.*, 2018.

[2] M.-S. Kim and H. Nishikawa, “Transmission electron microscopy investigation on the Oxidation behavior of Electroless Ni/Immersion Au surface finish at 250 C,” *J. Nanosci. Nanotechnol.*, vol. 17, no. 11, pp. 8522–8527, 2017.

[3] O. Mokhtari and H. Nishikawa, “Effects of in and Ni addition on microstructure of Sn-58Bi solder joint,” *J. Electron. Mater.*, vol. 43, no. 11, pp. 4158–4170, 2014.

[4] W. C. Oliver and G. M. Pharr, “An improved technique for determining hardness and elastic modulus using load and displacement sensing indentation experiments,” *J. Mater. Res.*, vol. 7, no. 6, pp. 1564–1583, 1992.

[5] O. Mokhtari and H. Nishikawa, “Correlation between microstructure and mechanical properties of Sn-Bi-X solders,” *Mater. Sci. Eng. A*, vol. 651, pp. 831–839, 2016.

[6] X. Chen, F. Xue, J. Zhou, and Y. Yao, “Effect of in on microstructure, thermodynamic characteristic and mechanical properties of Sn-Bi based lead-free solder,” *J. Alloys Compd.*, vol. 633, pp. 377–383, 2015.

[7] Z. Lai and D. Ye, “Microstructure and fracture behavior of non eutectic Sn–Bi solder alloys,” *J. Mater. Sci. Mater. Electron.*, vol. 27, no. 4, pp. 3182–3192, 2016.

[8] J. Shen, Y. Pu, H. Yin, D. Luo, and J. Chen, “Effects of minor Cu and Zn additions on the thermal, microstructure and tensile properties of Sn-Bi-based solder alloys,” *J. Alloys Compd.*, vol. 614, pp. 63–70, 2014.

[9] L. Shen, P. Septiwerdani, and Z. Chen, “Elastic modulus, hardness and creep performance of SnBi alloys using nanoindentation,” *Mater. Sci. Eng. A*, vol. 558, pp. 253–258, 2012.

[10] Y. Huo, J. Wu, and C. C. Lee, “Solid solution softening and enhanced ductility in concentrated FCC silver solid solution alloys,” *Mater. Sci. Eng. A*, vol. 729, pp. 208–218, 2018.

[11] V. P. Soldatov, V. D. Natsik, A. N. Diulin, and G. I. Kirichenko, “Low-temperature softening of β-tin single crystals on doping with substitutional impurities,” *Low Temp. Phys.*, vol. 26, no. 2, pp. 160–168, 2000.

[12] D. R. Trinkle and C. Woodward, “The chemistry of deformation: How solutes soften pure metals,” *Science*, vol. 310, no. 5754, pp. 1665–1667, 2005.

[13] D. Tabor, “Indentation hardness: fifty years on a personal view,” *Philos. Mag. A*, vol. 74, no. 5, pp. 1207–1212, 1996.

[14] L. Yang *et al.*, “Effects of Ni addition on mechanical properties of Sn58Bi solder alloy during solid-state aging,” *Mater. Sci. Eng. A*, vol. 667, pp. 368–375, 2016.

[15] X. Li and B. Bhushan, “A review of nanoindentation continuous stiffness measurement technique and its applications,” *Mater. Charact.*, vol. 48, no. 1, pp. 11–36, 2002.

[16] H. Ma and J. C. Suhling, “A review of mechanical properties of lead-free solders for electronic packaging,” *J. Mater. Sci.*, vol. 44, no. 5, pp. 1141–1158, 2009.

[17] L. Shen, P. Lu, S. Wang, and Z. Chen, “Creep behaviour of eutectic SnBi alloy and its constituent phases using nanoindentation technique,” *J. Alloys Compd.*, vol. 574, pp. 98–103, 2013.

[18] J.-M. Koo and S.-B. Jung, “Effect of surface finish of substrate on mechanical reliability of In-48Sn solder joints in MOEMS package,” *Microsyst. Technol.*, vol. 13, no. 11–12, pp. 1567–1573, 2007.

[19] J.-M. Koo, J.-W. Yoon, and S.-B. Jung, “Interfacial reactions between In–48Sn solder and electroless nickel/immersion gold substrate during reflow process,” *Surf. Interface Anal. Int. J. Devoted Dev. Appl. Tech. Anal. Surf. Interfaces Thin Films*, vol. 38, no. 4, pp. 426–428, 2006.

[20] J.-W. Yoon and S.-B. Jung, “Interfacial reactions and shear strength on Cu and electrolytic Au/Ni metallization with Sn-Zn solder,” *J. Mater. Res.*, vol. 21, no. 6, pp. 1590–1599, 2006.

[21] P. Yao, P. Liu, and J. Liu, “Interfacial reaction and shear strength of SnAgCu–xNi/Ni solder joints during aging at 150 C,” *Microelectron. Eng.*, vol. 86, no. 10, pp. 1969–1974, 2009.

Chapter 5

Effects of low Bi content on ductility and melting temperature

5.1 Introduction

In this chapter, a new approach of improving ductility of eutectic Sn58Bi alloy was proposed and a new Sn45Bi2.6Zn alloy was designed by reducing the Bi content in eutectic Sn58Bi. There were two steps involved to design this alloy. Step one, reducing the volume fraction of Bi in eutectic Sn58Bi alloy, since Bi was the primary source of brittleness in eutectic Sn58Bi alloy. However, according to the Sn-Bi phase diagram calculated by CALPHAD method, by reducing Bi volume fraction from eutectic point (54.48 wt. %) to 45 wt. %, the liquidus temperature increased over 15 ℃, as shown in Figure 5-1. This consequence was not ideal, because good wettability is greatly related to the melting behavior of a solder alloy. Therefore, in step two, we suggested to control the melting behavior by alloying another element Zn was selected in this study.

The target liquidus temperature of newly designed alloy was the same as that of eutectic Sn58Bi alloy, which was 139 ℃. The composition calculated by CALPHAD method was Sn46.3Bi2.7Zn.

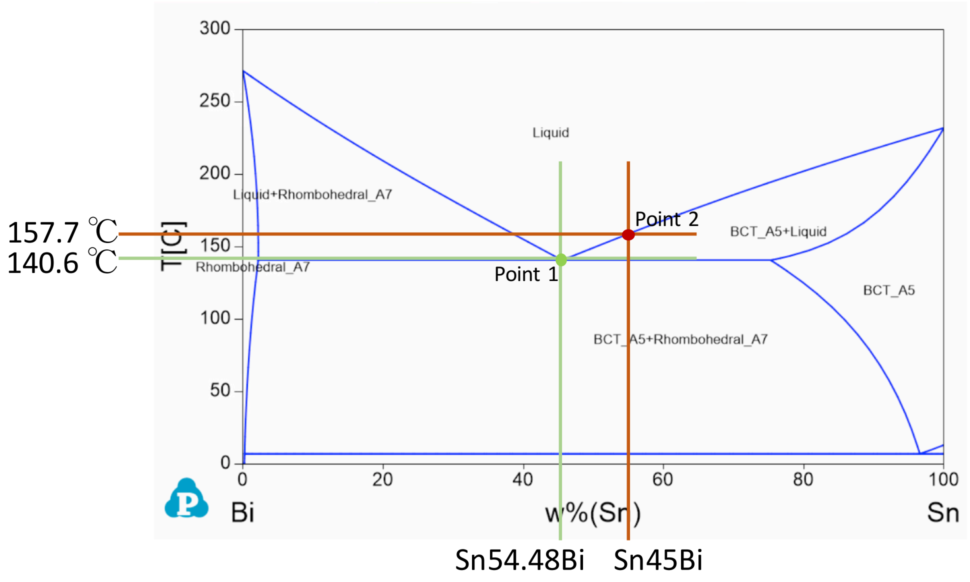

Figure 5-1 Calculated Sn-Bi phase diagram. Point 1 and 2 show the effect of composition on the liquidus temperature of Sm-Bi solder alloy.

5.2 Experimental

5.2.1 Materials

For solder bulk study, Sn-45Bi-2.6Zn alloy was prepared from a eutectic Sn-58Bi alloy bulk (NIHON GENMA MFG. Co. Ltd), a Sn sheet (99.99 %), and a Zn wire (99.99 %) (The Nilaco Co. Ltd). Firstly, precise amounts of the starting materials were melted at 700 °C for 5 h and then quenched in air. Then the compositions of the alloys were tested using ICP-OES, as shown in Table 5-1. The actual composition was Sn45Bi2.6Zn since a little amount of Zn was oxidized during alloying process. Therefore, the following experiments and calculation were based on the Sn45Bi2.6Zn alloy. Prior to casting in a bar-shaped mold, the alloy was remelted at 250 °C for 1 h to ensure good homogeneity. The composition of the alloy was determined to be 52.34 wt.% Sn, 45.04 wt.% Bi, and 2.61 wt.% Zn via ICP-OES. Some of the as-cast bar-shaped alloys were polished for microstructure observation, while others were machined into a dumbbell shape, as shown in Figure 5-2.

For solder joint investigation, ENIG/solder/ENIG sandwich structure was implemented. The schematic illustration of a solder joint was displayed in Figure 5-3(a). The disk-shaped alloy used in this chapter was cut by slicing machine and scissors. Thickness and diameter of a solder disk were controlled to be approximately 0.1 and 5 mm, respectively. ENIG top and bottom substrates used in this study were on each side of the solder disk, making it a

Table 5-1 The chemical composition of the solder alloys.

Solder alloy (wt %)	Sn58Bi	Sn45Bi2.6Zn
Sn	41.45	52.17
Bi	58.54	45.22
Ti	0.00	0.00
Pb	0.00	0.00
Ag	0.00	0.00
Sb	0.00	0.00
Cu	0.00	0.00
Zn	0.00	2.61
Fe	0.00	0.00
Al	0.00	0.06
As	0.00	0.00
Cd	0.00	0.00
In	0.01	0.00
Ni	0.00	0.00
Au	0.00	0.00

ENIG/Solder/ENIG sandwich structure. The main purpose of using this structure is to perform shear tests, which will be explained in detail in the following section. Figure 5-3(b) shows the reflow profile measured using a thermal couple. This profile consisted two phases, i.e., preheat and peaking. Preheat temperature was 100 °C for around 150 seconds, while peak was 182 °C for around 60 seconds. The structure of ENIG substrates used in this study was detailed investigated in the previous [1], in which Au and Ni (P) layers were measured to be 60 nm and 2 μm, respectively.

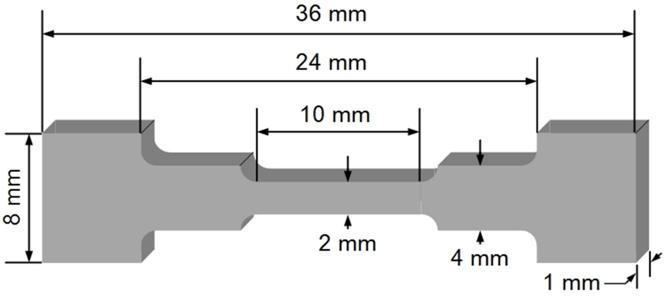

Figure 5-2 Illustration of a tensile test sample.

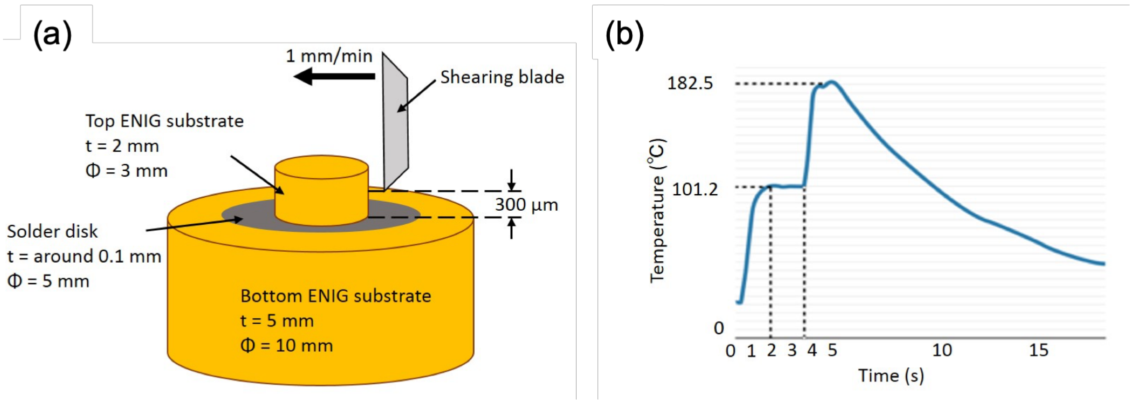

Figure 5-3 Solder joint samples and reflow profile. (a) Schematic illustration of solder joint. (b) Measured reflow profile.

5.2.2 Characterization methods

Differential scanning calorimetry (DSC) was used to determine the thermal behavior and reaction temperatures of the alloys during melting. Alloys samples of approximately 9 mg were sealed in a hermetic aluminum pan and examined under a nitrogen flow. These samples were heated to 170 °C at four different heating rates of 10, 5, 2, and 1 °C/min. Then, the temperature was maintained at 170 °C for 5 min before cooling. The reaction temperatures under equilibrium conditions were then calculated using the estimation method in the study [2]. The cross-sectional microstructures and fracture surfaces of the samples after tensile testing were observed using a field-emission scanning electron microscope (FESEM, Hitachi SU-70) and a JEOL JXA-8530F field-emission electron probe microanalyzer (EPMA). Tensile tests were performed on a Shimadzu Autograph AG-X machine at room temperature (25 °C) at a strain rate of 0.0005/s. Thermodynamic calculations based on the CALPHAD method were performed to obtain an isoplethal section and liquidus projection of the Sn-Bi-Zn ternary system using the PANDAT software with the ADAMIS Solder database [3].

Shear tests were conducted using a Rhesca STR-1000 testing machine at room temperature of 25 ℃. The shearing speed was 1 mm/min and the fly height was 300 μm from the top surface of the bottom substrate, as shown in Figure 5-3(a). Cross-sectional and fracture surface were investigated using SEM and EPMA.

5.3 Characteristic of bulk alloy

5.3.1 Microstructure before aging

Figure 5-4 compares the microstructures of the as-cast eutectic Sn-58Bi alloy and Sn-45Bi-2.6Zn alloy. Eutectic Sn-58Bi alloy was dominated by a eutectic mixture, where bright phase was rhombohedral Bi-rich, and grey phase was body-centered tetragonal Sn-rich. In addition, a very small amount of Sn-rich dendrite decorated with Bi precipitates was observed. Sn-45Bi-2.6Zn alloy showed a significantly higher volume fraction of Sn-rich dendrite than that in eutectic Sn-58Bi alloy. The precipitated grains of the Bi phase were finer than those in eutectic Sn-58Bi alloy. Additionally, a ternary mixture consisting of interlocked Bi-rich, Sn-rich, and dispersed hexagonal close-packed Zn (black contrast grains) were observed. Homogeneously dispersed Zn flakes were observed as well. The microstructure of Sn-45Bi-2.6Zn alloy was significantly finer than that of eutectic Sn-58Bi. The EPMA mapping images in Figure 5-4(c) to (f) produced from the regions indicated in Figure 5-4(b) showed a clear ternary Sn-Bi-Zn ternary structure on the right side, while some Zn phases are observed in Sn-rich phase on the left side.

5.3.2 Solidification behavior

Figure 5-5(a) shows the liquidus projection of Sn-Bi-Zn ternary system with a close-up at the Sn-Bi-rich region, where the isotherms of liquidus surface (thin green and red lines) are

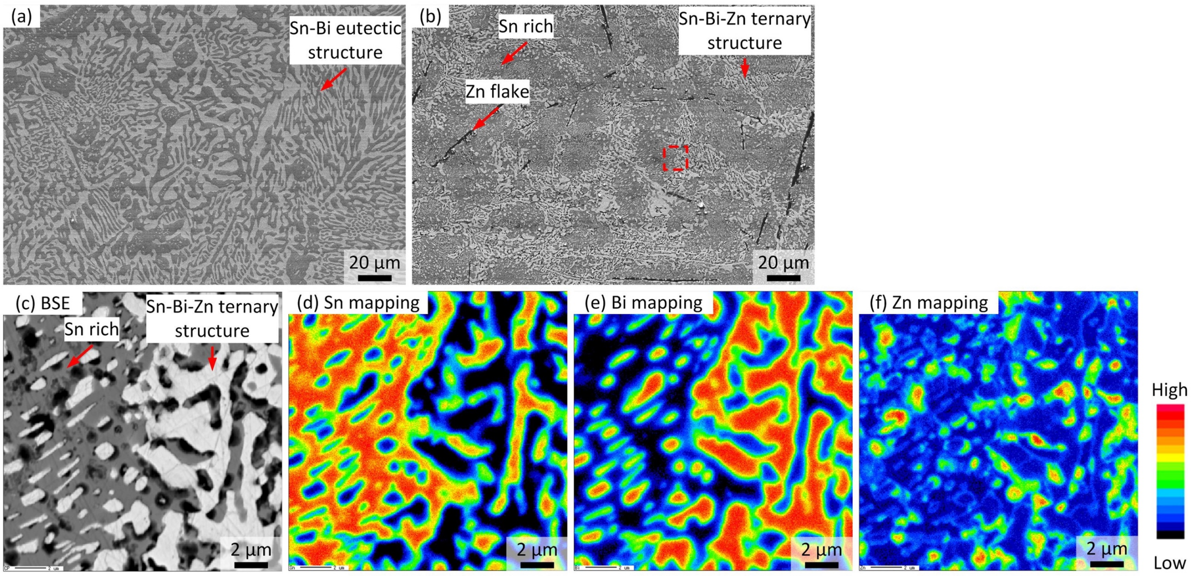

Figure 5-4 Microstructure of alloys before aging. SEM images of (a) eutectic Sn58Bi and (b) Sn45Bi2.6Zn. (c) to (f) are the magnified EPMA mappings of highlighted area in (b).

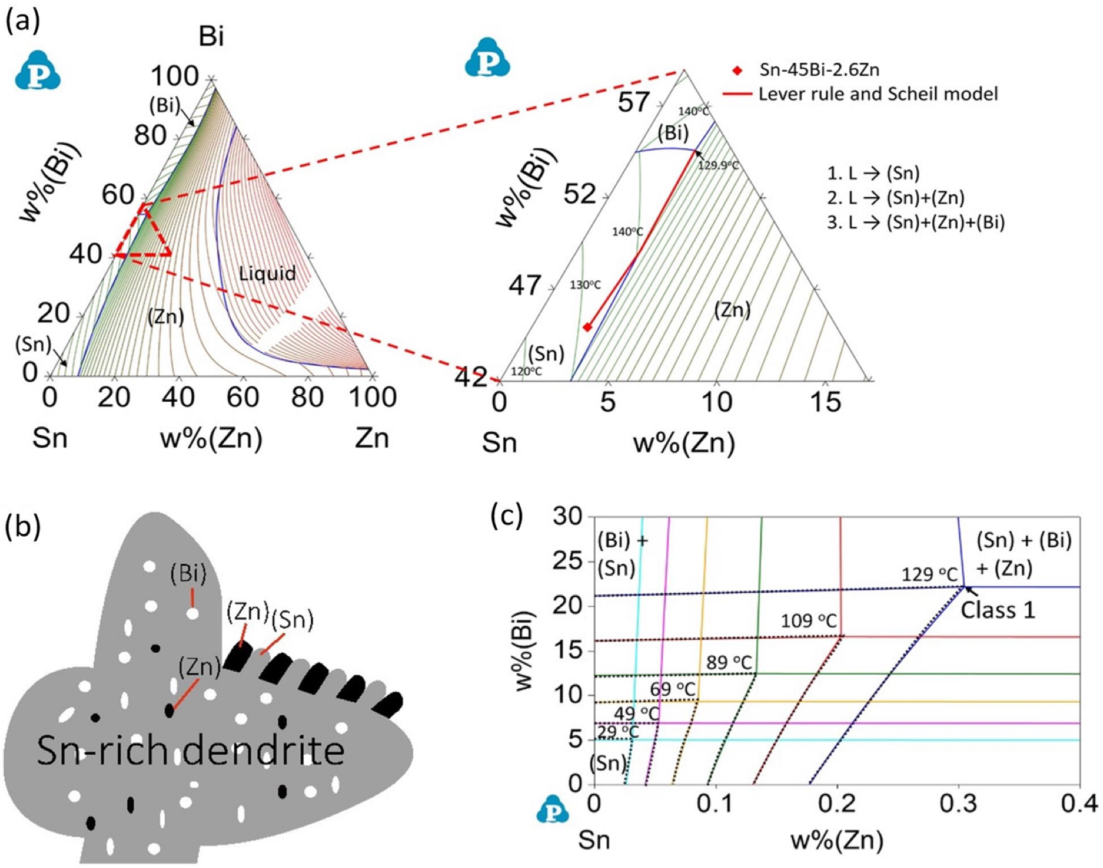

Figure 5-5 Thermal dynamic calculation results, revealing the microstructure formation history. (a) The liquidus projection of the Sn-Bi-Zn ternary system with a close-up at the Sn-Bi-rich region. (b) The calculated isothermal sections with the different temperature at Sn phase rich region. (c) Schematic diagram of Zn and Sn co-precipitation besides Sn-rich dendrite.

expressed with an interval of 10 °C, and the location of Sn-45Bi-2.6Zn alloy is labeled. The calculated solidification paths based on either the lever rule or the Scheil model of the alloy showed the same result was superimposed on the liquidus projection, as shown in Figure 5-5a. The Sn-rich phase was the primary solidification phase, *i.e.*, L → (Sn) reaction, which was observed as the Sn-rich dendrite phase in Figure 5-4(b). This was followed by the precipitation of the Sn phase. The Zn phase subsequently solidified via the L → (Sn) + (Zn) co-precipitation reaction, which was recognized as the Zn-rich flake phase shown in Figure 5-4(b). The appearance of Zn flakes is consistent with the eutectic Sn-9Zn alloy [4], [5]. Moreover, the initial Zn phase solidified in addition to the Sn-rich dendrite phase, which offered sufficient solidified sites as shown in Figure 5-5(b). Finally, solidification completed via the ternary eutectic reaction, namely Class I reaction: L → (Sn) + (Zn) + (Bi). This was evidenced by the presence of the Sn-Bi interlocked structure with small Zn phase dispersed inside, as shown on the right side of Figure 5-4c. Furthermore, as the solute could not easily dissolve in the Bi and

Zn phases in Sn–Bi–Zn system, we calculated isothermal sections with an interval of 20 °C, as shown by the Sn phase rich regions superimposed by colored dash lines shown in Figure 5-5c. This describes the solid phase after the liquid was completely solidified via the Class I reaction (129 °C). The solubility of Zn and Bi in the Sn phase decreased sharply with decreasing temperature. The results are consistent with the observation of small Zn and Bi phases precipitated in the Sn-rich phase (left side of Figure 5-4(c)) owing to the drastically reduced solubility of Zn and Bi in the Sn phase during cooling. Furthermore, this shows that the oversaturated Zn precipitated at the Sn grain boundary and obstructed the phase coarsened effect after thermal aging [6].

The melting temperature is the critical characteristic for low-temperature solder; hence DSC analysis during heating at a rate of 10 °C/min was carried out to investigate the fundamental thermal reaction of the alloys. Figure 5-6(a) shows DSC curves of eutectic Sn-58Bi and Sn-45Bi-2.6Zn alloys after annealing in order to ensure that the non-equilibrium phase was eliminated. For Sn-45Bi-2.6Zn alloy, T_S and T_O are the onset temperatures of peak 1 and 2, respectively, while T_L is the liquidus temperature. The corresponding calculated Sn-45Bi-2.6Zn isoplethal section, which represents the calculated phase boundary lines, is superimposed on the DSC results as shown in Figure 5-6(b). It is known that this alloy passes through three different temperatures to reach the complete liquid state: (1) (Sn) + (Bi) + (Zn) → (Sn) + (Zn) + liquid; (2) (Sn) + (Zn) + liquid → (Sn) + liquid; and (3) (Sn) + liquid → liquid. These experimental results were calculated from DSC curves, as shown in Figure 5-7, obtained under various heating rates using the estimation method mentioned in previous section, as shown in Figure 5-8. The experimental and calculated temperatures of Sn-45Bi-2.6Zn alloy and eutectic Sn-58Bi alloy are listed in Table 5-2. Sn-45Bi-2.6Zn alloy showed a lower solidus

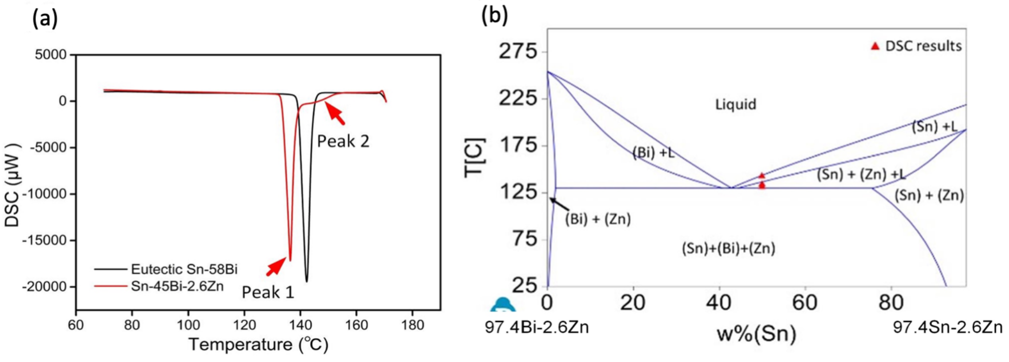

Figure 5-6 Comparing the DSC results with calculated result. (a) DSC curves of the eutectic Sn-58Bi and Sn-45Bi-2.6Zn alloys at the heating rate of 10 °C/min. (b) The calculated Sn-45Bi-2.6Zn isoplethal section superimposed with DSC results.

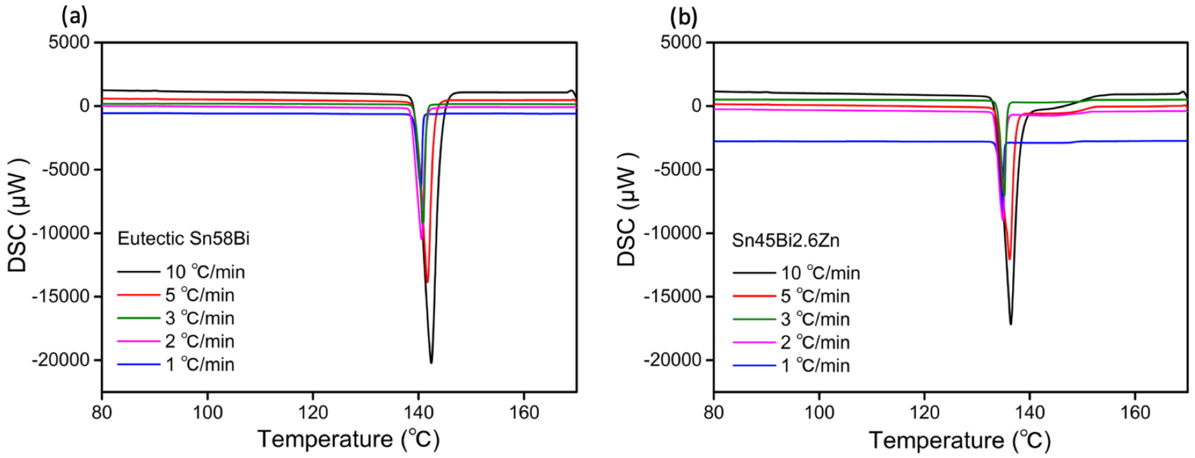

Figure 5-7 DSC curves at different heating rate. (a) Eutectic Sn58Bi; (b) Sn45Bi2.6Zn.

temperature but the higher liquidus temperature than eutectic Sn-58Bi. In addition, the calculated results were in good agreement with the experimental results, apart from a slight deviation (3 °C) in the solidus temperature values.

5.3.3 Microstructure change after aging

Figure 5-9 compares the microstructural change of eutectic Sn-58Bi and Sn-45Bi-2.6Zn alloy after 504 and 1008 h thermal aging. For eutectic Sn-58Bi, microstructure coarsened after 1008 h aging, represented by coarsened Bi grains and increased eutectic spacing. On the other hand, Sn-rich phase with an obvious higher volume fraction than that in eutectic Sn58Bi was obtained in Sn-45Bi-2.6Zn alloy. In addition, no coarsened Bi grain was observed in the Sn-Bi-Zn ternary area after aging. It was assumed that owing to decreased volume fraction of Bi, Sn-45-2.6Zn had much less Bi content than that of eutectic Sn-58Bi, thereby decreasing the possibility of coarsened Bi formation after aging.

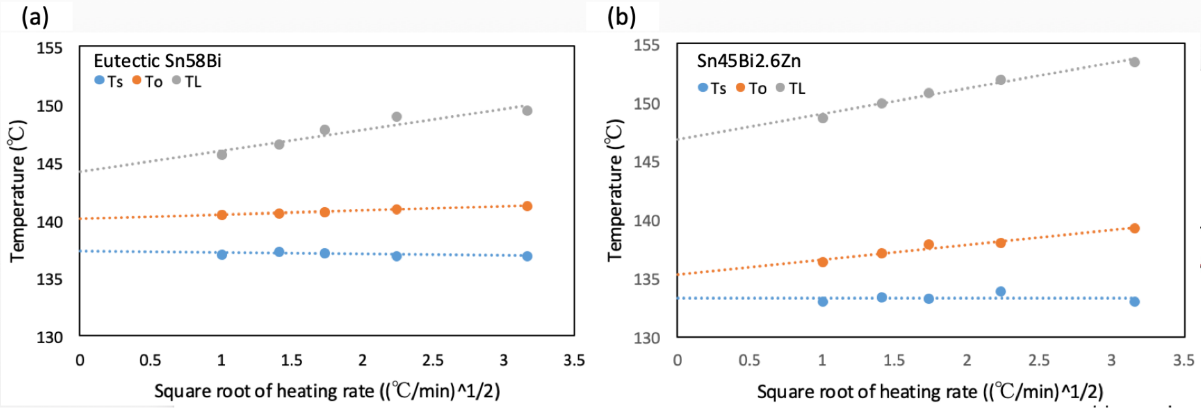

Figure 5-8 Relationship between DSC heating rate and T_S, T_O and T_L of each alloys. (a) Eutectic Sn58Bi; (b) Sn45Bi2.6Zn.

Table 5-2 The melting behavior comparison of calculated and experimental results.

Composition (wt. %)	Calculated (°C)			Experimental (°C)		
	T_S	T_O	T_L	T_S	T_O	T_L
Sn-45Bi-2.6Zn	129.9	139.4	147.9	133.3	135.8	147.1
Sn-58Bi	-	-	-	137.1	140.3	144.5

5.3.4 Tensile test

Figure 5-10 shows the SS curves of eutectic Sn-58Bi and Sn-45Bi-2.6Zn alloys during tensile tests and the mechanical properties change after thermal aging. Sn-45Bi-2.6Zn alloy showed an elongation more than double that of eutectic Sn-58Bi alloy was obtained. Simultaneously, the UTS increased (from 48 to 53 MPa). Moreover, Figure 5-11 shows the side views of fractured samples. Almost no plastic deformation was observed in eutectic Sn58Bi sample, while Sn45Bi2.6Zn deformed plastically significantly, indicating ductility of

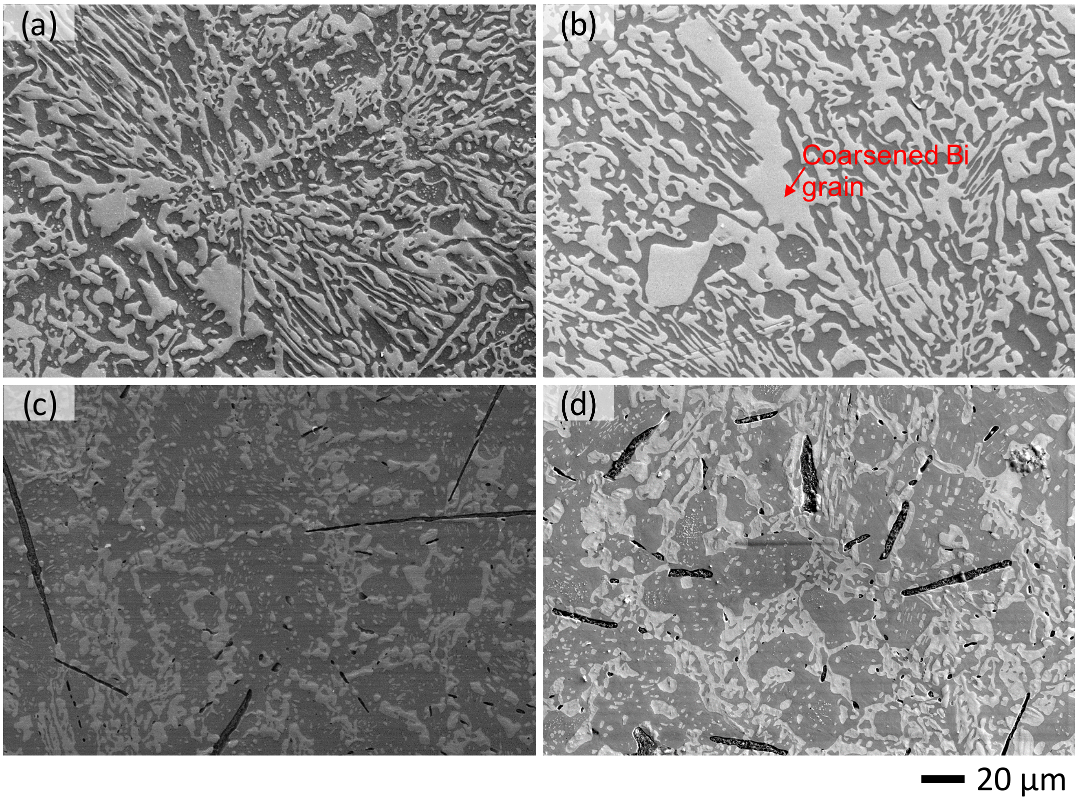

Figure 5-9 FE-SEM images. (a) and (b): eutectic Sn58Bi alloy aged 504 and 1008 h, respectively. (c) and (d) Sn45Bi2.6Zn alloy aged 405 and 1008 h, respectively.

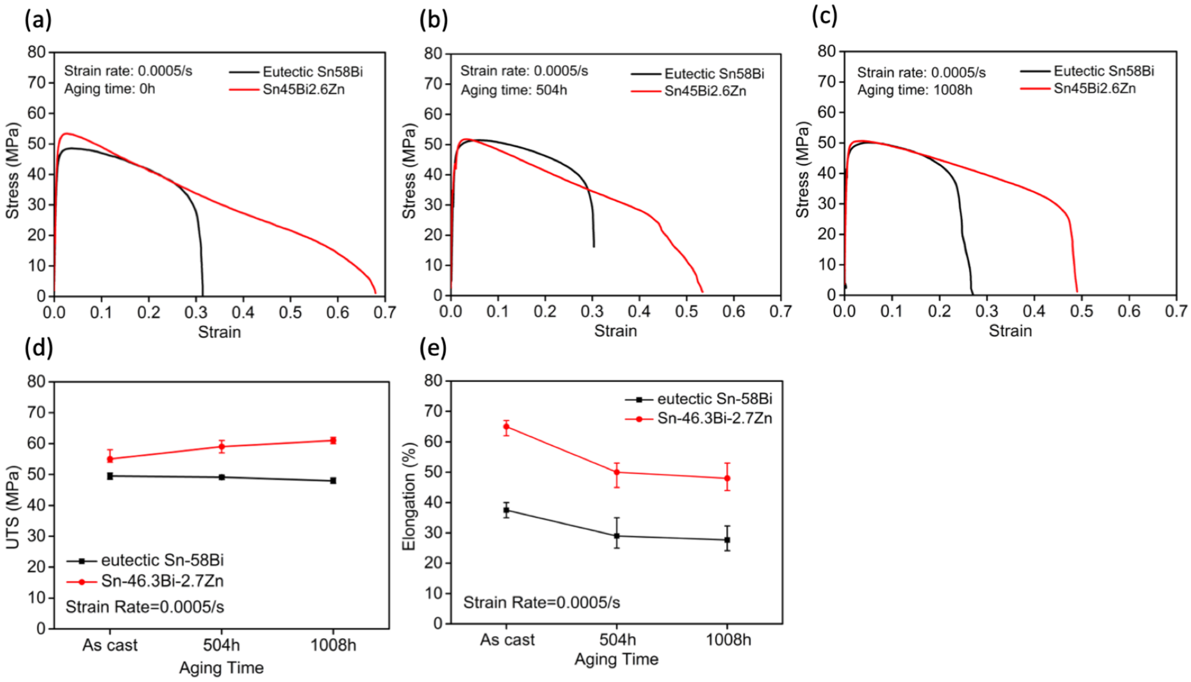

Figure 5-10 Mechanical property of tested alloys. (a) Representative SS curves before aging. (b) Elongation change during aging. (c) UTS change during aging.

Sn45Bi2.6Zn alloy was higher than that of eutectic Sn58Bi. Figure 5-12 shows the fracture morphology of the tested alloys. In the side views (Figure 5-12(a) and (d)), a mainly brittle fracture in Sn-58Bi alloy was observed, while Sn-45Bi-2.6Zn showed obvious necking before fracture. In the top views of the fractured area (Figure 5-12(b) and (e)), an obvious Sn-Bi eutectic structure was observed (Sn phase in grey contrast, while Bi phase in white contrast), indicating that the fracture path was on a flat plane, where the crack passed through the eutectic phase without any plastic deformation. Moreover, Bi and Sn phase showed cleavage and bulge fracture mode, respectively. In contrast, rough fracture surfaces were observed in Sn-45Bi-2.6Zn alloy, indicating an overall bulge fracture mode. Additionally, almost no cleavage fractured Bi phase was observed, owing to the lower Bi content and finer microstructure in the new alloy. Similar fracture morphologies of the Sn and Bi phases were also reported in other

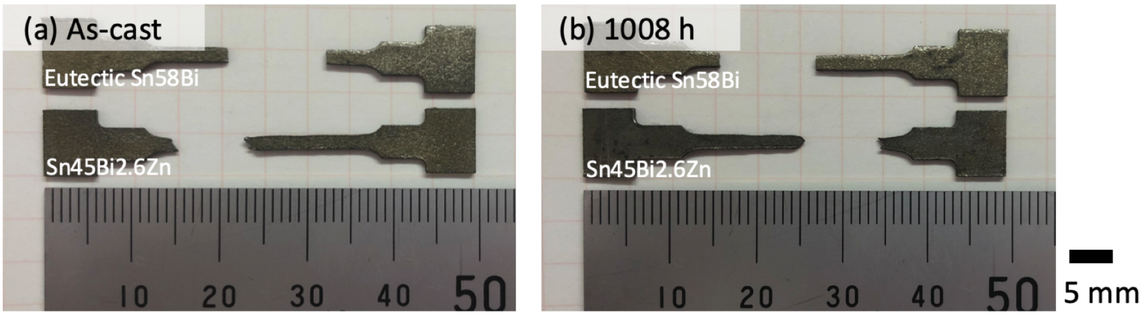

Figure 5-11 FE-SEM images of side views of tensile fracture surfaces.

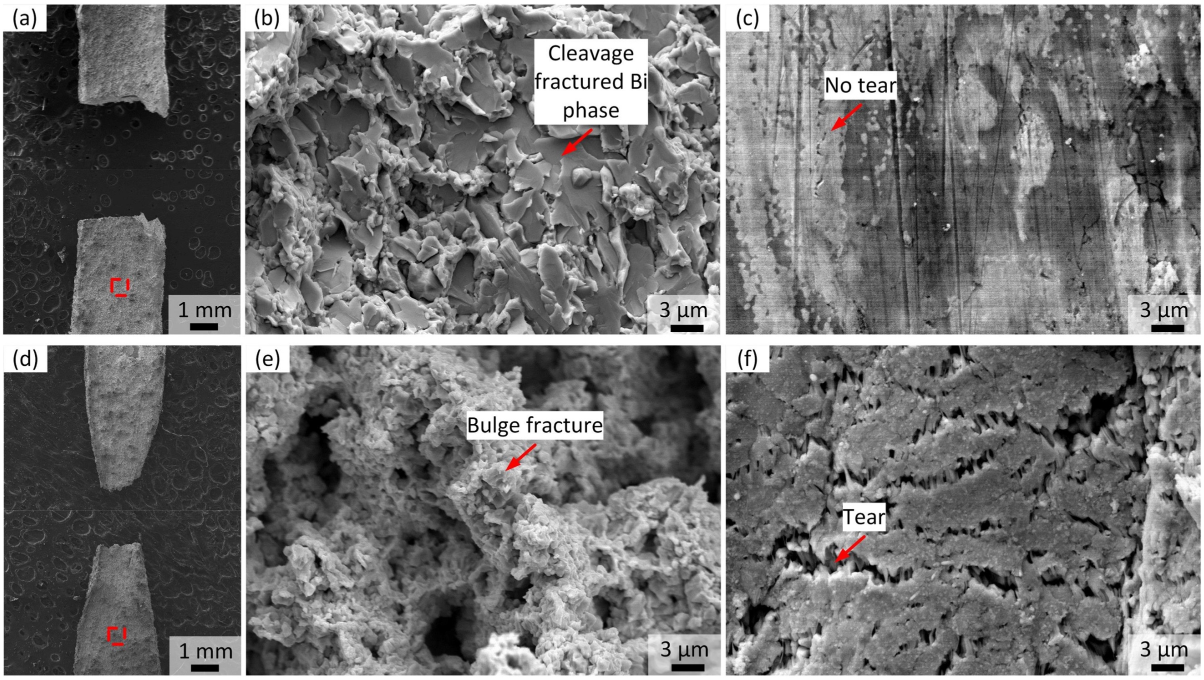

Figure 5-12 FE-SEM fracture morphology images of tensile tested samples, showing two different fracture modes. (a, b) low-magnification side-views of fractured Sn-58Bi and Sn-45Bi-2.6Zn alloys, respectively. (b, e) high-magnification top-view of these fractured samples. (c, f) high-magnification side-view of these fractured samples.

studies [6]–[8]. Figure 5-12(c) and (f) show high-magnification side views of the areas indicated in Figure 5-12(a) and (d), respectively. A large number of tears was observed on the surface of post-test Sn-45Bi-2.6Zn samples, where the ductile fractured structure was clearly observed. However, eutectic Sn-58Bi alloy showed a rather smooth sample side surface without any tearing after fracture. It is noted that the Sn phase normally fractures in the ductile mode, while Bi shows cleavage fracture [7], [8]. Therefore, under the same strain rate, different fracture modes observed in these two alloys, induced by the drastically different microstructures. Sn-45Bi-2.6Zn alloy has a very fine microstructure consisting of a large area fraction of Sn-rich phase and a fine Sn-Bi-Zn ternary structure. On the other hand, we observed a Sn-Bi eutectic structure with a relatively larger eutectic spacing in eutectic Sn-58Bi than in the case of Sn-45Bi-2.6Zn alloy. Since eutectic Sn-Bi structure has a low fracture energy compared with the Sn-rich phase [7], the improved toughness of Sn-45Bi-2.6Zn alloy seems reasonable.

Moreover, Figure 5-13 reveals the fracture morphology of the tested alloys after 1008 h aging. In the top views of the fracture point, an obvious Sn-Bi eutectic structure was observed, indicating that the fracture path was on a flat plane where passed through a eutectic phase without any plastic deformation. Moreover, cleavage fractured Bi phase was observed. In contrast, rough fracture surfaces in the Sn-46.3Bi-2.7Zn alloy, indicating a bulge fracture mode,

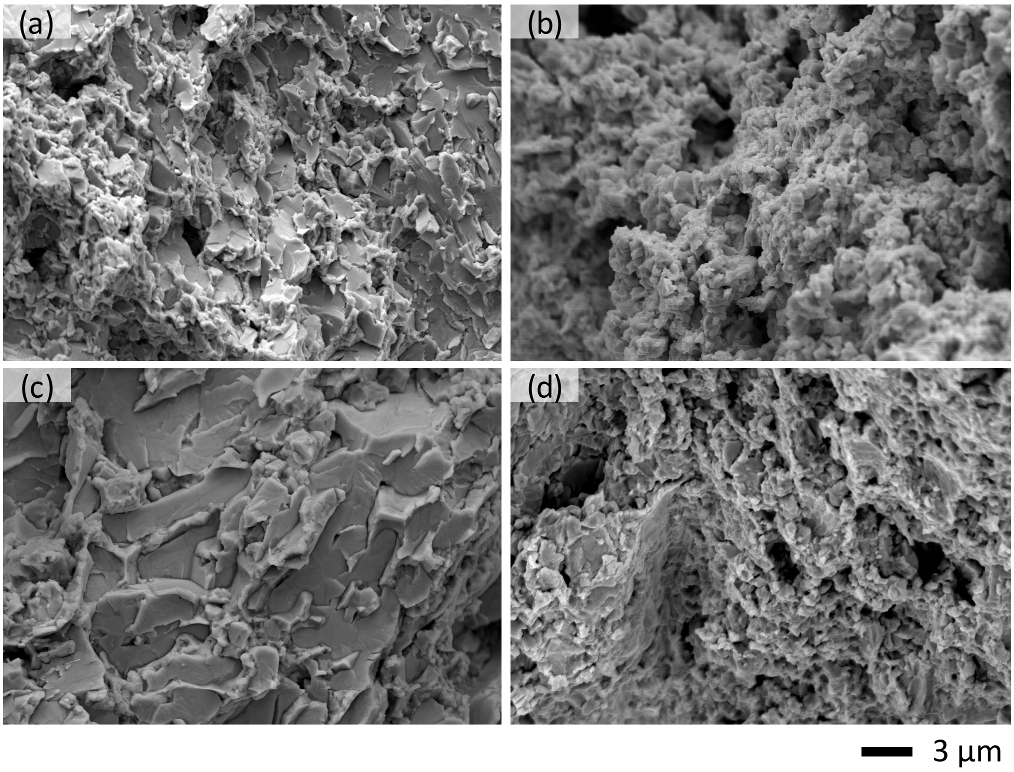

Figure 5-13 Top-view FE-SEM images fracture surfaces. (a) and (c) eutectic Sn58Bi after 504 and 1008 h aging, respectively. (b) and (d) Sn45Bi2.6Zn after 504 and 1008 h aging, respectively.

was observed. Additionally, almost no cleavage fractured Bi phase was observed, owing to the decreased Bi content in this new alloySn-46.3Bi-2.7Zn alloy has very fine microstructure which consists of a large area fraction of Sn-rich phase and a fine Sn-Bi-Zn ternary structure. On the other hand, there is a Sn-Bi eutectic structure with relatively larger eutectic spacing in eutectic Sn-58Bi than that in the Sn-46.3Bi-2.7Zn alloy.

After aging, due to the microstructure coarsening of both tested alloys, elongation decrease was detected for both alloy. However, due to the significant elongation improvement of Sn-45Bi-2.6Zn over eutectic Sn-58Bi before aging, the elongation of Sn-45Bi-2.6Zn was still superior. Additionally, fracture morphology was almost the same for Sn-45Bi-2.6Zn before and after aging, indicating the fine microstructure. By contrast, cleavage fractured Bi became much easier to distinguish in aged eutectic Sn-58Bi, as well as increase of eutectic spacing was observed, indicating coarsened microstructure.

5.4 ENIG/alloy/ENIG joint

5.4.1 Wettability of alloy on ENIG

In order to verify the solderability of the Sn45Bi2.6Zn alloy, wettability of this alloy was tested on a SEM and a 3D laser microscopy (VK-9710). As shown in Figure 5-14 and 5-15. Figure 5-14(a) presents the representative (Optical microscopy) OM images and corresponding laser mapping images of eutectic Sn58Bi/ENIG and Sn45Bi2.6Zn/ENIG, respectively. Average wetting angles were measured to be 19.8 ° and 21.6 ° for eutectic Sn58Bi and Sn45Bi2.6Zn, respectively. The angle difference between these two alloys were almost the same. Figure 5-15 shows the cross-sectional SEM images of eutectic Sn58Bi and Sn45Bi2.6Zn joints. Sound joints was obtained for both solder alloys. The results in Figure 5-14 and 5-15 indicate the solderability of new Sn45Bi2.6Zn was comparable to the eutectic Sn58Bi.

5.4.2 Interfacial reaction before thermal aging

Figure 5-16 shows the EPMA mappings of solder/ENIG interfacial regions. The interfacial layer of eutectic Sn58Bi/ENIG was discussed in the previous sections. The interfacial layer for Sn45Bi2.6Zn/ENIG was displayed in Figure 5-16(b). A very thin IMC layer was observed on the interface. EPMA point analysis indicated the composition of this IMC layer was $AuZn_3$, as shown in point 1 in Table 5-3. Additionally, no Sn was involved in the interfacial reaction. It is noted that the same $AuZn_3$ IMC layer was obtained on the Sn58Bi1Zn/ENIG interface, which have been discussed in the Chapter 3. However, on Sn58Bi1Zn/ENIG interface, detached $AuZn_3$ IMC layer was observed and, on top of the Ni(P) layer, a very thin Au-Zn-Ni-Sn was observed. The different morphology of $AuZn_3$ IMC layers on Sn58Bi1Zn/ENIG and Sn45Bi2.6Zn/ENIG was still unknown. However, this phenomenon could be contributed to the different composition of solder alloys.

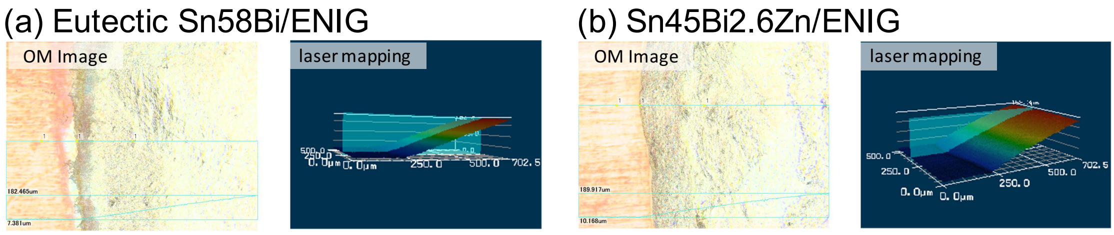
(a) Eutectic Sn58Bi/ENIG

(b) Sn45Bi2.6Zn/ENIG

(c) Wetting angles

Composition (wt %)	Average wetting angle (°)
Sn58Bi	15.8
Sn45Bi2.6Zn	16.6

Figure 5-14 Wetting angle measurement.

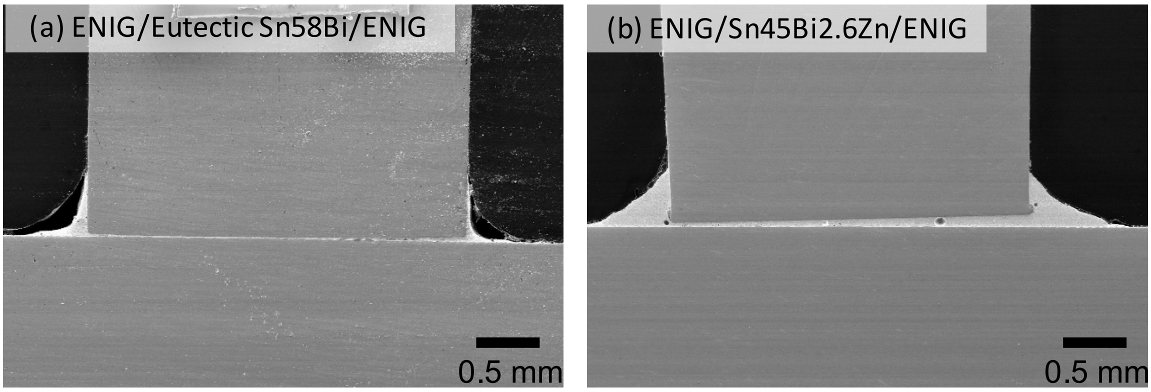

Figure 5-15 Cross-sectional FE-SEM images of solder joints, showing the condition of joints.

5.4.3 Effect of thermal aging on interfacial IMC layers

Figure 5-17 compares the solder/ENIG interfacial IMC layer growth behaviors of two tested alloys. As discussed in the Chapter 3, two IMC layers, i.e. Ni_3Sn_4 and $(Au, Ni)(Sn, Bi)_4$ structure was observed on eutectic Sn58Bi/ENIG interface after 1008 h aging. On the other hand, the morphology of $AuZn_3$ IMC layer on Sn45Bi2.6Zn/ENIG interface remained unchanged after 1008 h aging, compared with the result before aging. The composition of the $AuZn_3$ IMC layer after 1008 h was identified as point 2 in Table 5-3. Figure 5-18 shows the EPMA mappings of the Sn45Bi2.6Zn/ENIG interface after 1008 h aging. The result was very much identical to that in Figure 5-17(b). This result indicated that $AuZn_3$ IMC layer did not growth its thickness during thermal aging, since the amount of Au and Zn in ENIG/Sn45Bi2.6Zn/ENIG joint were limited and they were assumed mostly consumed during reflow process. Figure 5-19 shows the IMC layer thickness change of tested solder joints. Eutectic Sn58Bi joints experienced continuous IMC layer growth from approximately 0.5 μm before aging to around 1.1 μm after 1008 h aging. By contrast, the Sn45Bi2.6Zn joints had a stable $AuZn_3$ IMC layer and its thickness remained unchanged during aging (approximately 0.3 μm).

5.4.4 Fracture surfaces and shear test

Figure 5-20 and 5-21 show the top and bottom fracture surfaces of eutectic Sn58Bi joints and Sn45Bi2.6Zn joints before and after thermal aging. As discussed in Chapter 2, fracture path for eutectic Sn58Bi joints changed from within solder bulk to partially inside IMC layer and Ni(P) layer due to the IMC layer growth. On the other hand, no sign of Ni and P was

(a) Eutectic Sn58Bi/ENIG

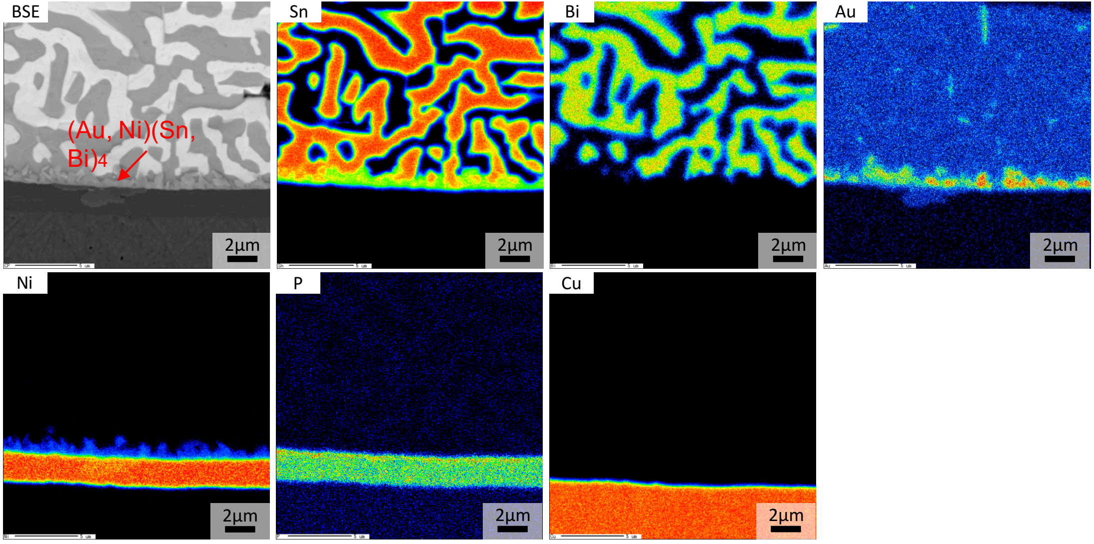

(b) Sn45Bi2.6Zn/ENIG

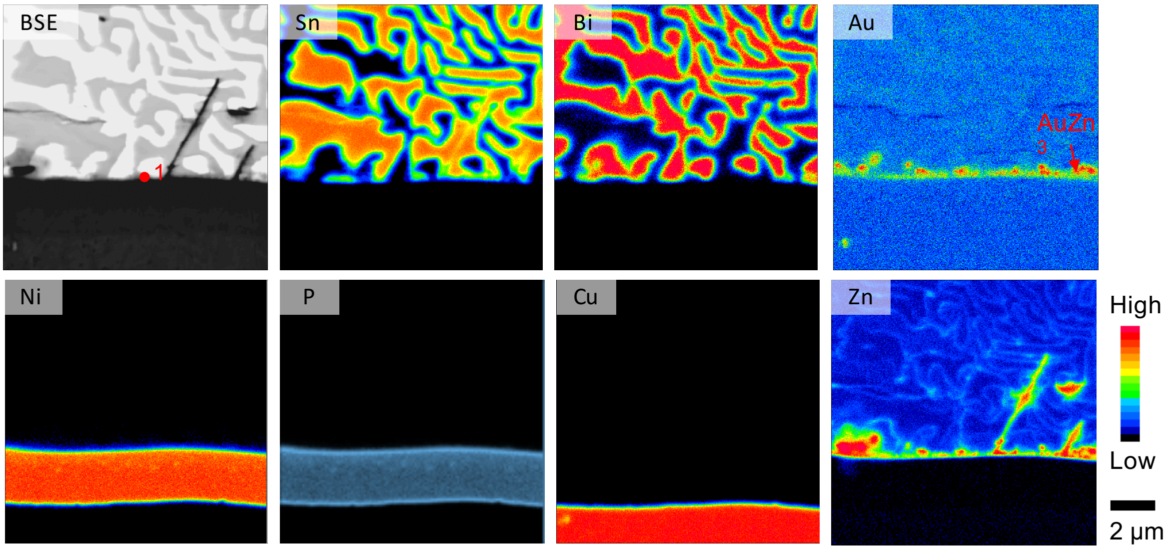

Figure 5-16 EPMA mappings of (a) eutectic Sn58Bi/ENIG interface and (b) Sn45Bi2.6Zn/ENIG interface before aging.

observed in fracture surfaces of Sn45Bi2.6Zn joints. Moreover, Au was barely detected as well. The results indicate the fracture path was remained inside solder bulk both before and after thermal aging.

Shear strength results were shown in Figure 5-22. Shear strength of Sn45Bi2.6Zn remained unchanged at approximately 55 MPa both before and after 1008 h aging. This was attributed to the thin and stable $AuZn_3$ IMC layer at the solder/ENIG interface. On the other hand, thick IMC layer induced shear strength decrease of eutectic Sn58Bi joints after 1008 h aging.

There was an interesting point should be noted. In Chapter 3, $AuZn_3$ IMC layer detached into separate pieces in Sn58Bi1Zn joints, while on Sn45Bi2.6Zn/ENIG interface, $AuZn_3$ IMC

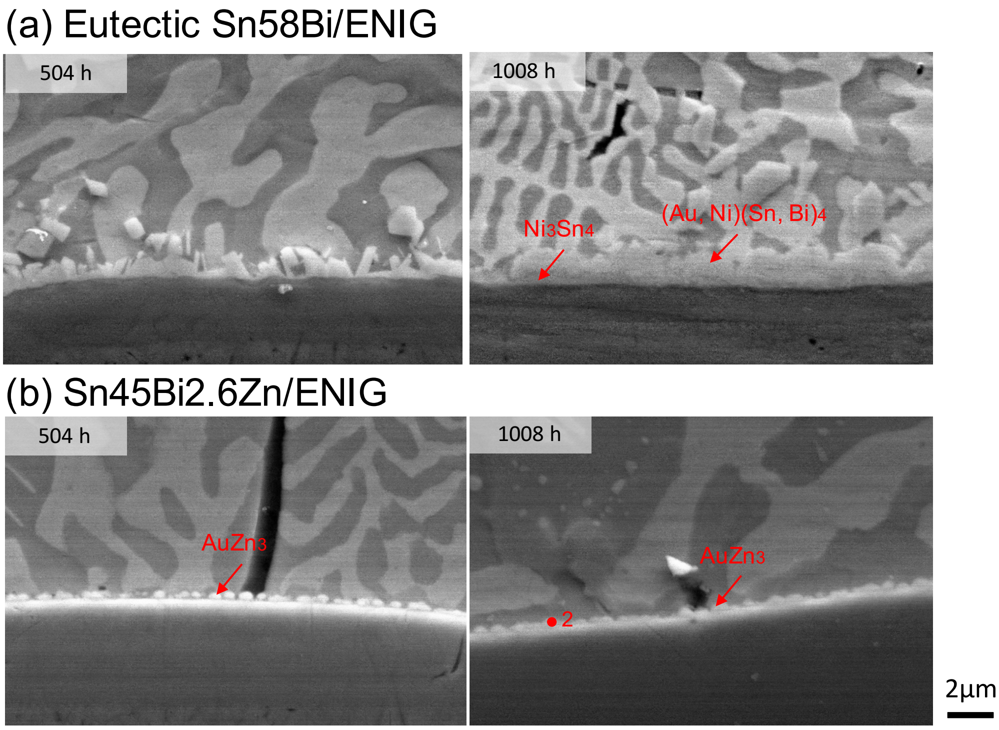

Figure 5-17 FE-SEM images of after aged (a) eutectic Sn58Bi/ENIG interface and (b) Sn45Bi2.6Zn/ENIG interface.

layer did not detach from the substrate. The reason is still unknown, however, it should be associated with the composition difference of the solder alloys.

Conclusion

For solder bulk study, due to the simultaneous increase in the ductility and UTS of the newly designed Sn-45Bi-2.6Zn alloy, it is considered a promising low-temperature alloy to replace eutectic Sn-58Bi alloy.

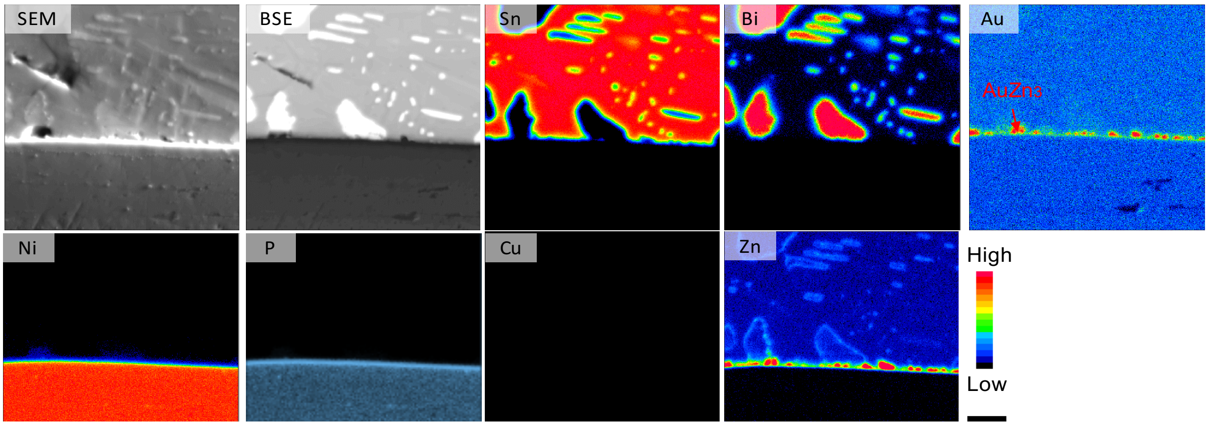

Figure 5-18 EMPA mappings of Sn45Bi2.6Zn/ENIG interface after 1008 h thermal aging.

Table 5-3 EPMA elemental-point analyses at various locations shown in the SEM images (locations are indicated by red dots and numbers).

Location	IMC type	Composition (at.%)				
		Sn	Bi	Ni	Zn	Au
Figure 5-12, point 1	$AuZn_3$	0.1	0	0.5	72.4	27.0
Figure 5-13, point 2	$AuZn_3$	0.3	0.1	0	70.4	29.2

In Sn-45Bi-2.6Zn alloy, a very fine cross-sectional microstructure, Sn-Bi-Zn ternary structure, and higher volume fraction of Sn-rich phase compared to the eutectic Sn-58Bi alloy were observed. Thermodynamic calculations revealed the solidification reaction sequence of the Sn-45Bi-2.6Zn alloy. The reaction temperatures were comparable to those measured by DSC. Meanwhile, the reaction sequence was verified by the cross-sectional microstructure.

The 112% increase in elongation of Sn-45Bi-2.6Zn alloy compared to eutectic Sn-58Bi was attributed to the higher Sn-to-Bi volume ratio.

For solder joint study, sound ENIG/Sn45Bi2.6Zn/ENIG sandwich structure solder joints were obtained by using the same reflow profile of eutectic Sn58Bi solder alloy. A thin and thermally stable AuZn3 IMC layer formed on the Sn45Bi2.6Zn/ENIG interface. As a result, shear strength remained almost unchanged after aging for 1008 h.

Reference

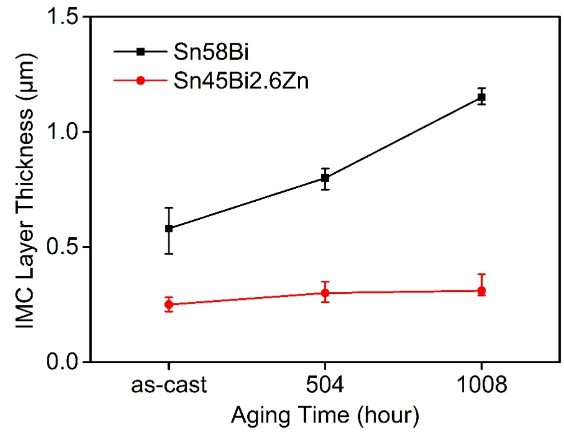

Figure 5-19 IMC thickness change of tested solder joints.

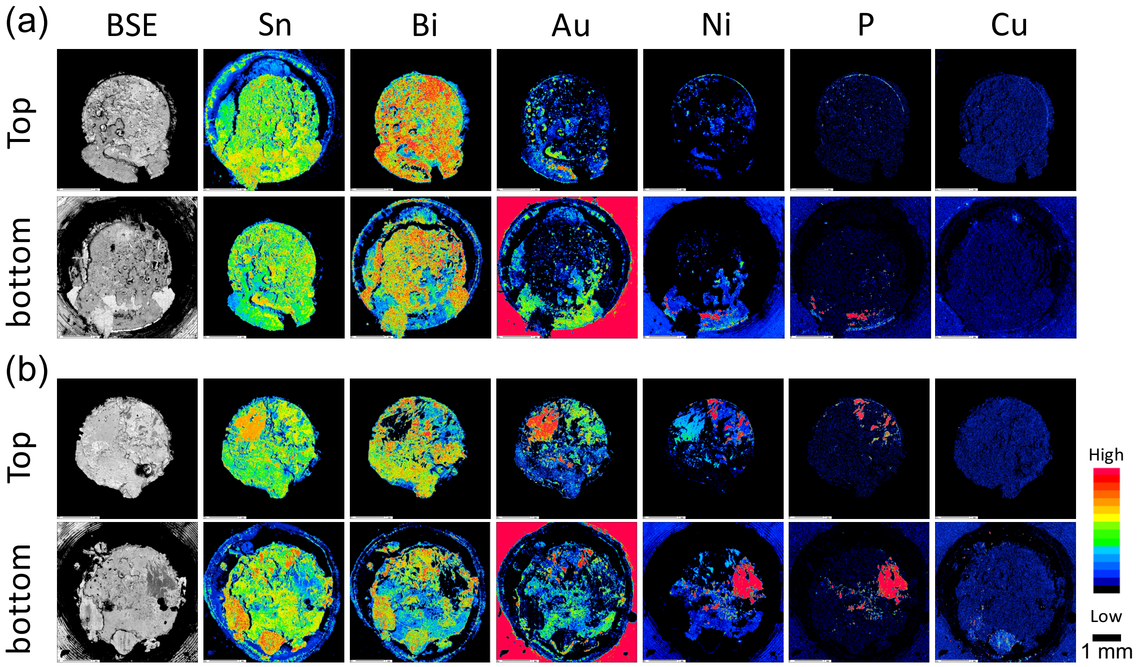

Figure 5-20 EPMA mappings of fracture surfaces of eutectic Sn58Bi joints. (a) before aging and (b) after 1008 h aging.

[1] M.-S. Kim and H. Nishikawa, "Transmission electron microscopy investigation on the Oxidation behavior of Electroless Ni/Immersion Au surface finish at 250 C," *J. Nanosci. Nanotechnol.*, vol. 17, no. 11, pp. 8522–8527, 2017.

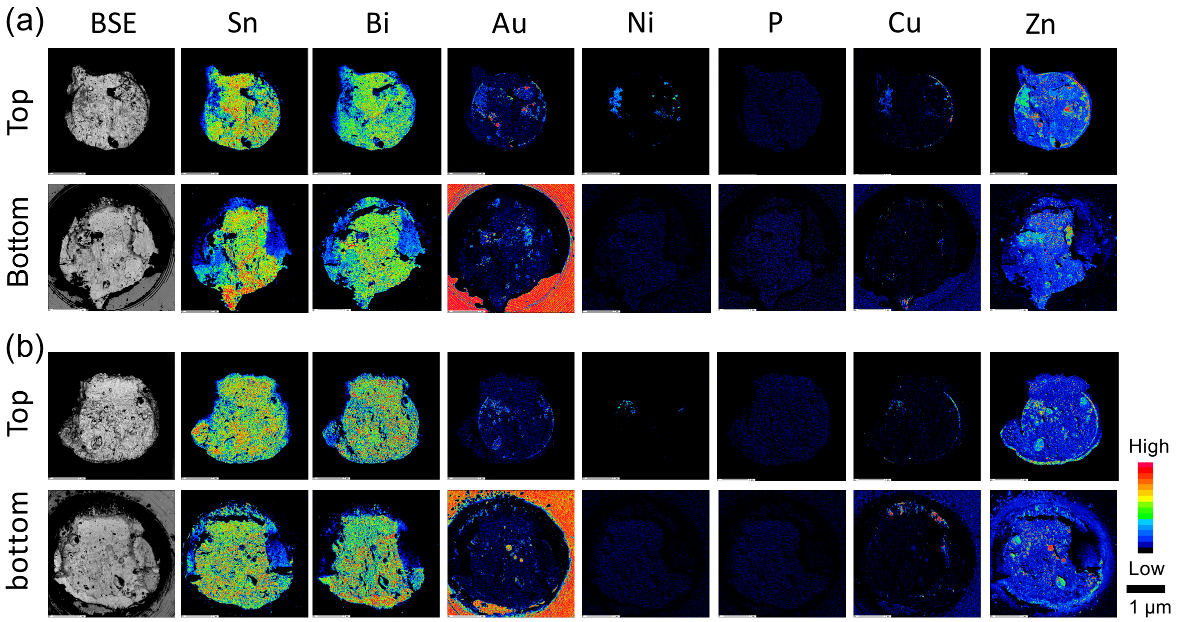

Figure 5-21 EPMA mappings of fracture surfaces of Sn45Bi2.6Zn joints. (a) before aging and (b) after 1008 h aging.

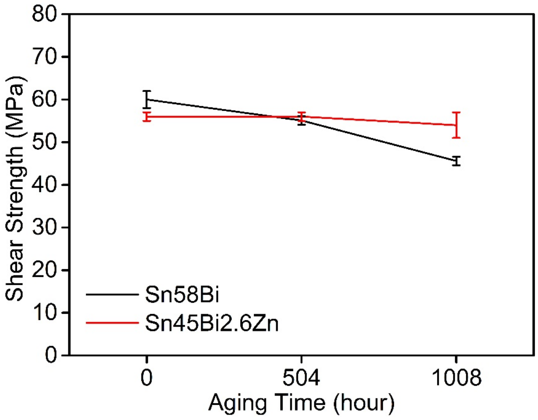

Figure 5-22 Shear strengths of tested solder joints.

[2] H. Nishikawa, Y. Hamada, and T. Takemoto, “Estimation method for liquidus temperature of lead-free solder using differential scanning calorimetry profiles,” *J. Electron. Mater.*, vol. 38, no. 12, p. 2610, 2009.

[3] W. Cao *et al.*, “PANDAT software with PanEngine, PanOptimizer and PanPrecipitation for multi-component phase diagram calculation and materials property simulation,” *Calphad*, vol. 33, no. 2, pp. 328–342, 2009.

[4] R. A. Islam, B. Y. Wu, M. O. Alam, Y. C. Chan, and W. Jillek, “Investigations on microhardness of Sn–Zn based lead-free solder alloys as replacement of Sn–Pb solder,” *J. Alloys Compd.*, vol. 392, no. 1–2, pp. 149–158, 2005.

[5] K. Suganuma, T. Murata, H. Noguchi, and Y. Toyoda, “Heat resistance of Sn-9Zn solder/Cu interface with or without coating,” *J. Mater. Res.*, vol. 15, no. 4, pp. 884–891, 2000.

[6] S. Zhou, O. Mokhtari, M. G. Rafique, V. C. Shunmugasamy, B. Mansoor, and H. Nishikawa, “Improvement in the mechanical properties of eutectic Sn58Bi alloy by 0.5 and 1 wt.% Zn addition before and after thermal aging,” *J. Alloys Compd.*, 2018.

[7] Z. Lai and D. Ye, “Microstructure and fracture behavior of non eutectic Sn–Bi solder alloys,” *J. Mater. Sci. Mater. Electron.*, vol. 27, no. 4, pp. 3182–3192, 2016.

[8] J. Shen, Y. Pu, H. Yin, D. Luo, and J. Chen, “Effects of minor Cu and Zn additions on the thermal, microstructure and tensile properties of Sn-Bi-based solder alloys,” *J. Alloys Compd.*, vol. 614, pp. 63–70, 2014.

Chapter 6

Conclusion and future work

6.1 Summary

In this thesis, the author designed several new solder alloys based on eutectic Sn58Bi alloy. The motivation was to overcome some issues of eutectic Sn58Bi alloy, including phase coarsening, brittleness and rapid IMC growth on the solder/ENIG substrate. By alloying minor elements into eutectic Sn58Bi alloy, Sn58Bi0.5Ti, Sn58Bi1Ti, Sn58Bi0.5Zn, Sn58Bi1Zn, and Sn58Bi0.5In1Zn were designed. In addition, by implementing thermodynamic calculation using CALPHAD method, Sn45Bi2.6Zn was designed to achieve reduced Bi content and low melting temperature. Tensile tests and nanoindentation were conducted to reveal the correlation between mechanical properties of macroscopic solder bulk and microcosmic individual phase. ENIG/solder/ENIG sandwich solder joints were made and the shear strengths were tested. The evolution of solder bulk microstructure and solder/ENIG interfacial IMC layer were studied before and after aging.

In Chapter 2, The effects of the Ti addition on the microstructures and tensile properties of eutectic Sn58Bi alloys were investigated before and after thermal aging.

For solder bulk, compositional characterizations and thermodynamic analyses show that in addition to the large Ti_6Sn_5 IMCs, a large amount of Ti_2Sn_3 IMCs of two particle sizes are uniformly dispersed in the Ti added Sn58Bi alloy matrices. During thermal aging, these IMCs remained in their original morphologies and stabilized the grain structure of the solder matrix.

The pre-existing Ti_6Sn_5 inclusions suppressed the undercooling of the Ti added Sn58Bi alloys during re-melting (or reflow) process because they served as the heterogeneous nucleation sites in the matrix during solidification. The UTS and YS of Ti added Sn58Bi solders increased with increasing Ti content and remained constant during thermal aging. The elongation of Sn58Bi0.5Ti remained almost unchanged during thermal aging and surpassed the eutectic Sn58Bi after 1008 h aging. The fracture path of eutectic Sn58Bi during aging changed from in the eutectic cell to mainly in the Bi-rich phase, while no clear fracture morphology change was observed in the Ti added samples.

The tested electrical resistivity of the eutectic Sn58Bi alloy was verified by the resistivity mixture rule. On the other hand, the lower electrical resistivity of Ti added Sn58Bi alloy was obtained.

For solder joints, (Au, Ni)(Sn, Bi)4 was observed on both the eutectic Sn58Bi/ENIG and Sn58Bi0.5Ti/ENIG interfaces before aging. After 1008 h thermal aging, another Ni3Sn4 IMC layer formed underneath the (Au, Ni)(Sn, Bi)4 layer on eutectic Sn58Bi/ENIG interface, while no change for Sn58Bi0.5Ti/ENIG interface. The IMC layer thickness for Sn58Bi0.5ti joint was much lower than that of eutectic Sn58Bi joint after 1008 h thermal aging (0.6 vs 1.2 μm). We assumed the Ti solid solutes in solder matrix was responsible to the IMC layer suppression. Owing to the suppressed IMC layer on the Sn58Bi0.5Ti/ENIG interface during thermal aging, fracture occurred inside the Sn58Bi0.5Ti solder bulk but not IMC layer. On the other hand, fracture pathed through IMC layer and Ni(P) layer on eutectic Sn58Bi/ENIG interface due to the growth of the IMC layer. Shear strength of Sn58Bi0.5Ti joints was higher than that of eutectic Sn58Bi joints, although both of them experienced strength decrease during aging. Ti-Sn IMCs distributed inside the Sn58Bi0.5Ti solder acted as a strengthening phase and increased the shear strength.

In Chapter 3, the effects of the microstructure and the mechanical properties induced by 0.5 and 1 wt.% Zn addition in the eutectic Sn58Bi alloy were studied. A new method of how to refine the eutectic Sn58Bi alloy microstructure was proposed.

For solder bulk, both 0.5 and 1 wt.% Zn effectively refined the eutectic Sn58Bi alloy microstructure. Before aging, Zn atoms can act as extra solidification sites and result in a refined microstructure. During aging, Zn atoms were found to move from the solid solution within both the Sn and Bi phases to the Sn–Bi phase boundaries as a Zn segregation, which was believed to suppress the microstructure from coarsening. A significant hardness decrease of the Sn phase was observed in the Sn58Bi1Zn sample. And a potential SSS phenomenon of 1 wt.% Zn solid solution in the Sn phase was proposed. The improved mechanical properties, i.e., elongation and UTS were obtained both before and after thermal aging by conducting the tensile test. The microstructure refinement and the potential SSS were responsible for these improvements. In addition, the fracture surfaces showed a mainly ductile fracture in the Zn-added samples and a brittle fracture in the eutectic Sn58Bi samples, especially after 1008 h thermal aging.

For solder joint, the interfacial reaction and shear strength of eutectic Sn58Bi and 1 wt.% Zn-added Sn58Bi solder on ENIG substrates during solid-state thermal aging were investigated in section 3.4. Interfacial IMC layer formation and growth of the two solder materials were characterized to understand the observed variations in the shear strength before and after aging. The (Au, Ni)(Sn, Bi)$_4$ IMC layer formed on the eutectic Sn58Bi/ENIG interface after reflow. Then, a Ni_3Sn_4 IMC layer was observed underneath the (Au, Ni)(Sn, Bi)$_4$ IMC layer after 504 h of aging. For Sn58Bi1Zn solder joints, the $AuZn_3$ IMC formed and then detached from the Sn58Bi1Zn/ENIG interface after reflow. After detachment, a very thin Au-Zn-Ni-Sn IMC layer was observed on the Sn58Bi1Zn/ENIG interface. The thickness of this IMC layer stayed constant during aging. The shear strength of eutectic Sn58Bi joints decreased after aging, due to increased IMC layer thickness and Ni_3Sn_4 IMC layer formation. By contrast, Sn58Bi1Zn joints had a stable shear strength during thermal aging due to the stable IMC layer structure. Fracture paths were revealed by EPMA mapping. Fracture path in eutectic Sn58Bi joints changed from within the solder bulk to partially within the IMC and Ni(P) layers. However, fracture paths stayed inside the solder bulk for Sn58Bi1Zn joints after aging. We hypothesize that the very thin Au-Zn-Ni-Sn IMC layer on the Sn58Bi1Zn/ENIG interface was crucial for suppressing IMC layer growth and stabilizing the shear strength during aging.

In Chapter 4, for solder bulk. Sn58Bi0.5In and Sn58Bi0.5In1Zn alloys were synthesized. The microstructural and mechanical properties of these new alloys were investigated in depth. The results show that the minor In and Zn addition has potential in solving the brittle issue of eutectic Sn58Bi alloy. Compared to eutectic Sn58Bi, the In & Zn-added Sn58Bi had finer microstructure, i.e., smaller eutectic spacing and fewer coarsened Bi grains, due to the Zn segregation phenomenon, while In had a negligible effect on the microstructure refinement. Elongation improvements of 36 % and 41 % were obtained in the Sn58Bi0.5In1Zn before and after 1008 h aging by conducting tensile tests. The softening of the Sn phase induced by the In solid solution was proposed in Sn58Bi0.5In and Sn58Bi0.5In1Zn. Quantitative hardness and creep data of individual Sn and Bi phases in each alloy were obtained. The fine microstructure induced by the Zn addition as well as the In solid solution triggered SSS were combined responsible for the elongation improvement and mechanical thermal reliability in Sn58Bi0.5In1Zn.

For solder joint, on Sn58Bi0.5In/ENIG interface, we observed a continues (Au, Ni)(Sn, In)4 IMC layer, which maintained its thickness and morphology during thermal aging. The shear strength, as a result, remained almost unchanged during aging (approximately 62 MPa both before and after aging). On the other hand, Au-In/AuZn3 IMC layers were observed on Sn58Bi0.5In1Zn/ENIG interface. The thickness and morphology of these IMC layers did not change during thermal aging as well. However, due to the brittleness of AuZn3 IMC layer, the fracture pathed through Au-In/AuZn3 IMC layers and Ni(P) layer. The shear strength of Sn58Bi0.5In1Zn joint was lower than that of Sn58Bi0.5In joint, but they were remained almost unchanged despite the aging time.

In Chapter 5, for solder bulk study, due to the simultaneous increase in the ductility and UTS of the newly designed Sn-45Bi-2.6Zn alloy, it is considered a promising low-temperature alloy to replace eutectic Sn-58Bi alloy. In Sn-45Bi-2.6Zn alloy, a very fine cross-sectional microstructure, Sn-Bi-Zn ternary structure, and higher volume fraction of Sn-rich phase compared to the eutectic Sn-58Bi alloy were observed. Thermodynamic calculations revealed the solidification reaction sequence of the Sn-45Bi-2.6Zn alloy. The reaction temperatures were comparable to those measured by DSC. Meanwhile, the reaction sequence was verified by the cross-sectional microstructure. The 112% increase in elongation of Sn-45Bi-2.6Zn alloy compared to eutectic Sn-58Bi was attributed to the higher Sn-to-Bi volume ratio. For solder joint study, sound ENIG/Sn45Bi2.6Zn/ENIG sandwich structure solder joints were obtained by using the same reflow profile of eutectic Sn58Bi solder alloy. A thin and thermally stable AuZn3 IMC layer formed on the Sn45Bi2.6Zn/ENIG interface. As a result, shear strength remained almost unchanged after aging for 1008 h.

Figure 6-1 and 6-2 show the elongation and UTS comparison of alloys in this thesis and some of commercialized SAC alloys as well as some InBi-based low temperature alloys. It is noted that the elongation of SAC alloys often located in the range between 40 % to 60 %. We set this range as our target elongation. On the other hand, for eutectic Sn58Bi, the elongation was 34.1 % before aging, which was lower than the target. By contrast, Zn added Sn58Bi, Sn58Bi0.5In1Zn and Sn45Bi2.6Zn all met the elongation target. Even after thermal aging for 1008 h, Sn58Bi0.5In1Zn and Sn45Bi2.6Zn were above the target. For the UTS, eutectic Sn58Bi based alloy all experiences superior UTS comparing with SAC alloys.

All in all, the Sn45Bi2.6Zn alloy was considered the best among all other newly designed alloys. For bulk alloy, Sn45Bi2.6Zn had the best tensile elongation and UTS properties both

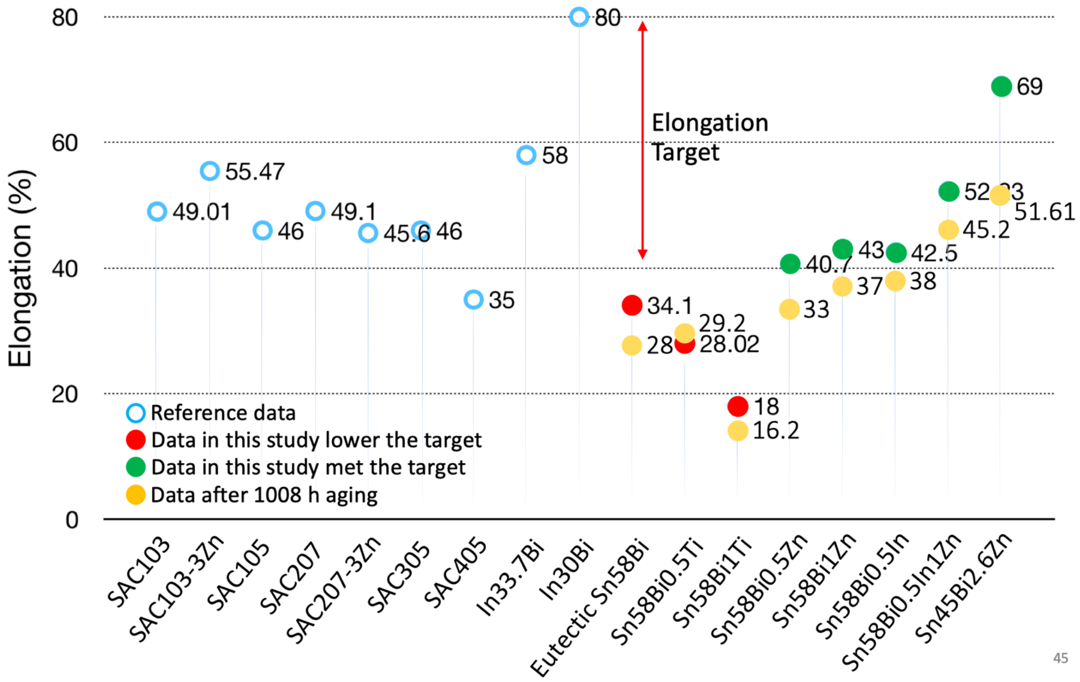

Figure 6-1 Elongation comparison of alloys in this study with commercialized SAC alloys and low temperature InBi alloy at the strain rate of approximately 0.0005/s [1]-[7].

before and after aging, owing to the largely reduced Bi content. For soldered joints, the Sn45Bi2.6Zn had low-melting temperature which similar to that of eutectic Sn58Bi alloy and better reliability than that of eutectic Sn58Bi.

6.2 Environmental assessment on various bonding materials

Low temperature lead-free solder alloys were considered environmentally friendly when considering energy consuming. The reflow peak temperature of the eutectic Sn58Bi alloy was generally decided to be round 182 °C, owing to its low-melting temperature of 139 °C. Comparing with some of the more traditional solder alloys, such as SAC305 with a melting point of 227 °C and Sn37Pb with a melting point of 183 °C. Low temperature solder alloys have their advantages in terms of energy consumption in mass production.

In the low temperature solder alloy category, the performance and cost of solder materials are imperative to be considered. Beside eutectic Sn58Bi alloy, a large amount of In is often included in other low temperature alloys, such as Bi33In, Sn52In, and Sn50In. The cost is high, which really is the reason restricting them from mass production. Table 6-1 shows the market price of solder elements appeared in this thesis [8]. Therefore, despite the mechanical performance and different usages of these solder alloys; Table 6-2 shows the accessibility of

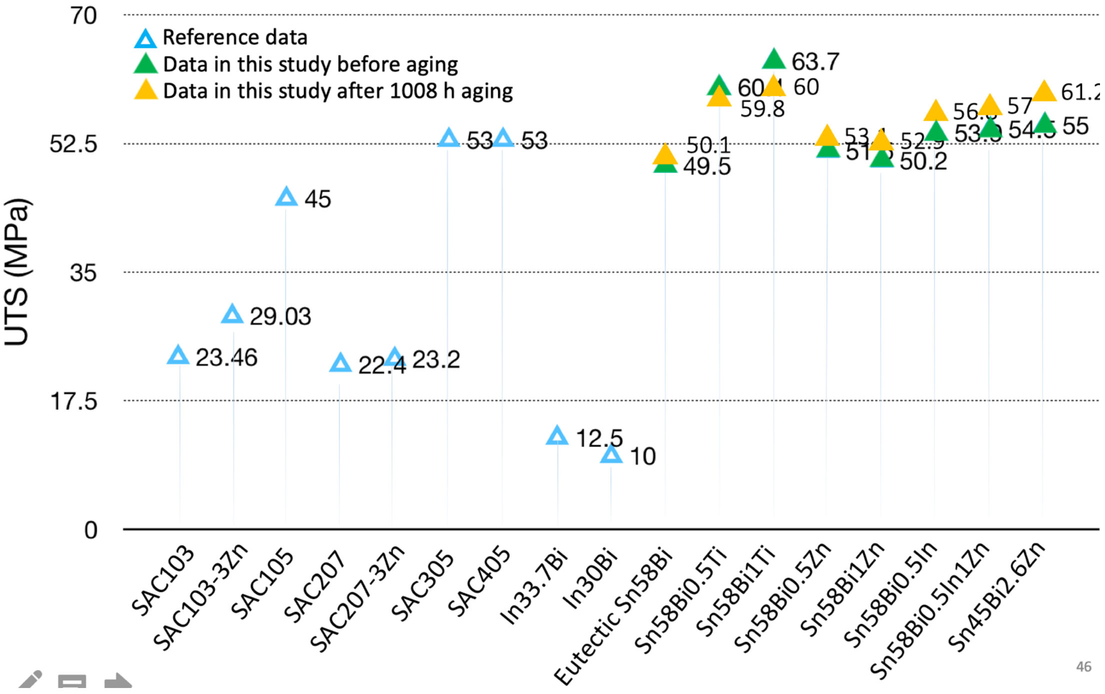

Figure 6-2 UTS comparison of alloys in this study with commercialized SAC alloys and low temperature InBi alloy at the strain rate of approximately 0.0005/s [1]-[7].

various element additions used in this thesis; Table 6-3 compares some popular solder alloys and various solder alloys developed in this thesis in terms of toxicity, reflow peak temperature, and price.

As shown in Table 6-2, the amount of Ti and Zn natural resources is sufficient, while In is rarer compared to the other two [9]–[11]. As Table 6-3 listed, Sn37Pb is banned in most consumer products due to its toxicity. Due to the high cost of In, the use of eutectic Bi33In solder alloy was limited greatly. For the solder alloys developed based on the eutectic Sn58Bi alloy. The same reflow profile used on eutectic Sn58Bi alloy was used for all newly developed alloys. Therefore, the energy consumption of these solder alloys were considered identical. By considering the cost, Ti added Sn58Bi alloys were relatively high compared with eutectic Sn58Bi alloy. The costs of Zn added Sn58Bi, Sn58Bi0.5In1Zn, and Sn45Bi2.6 were almost identical. In summary, a number of new alloys developed in this thesis, including Sn58Bi0.5Ti, Sn58Bi1Ti, Sn58Bi0.5Zn, Sn58Bi1Zn, Sn58Bi0.5In1Zn, and Sn45Bi2.6Zn were all evaluated as replacements of eutectic Sn58Bi in terms of environmental point of view. Basically same reflow temperature profile, reflow atmosphere (N_2 atmosphere) and same manufacturing processes were applied to all of these alloys. However, considering some toxic concern and relatively low accessibility of In compared to Ti and Zn. We consider the aforementioned

Table 6-2 Chemical elements by market price.

Element	Price (USD/kg)
Sn	20
Pb	2.29
Ag	463
Cu	5.9
In	341.6
Bi	10.34
Ti	7400
Zn	2.83

Sn58Bi0.5Ti, Sn58Bi1Ti, Sn58Bi0.5Zn, Sn58Bi1Zn and Sn45Bi2.6Zn are selected in the point of environmental impact.

In addition, the free zinc ion in solution is highly toxic to bacteria, plants, invertebrates, and vertebrate fish [12], [13]. On the other hand, Zinc is an essential trace element with very low toxicity in humans [14]. Therefore, recycling of electronic products contain Zn-added solder alloys should be of importance after the life cycle of these products.

6.3 Future work

6.3.1 Reduce the size of the Ti-Sn IMCs in Ti added Sn58Bi alloy.

In Chapter 2, it is noted that the size of Ti-Sn IMCs, especiallyTi6Sn5 IMCs had a size approximately several micrometers and some even over 10 micrometers in length. Even though

Table 6-3 Comparison of various solder alloys in terms of the environmental perspective. The summery is only depend on the impact factors listed in the table.

Solder alloys	Toxicity	Reflow peak temperature (°C)	Price (USD/kg)	Summery
Eutectic Sn37Pn	Toxic ban from ROHS	213	13.45	Forbidden
SAC305	-	Around 230	33.22	Fair
Eutectic Bi33In	Toxic of Indium compound	Around 120	119.65	Doubtful
Eutectic Sn58Bi	-	182	14.40	Excellent
Sn58Bi with 0.5/1Ti	-	182	51.33/ 88.26	Fair
Sn58Bi with 0.5/1Zn	-	182	14.45/ 17.13	Excellent
Sn58Bi0.5In1Zn	Toxic of Indium compound	182	15.89	Fair
Sn45Bi2.6Zn	-	182	15.01	Excellent

the microstructure of Sn58Bi0.5Ti and Sn58BiTi were greatly refined because the present of Ti-Sn IMCs. The large size Ti-Sn IMCs could cause the stress concentration and cracks may initiate from these IMCs. As a consequence, the mechanical property of either solder bulk or solder joint maybe deteriorated. We measured the elongation of Ti added Sn58Bi was lower than eutectic Sn58Bi alloy before aging and the reason was contributed to the existence of large size Ti-Sn IMCs. On the other hand, after the shear test, voids were observed inside the solder joints. The existence of Ti6Sn5 was the season as well. In the future study, we propose that, by control the cooling rate of solder alloy during casting, to achieve refined Ti-Sn IMCs with much uniformed size.

Table 6-3 Accessibility of the minor additives used in the thesis [2]-[4].

Element	Accessibility	Production and reservation
Ti	Common	World production of the metal is about 90,000 tons per year, and that of titanium dioxide is 4.3 million tons per year.
Zn	Very common	World production exceeds 7 million tons per year.
In	Rare	Estimated reserved amount is 1500 tones.

6.3.2 Optimizing the Sn45Bi2.6Zn alloy

In Chapter 5, the design of the Sn45Bi2.6Zn alloy was based on the idea of having the same liquidus temperature of eutectic Sn58Bi alloy, which is 140 °C. In the future work, another idea based on the thermal dynamic calculation should be implemented. Figure 6-1a shows the liquidus projection of Sn-Bi-Zn ternary diagram. The ternary eutectic point was indicated in the diagram. The eutectic point was calculated to be 129.86 °C, which was lower than the eutectic point of eutectic Sn58Bi alloy (140 °C). Moreover, the composition of each element on this eutectic point was Sn54.58Bi2.71Zn. Because of the lower melting temperature than that of eutectic Sn58Bi, reflow profiles with lower peak temperature can be potentially applied during reflow process. However, in order to control the accurate composition of the designed alloy, vacuumed alloying environment is required by eliminating the oxidation and contamination.

In addition, the elongation of Sn45Bi2.6Zn decreased from approximately 69 % to 52 %. This elongation decrease was considered not ideal in terms of reliability. As discussed in Chapter 5, microstructure coarsened for Sn45Bi2.6Zn after thermal aging as well, although it was much finer than that of eutectic Sn58Bi. Therefore, I propose a solution of alloying a minor amount of In (approximately 0.5 wt.%) into Sn45Bi2.6Zn, since In has softening effect on Sn phase in eutectic Sn58Bi, as we discussed in Chapter 4. The addition of In may make up the elongation decrease of Sn45Bi2.6Zn after aging.

6.3.3 Nanoindentation test on alloys after been thermal aged

In Chapter 3 and 4, nanoindentation test was implemented to reveal the mechanical property of individual phases, i.e., Sn and Bi phases. A clear and strong correlation between the mechanical properties of each phases and the mechanical properties of entire solder bulk was understood. However, we only implemented the nanoindentation test on before aged samples and we believe after aged samples also need to be tested. We use Sn58Bi1Zn alloy as an example. The SSS of Sn phase in Sn58Bi1Zn was proposed because of the Zn solid solution. The evidence of SSS was represented by the large hardness decrease of Sn phase in Sn58Bi1Zn revealed by nanoindentation test. However, during thermal aging, it was observed that Zn segregated from solid solution to on the Sn-Bi phase boundary. Tensile test results show that elongation decreased for Sn58Bi1Zn after aging and we suggested the reduce of SSS effect on Sn phase could be the reason since the amount of Zn solid solution reduced. However, this assumption was not proved. In the future project, nanoindentation tests on Sn and Bi phase in after aged Sn58Bi1Zn alloy was proposed.

References

[1] El-Daly, A.A., Hammad, A.E., Al-Ganainy, G.S. and Ragab, M., 2014. Properties enhancement of low Ag-content Sn–Ag–Cu lead-free solders containing small amount of Zn. *Journal of Alloys and Compounds*, *614*, pp.20-28.

[2] Suh, D., Kim, D.W., Liu, P., Kim, H., Weninger, J.A., Kumar, C.M., Prasad, A., Grimsley, B.W. and Tejada, H.B., 2007. Effects of Ag content on fracture resistance of Sn–Ag–Cu lead-free solders under high-strain rate conditions. *Materials Science and Engineering: A*, *460*, pp.595-603.

[3] El-Daly, A.A., El-Hosainy, H., Elmosalami, T.A. and Desoky, W.M., 2015. Microstructural modifications and properties of low-Ag-content Sn–Ag–Cu solder joints induced by Zn alloying. *Journal of Alloys and Compounds*, *653*, pp.402-410.

[4] Zhou, S., Yang, C.H., Lin, S.K., AlHazaa, A.N., Mokhtari, O., Liu, X. and Nishikawa, H., 2019. Effects of Ti addition on the microstructure, mechanical properties and electrical

resistivity of eutectic Sn58Bi alloy. *Materials Science and Engineering: A*, *744*, pp.560-569.

[5] Zhou, S., Mokhtari, O., Rafique, M.G., Shunmugasamy, V.C., Mansoor, B. and Nishikawa, H., 2018. Improvement in the mechanical properties of eutectic Sn58Bi alloy by 0.5 and 1 wt% Zn addition before and after thermal aging. *Journal of Alloys and Compounds*, *765*, pp.1243-1252.

[6] Zhou, S., Shen, Y.A., Uresti, T., Shunmugasamy, V.C., Mansoor, B. and Nishikawa, H., 2019. Improved mechanical properties induced by In and In & Zn double additions to eutectic Sn58Bi alloy. *Journal of Materials Science: Materials in Electronics*, pp.1-12.

[7] Zhou, S., Yang, C.H., Shen, Y.A., Lin, S.K. and Nishikawa, H., 2019. The newly developed Sn-Bi-Zn alloy with a low melting point, improved ductility, and high ultimate tensile strength. *Materialia*, p.100300.

[8] “Chemical elements by market price.” [Online]. Available: http://www.leonland.de/elements_by_price/en/. [Accessed: 22-Apr-2019].

[9] “Zinc (Zn) - Chemical properties, Health and Environmental effects.” [Online]. Available: https://www.lenntech.com/periodic/elements/zn.htm. [Accessed: 25-May-2019].

[10] “Indium (In) - Chemical properties, Health and Environmental effects.” [Online]. Available: https://www.lenntech.com/periodic/elements/in.htm. [Accessed: 25-May-2019].

[11] “Titanium (Ti) - Chemical properties, Health and Environmental effects.” [Online]. Available: https://www.lenntech.com/periodic/elements/ti.htm. [Accessed: 25-May-2019].

[12] Rout, Gyana Ranjan; Das, Premananda (1 January 2003). "Effect of Metal Toxicity on Plant Growth and Metabolism: I. Zinc". *Agronomie*. **23** (1): 3–11.

[13] Brita, T. A.; De Schamphelaere, Muyssen; Karel, A. C.; Janssen, Colin R. (2006). "Mechanisms of chronic waterborne Zn toxicity in Daphnia magna". *Aquatic Toxicology*. **77** (4): 393–401.

[14] Fosmire GJ (February 1990). "Zinc toxicity". *Am. J. Clin. Nutr*. **51** (2): 225–7.

Research achievement

I List of publication

Peer-reviewed journal articles

- **Zhou, S**., Mokhtari, O., Rafique, M.G., Shunmugasamy, V.C., Mansoor, B. and Nishikawa, H., 2018. Improvement in the mechanical properties of eutectic Sn58Bi alloy by 0.5 and 1 wt.% Zn addition before and after thermal aging. *Journal of Alloys and Compounds. 765,* pp.1243-1252.
- **Zhou, S.**, Yang, C.H., Lin, S.K., AlHazaa, A.N., Mokhtari, O., Liu, X. and Nishikawa, H., 2018. Effects of Ti addition on the microstructure, mechanical properties and electrical resistivity of eutectic Sn58Bi alloy. *Materials Science and Engineering: A. 744,* pp.560-569.
- **Zhou, S.**, Shen, Y.A., Uresti, T., Shunmugasamy, V.C., Mansoor, B. and Nishikawa, H., 2019. Improved mechanical properties induced by In and In & Zn double additions to eutectic Sn58Bi alloy. *Journal of Materials Science: Materials in Electronics*, pp.1-12.
- **Zhou, S.,** Yang, C.H., Shen, Y.A., Lin, S.K. and Nishikawa, H., 2019. The newly developed Sn-Bi-Zn alloy with a low melting point, improved ductility, and high ultimate tensile strength. *Materialia*, p.100300.
- **Zhou, S.**, He, S., Nishikawa, H., Effect of Zn addition on interfacial reactions and mechanical properties between eutectic Sn58Bi solder and ENIG substrate. *Journal of Nanoscience and Nanotechnology*, Accepted.

- Shen, Y.A., **Zhou, S.** and Nishikawa, H., 2019. Preferred Orientation of Bi and Effect of Sn-Bi Microstructure on Mechanical and Thermomechanical Properties in Eutectic Sn-Bi Alloy. *Materialia*, p.100309.
- Yang, C.H., **Zhou, S.**, Lin, S.K. and Nishikawa, H., 2019. A Computational Thermodynamics-Assisted Development of Sn-Bi-In-Ga Quaternary Alloys as Low-Temperature Pb-Free Solders. *Materials*, *12*(4), p.631.
- Shen, Y.A., **Zhou, S.**, Li, J., Tu, K.N. and Nishikawa, H., 2019. Thermomigration induced microstructure and property changes in Sn-58Bi solders. *Materials & Design*, *166*, p.107619.
- Liu, X., **Zhou, S**. and Nishikawa, H., 2017. Thermal stability of low-temperature sintered joint using Sn-coated Cu particles during isothermal aging at 250° C. *Journal of Materials Science: Materials in Electronics*, *28*(17), pp.12606-12616.
- Mokhtari, O., **Zhou, S**. and Nishikawa, H., 2016. Effect of Zn addition on interfacial reactions between Sn-Bi solder and Cu substrate. *Materials Transactions*, *57*(8), pp.1272-1276.
- (In preparation for Journal of Alloys and Compounds) Yu-An, S., **Zhou, S.**, Li, J.H., He, S., Nishikawa, H. Cu/Composite Solder/Cu Joints with melting Point at 176C Assembled by Low-temperature Reflow Profile

Conference Proceedings

- **Zhou, S.**, Liu, X., Mokhtari, O. and Nishikawa, H., 2017, August. The evaluation of mechanical properties of Sn58BiXTi solder by tensile test. In *Electronic Packaging Technology (ICEPT), 2017 18th International Conference on* (pp. 703-707). IEEE.
- **Zhou, S.**, Mokhtari, O. and Nishikawa, H., 2018, May. Improvement of Mechanical Properties of Zn-Added Sn58Bi Alloy by Zn Segregation on the Sn-Bi Phase Boundaries During Thermal Aging. In *2018 IEEE 68th Electronic Components and Technology Conference (ECTC)* (pp. 1899-1905). IEEE.
- Yang, C.H., **Zhou, S.**, Nishikawa, H. and Lin, S.K., 2018, April. Mechanical properties of Sn-Bi-In-Ga low melting temperature solder alloys. In *Electronics Packaging and iMAPS All Asia Conference (ICEP-IAAC), 2018 International Conference on* (pp. 409-410). IEEE.

II List of presentations

- (Oral) 2019 IEEE 69th Electronic Components and Technology Conference (ECTC 2019)
- (Oral) 2019 International Conference on Electronics Packaging (ICEP 2019)
- (Poster) 2018 IEEE 68th Electronic Components and Technology Conference (ECTC 2018)
- (Oral) the 5th International Conference on Electronic Materials and Nanotechnology for Green Environment (ENGE 2018)
- (Oral) 2018 Japan-Taiwan Workshop on Electronic Interconnection II
- (Oral) Electronic Packaging Technology (ICEPT), 2017 18th International Conference
- (Oral) 2017 International Conference on Electronics Packaging (ICEP 2017)

Acknowledgment

In the doctoral course study, I had to take the help and guidance of some respected person, who deserve my deepest gratitude.

Firstly, I would like to show my gratitude to my adviser, Professor Hiroshi Nishikawa, for giving me the opportunity to do research and providing me invaluable guidance throughout the research and preparing the thesis. His dynamism, vison, kindness and motivation have deeply inspired me. It was a great privilege and honor to work and study under his guidance.

Besides my adviser, I thank the rest of my thesis committee:. In addition, I thank the technical support from Mr. Kenji Asano and Ms. Kunisuke Uehara for their irreplaceable guidance.

I thank members and alumni of Nishikawa Lab, especially, Ms. Satomi Takahashi, Dr. Omid Mokhtari, Dr. Myonghoon Roh, Dr. Min-Su Kim, Dr. Yu-An Shen, Dr. Xiangdong Liu, Mr. Siliang He, Mr. Sanghun Jin, Mr. Runhua Gao, Mr. Zhi Jin, Mr. Fupeng Huo, Mr. Jiahui Li, Mr. Sijie Huang and Mr. Laizhou Zhou. Without their support and advices, it would be impossible to finish this research.

Also, I give my great appreciation to Associate Professor Shih-kang Lin in National Cheng Kung University for providing me a number of opportunities to do collaborations. I thank Mr. Chih-han Yang in Lin's lab for helping me on several of collaborated projects.

I thank Ms. Yu-Shan Chiu for her patience and endless love and support.

Last but not least, I thank my parents for their love and care. Without them, I would not pursue my dream.